

X-RAY AND INFRARED DIAGNOSTICS OF STAR FORMATION AND
BLACK HOLE ACCRETION IN GALAXIES

by
Jane Rebecca Rigby

A Dissertation Submitted to the Faculty of the
DEPARTMENT OF ASTRONOMY
In Partial Fulfillment of the Requirements
For the Degree of
DOCTOR OF PHILOSOPHY
In the Graduate College
THE UNIVERSITY OF ARIZONA

2006

THE UNIVERSITY OF ARIZONA
GRADUATE COLLEGE

As members of the Dissertation Committee, we certify that we have read the dissertation prepared by Jane Rebecca Rigby entitled "X-ray and Infrared Diagnostics of Star Formation and Black Hole Accretion in Galaxies" and recommend that it be accepted as fulfilling the dissertation requirement for the Degree of Doctor of Philosophy.

George Rieke

Date: 8 March 2006

Peter Strittmatter

Date: 8 March 2006

Jill Bechtold

Date: 8 March 2006

Xiaohui Fan

Date: 8 March 2006

Richard Green

Date: 8 March 2006

Final approval and acceptance of this dissertation is contingent upon the candidate's submission of the final copies of the dissertation to the Graduate College.

I hereby certify that I have read this dissertation prepared under my direction and recommend that it be accepted as fulfilling the dissertation requirement.

Dissertation Director: George Rieke

Date: 8 March 2006

STATEMENT BY AUTHOR

This dissertation has been submitted in partial fulfillment of requirements for an advanced degree at The University of Arizona and is deposited in the University Library to be made available to borrowers under rules of the Library.

Brief quotations from this dissertation are allowable without special permission, provided that accurate acknowledgment of source is made. Requests for permission for extended quotation from or reproduction of this manuscript in whole or in part may be granted by the head of the major department or the Dean of the Graduate College when in his or her judgment the proposed use of the material is in the interests of scholarship. In all other instances, however, permission must be obtained from the author.

SIGNED: Jane Rebecca Rigby

ACKNOWLEDGMENTS

Boy, I'd better thank some people!

First, astronomers who aided my research: Almudena Alonso-Herrero, Lei Bai, Jeremy Bailin, Jill Bechtold, Myra Blaylock, Jenn Donley, Romeel Davé, Eiichi Egami, Chad Engelbracht, John Feldmeier, Gary Ferland, Rob Kennicutt, Lisa Kewley, Emeric Le Floc'h, Andrea Leistra, Claus Leitherer, John Moustakas, Jane Morrison, Gerry Neugebauer, Matt Page, Casey Papovich, Pablo Pérez-González, Marcia Rieke, Yong Shi, Gyula Szokoly, Christy Tremonti, Marianne Vestergaard, Mike Werner, my prelim committee, and my thesis committee.

Second, the indispensable people of Steward: Erin Carlson, Michelle Cournoyer, Catalina Diaz-Silva, Joy Facio, Jeff Fookson, Carmen Henley, Neal Lauver, and Lee Ann Norvelle.

Third, the current and former graduate students of Steward Observatory and especially the Not Ready for Dark Time Players, with special shouts out to Jeremy Bailin, Beth Biller, Richard Cool, Jenn Donley, Kris Eriksen, Kristian Finlator, Chris Groppi, Abby Hedden, Karen Knierman, Craig Kulesa, Wilson Liu, Eric Mamajek, Andy Marble, Iva Momcheva, Jackie Monkiewicz, Eric Nielsen, Tim Pickering, Moire Prescott, Wayne Schlingman, and Suresh Sivanandam.

Also Matt "Zernike Boy" Kenworthy, Murray Silverstone, and Alyson Ford.

Next, the Penn State Astronomy department, especially Don Schneider, Robin Ciardulo, Niel Brandt, and my undergraduate research advisor, Jane Charlton.

I gratefully acknowledge the following financial support: a Graduate Research Fellowship from the National Science Foundation; a Graduate Research Fellowship from UofA; and research funding from NASA through George Rieke's MIPS grant. And ultimately, the American taxpayers for supporting astronomical research. I'd also like to thank the thousands of people whose efforts brought to life the *Spitzer*, *Chandra*, and *Hubble* space observatories.

Special thanks to my advisor, George Rieke. For the last five years I've been trying to figure out how he does it – staying current on many fields; managing projects and people; seeing the big picture and triaging the most important science; really enjoying doing great science. I'm not sure how much I've learned, but I've been watching closely.

Last, let me thank especially thank Catamaran Fleet 42, the Olszewski/Bechtolds, the Roses, the Rosens, the Leistras, and the Rigbys.

Thanks also to the musicians I listened to while working on this research: Amy Ray, Emily Saliers, Edgar Meyer, John Hiatt, Bill Morrissey, Bob Mould, Bela Fleck, The Butchies, Sleater-Kinney, Jawbox, Hum, Bessie Smith, Louis Armstrong, and Ella Fitzgerald.

DEDICATION

This thesis is dedicated to my family:

To my parents, Julie and Wayne Rigby, for encouragement, patience, and love.
When I asked them why the sky is blue, they told me.
When I asked them if the stars in the Big Dipper move, they gave me *Cosmos*.
And always, they believed in me.

To my sister, Elizabeth Rigby, for being herself.

To Roger, Cleone, Paul, and Daniel Leistra, for welcoming me to their family.

And to my partner, Andrea Leistra, for more than I have words to say.

As I sat out front on the walk afterward, in the evening air, the church-choir and organ on the corner opposite gave Luther's hymn, Ein feste berg, very finely. The air was borne by a rich contralto. For nearly half an hour there in the dark. . . came the music, firm and unhurried, with long pauses. The full silver star-beams of Lyra rose silently over the church's dim roof-ridge. Varicolor'd lights from the stain'd glass windows broke through the tree-shadows. And under all—under the Northern Crown up there, and in the fresh breeze below, and the chiaroscuro of the night, that liquid-full contralto.

—Walt Whitman, from *Prose Works*

TABLE OF CONTENTS

LIST OF FIGURES	9
LIST OF TABLES	10
ABSTRACT	11
CHAPTER 1 INTRODUCTION	13
CHAPTER 2 MISSING MASSIVE STARS IN STARBURSTS: STELLAR TEMPERA- TURE DIAGNOSTICS AND THE IMF	19
2.1 Introduction	20
2.2 Observations, Data Reduction, and Calibration	22
2.2.1 Data Reduction	23
2.2.2 Combining Spectra	26
2.2.3 Subtracting the Stellar Continuum	27
2.2.4 Measuring Line Ratios	28
2.3 Modelling Line Ratio Behavior	31
2.3.1 Models Using Individual Stars	34
2.3.2 Spectral Synthesis Models	37
2.4 Diagnostics of Stellar T_{eff} In Starburst Galaxies	40
2.4.1 Approaches to Estimating T_{eff}	40
2.4.2 Testing He I 2.06 μm /Br γ	46
2.4.3 Testing Optical T_{eff} Indicators	50
2.4.4 Testing the Mid-Infrared Fine Structure Line Ratios	55
2.5 Diagnosing Ionizing Conditions in Starbursts	61
2.5.1 Mid-Infrared Line Ratio Dependencies	61
2.5.2 The Spectrum of the Ionizing Radiation	65
2.5.3 Ionizing Conditions in Low Metallicity Starbursts	69
2.5.4 Caveats and Assumptions	70
2.5.5 UV and Nebular Diagnostics in Conflict?	72
2.6 Discussion	75
2.7 Conclusion	80
CHAPTER 3 THE 24 μm PROPERTIES OF X-RAY SELECTED AGN	83
3.1 Introduction	83
3.2 The Data and Catalogs	84
3.3 Sample Selection	86
3.4 Comparing X-ray and 24 μm colors	87
3.5 Discussion	92
3.6 Conclusions	97

TABLE OF CONTENTS — *Continued*

CHAPTER 4	THE NATURE OF LUMINOUS X-RAY SOURCES WITH MID-INFRARED COUNTERPARTS	99
4.1	Explanatory Note	99
4.2	Introduction	99
4.3	Spitzer Observations	101
4.4	X-ray Observations	101
4.5	Cross-correlation of X-ray and $24\,\mu\text{m}$ sources	102
4.6	Activity classification	102
4.7	Spectral Energy Distributions	107
CHAPTER 5	WHY OPTICALLY-FAINT AGN ARE OPTICALLY-FAINT: THE <i>Spitzer</i> PERSPECTIVE	112
5.1	Introduction	112
5.2	The X-ray-to-Optical Flux Ratio and Sample Selection	114
5.3	<i>Spitzer</i> Observations, Photometry, and SEDs	116
5.4	Properties of the Complete SED sample	117
5.4.1	Spectral Properties	117
5.4.2	Redshift Techniques and Previously-Estimated Redshifts	123
5.4.3	New Photometric Redshift Estimations	125
5.4.4	The Redshift Distribution of the Optically-Faint CSS AGN	127
5.4.5	The Luminosity Function of Optically-Faint AGN	128
5.5	Other Optically-Faint Sources	130
5.6	Conclusions	131
CHAPTER 6	WHY X-RAY-SELECTED AGN APPEAR OPTICALLY DULL	133
6.1	Introduction	133
6.2	Insight from low-redshift Seyfert samples	135
6.3	Sample selection and data	136
6.4	Do optically-dull AGN have weak ionizing continua?	144
6.4.1	Do the low-obscuration AGN have big blue bumps?	144
6.4.2	Do their SEDs show AGN-like mid-IR emission?	145
6.4.3	Do they have stellar or AGN-like $\text{H}\beta/24\,\mu\text{m}$ ratios?	146
6.4.4	Do they have AGN-like mid-IR to X-ray luminosities?	152
6.5	How important is dilution to optical dullness?	155
6.5.1	Are optically-dull AGN at $z\sim 1$ like weak-line AGN at $z\sim 0$?	156
6.5.2	X-ray to optical flux and luminosity ratios	157
6.6	Can Host Galaxy Obscuration Cause Optical-Dullness in AGN?	160
6.6.1	Measuring Axis Ratios	162
6.6.2	Axis Ratios of the $0.5 < z < 0.8$ Subsample	163
6.6.3	Additional Axis Ratios from $z < 0.5$ and $z > 0.8$ AGN	175

TABLE OF CONTENTS — *Continued*

6.6.4	Column density evidence for extra obscuration	176
6.7	Discussion	176
6.8	Conclusions	180
CHAPTER 7 CONCLUSIONS, CONTEXTUALIZATION, AND FUTURE DIRECTIONS		182
7.1	Starburst Effective Temperature and the Starburst Initial Mass Function	182
7.2	Infrared SEDs of X-ray–Selected AGN, and Nuclear Geometry . . .	184
7.3	Redshift Distribution of X-ray–Selected AGN	185
7.4	Nuclear and Host Galaxy Obscuration of AGN	186
7.5	Missing and Highly Obscured AGN	188
REFERENCES		192

LIST OF FIGURES

2.1	H-band spectra of starburst galaxies.	29
2.2	K-band spectra of starburst galaxies.	30
2.3	Line ratios for solar-metallicity Cloudy models.	39
2.4	Line ratios for low-metallicity Cloudy models.	41
2.5	Comparison of the near-infrared line ratios.	47
2.6	Comparison of [Ne III]/[Ne II] with He I 2.06 μm /Br γ	49
2.7	Testing optical indicators of T_{eff}	51
2.8	Testing [O III]/H β against He I 1.7 μm /Br 10.	52
2.9	[O III]/H β versus [Ne III]/[Ne II].	53
2.10	Ionization parameters for local starburst galaxies.	64
2.11	[Ne III]/[Ne II] ratios, observed and predicted from bursts.	67
2.12	[Ne III]/[Ne II] ratios, predicted from continuous star formation.	68
3.1	24 μm image of CDF-S.	88
3.2	Comparison of optical and X-ray AGN classification.	89
3.3	IR/X-ray color versus X-ray hardness.	91
3.4	Behavior of 24 μm /2-8 keV flux ratio with increasing obscuration.	93
3.5	24 μm to 2-8 keV flux ratios for CDFS AGN.	95
4.1	24 μm fluxes vs. 2 – 10 keV X-ray fluxes.	103
4.2	SED for EGS X-ray/24 μm sources.	104
4.3	Hard to soft flux ratio distributions for bright X-ray/24 μm sources.	106
4.4	SEDs of sources not detected at 24 μm	108
5.1	X-ray photon indices for Optically-faint AGN.	118
5.2	SEDs of Optically-faint AGN.	119
5.3	The rest-frame 2-8 keV AGN luminosity function.	129
6.1	SEDs of optically-dull AGN: subsample A.	147
6.2	SEDs of optically-dull AGN: subsample B.	148
6.3	SEDs of the remaining optically-dull AGN.	149
6.4	Observed $f_{\nu}(24 \mu\text{m})/f(H\beta)$ ratio.	151
6.5	Ratio of L(6 μm) and L(X) versus inferred column density.	154
6.6	Column densities of optically-dull AGN.	158
6.7	R-band magnitude versus X-ray flux.	159
6.8	M_R versus absorption-corrected rest-frame 2-8 keV L(X).	161
6.9	Postage stamp images of optically-dull and optically-active AGN.	172
6.10	Axis ratio distributions.	173
6.11	Column density distributions.	177
7.1	Effect of absorption on Chandra spectra.	190

LIST OF TABLES

2.1	Log of Observations for Circumnuclear Starburst Galaxies	23
2.2	Near-Infrared Vacuum Line Wavelengths	28
2.3	Measured Line Ratios of Starburst Nuclei.	32
2.4	Model Predictions for Line Ratios.	38
2.5	Dependence of $C_{1.7}$ on Electron Temperature.	45
2.6	Testing optical T_{eff} diagnostics.	56
2.7	Comparison of Mid-IR and Near-IR T_{eff} diagnostics.	58
2.7	Comparison of Mid-IR and Near-IR T_{eff} diagnostics.	60
4.1	Positions, fluxes, and SEDs types for X-ray-selected AGN.	111
5.1	Multi-band Photometry and Redshifts for Optically-Faint AGN. . .	120
5.1	Multi-band Photometry and Redshifts for Optically-Faint AGN. . .	121
5.2	X-ray Photometry for the Optically-Faint AGN Sample.	122
5.2	X-ray Photometry for the Optically-Faint AGN Sample.	123
6.1	Optically-Dull AGN	138
6.1	Optically-Dull AGN	140
6.2	Optically-Active AGN	141
6.2	Optically-Active AGN	143
6.3	Axis Ratios for the Optically-Dull Sample.	165
6.3	Axis Ratios for the Optically-Dull Sample.	166
6.3	Axis Ratios for the Optically-Dull Sample.	167
6.4	Axis Ratios for the Optically-Active Sample.	168
6.4	Axis Ratios for the Optically-Active Sample.	169
6.4	Axis Ratios for the Optically-Active Sample.	170

ABSTRACT

Using infrared and X-ray diagnostics, we study star-formation and black hole accretion in nearby and distant galaxies.

We examine diagnostics of the hardness of the ionizing field in low-redshift starburst galaxies, to constrain the initial mass function. We obtain new measurements of HeI $1.7\ \mu\text{m}/\text{Br}\ 10$, a physically simple diagnostic, then test ISO mid-infrared line ratios, finding them reliable. Compared to new photoionization models, the ISO ratios in 27 nearby starburst galaxies are systematically low. This argues that solar-metallicity starbursts are deficient in massive stars, or that such stars are present but highly embedded.

Using Spitzer, HST, Chandra, and ground-based data, we examine the multi-wavelength ($0.4\text{--}24\ \mu\text{m}$) spectral energy distributions and X-ray properties of X-ray-selected active galactic nuclei (AGN) in several deep fields: the Chandra Deep Field South, the Lockman Hole, and the extended Groth Strip. We examine the $24\ \mu\text{m}$ to X-ray flux and luminosity ratios for 157 AGN at $z \sim 1$; the luminosity ratios have not strongly evolved since $z \sim 0$, and we find no trend with X-ray column density. This means that highly-obscured AGN do not have exceptional infrared fluxes. We examine the SEDs of 45 bright X-ray and $24\ \mu\text{m}$ sources: only 22% are classified as unobscured “type 1” AGN; 18% are classified as ULIRG-like SEDs; and the majority are classified as obscured (“type 2”) AGN or spiral-like SEDs. This supports the picture from X-ray surveys that much of the AGN activity in the distant universe is significantly obscured. We examine why 20% of X-ray-selected AGN are optically-faint; they lie at significantly higher redshifts (median $z = 1.6$) than most X-ray-selected AGN, and their spectra are intrinsically red. Their contribution to the X-ray Seyfert luminosity function is com-

parable to that of optically-bright AGN at $z > 1$, but they do not significantly alter the redshift distribution. Lastly, we investigate why half of X-ray-selected AGN lack signs of accretion in optical spectra. We find that these “optically-dull” AGN have Seyfert-like mid-infrared emission, which argues that they do not have abnormally-weak UV/optical continua. The axis ratios of their host galaxies argue that extinction by host galaxies plays a key role in hiding nuclear emission lines.

CHAPTER 1

INTRODUCTION

The history of the Universe’s star formation and black hole growth is recorded in the optical, infrared, and X-ray background radiation fields. As telescopes and detectors improve, we resolve these backgrounds into discrete sources, so that we may map out the growth of black holes and the stellar masses of galaxies with time.

Energetically, the most important background is the Cosmic Microwave Background (Penzias & Wilson, 1965), a relic of the formation of the universe. In second place with one-tenth the integrated energy content is the optical/infrared background, with a frequency-integrated brightness of $10^{-4} \text{ erg s}^{-1} \text{ cm}^{-2} \text{ Sr}^{-1}$ (0.16–1000 μm , Hauser & Dwek 2001). The energy in this background is divided roughly evenly above and below 3.5 μm ; longward of this, the background is dominated by thermal dust emission. Shortward of 3.5 μm , the background is comprised of emission from stars and active galactic nuclei (AGN) not reprocessed by dust. *This thesis focuses on the sources responsible for the IR background, namely star-forming galaxies and active galactic nuclei.*

Starting in the 1970s, several nearby star-forming galaxies (e.g. M82 and NGC 253) were discovered to be IR-luminous (see review in Rieke & Lebofsky 1979.) The IRAS satellite, launched in 1983, expanded this work, detecting over 2×10^4 galaxies in the infrared, including galaxies whose bolometric luminosities are emitted almost entirely in the infrared (Neugebauer et al., 1984). ISO, launched in 1993, pushed our understanding of luminous IR galaxies out to $z \sim 1$ (Rowan-Robinson et al., 2004), and showed that the mid-IR spectra of star-forming galaxies are dominated by strong emission lines, known as “unidentified infrared bands”,

and now assumed to be due to polycyclical aromatic hydrocarbons (PAHs). The study of IR-luminous galaxies took giant steps forward with the launch of the Spitzer Space Telescope on 25 August 2003. Spitzer’s 24 μm MIPS band can easily detect distant, star-forming galaxies: $L_{IR} = 10^{11} L_{\odot}$ galaxies out to $z \sim 1$, $L_{IR} = 10^{12} L_{\odot}$ galaxies out to $z \sim 2$, and $L_{IR} = 10^{13} L_{\odot}$ galaxies out to $z \sim 3$ (E. Le Floc’h, private comm.) This new view has shown us that the Universe’s star-formation rate above redshifts of $z = 0.7$ is dominated by galaxies with $L_{IR} > 10^{11} L_{\odot}$ (Le Floc’h et al., 2005); and that at redshifts above $z \sim 1.5$, the star-formation rate is dominated by galaxies with $L_{IR} > 10^{12} L_{\odot}$ (Pérez-González et al., 2005). Thus, most of the Universe’s stars were formed in dramatic bursts, rather than in slow, trickling star formation as still proceeds in the local universe.

Work in the 1970s also revealed that IR-brightness is a near-universal property of quasars (Oke et al., 1970) and Seyfert galaxies (Rieke 1978 and review in Rieke & Lebofsky 1979). IRAS dramatically expanded the number of known IR-luminous AGN to 900 (Spinoglio & Malkan 1989 and Rush et al. 1993, known respectively as the 12 μm and extended 12 μm samples.) ISO detected high-excitation fine-structure emission lines from AGN (e.g. [Ne III], [Ne V], [Ar III]), and showed that PAH features are weaker in galaxies with active nuclei (Genzel & Cesarsky, 2000). Diagnostic diagrams were made from the ISO emission line ratios and PAH feature strength ratios, and used to estimate the AGN contribution to ultraluminous infrared galaxies (Genzel et al., 1998).

Spitzer has further advanced AGN science. As I show in this thesis, deep surveys with Spitzer detect the majority of X-ray-selected AGN (see Rigby et al. 2004 and chapter 3). Spitzer has also proven an effective way to identify new samples of AGN, as I will discuss in chapter 7. This is important because existing selection methods (e.g. X-ray selection) may overlook roughly half the $z \sim 1$

AGN, especially the most obscured.

Thus, it is clear that the IR background is dominated by thermal emission from dust heated by newly-formed stars, and that by studying the sources responsible for the IR background, it's possible to map out the formation of stars with cosmic time. However, the IR background is not created solely by star-forming galaxies; dust heated by AGN is expected to contribute significantly, but this fractional contribution has not yet been well measured. Doing so requires obtaining high-quality SEDs for distant AGN (see chapter 4), as well as creating more complete AGN samples so that the most obscured AGN are not missed (see chapter 7).

While AGN are probably a minority contributor to the infrared background, they dominate the energetics of the extragalactic X-ray background (XRB) above 1 keV. This background is much weaker, with a frequency-integrated brightness of $\sim 2.4 \times 10^{-7} \text{ erg s}^{-1} \text{ cm}^{-2} \text{ Sr}^{-1}$ (converting fig. 1 of Gilli (2004) to specific intensities and integrating). Approximately 30% of that energy is contained in the 1–10 keV band. The spectrum of the X-ray background peaks in νf_ν at 30 keV, and is therefore harder than unobscured AGN. Thus, it has long been suspected that the X-ray background is produced by obscured AGN whose column densities exceed 10^{22} cm^{-2} (Setti & Woltjer, 1989; Comastri et al., 1995). Deep surveys with XMM/Newton and the Chandra X-ray Observatory have confirmed this by resolving 80–90% of the 2–6 keV background (Worsley et al., 2005).

Though pre-Chandra models of the X-ray background predicted that the unresolved sources were quasars at redshifts of $z \sim 1.4\text{--}2$ (Comastri et al., 1995; Pompilio et al., 2000; Wilman & Fabian, 1999; Wilman et al., 2000), the resolved sources turn out to be moderate-luminosity ($L \sim 10^{44} \text{ erg s}^{-1}$) AGN at moderate ($z = 1$) redshifts, with high space densities (as high as $10^{-4} \text{ Mpc}^{-1} \log L^{-1}$ at $10^{42} \text{ erg s}^{-1}$) La Franca et al. (2005); Steffen et al. (2003); Cowie et al. (2003). This is

a very different picture of black holes than presented by optically-selected QSO samples, e.g. the sample from the Sloan Digital Sky Survey, which has a median redshift of $z = 1.47$ (Schneider et al., 2005), higher luminosities, and lower space densities. These two pictures can be reconciled by luminosity-dependent density evolution, wherein low-luminosity AGN ($L_x \sim 10^{43} \text{ erg s}^{-1}$) are most common at $z \sim 0.7$, whereas high-luminosity AGN ($L_x > 10^{45} \text{ erg s}^{-1}$) are most common at $z \sim 2.0$ (La Franca et al., 2005). Thus, the sources that comprise the X-ray background have lower luminosities and redshifts than bright quasars.

Another surprise was that half the AGN selected by Chandra looked normal in follow-up optical spectra, i.e. no AGN emission lines (Mushotzky et al., 2000; Barger et al., 2001a,b; Szokoly et al., 2004). This was more evidence that X-ray and optical selection finds very different AGN, and begged for follow-up investigations to determine whether the lack of AGN lines was an observational effect or something intrinsically different about these AGN.

It should be pointed out that the harder ($> 10 \text{ keV}$) background remains largely unresolved, due to the difficulty of building telescopes that image high energy photons. Highly obscured AGN (with column densities exceeding 10^{24} cm^{-2}) are expected to contribute significantly near the 30 keV peak of the XRB, based on fits to the XRB shape (Comastri et al., 2001; Gilli et al., 2001; Ueda et al., 2003).

Why are obscured AGN the sources that so dominate the X-ray background? First off, local surveys (Maiolino & Rieke, 1995) and distant surveys (e.g. Barger et al. 2005) show that most AGN are indeed obscured, and that obscuration may correlate inversely with luminosity; so it's not surprising that the AGN that dominate the XRB are obscured. Non-AGN X-ray emitters like supernovae, x-ray binaries, and hot gas simply lack the luminosities and number densities to make an important contribution to the $> 1 \text{ keV}$ XRB. So even though AGN emit only a

few percent of their total energy in hard (2–8 keV) X-rays (e.g. Barger et al. 2005), they still dominate the XRB.

Thus, the X-ray background is overwhelmingly dominated by obscured AGN, with minor contributions from star-forming galaxies; whereas the infrared background is created by both AGN and stellar light. We can select AGN by their X-ray properties, then study their IR properties to learn more about the contribution AGN make to the IR background. The infrared data can also help us better understand these AGN, since AGN are IR-bright and IR photons are robust to large amounts of obscuration.

In this thesis I take advantage of two Great Observatories, the Chandra X-ray Observatory and the Spitzer Space Telescope, to explore star-forming galaxies and AGN. Chandra allows clean (but not complete) selection of AGN; Spitzer probes the energy emitted by buried AGN and stars that has been re-radiated by dust. The Spitzer data used in this thesis are from the MIPS GTO deep survey (PI: G. Rieke); the X-ray data are largely drawn from the deep Chandra surveys (Giacconi et al., 2002; Alexander et al., 2003); and ancillary data from the rest-frame UV to near-IR come from a variety of telescopes, including the Hubble Space Telescope.

This thesis is organized as follows. Chapter 2 develops and tests line diagnostics to measure the hardness of ionizing radiation from star-forming galaxies, and thus to measure the initial mass function of the newly-formed stars. We need to understand the initial mass function of starburst galaxies if we're to understand how starbursts have built up the stellar masses of galaxies. These techniques can also be used to measure the contribution (if any) from AGN. Chapter 3 presents the first look at the Spitzer 24 μm properties of Chandra-selected AGN, with the goal of testing whether X-ray obscuration and IR luminosity are correlated.

Chapter 4 examines the broad-band ($0.1 < \lambda_{rest} < 20 \mu\text{m}$) spectral energy distributions of AGN selected by XMM-Newton and Chandra. This bears on the connection between the infrared and X-ray backgrounds. Chapters 5 and 6 use Spitzer to address two mysteries concerning the X-ray-selected AGN that make up the X-ray background: why 20% have very high X-ray-to-optical flux ratios; and why half of X-ray-selected AGN show no signs of AGN activity in optical spectra. Chapter 7 puts these results in context and suggests avenues for future progress, including ways to identify AGN that are missed by X-ray selection (and thus are missing from this thesis' samples).

CHAPTER 2

MISSING MASSIVE STARS IN STARBURSTS: STELLAR TEMPERATURE
DIAGNOSTICS AND THE IMF

Determining the properties of starbursts requires spectral diagnostics of their ultraviolet radiation fields, to test whether very massive stars are present. We test several such diagnostics, using new models of line ratio behavior combining Cloudy, Starburst99 and up-to-date spectral atlases (Pauldrach et al., 2001; Hillier & Miller, 1998). For six galaxies we obtain new measurements of $\text{HeI } 1.7 \mu\text{m}/\text{Br } 10$, a difficult to measure but physically simple (and therefore reliable) diagnostic. We obtain new measurements of $\text{HeI } 2.06 \mu\text{m}/\text{Br } \gamma$ in five galaxies. We find that $\text{HeI } 2.06 \mu\text{m}/\text{Br } \gamma$ and $[\text{OIII}]/\text{H}\beta$ are generally unreliable diagnostics in starbursts. The heteronuclear and homonuclear mid-infrared line ratios (notably $[\text{NeIII}] 15.6 \mu\text{m} / [\text{NeII}] 12.8 \mu\text{m}$) consistently agree with each other and with $\text{HeI } 1.7 \mu\text{m}/\text{Br } 10$; this argues that the mid-infrared line ratios are reliable diagnostics of spectral hardness. In a sample of 27 starbursts, $[\text{NeIII}]/[\text{NeII}]$ is significantly lower than model predictions for a Salpeter IMF extending to $100 M_{\odot}$. Plausible model alterations strengthen this conclusion. By contrast, the low-mass and low-metallicity galaxies II Zw 40 and NGC 5253 show relatively high neon line ratios, compatible with a Salpeter slope extending to at least $\sim 40\text{--}60 M_{\odot}$. One solution for the low neon line ratios in the high-metallicity starbursts would be that they are deficient in $\gtrsim 40 M_{\odot}$ stars compared to a Salpeter IMF. An alternative explanation, which we prefer, is that massive stars in high-metallicity starbursts spend much of their lives embedded within ultra-compact HII regions that prevent the near- and mid-infrared nebular lines from forming and escaping. This hypothesis has important consequences for starburst modelling and

interpretation.

2.1 Introduction

In the very local ($D < 5h_{100}^{-1}$) Universe, the circumnuclear regions of just four galaxies (M82, NGC 253, NGC 4945, and M83) are responsible for $\sim 25\%$ of the current massive star formation (Heckman, 1997). In these “circumnuclear starburst galaxies”, the star formation is confined to the inner 0.2 to 2 kpc, in a dense, gas-rich disk where star formation rates can reach $1000 \text{ M}_{\odot} \text{ yr}^{-1}$ (Kennicutt, 1998a). If the starburst initial mass function (IMF) includes significant numbers of low-mass stars, then each starburst is currently building up the stellar component of its host galaxy as well. A starburst enriches and heats its interstellar medium, as well as the local intergalactic medium. Starbursts can also drive large-scale winds that eject interstellar gas, presumably casting metals into the voids and heating the gas between galaxies. Starburst galaxies thus play a number of important roles in galaxy evolution.

If starbursts could be dated, then a sequence could be pieced together, charting starburst evolution from triggering to post-starburst quiescence. Starburst ages are most directly determined by understanding the population of rapidly evolving massive stars. The feedback effect of a starburst on its gas supply is transmitted through massive stellar winds and supernovae-driven superwinds. Thus, understanding the evolution of starbursts and their effects on the interstellar and intergalactic media both critically depend on understanding the populations of massive stars.

Unfortunately, since starburst galaxies are too far away to count individual stars, the high-mass IMF must be determined indirectly, in ways that are model-dependent and crude. Leitherer (1998) reviews these techniques and divides

them into three categories: techniques to determine a lower mass cutoff by measuring the mass-to-light ratio; to find the slope of the IMF above $\sim 10 M_{\odot}$; and to determine an upper mass cutoff from the hardness of the ionizing radiation field.

The ionizing spectrum is set by the starburst's age, IMF, and star formation history. Consequently, the shape of the ionizing field spectrum is an important boundary condition on starburst models (Rieke, 2000). Ionizing continua are often parameterized by an effective temperature (T_{eff}), as if one stellar spectral type were responsible for the flux. The UV spectrum cannot be measured directly because little ionizing continuum radiation escapes from a starburst (Leitherer et al., 1995). Instead, the presence or absence of massive stars must be inferred using spectral diagnostics. Extinction in circumnuclear starbursts means that infrared diagnostics are preferred.

Many line ratios have been used to estimate starburst T_{eff} : forbidden line ratios, mixed forbidden–recombination line ratios like $[OIII]/H\beta$, optical lines of HeI, the near-infrared line HeI 2.06 μm , and mid-infrared fine structure lines for example. Unfortunately, these diagnostics disagree by 2,000 to 5,000 K (Vanzi & Rieke, 1997; Thornley et al., 2000; Rieke, 2000), and suffer variously from intrinsic faintness, susceptibility to shocks and reddening, dependence on nebular conditions, and uncertain atomic constants.

In this paper, we use the ratio of HeI 1.7 μm to Brackett 10 (Br10) to diagnose the hardness of starburst ionizing fields. The faintness of the HeI 1.7 μm line restricts its measurement to nearby galaxies with strong emission lines. In these galaxies, the HeI/Br10 ratio should allow estimates of T_{eff} that are largely independent of reddening or nebular conditions. We then use HeI/Br10 to assess the accuracy of diagnostics that can reach distant galaxies. Using diagnostics we find reliable, we confirm that few massive starburst galaxies have high–

excitation spectra. While this may occur because the IMF is biased against high-mass stars, we propose that high-excitation spectra are scarce because the massive stars spend most of their main sequence lifetimes embedded in ultracompact HII regions.

2.2 Observations, Data Reduction, and Calibration

To assist in evaluating T_{eff} diagnostics, we have obtained new measurements of HeI $1.7 \mu\text{m}/\text{Br}10$. This diagnostic is unaffected by metallicity, shocks, or level pumping. Regrettably, the HeI $1.7 \mu\text{m}$ line is very weak, less than 10% the intensity of $\text{Br}\gamma$. Thus, the HeI $1.7 \mu\text{m}/\text{Br}10$ ratio can only be measured in nearby starbursts with bright lines.

For our sample, we chose six nearby starburst galaxies with large measured $\text{Br}\gamma$ fluxes and, when possible, supporting observations in the literature such as mid-infrared spectra. Near-infrared spectra were obtained on the nights of 2001 April 6 and 7, using the FSPEC near-infrared spectrometer (Williams et al., 1993) on the Steward Observatory Bok 2.3 m telescope.

Table 2.2 lists target objects and integration times. All observations were taken with the $600 \text{ lines mm}^{-1}$ grating, which produces effective resolutions of $R \approx 2000$ at $1.7 \mu\text{m}$ and $R \approx 3000$ at $2.1 \mu\text{m}$. The slit was $2.4''$ by $90''$. All exposures were guided by hand using an H-band camera that images the mirrored slit. Spectra of the six targets were obtained in H-band ($1.7 \mu\text{m}$). K-band ($2.1 \mu\text{m}$) spectra were also obtained unless high-quality spectra already existed in the literature.

The angular sizes of the nuclear starburst regions are small compared to the length of the FSPEC slit. For each integration, nuclear spectra were obtained at four successive positions along the slit. For the calibration stars, six spectra were

Table 2.1 Log of Observations for Circumnuclear Starburst Galaxies

Source	Integration times (seconds)		
	@1.7 μm	@2.08 μm	@2.15 μm
He 2-010	3840
NGC 3077	5760	960	960
NGC 3504	5760	480	480
NGC 4102	6720	960	960
NGC 4214	1920	480	480
NGC 4861	5760
NGC 6217	...	960	960

taken along the slit. (For brevity, we will call each resulting two-dimensional spectrum a “frame”, and each group of frames in an integration a “set”.)

2.2.1 Data Reduction

The infrared H I and He I lines are faint, making the data reduction approach critical. We therefore describe it in detail. The data were reduced using *iraf*.¹ First, dark frames were subtracted from the object frames. Each frame was then flat-fielded using a median-averaged lamp flat. The airglow and bias were removed by differencing neighboring frames. For the first and last frames of a set, the neighbor was subtracted. For each middle frame, the mean of the immediately-bracketing frames was subtracted. For the calibration stars the subtraction was simple. Over the longer integration times required for the galaxies (~ 4 minutes per frame), the sky background is variable. Accordingly, prior to subtraction, we

¹IRAF is distributed by the National Optical Astronomy Observatories, which are operated by the Association of Universities for Research in Astronomy, Inc., under cooperative agreement with the National Science Foundation.

scaled each galaxy frame by a constant, generally within a percent of unity, to optimize the sky cancellation. This technique of differencing neighboring two-dimensional spectra usually removes the sky emission lines accurately. For a few galaxies, the resultant sky subtraction was not adequate. In these exposures, the sky lines in a set of frames were offset along the dispersion axis by 0.005 to 0.01 pixels, suggesting a slight, monotonic shift in the grating tilt. To improve the cancellation, we used `onedspec.identify` and `onedspec.reidentify` to fit, for each frame, a linear shift in the position of the airglow lines with respect to a reference frame. We then used `images.imgeom.imshift` to shift the frames, using linear interpolation, to zero the offsets. This was done for H-band frames of NGC 4861, He 2–10, NGC 4102, and NGC 3504 as needed.

The next step in the reduction was to combine the frames within a set. Offsets were determined by summing each frame down the dispersion axis and measuring the location of the continuum peak in the resulting one-dimensional image. Frames were magnified by a factor of six to permit fractional pixel shifts, which minimizes smearing of the data and maximizes preservation of flux during the next step of straightening. Magnified images were then remapped to make the spatial axis perpendicular to the dispersion axis. This remapping is accomplished by fitting the tilt of the dispersion axis as a cubic polynomial; this function is well-defined and does not vary with time. Straightening the spectra in this manner simplifies subsequent extraction, stacking, and wavelength calibration (Engelbracht, 1996).

Frames were then median combined with `imcombine` using no rejection, and using scale and weight factors determined from each frame’s median continuum strength (generally within 20% of unity). Frames were then de-magnified. Bad pixels were replaced with the average of their immediate two neighbors along

the dispersion axis.

A similar procedure created two-dimensional sky frames suitable for wavelength calibrations. The frames were straightened and median combined as before, but without weights, scales, or offsets. The resulting images have no continua, only sky lines. A high signal-to-noise 1-D sky spectrum was then created by taking, at each wavelength, the median value over all spatial positions.

We then extracted the spectra of the galaxies and calibration stars. Using `apall` in `iraf`, we traced each continuum interactively using low-order Legendre polynomials. The aperture width was chosen to be where the signal at the brightest part of the continuum dropped to 30% of peak. No extra background was subtracted at this point; trials with additional subtraction (to remove residual sky lines) added more noise than they eliminated. Spectra were extracted from the sky frames by using the apertures fitted for the corresponding objects.

Next, the spectra were corrected for telluric absorption. To do this, each galaxy spectrum was first divided, in pixel space, by the spectrum of a calibration star. When a target observation was bracketed by calibration star observations, the average of the two stellar spectra was divided into the target spectrum. Otherwise, the calibration spectrum taken closest in time to the target was used. Calibration stars were dwarfs of spectral types F6 to G0, most within 5° of the target object. Such stars have relatively featureless intrinsic spectra at $\sim 2 \mu\text{m}$, so their observed spectra reflect the variable absorption of the Earth's atmosphere.

We wavelength-calibrated the sky spectra of the galaxies, using `onedspec`. `identify` and tabulated vacuum wavelengths of the OH lines calculated by C. Kulesa (1996, private communication). Scatter in the wavelength calibration of the galaxies was less than $\pm 0.2 \text{ \AA}$, and usually below $\pm 0.1 \text{ \AA}$.

Wavelength solutions of the sky spectra were transferred to the [target/calibrator]

spectra. Due to the longer integration times, the sky spectra derived from galaxy frames give wavelength solutions more precise than those derived from sky spectra of the star frames. The wavelength solution is quite stable with time.

The calibration stars are not completely featureless; their metal absorption lines produce spurious emission lines in the [target/calibrator] spectra. To correct for this effect, we multiplied the [target/calibrator] spectra by the solar spectrum, which has been corrected for atmospheric absorption (Livingston and Wallace, 1991). The solar spectrum was first normalized and broadened to 10 Å in H and 9 Å in K to match our observations. Since the calibration stars are similar in spectral type to the Sun, the solar multiplication cures the final spectrum of the metal lines and the global Rayleigh–Jeans slope that the calibration star introduced. The resulting spectrum is [target/calibrator]*[☉]. This procedure is explained more fully by Maiolino, Rieke, & Rieke (1996).

At this point, NGC 4861 and NGC 4214 still showed residual sky lines. The spectra were improved by subtracting a scaled, extracted sky spectrum. For both galaxies, Br 11 and HeI 1.7 μm are uncontaminated by OH lines, whereas Br 10 is somewhat contaminated in NGC 4861 and seriously contaminated in NGC 4214 (the lowest redshift galaxy in our sample). Accordingly, we will consider only Br 11 in lieu of both Br 10 and Br 11 for these two galaxies.

2.2.2 Combining Spectra

For the H-band spectra, we observed targets for 0.5 hr between calibrators. Because our total integration times on each galaxy were substantially longer than this, the spectra must be combined. To do this, we used `onedspec.scombine`, median combining groups of ≥ 4 images, and average combining otherwise.

The HeI 2.06 μm and Br γ lines were covered by different grating settings. We spliced together the two grating settings for each target by scaling the 2.085 μm

spectrum by a constant until it matched the flux level of the $2.15\ \mu\text{m}$ spectrum in the region of overlap. Scaling constants were between 1.08 and 1.3. We then joined the spectra using `scombine`.

2.2.3 Subtracting the Stellar Continuum

The nebular lines we seek sit atop a stellar continuum, whose absorption lines can mask or alter the emission line ratios. Before faint emission line fluxes can be measured, the stellar continuum must be removed.

The lines of interest at K ($\text{Br}\gamma$ and $\text{HeI}\ 2.06\ \mu\text{m}$) are strong enough that subtraction of the stellar continuum is not necessary. For H-band, we used a stellar continuum template made by combining the 15 stars from a stellar atlas (observed with the same spectrometer: V. D. Ivanov, in preparation) which minimized the residuals when subtracted from NGC 253 (Engelbracht et al., 1998). Thus, the template was chosen to be a good fit to a \sim solar metallicity starburst galaxy, and was not made by modelling the stellar populations of each galaxy in our sample. The stars in the template are of stellar types K0 to M3, with metallicities between solar and half-solar. Two of the stars are supergiants, five are bright giants, five are giants, and three are dwarfs.

The resolution of the template is $130\ \text{km s}^{-1}$ in H. To match the intrinsic velocity dispersion of the galaxy spectra, we convolved this template with a Gaussian kernel as necessary to lower the resolution. He 2-10 and NGC 3077 were best fit with no convolution; NGC 3504 required a template with $150\ \text{km s}^{-1}$ resolution, and NGC 4102 required a $175\ \text{km s}^{-1}$ template. For NGC 4214 and NGC 4861, continuum subtraction was unimportant because the continua are much weaker than the nebular emission lines.

The stellar continuum template has an absorption feature at $1.7010\ \mu\text{m}$. By comparison with spectra of the Sun (Livingston and Wallace, 1991) and Arcturus

Table 2.2 Near-Infrared Vacuum Line Wavelengths

Transition	λ (μm)
Br11	1.6811
HeI	1.7007
Br10	1.7367
HeI	2.0587
H ₂	2.1218
Br γ	2.1661

(Montgomery et al., 1969), we identify this feature as a blend of three nickel lines and four (weaker) iron lines. At a resolution of 130 km s^{-1} , the blend has an equivalent width of $\leq 1.5 \text{ \AA}$, and dips to 94% of the continuum level. Because the absorption feature is a metal line blend, its strength will depend on metallicity.

Besides a simple subtraction of the stellar continuum, we also added a 20% featureless continuum to the template, renormalized, and subtracted the new continuum from the galaxy spectra. This procedure crudely approximates the effect of lower metallicity. These two realizations of the continuum subtraction provide some estimate of the associated uncertainty.

Continuum-subtracted H-band spectra of the galaxies and the stellar template are plotted in figure 2.1. K-band spectra are plotted in figure 2.2.

2.2.4 Measuring Line Ratios

To set the continuum level, we fit a low-order Chebyshev function across each spectrum, excluding emission lines from the fit. Each line was fit by a Gaussian to measure the line fluxes listed in table 2.2.4. For the noisy, non-Gaussian line profiles of NGC 4102, we directly summed flux rather than fit Gaussians.

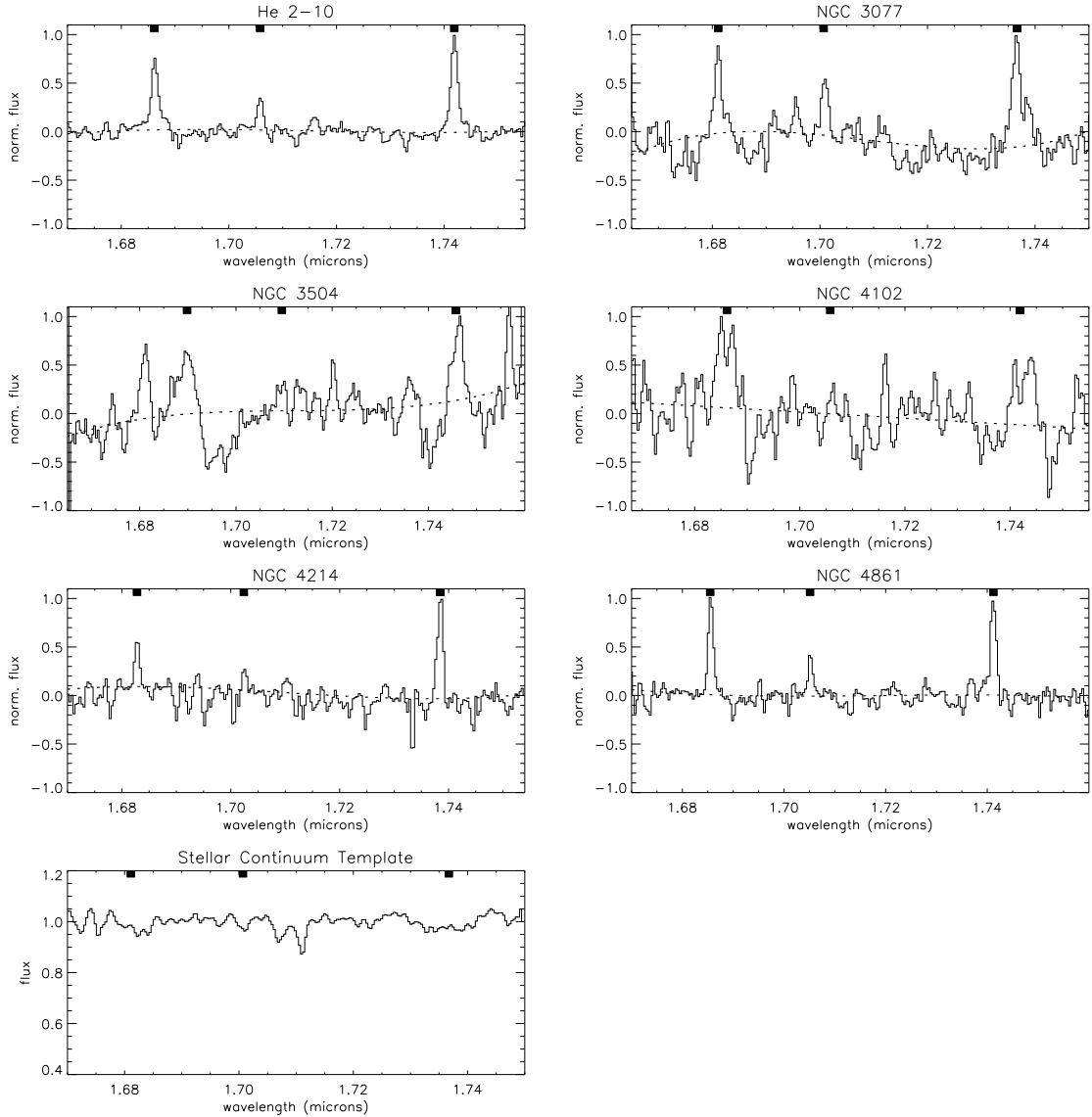


Figure 2.1 H-band spectra of the starburst galaxies in our sample. For presentation, the median continuum levels were set to zero, and the spectra normalized so that the maximum values were unity. The galaxy spectra are plotted versus observed (redshifted) wavelength. The expected positions of Br 11, HeI $1.7\ \mu\text{m}$, and Br 10 are marked. Dashed lines show the continuum fits. (Note that Br 10 in NGC 4214 is contaminated by a telluric OH line.) For reference, the rest-frame stellar continuum template is also plotted, without renormalization.

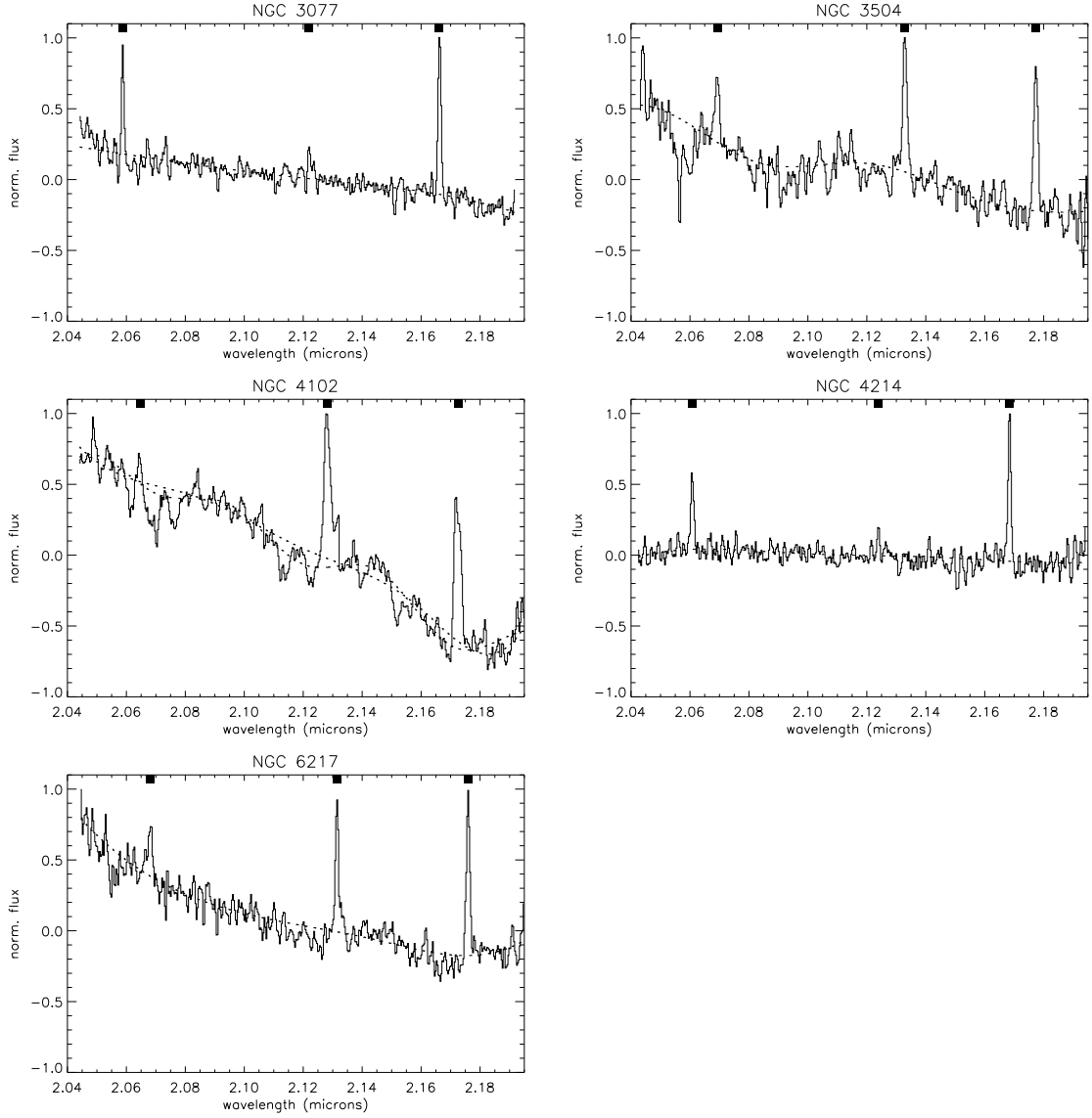


Figure 2.2 K-band spectra of the starburst galaxies in our sample. Spectra are normalized as in figure 2.1, and wavelengths are observed. The expected positions of HeI 2.06 μ m, H₂ 2.12 μ m, and Br γ are marked. Dashed lines show continuum fits. For NGC 4102, two different continuum fits were used.

To measure the relative strength of HeI 1.7 μm , we considered two ratios: HeI 1.7 $\mu\text{m}/\text{Br}10$, and $[\text{HeI } 1.7 \mu\text{m}/\text{Br}11] \times [\text{Br}11/\text{Br}10]_{\text{caseB}}$. We assumed the value $[\text{Br}11/\text{Br}10]_{\text{caseB}} = 0.75$, which is appropriate for $n = 10^2 \text{ cm}^{-3}$ and $T_e = 5,000 \text{ K}$ (Engelbracht et al., 1998; Hummer & Storey, 1987). For each galaxy, we computed both these ratios for both realizations of the continuum subtraction (with or without the 20% featureless continuum), and used the mean of these four values as the HeI 1.7 $\mu\text{m}/\text{Br}10$ ratio, and the standard deviation as an estimate of the uncertainty associated with the continuum subtraction. We also computed the ratio HeI 2.06 $\mu\text{m}/\text{Br}\gamma$. Our measured line ratios are listed in table 2.3, along with values of HeI 2.06 $\mu\text{m}/\text{Br}\gamma$ from the literature, and a weighted mean for HeI 2.06 $\mu\text{m}/\text{Br}\gamma$ that combines new and literature values. (The quoted uncertainty for the weighted mean is the error in the mean.)

Because of the 1.7 μm stellar absorption feature, studies that do not subtract the continuum in galaxies with weak HeI 1.7 μm will somewhat underestimate the HeI 1.7 μm line strength and therefore underestimate T_{eff} . To test the magnitude of this effect, in table 2.3 we list both continuum-subtracted and raw (unsubtracted) HeI 1.7 $\mu\text{m}/\text{Br}10$ ratios. For galaxies NGC 3504 and NGC 4102, the lines are so weak relative to the stellar continuum that the HeI 1.7 $\mu\text{m}/\text{Br}10$ cannot be measured without continuum subtraction. For the other galaxies in table 2.3, the raw and continuum-subtracted line ratios are very similar; for these galaxies (He 2–10, NGC 3077, NGC 4214, and NGC 4861), the continuum subtraction is not an important source of uncertainty.

2.3 Modelling Line Ratio Behavior

Because the emission lines used to diagnose effective temperature have different excitation energies, one cannot verify that a particular diagnostic works by sim-

Table 2.3. Measured Line Ratios of Starburst Nuclei.

Object	HeI 1.7 μm /Br 10	HeI 1.7/Br 10	HeI 2.06/Br γ	HeI 2.06/Br γ	HeI 2.06/Br γ
source:	continuum-subtr	raw, this work	this work	literature	weighted mean
He 2-10	0.27 ± 0.013	0.23 ± 0.05	...	0.52 ± 0.03 (1); 0.64 ± 0.09 (2)	0.53 ± 0.03
NGC 3077	0.46 ± 0.085	0.49 ± 0.1	0.49 ± 0.07	0.59 ± 0.01 (1)	0.54 ± 0.05
NGC 3504	0.23 ± 0.065	... ^a	0.49 ± 0.05	0.27 ± 0.05 (3) ^b	0.49 ± 0.05
NGC 4102	0.141 ± 0.04^c	... ^a	0.08 ± 0.08	< 0.12 (3); 0.20 ± 0.03 (4)	0.08 ± 0.08
NGC 4214	0.31 ± 0.03^d	0.31 ± 0.03^d	0.55 ± 0.05	0.57 ± 0.07 (1)	0.56 ± 0.04
NGC 4861	0.3 ± 0.02^d	$0.3 \pm 0.02^{d,e}$...	0.36 ± 0.03 (1)	0.36 ± 0.03
NGC 6217	0.39 ± 0.04	...	0.39 ± 0.04

References– (1) Vanzi & Rieke (1997); (2) Doyon et al. (1992); (3) Doherty et al. (1995); (4) Engelbracht (1997).

a: Without stellar continuum subtraction, the HeI 1.7 μm line cannot be measured.

b: Value ignored in computation of weighted mean. Our spectrum has much higher signal-to-noise.

c: For the HeI 1.7 μm feature, we directly summed flux rather than fit a Gaussian.

d: Br 10 was contaminated by an OH sky line in this galaxy, so the HeI 1.7 μm /Br 10 ratio quoted is scaled from HeI 1.7 μm /Br 11, assuming $[\text{Br } 11/\text{Br } 10] = 0.75$ for Case B.

e: Only one measurement was made, so the quoted error is an estimate based on the quality of the spectrum.

ply testing whether it exhibits a one-to-one correlation with another diagnostic. Instead, one must test diagnostics in light of photoionization models that, given realistic hot stellar ionizing spectra, predict line ratios appropriate to idealized nebulae. One can then ask a) whether the observed ratios populate the line ratio space permitted by models; and b) whether many observed line ratios for a particular galaxy are consistent, that is, can all be produced by one set of physical parameters. Thus, translating a nebular line ratio to a statement about stellar content is necessarily model-dependent.

Past studies have run series of models in which a single main sequence star photoionizes a nebula, producing tabulated line ratios as a function of stellar T_{eff} . A measured galactic line ratio is then translated into an effective temperature using this tabulation (Doyon et al., 1992; Achtermann & Lacy, 1995; Vanzi & Rieke, 1997; Beck et al., 1997; Förster Schreiber et al., 2001). This method has its uses: namely, to compare model inputs and assumptions, and understand what line ratios different stellar classes can produce. However, in § 2.3.2 we will argue that, especially for mid-infrared line ratios and HeI $1.7 \mu\text{m}/\text{Br}10$, starbursts are poorly approximated by single main sequence stars; to translate a line ratio into a meaningful statement about a stellar population, one must consider the flux from *all* the stars as a function of time. First, though, we will consider the insights and limitations of simple one-star models.

All our models (single-star and population synthesis) are radiation-bounded thin shells created by the photoionization code Cloudy 94.00 (Ferland, 1997). Using parameters determined by Förster Schreiber et al. (2001) for M82, we set the total hydrogen number density to $n_H = 300 \text{ cm}^{-3}$ and inner radius to $R = 25 \text{ pc}$. This choice of radius produces line ratios within 2% of the plane-parallel ($R = \infty$) case. This is because the shell is thin. Thus, the choice of radius only slightly af-

fects the models, which are effectively plane-parallel. For single-star models, we use a constant ionization parameter of $\log U = -2.3$. We ran two sets of models, one with gas-phase abundances of solar, and the other with 1/5 solar abundances (“the low- Z models”); neither abundance set includes depletion onto dust grains. (We address the effects of dust in § 2.5.4.) Because Cloudy does not predict the intensity of HeI 1.7 μm , we scaled the intensity from HeI 4471 \AA , which shares the same upper level. For Case B and $T_e = 5,000$ K, the HeI 1.7 μm line is a factor of 7.4×10^{-3} fainter than HeI 4471 \AA .

2.3.1 Models Using Individual Stars

We first consider the ratio of [NeIII] 15.6 μm to [NeII] 12.8 μm . For reference, it requires 22 eV to make singly-ionized neon, and 41 eV to make doubly-ionized neon. We took ionizing spectra from the O star models of Pauldrach, Hoffmann, & Lennon (2001), as prepared by Smith et al. (2002), and also the CoStar model spectra of Schaerer & de Koter (1997) as hardwired in Cloudy. These two stellar libraries predict dramatically different line ratios. Dwarf, giant, and supergiant Pauldrach stars all produce a maximum [NeIII]/[NeII] ratio of 10 at $T_{eff} = 50,000$ K. By contrast, the CoStar dwarf and giant atmospheres yield [NeIII]/[NeII] = 40 at $T_{eff} = 50,000$ K. At $T_{eff} = 35,000$ K, the predicted line ratios disagree by an order of magnitude. Förster Schreiber et al. (2001) used Pauldrach atmospheres and an earlier version of Cloudy to make their figure 8, which our Pauldrach models reproduce.

The other mid-infrared line ratios also show this discrepancy. CoStar models predict ten times higher [SIV]/[SIII] and [SIV]/[NeII] ratios than Pauldrach models for most of the $25,000 < T_{eff} < 50,000$ K range; for [ArIII]/[ArII] and [ArIII]/[NeII], CoStar gives 2 and 3 times higher ratios, respectively. The near-infrared line ratios HeI 1.7 μm /Br10 and HeI 2.06 μm /Br γ are not sensitive to

the choice of stellar atlas.

It is sobering that current O star models predict such different mid-infrared line ratio strengths. On the bright side, this sensitivity suggests that mid-IR line ratios may provide astrophysical tests of O star spectral models in simple HII regions. Giveon et al. (2002) performed such a test in Galactic HII regions; they find that Pauldrach et al. (2001) atmospheres fit the observed $[\text{Ar III}]/[\text{Ar II}]$ versus $[\text{Ne III}]/[\text{Ne II}]$ relation, whereas stellar models that assume LTE do not. In another test, Pauldrach et al. (2001) argued that their models successfully reproduce the observed far-UV spectra of hot stars, as opposed to other models. Finally, Smith et al. (2002) argue that Pauldrach et al. (2001) atmospheres should be more realistic than those of Schaerer & de Koter (1997) because the latter neglect line broadening, and thus underestimate line blanketing. As a result, CoStar atmospheres have significantly higher ionizing fluxes, especially at energies exceeding the He^+ edge.

Given these problems, and that the CoStar atmospheres predict much higher $[\text{Ne III}]/[\text{Ne II}]$ line ratios than are observed, we will use the Pauldrach et al. (2001) atmospheres in this paper. Still, that the Pauldrach spectra are better does not mean they are correct; the CoStar-Pauldrach discrepancy should serve as some warning of the current uncertainties regarding hot star spectra—a critical input to the models.

We also consider Wolf-Rayet (WR) stars in simple nebulae. We use WN and WC model spectra compiled by Smith et al. (2002), which were generated using the code of Hillier & Miller (1998). For a given T_{eff} , these model WR stars yield much lower $[\text{Ne III}]/[\text{Ne II}]$ ratios compared to Pauldrach O stars: at $T_{eff} = 50,000$ K, the difference is a factor of 30 for WN, and a factor of 10^4 for WC stars. This is because of the very strong line blanketing found in WR stars. Since

Wolf–Rayet stars can reach much hotter temperatures than main sequence stars, a $T_{eff} \lesssim 140,000$ K WC star can reach $[\text{Ne III}]/[\text{Ne II}] \sim 10$ (comparable to the ratio produced by a $T_{eff} = 50,000$ K Pauldrach O star). Similarly, a 120,000 K WN star can reach $[\text{Ne III}]/[\text{Ne II}] = 100$. Thus, given these stellar atmospheres, only a WN star can give rise to a neon ratio between 10 and 100.

As a result, there are mid–infrared line ratio regimes that only Wolf–Rayet stars can populate (again assuming solar metallicity.) For maximum effective temperatures of $T_{eff}^{MS} = 50,000$ K, $T_{eff}^{WN} = 120,000$ K, and $T_{eff}^{WC} = 150,000$ K, for Pauldrach et al. (2001) model O stars and Hillier & Miller (1998) WR stars, we find the following:

- Main sequence O stars can only produce $[\text{Ar III}]/[\text{Ar II}] \leq 18$, whereas WN and WC stars can reach ratios of 40.
- MS O stars can only produce $[\text{Si IV}]/[\text{Si III}] = 0.5$, while WC stars can reach 1.2, and WN can reach 3.
- MS O stars can only produce $[\text{Si IV}]/[\text{Ne II}] = 4$, whereas WC can reach 12 and WN can reach 130.
- MS O stars and WC stars can only produce $[\text{Ar III}]/[\text{Ne II}] = 2.5$, whereas WN stars can reach 14.

We have just seen that the conversion from mid–infrared line ratio to T_{eff} is very different for main sequence stars than for Wolf–Rayet stars. Thus, even a modest portion of WR stars within a hot stellar population can significantly affect the line ratios. We also conclude that in a solar–metallicity starburst, if the line flux ratios exceed the maximum that main sequence stars can produce, then WR stars dominate the ionizing flux.

2.3.2 Spectral Synthesis Models

Given the influence of WR stars, we must consider the more realistic scenario of an evolving stellar population as the ionizing source. We used the spectral synthesis code Starburst99 version 4.0 (Leitherer et al., 1999) to create instantaneous starbursts with an initial mass function of Salpeter–slope (Salpeter, 1955) and initial stellar masses between $1 M_{\odot}$ and a variable upper mass cutoff, “ M_{up} ” ($M_{up} = 100, 75, 60, 50, 40,$ and $30 M_{\odot}$.) (M_{up} in this paper always refers to the IMF, not the present-day mass function.) As in our single–star models, this version of Starburst99 uses O star model spectra from Pauldrach et al. (2001) and Wolf–Rayet model spectra from the code of Hillier & Miller (1998), as prepared by Smith et al. (2002).

We created two suites of models: the first set assumed solar metallicity in Starburst99 and Cloudy, and the “solar metallicity, high–mass loss” option, which is recommended as the default for Starburst99. (The alternative “standard mass loss” option gives qualitatively similar results.) The second set of models used a gas–phase metallicity of $1/5$ solar in Cloudy, and the “high–mass loss, $Z=1/5$ solar” and “uvlines = Magellanic” settings in Starburst99. Dust was ignored (and will be addressed in § 2.5.4.) Other parameters were set as for the single–star models. Starburst99 calculated the spectral energy distribution (SED) of the burst every 0.1 Myr for 10 Myr after the starburst. The ionization parameter was normalized to a maximum value of $\log U = -2.3$, and scaled by the number of hydrogen–ionizing photons present in the SED. Given the SEDs as input, Cloudy calculated line ratios as a function of starburst age.

Figure 2.3 plots line ratios as a function of time for these simulations. Table 2.4 summarizes the spectral synthesis models with $M_{up} = 100 M_{\odot}$ and compares to line ratios from the single–star models. Line ratios versus time for the

Table 2.4. Model Predictions for Line Ratios.

line ratio	value for $t < 5.5$ Myr, $M_{up} = 100 M_{\odot}$	peak value, $M_{up} = 100 M_{\odot}$	MS star at 50,000 K	WN at 100,000 K	WC at 100,000 K
[Ar III]/[Ar II]	> 0.6	13	14	25	35
[Ne III]/[Ne II]	> 0.05	7	10	70	0.8
[S IV]/[S III]	> 0.01	0.32	0.45	2.7	0.4
[Ar III]/[Ne II]	> 0.2	2	2.5	12	0.65
[S IV]/[Ne II]	> 0.02	2	4	90	0.9
He I 2.06 μm /Br γ	> 0.5	0.8	0.75	0.25	0.4
He I 1.7 μm /Br 10	> 0.17	0.35	0.35	0.35	0.35

Note. — Columns 2 and 3 list results from Starburst99/Cloudy models. For comparison, column 4 gives peak line ratio values for a single-star model using a $T_{eff} = 50,000$ K main sequence star, and columns 5 and 6 list peak values for single-star nebulae with Wolf-Rayet stars.

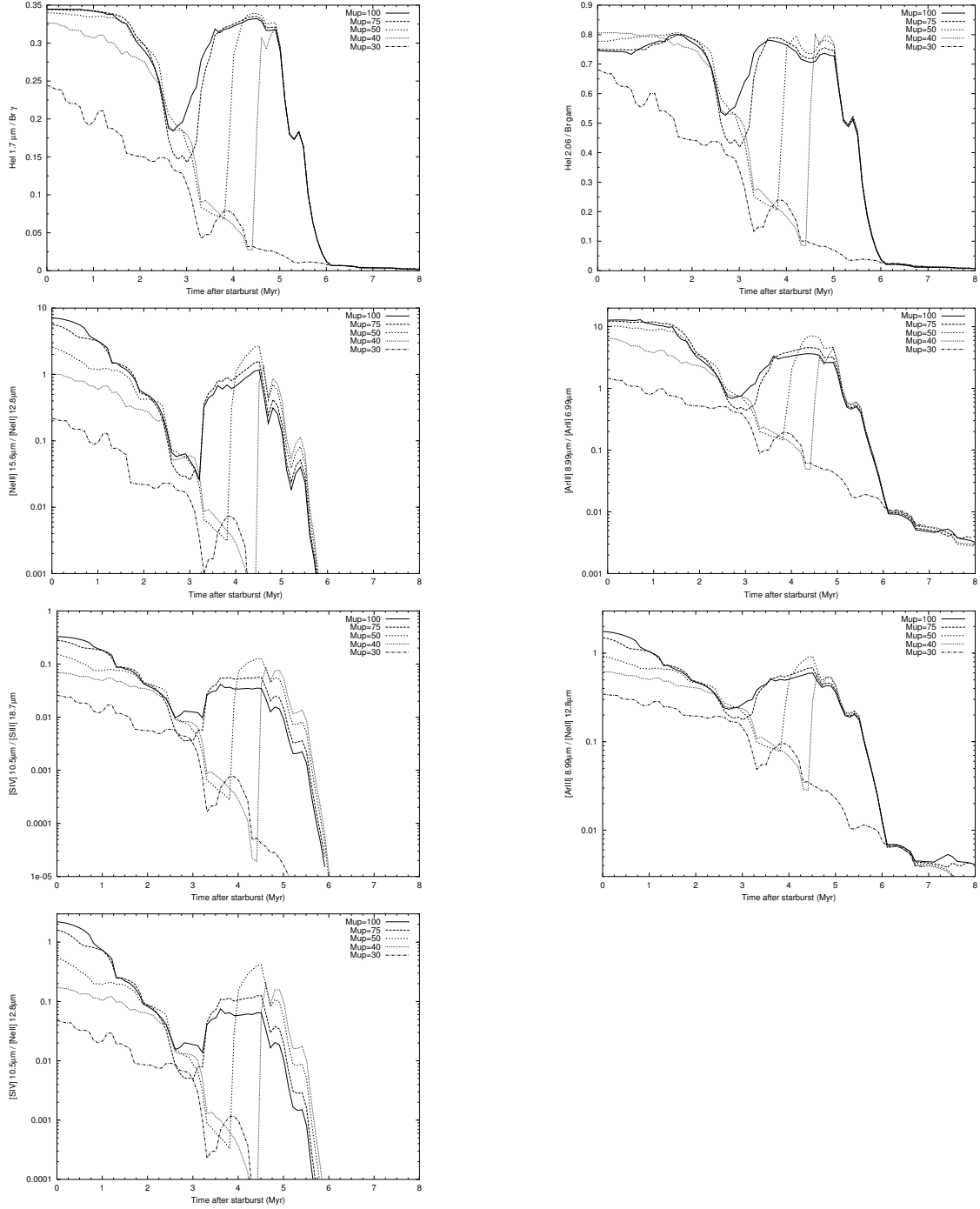


Figure 2.3 Line ratios versus time for Cloudy photoionization models with Starburst99 SEDs. Models have solar metallicity, and assume an instantaneous burst of star formation and an IMF with Salpeter slope and stars with masses between $1 M_{\odot}$ and an upper mass cutoff (M_{up}).

low-metallicity models are shown in figure 2.4.

Figure 2.3 shows that in the first 2 Myr, the mid-infrared line ratios fall from an initial plateau. By 2 Myr, the O3 through O5 dwarfs ($T_{eff} > 44,500$ K) stars in the models have left the main sequence; by 2.5 Myr, no O3 or O4 star of any luminosity class remains. Wolf-Rayet stars, together with the remaining main sequence stars, create a second period of relatively high line ratios from 3.5 to 5 Myr.² While the line ratios predicted for the Wolf-Rayet phase are lower than predicted for WR-only nebulae, clearly the Wolf-Rayet stars are important: they produce a renaissance of high line ratios after the O stars have left the main sequence. It does not make sense to parameterize a mid-infrared line ratio as though the flux came from a single main sequence star; the ensemble of stars, including the Wolf-Rayets, must be considered.

The models of Thornley et al. (2000), which otherwise used similar input spectra and nebular parameters to this work, did not include Wolf-Rayet stars. As a result, $[\text{Ne III}]/[\text{Ne II}]$ drops monotonically with time in their figures 6 and 10, while our solar-metallicity curves (figure 2.3) are double-peaked.

2.4 Diagnostics of Stellar T_{eff} In Starburst Galaxies

2.4.1 Approaches to Estimating T_{eff}

In general, line ratios capable of indicating T_{eff} also depend on metallicity, electron temperature, density, ionization parameter, and the morphology of the ionized regions. Without constraints on these other parameters, T_{eff} can be difficult to determine (e.g., Morisset (2003)). However, in the extreme conditions in star-

²The Starburst99 model for $t = 3.0$ Myr and $M_{up} = 100 M_{\odot}$ predicts line ratios that are sharply discontinuous from ratios at 2.8, 2.9, 3.1, and 3.2 Myr. (The $[\text{Ne III}]/[\text{Ne II}]$ spike is 25 times higher than the surrounding points.) The $M_{up} < 100 M_{\odot}$ models and sub-solar metallicity models have no spike. Though we have been unable to pinpoint the cause from the Starburst99 output, we feel the 3 Myr spike is spurious, not a physical effect, and we have removed it from the figures.

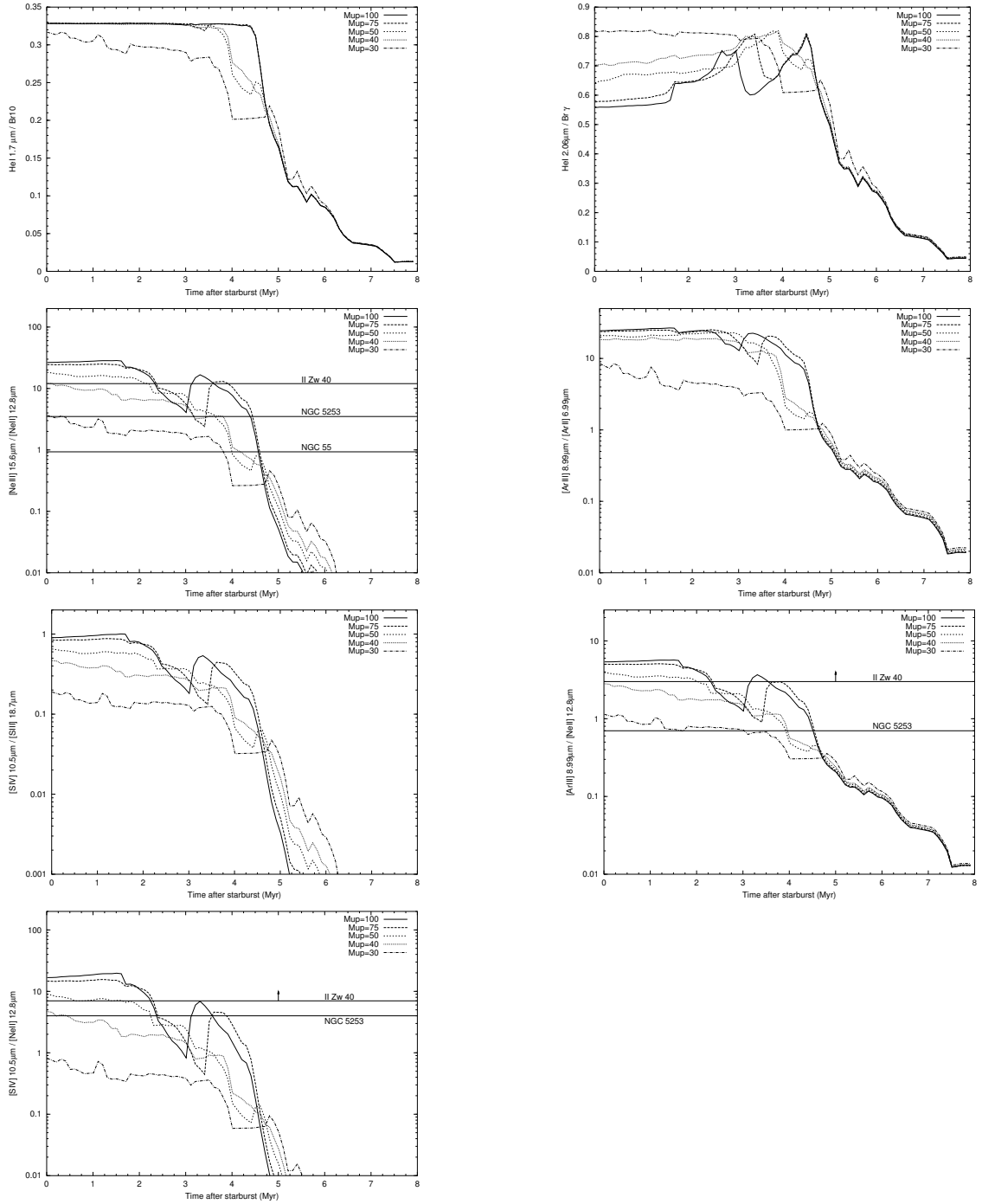


Figure 2.4 Line ratios versus time for low-metallicity Cloudy/Starburst99 models. Models assume $Z = 0.2 Z_{\odot}$, an instantaneous burst of star formation, and an IMF with Salpeter slope and stars with masses between $1 M_{\odot}$ and M_{up} . Horizontal lines indicate observed line ratios for low-metallicity galaxies II Zw 40, NGC 5253, and NGC 55, as given in table 2.7.

bursts, we expect less range in ionization parameter and morphology than in broad samples of HII regions, and starburst metallicities can be constrained by other line ratios. Therefore, it is plausible that useful constraints on T_{eff} can be derived for these regions. We return to this topic in § 2.5.1.

At optical wavelengths, the ratio of [OIII] 5007 to $H\beta$ is frequently used as a diagnostic since both lines are easily observed (see for example Stasińska & Leitherer (1996).) They are relatively close in wavelength, and Balmer ratios can be used to correct for residual extinction. However, large optical depths of interstellar extinction can make [OIII]/ $H\beta$ reflect the conditions of the outer skin of starbursts only. Thus, [OIII]/ $H\beta$ may not indicate the average conditions throughout a highly-extincted starburst. Also, a ratio composed of a forbidden metal line and a hydrogen recombination line is particularly sensitive to the metallicity, electron temperature, and density of the nebular region. Additionally, [OIII] can be shock excited (Raymond et al., 1988).

Vílchez & Pagel (1988) have proposed an all-forbidden line diagnostic η' , which uses lines of [OII], [OIII], [SII], and [SIII] with wavelengths from 3726 Å to 9532 Å. This diagnostic was initially reported to work well for HII regions (Kennicutt et al., 2000), but it is sensitive to morphology and shocks (Oey et al., 2000). Moreover, the diagnostic is poorly suited to starburst galaxies because it involves red lines that are seldom observed, and is extremely subject to reddening.

More robust optical line diagnostics can be made by comparing strengths of helium recombination lines with recombination lines of hydrogen (Kennicutt et al. 2000; Ho, Filippenko, & Sargent 1997; Doherty et al. 1995). HeI 6678 Å and HeI 4471 Å are attractive for this purpose because their proximity to $H\alpha$ and $H\beta$, respectively, reduces reddening effects. However, these diagnostics still sample only the outer skin of the starburst, and the helium lines are weak, as discussed

further in § 2.4.3.

Because they suffer less extinction, infrared spectral diagnostics probe more deeply into a starburst than optical ones. For example, 10 magnitudes of extinction at 5500 Å corresponds to only 1.1 magnitudes at 2.2 μm , and 0.8 magnitudes at 10 μm (Rieke & Lebofsky, 1985). The mid-infrared fine structure lines are the most successful tools in this spectral region to estimate T_{eff} (Roche et al., 1991; Kunze et al., 1996; Achtermann & Lacy, 1995; Thornley et al., 2000; Förster Schreiber et al., 2001). These lines are less dependent on electron temperature than optical forbidden lines. However, their atomic constants are not well known (Feuchtgruber et al., 1997, 2001; van Hoof et al., 2000; Galavis et al., 1997), and they are still sensitive to metallicity and ionization parameter (see figure 10 of Thornley et al. 2000).

Because of the lack of strong atomic lines, attempts to use near-infrared lines to measure T_{eff} have focused on recombination lines of helium and hydrogen. For stellar ionizing sources, the hardness of the ionizing continuum determines the volume of He^+ relative to H^+ (Osterbrock, 1989). For $T_{eff} > 40,000$ K, the He^+ and H^+ regions coincide; the Strömgren radii are approximately equal. For lower T_{eff} , the zone of ionized H extends beyond the central zone of singly-ionized He (see figures 2.4 and 2.5 of Osterbrock (1989), and figure 1 of Shields (1993)). Thus, by measuring the relative volumes of He^+ and H^+ within a nebula, one can constrain the effective temperature of the ionizing stellar source(s).

The line ratio of $\text{HeI } 2.06 \mu\text{m}/\text{Br}\gamma$ has been used to estimate T_{eff} in starbursts (Doyon, Puxley, & Joseph 1992; Doherty et al. 1995) and planetary nebulae (Lumsden, Puxley, & Hoare 2001a). However, the strength of the $\text{HeI } 2.06 \mu\text{m } 2^1P \rightarrow 2^1S$ line is not determined simply by recombination cascade, but also by the population in the 2^1P state (Shields, 1993). This level is pumped from

the ground state by $\lambda = 584 \text{ \AA}$ photons in the resonance transition $1^1S \rightarrow 2^1P$ (Shields, 1993; Bashkin & Stoner, 1975). Photoionization of hydrogen, dust absorption, or Doppler shifting can change the resonance efficiency and thus the occupation of the 2^1P state. The state can be further populated by collisions from the triplet states, primarily from 2^3S (Shields, 1993). A small HeI $2.06 \text{ }\mu\text{m}/\text{Br}\gamma$ ratio should indicate a soft continuum where there are few 584 \AA photons and few helium recombinations. Otherwise, the ratio is likely to be a poor measure of starburst T_{eff} due to the dependence on nebular dust content, electron temperature, and density, as well as on the ionizing continuum. Some of this complex behavior is seen in photoionization models (figure 1d of Shields 1993).

The HeI $1.7 \text{ }\mu\text{m}/\text{Br}10$ ratio was proposed as a T_{eff} diagnostic by Vanzi et al. (1996), and has been measured in several starburst galaxies (Vanzi et al. 1996; Vanzi & Rieke 1997; Engelbracht, Rieke, & Rieke 1998; Förster Schreiber et al. 2001) and planetary nebulae (Lumsden, Puxley, & Hoare 2001b). The HeI $1.7 \text{ }\mu\text{m}$ line and Br10 are close in wavelength, and $A_{1.7 \text{ }\mu\text{m}}$ is only one-sixth of A_V , making their ratio nearly reddening-independent and also allowing the photons to escape from relatively obscured regions. Unlike HeI $2.06 \text{ }\mu\text{m}$, the HeI $1.7 \text{ }\mu\text{m}$ $4^3D \rightarrow 3^3P^0$ transition arises almost entirely from recombination cascade. The relevant levels are triplet states, so they cannot be pumped from the ground state, because an electron spin flip would be required (Bashkin & Stoner, 1975). As a result, the line ratio is insensitive to nebular conditions, and is determined almost entirely by the relative sizes of the H and He ionization zones.

Figure 8 of Förster Schreiber et al. (2001) plots the behavior of the HeI $1.7 \text{ }\mu\text{m}/\text{Br}10$ ratio as a function of T_{eff} , as predicted by photoionization models for a starburst environment ionized by hot main sequence stars. The HeI $1.7 \text{ }\mu\text{m}/\text{Br}10$ ratio is small for $T_{eff} < 30,000 \text{ K}$ because there are many more photons capable of ion-

Table 2.5 Dependence of $C_{1.7}$ on Electron Temperature (from Vanzi et al. (1996)).

T_e (K)	$C_{1.7}$
5000	0.95
10000	1.000
20000	1.05

izing hydrogen (ionization potential of 13.6 eV) than neutral helium (ionization potential of 24.6 eV). For $T_{eff} > 30,000$ K, the ratio rapidly increases as the zone of singly-ionized helium overlaps more of the hydrogen Strömgren sphere. The ratio then saturates for $T_{eff} > 40,000$ K, as the He^+ and H^+ regions coincide. For $n_e = 100 \text{ cm}^{-3}$, the saturated ratio is

$$\text{HeI } 1.7/\text{Br } 10 = 3.60 C_{1.7} [n(\text{He})/n(\text{H})], \quad (2.1)$$

where $n(\text{He})/n(\text{H})$ is the gas-phase abundance of helium (by number) relative to hydrogen, and the term $C_{1.7}$ expresses the weak dependence on electron temperature (Vanzi et al., 1996). For $T_e = 10^4$ K, $C_{1.7} = 1.000$; other values are listed in table 2.4.1. The helium abundance $n(\text{He})/n(\text{H})$ increases from the primordial value of approximately 0.08 (Izotov & Tikhonova, 1998; Bono et al., 2002) to 0.1 for the Milky Way. Thus, HeI $1.7 \mu\text{m}/\text{Br } 10$ should saturate at a value of 0.27 to 0.38.

The T_{eff} diagnostics discussed above do not necessarily agree. For example, in the starburst galaxy He 2-10, $[\text{OIII}]/\text{H}\beta$ and $[\text{OI}]/\text{H}\alpha$ indicate $T_{eff} > 39,000$ K (Sugai & Taniguchi, 1992), whereas mid-infrared line ratios indicate $T_{eff} < 37,000$ K (Roche et al., 1991). The HeI $2.06 \mu\text{m}/\text{Br } \gamma$ observed by Vanzi & Rieke (1997) would indicate $T_{eff} = 39,000$ K using the conversion of Doyon et al. (1992). At poor signal-to-noise, Vanzi & Rieke (1997) measure HeI $1.7 \mu\text{m}/\text{Br } 10$ and find $T_{eff} = 36,000$ K. This few thousand Kelvin disagreement translates into

a serious disagreement in stellar mass: a T_{eff} of 36,000 K corresponds to approximately an O8V spectral type, which from eclipsing binaries should have a mass of ~ 22 to $25 M_{\odot}$ (Andersen, 1991; Ostrov et al., 2000; Niemela & Bassino, 1994; Gies et al., 2002); whereas a T_{eff} of 40,000 K corresponds to an O6.5V to O7V spectral type, which should have a mass of $\sim 35 M_{\odot}$ (Gies et al., 2002; Niemela & Bassino, 1994).

We now test T_{eff} diagnostics against each other in light of the stellar synthesis models detailed above. Because the line physics of HeI $1.7 \mu\text{m}/\text{Br}10$ is simple and well-understood (see § 2.4), we assume this diagnostic is unbiased, and thus accurately reflects the ionizing continuum, within the limitations of measurement error.

2.4.2 Testing HeI $2.06 \mu\text{m}/\text{Br}\gamma$

In this section we consider the galaxies for which we obtained HeI $1.7 \mu\text{m}/\text{Br}10$ measurements, as well as three galaxies with HeI $1.7 \mu\text{m}/\text{Br}10$ measurements available in the literature: NGC 253 (Engelbracht et al., 1998), for which the stellar continuum was subtracted as in this work; M82 (Förster Schreiber et al., 2001), for which representative stellar spectra were subtracted; and NGC 5253 (Vanzi & Rieke, 1997), for which the stellar continuum is weak enough to ignore. These three galaxies, together with the six galaxies for which we observed HeI $1.7 \mu\text{m}/\text{Br}10$, we term our expanded sample. We also take measurements of HeI $2.06 \mu\text{m}/\text{Br}\gamma$ from the literature for the galaxies in the expanded sample.

Figure 2.5 plots HeI $2.06 \mu\text{m}/\text{Br}\gamma$ versus HeI $1.7 \mu\text{m}/\text{Br}10$. NGC 3077, NGC 4861, NGC 4214, and He 2–10 all have HeI $1.7 \mu\text{m}/\text{Br}10$ ratios consistent with the saturated value of ≈ 0.3 , within the measurement errors and the expected variation of helium abundance. Thus, these starburst regions appear to contain massive stars ($T_{eff} > 39,000$ K if main sequence stars.) By contrast, NGC 253, NGC 4102,

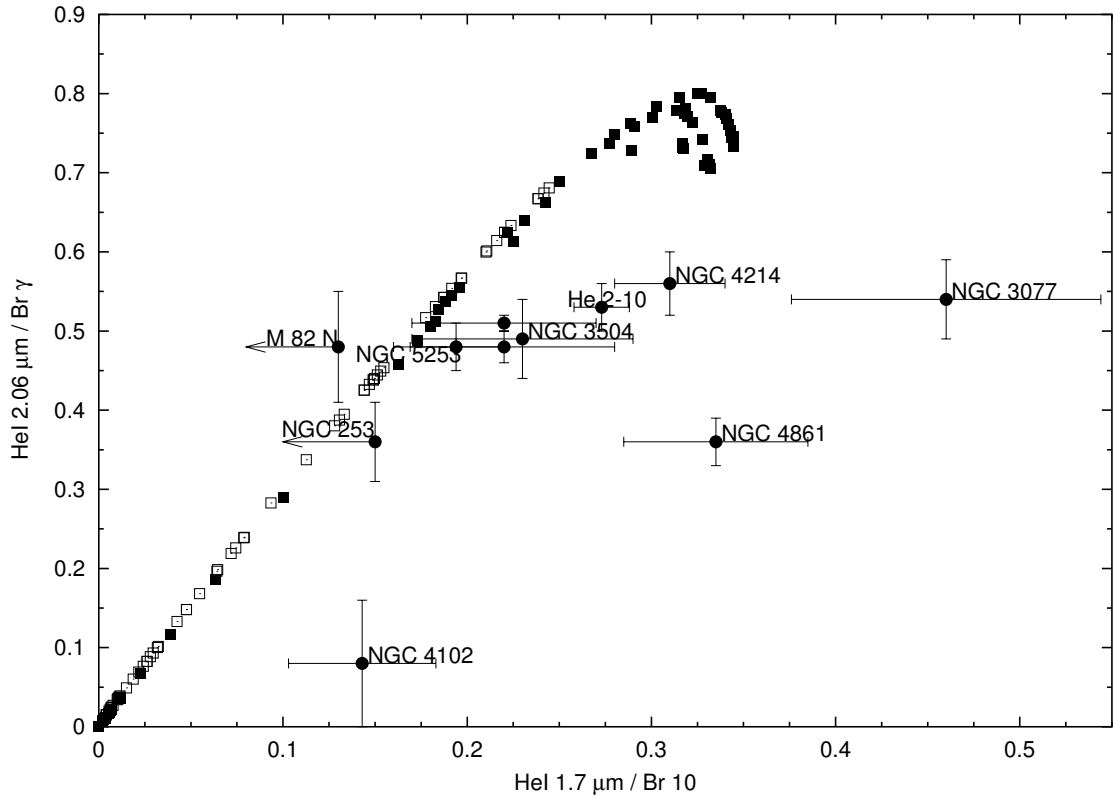


Figure 2.5 Comparison of the near-infrared line ratios. Included are the galaxies we observed as well as NGC 5253 (Vanzi & Rieke, 1997; Lumsden et al., 1994), NGC 253 (Engelbracht et al., 1998), and three regions of M82 (Förster Schreiber et al., 2001). The M82 regions are: the nucleus, labeled “M82 N”; the Br γ source “B1” located 10" southwest of the nucleus (the upper unlabeled point in this plot); the Br γ source “B2” located 5" southwest of the nucleus (the lower unlabeled point.) Coordinates for the M82 regions are given in the footnotes to table 2.7. Filled squares show line ratio values from Starburst99/Cloudy models with solar metallicity and $M_{up} = 100 M_{\odot}$, run every 0.1 Myr after an instantaneous burst. The open squares represent models with $M_{up} = 30 M_{\odot}$. Lowering the metallicity changes the tracks insignificantly.

and the nucleus of M82 have $\text{HeI } 1.7 \mu\text{m}/\text{Br } 10 < 0.15$, and thus are inferred to have softer ionizing continua ($T_{\text{eff}} \lesssim 37,000 \text{ K}$ if main sequence stars.) NGC 3504 and the two off-nuclear regions of M82 have line ratios intermediate to these extremes.

Figure 2.5 illustrates that $\text{HeI } 2.06 \mu\text{m}/\text{Br } \gamma$ does not trace $\text{HeI } 1.7 \mu\text{m}/\text{Br } 10$ as the models predict. The nucleus of M82 demonstrates that $\text{HeI } 2.06 \mu\text{m}$ may be strong while $\text{HeI } 1.7 \mu\text{m}$ is weak, contrary to the expected behavior (but expected if $\text{HeI } 2.06 \mu\text{m}$ is pumped.) However, for most galaxies, $\text{HeI } 2.06 \mu\text{m}$ is *too weak* for the measured $\text{HeI } 1.7 \mu\text{m}$. This is the first direct demonstration that $\text{HeI } 2.06 \mu\text{m}/\text{Br } \gamma$ is a poor diagnostic of T_{eff} in starburst galaxies. Radiative transfer considerations have predicted that the behavior of $\text{HeI } 2.06 \mu\text{m}$ should not be a simple function of T_{eff} (Shields, 1993). Lumsden et al. (2001a) confirm this complex behavior for planetary nebulae, though they attempt to constrain the dependence on T_e and density by also considering optical HeI lines (Doherty et al., 1995). However, the data do not contradict the expectation that a very low $\text{HeI } 2.06 \mu\text{m}/\text{Br } \gamma$ ratio (below ~ 0.2) indicates that the continuum is fairly soft, because there would be few ionizing photons and also few resonantly scattered photons.

We further consider the reliability of the $\text{HeI } 2.06 \mu\text{m}/\text{Br } \gamma$ ratio in figure 2.6, by comparing it to the mid-infrared line ratio $[\text{NeIII}] 15.6 \mu\text{m}/[\text{NeII}] 12.8 \mu\text{m}$. Here, too, $\text{HeI } 2.06 \mu\text{m}/\text{Br } \gamma$ is too low for a given $[\text{NeIII}]/[\text{NeII}]$ (compared to model predictions) and there is no obvious correlation between the two ratios. An alternative interpretation of figure 2.6 would be that $\text{HeI } 2.06 \mu\text{m}/\text{Br } \gamma$ is correct and $[\text{NeIII}]/[\text{NeII}]$ is systematically overproduced; we feel this is unlikely because, as we will demonstrate in § 2.4.4, $[\text{NeIII}]/[\text{NeII}]$ is *underproduced* in starburst galaxies with respect to the predictions of a Salpeter IMF extending

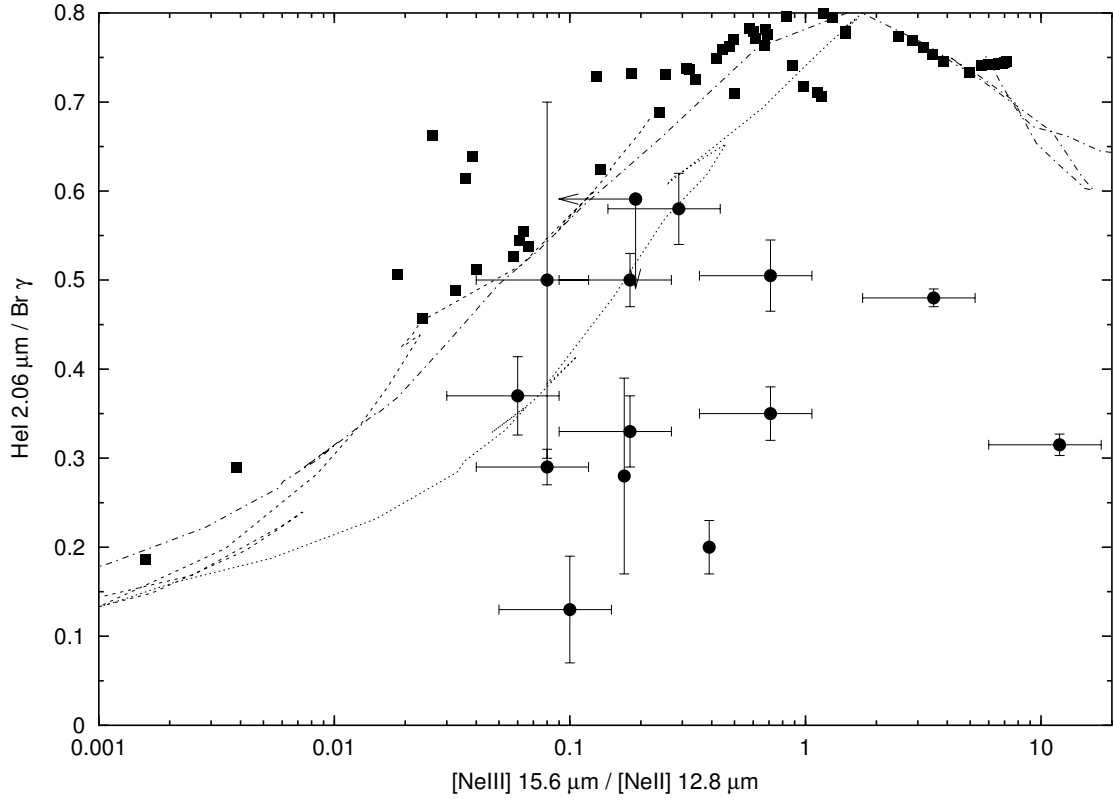


Figure 2.6 Comparison of $[\text{NeIII}]/[\text{NeII}]$ with $\text{HeI } 2.06 \mu\text{m}/\text{Br}\gamma$. Mid-infrared ratios are from Thornley et al. (2000), and $\text{HeI } 2.06 \mu\text{m}/\text{Br}\gamma$ measurements from the literature (Doherty et al., 1995; Doyon et al., 1992; Engelbracht, 1997; Förster Schreiber et al., 2001; Genzel et al., 1995; Lester et al., 1990; Lumsden et al., 1994; Schinnerer et al., 1997; Vanzi et al., 1996). Starburst99/Cloudy models are overplotted: filled squares show solar-metallicity models with $M_{\text{up}} = 100 M_{\odot}$; the dashed line shows solar-metallicity models with $M_{\text{up}} = 30 M_{\odot}$; the dot-dashed line shows the low-metallicity, $M_{\text{up}} = 100 M_{\odot}$ models; and the finely dotted line shows the low-metallicity, $M_{\text{up}} = 30 M_{\odot}$ models.

to $100 M_{\odot}$.

2.4.3 Testing Optical T_{eff} Indicators

How well do optical forbidden and recombination line ratios estimate T_{eff} in starbursts? Figures 9 and 10 of Kennicutt et al. (2000) show that the recombination ratios $\text{HeI } 5876/\text{H}\beta$ and $\text{HeI } 6678/\text{H}\alpha$, as well as $[\text{OIII}]/\text{H}\beta$, all track T_{eff} well in Milky Way, LMC, and SMC HII regions, where T_{eff} could be determined by classifying all the ionizing stars. How well do these diagnostics perform in starburst galaxies?

In figure 2.7, using dereddened data from Ho et al. (1997), we compare the behaviors of $\text{HeI } 6678/\text{H}\alpha$ and $[\text{OIII}]/\text{H}\beta$ in nuclear starbursts to the predictions of Starburst99/Cloudy photoionization models. Galaxies with $[\text{OIII}]/\text{H}\beta < 0.5$ generally have low $\text{HeI } 6678/\text{H}\alpha$, indicating general agreement that T_{eff} is low in these galaxies. At higher line ratios, there is considerable scatter. For most of the plotted galaxies, $[\text{OIII}]/\text{H}\beta$ is systematically high for a given $\text{HeI } 6678/\text{H}\alpha$, compared to a solar-metallicity, $M_{up} = 100 M_{\odot}$ track. Lowering the metallicity of the model reduces but does not eliminate the disagreement between diagnostics. Only an extreme model (low metallicity, $M_{up} = 30 M_{\odot}$) can fit the data reasonably well.

A possible explanation would be that $[\text{OIII}]$ in starbursts is often shock-excited by supernovae (Raymond et al., 1988), which would be a rare effect in HII regions and thus not affect the Kennicutt et al. (2000) plots. In particular, $[\text{OIII}]/\text{H}\beta$ values above ~ 2.5 require sub-solar metallicity or excitation by shocks. Thus, figure 2.7 suggests that $[\text{OIII}]/\text{H}\beta$ is systematically high or $\text{HeI } 6678/\text{H}\alpha$ is systematically low in starburst galaxies.

As a further test, figure 2.8 plots $[\text{OIII}]/\text{H}\beta$ versus $\text{HeI } 1.7 \mu\text{m}/\text{Br } 10$ for our expanded sample. Overplotted are Starburst99/Cloudy models as in figure 2.7.

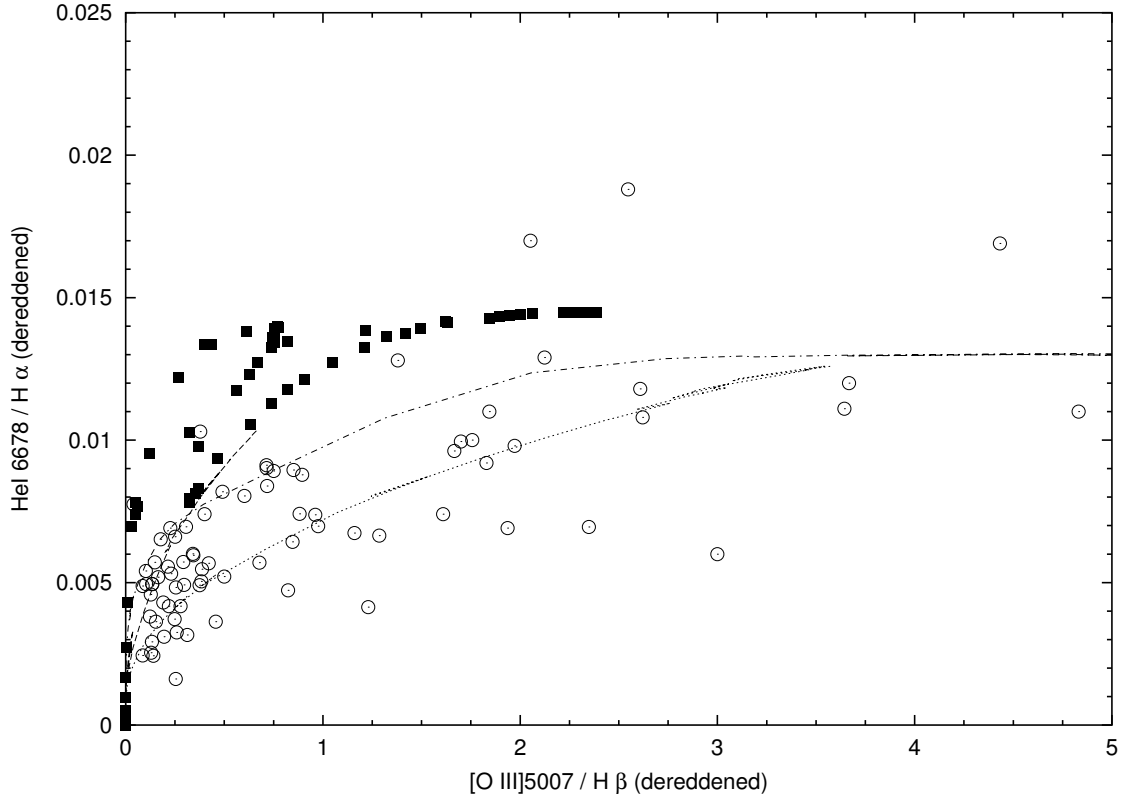


Figure 2.7 Testing optical indicators of T_{eff} . Circles represent the subsample of galaxy nuclei that Ho et al. (1997) classify as being “HII region-like”. Line fluxes are from Ho et al. (1997), dereddened by us following the extinction law of Cardelli, Clayton, & Mathis (1989), with $R_V = 3.1$. Starburst99/Cloudy models are represented as in figure 2.6. Note that the $[\text{O III}]/\text{H}\beta$ ratios tabulated in Ho et al. (1997) are incorrectly labeled as dereddened, when in fact they are observed values.

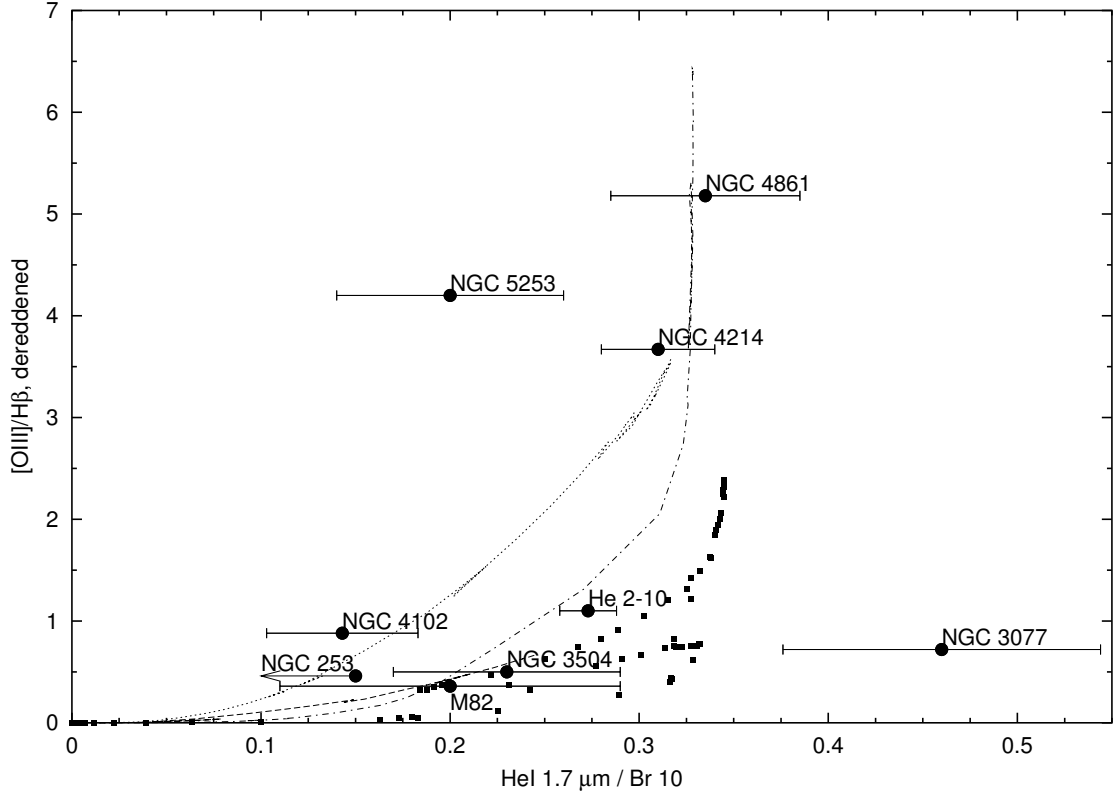


Figure 2.8 Testing $[\text{OIII}]/\text{H}\beta$ against $\text{HeI } 1.7 \mu\text{m}/\text{Br } 10$. The filled circles are measurements from the literature: dereddened $[\text{OIII}]/\text{H}\beta$ measurements were taken from Osterbrock & Pogge (1987); Vaceli et al. (1997); Vacca & Conti (1992); we also took observed $[\text{OIII}]/\text{H}\beta$ ratios from Ho et al. (1997) and dereddened them following Cardelli et al. (1989). For M82, we use the dereddened value of Ho et al. (1997), averaged with observed values from Armus, Heckman, & Miley (1989) and Wu et al. (1998). Starburst99/Cloudy models are represented as in figure 2.6.

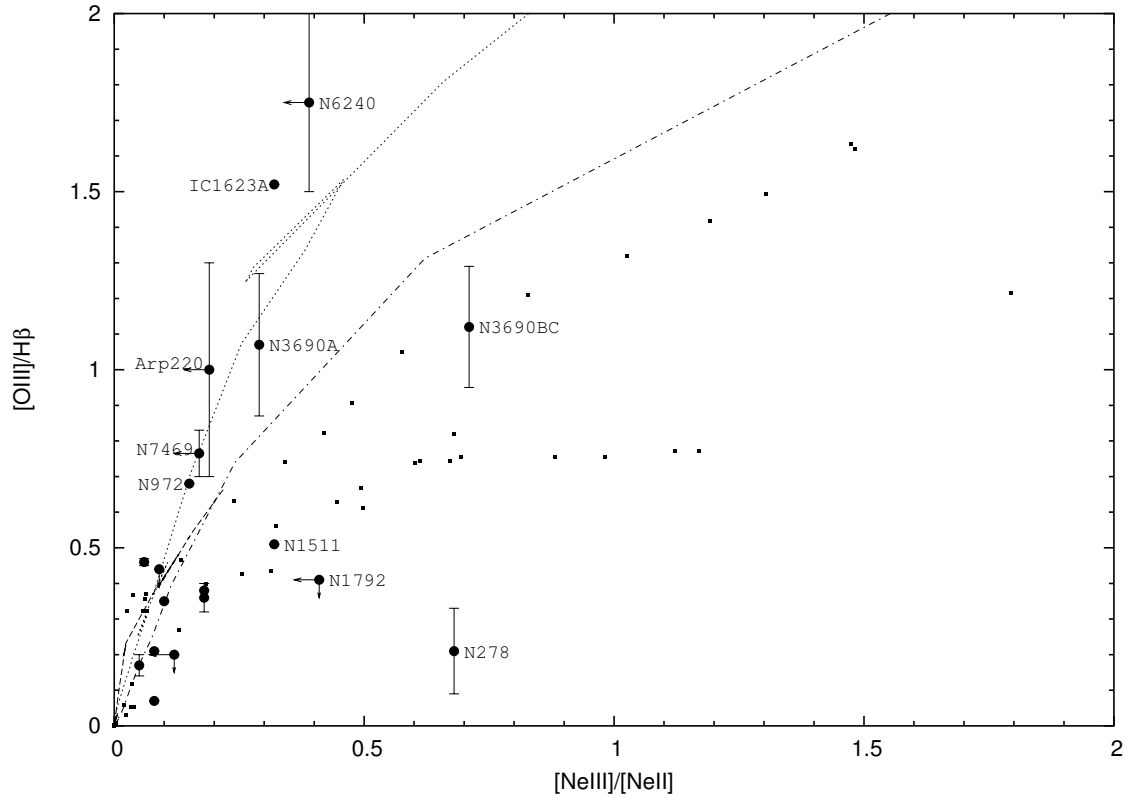


Figure 2.9 $[\text{OIII}]/\text{H}\beta$ from the literature versus $[\text{NeIII}]/[\text{NeII}]$ from Thornley et al. (2000) (filled circles). Starburst99/Cloudy models are represented as in figure 2.6. For clarity, we omit labels for the galaxies with smallest line ratios. In order of increasing $[\text{OIII}]/\text{H}\beta$ flux (or flux upper limit), they are: IC 342, M83, NGC 986, NGC 7552, NGC 6946, M82, NGC 3256, NGC 4945, and NGC 253.

For low values of $[\text{OIII}]/\text{H}\beta$, the error bars are too large to judge whether the two diagnostics correlate. As in figure 2.7, the highest $[\text{OIII}]/\text{H}\beta$ values observed require sub-solar metallicity or shock excitation of $[\text{OIII}]$.

Next, we examine the behavior of $[\text{OIII}]/\text{H}\beta$ versus $[\text{NeIII}]/[\text{NeII}]$ in figure 2.9 (omitting for now NGC 5253, II Zw 40, and NGC 55 because of their low metallicity.) Optical line ratios are from the literature, and *ISO* observations of $[\text{NeIII}]/[\text{NeII}]$ are from Thornley et al. (2000). Galaxies with $[\text{OIII}]/\text{H}\beta < 0.5$ generally have line ratios consistent with the overplotted Starburst99/Cloudy models. With higher $[\text{OIII}]/\text{H}\beta$, the scatter increases. Without accurately knowing

the metallicity of each galaxy in figure 2.9, it is difficult to judge how much of the scatter in $[\text{OIII}]/\text{H}\beta$ versus $[\text{NeIII}]/[\text{NeII}]$ is due to the sensitivity of $[\text{OIII}]/\text{H}\beta$ to metallicity rather than effective temperature.

According to the Cloudy models, metallicity alone cannot explain the line ratios of NGC 6240, IC 1623A, Arp 220, NGC 3690A, and NGC 7469 (and possibly NGC 972) in figure 2.9. Low metallicity and a upper mass cutoff of $30 M_{\odot}$ could together explain all but IC 1623A and NGC 6240. Alternatively, aperture mismatch, severe extinction, or shock excitation of $[\text{OIII}]$ could be at work. NGC 972 is not strongly centrally concentrated in optical emission line images, so the explanation may lie in aperture mismatch: the optical line ratios were measured with slitwidths of a few arcseconds, while the *ISO* neon lines were measured with a $14''$ by $27''$ aperture. The remaining discrepant galaxies all have very heavily obscured star formation regions, and it is likely that the discrepancy arises because the optical and mid-infrared spectra sample distinctly different regions along the line of sight. We also note that NGC 278 has extremely low $[\text{OIII}]/\text{H}\beta$ for its measured $[\text{NeIII}]/[\text{NeII}]$. Higher-spatial resolution mid-infrared spectroscopy (e.g., with SIRTf) may resolve this discrepancy. We will delay discussion of whether $[\text{NeIII}]/[\text{NeII}]$ is a reliable T_{eff} diagnostic until § 2.4.4.

Next, we consider the optical helium and hydrogen recombination lines, which should form more accurate starburst T_{eff} diagnostics than a forbidden and recombination pair like $[\text{OIII}]/\text{H}\beta$. To reduce reddening effects, we select HeI lines close in wavelength to H lines. Unfortunately, the helium lines are weak: HeI 6678 saturates at 0.014 of the strength of $\text{H}\alpha$, and HeI 4471 saturates at 0.05 of $\text{H}\beta$. As such, in the spectral atlas of Ho et al. (1997), HeI 6678 was detected in only 108 of 418 galactic nuclei, and HeI 4471 in only 16 nuclei. The small sample indicates that HeI 4471 is only marginally detected, and we do not consider it

further.

Figures 2.7 and 2.9 have already implicated $[\text{OIII}]/\text{H}\beta$ as an unreliable T_{eff} indicator for $[\text{OIII}]/\text{H}\beta \gtrsim 0.5$. This makes it hard to gauge the reliability of $\text{HeI } 6678/\text{H}\alpha$ in figure 2.7. Also, the sample sizes are too small to compare the optical recombination line ratios to $[\text{NeIII}]/[\text{NeII}]$, $\text{HeI } 1.7 \mu\text{m}/\text{Br } 10$, or $\text{HeI } 2.06 \mu\text{m}/\text{Br } \gamma$ individually. Instead, we use the latter three T_{eff} indicators together to test how well the optical recombination line ratios correlate with T_{eff} . In table 2.6, we list galaxies with measurements of at least two different T_{eff} indicators, in order of increasing T_{eff} , as determined from $[\text{NeIII}]/[\text{NeII}]$, $\text{HeI } 1.7 \mu\text{m}/\text{Br } 10$, and $\text{HeI } 2.06 \mu\text{m}/\text{Br } \gamma$ (when ≤ 0.2), as available. Due to measurement error and uncertainty in the relative calibrations of the diagnostics, the ordering is somewhat uncertain. The published plots of the Ho et al. (1997) spectra lack the dynamic range to assign upper limits to the undetected optical recombination lines. These are marked as “non det” in table 2.6.

In general, table 2.6 shows some correlation between $\text{HeI } 6678/\text{H}\alpha$ and T_{eff} , though with considerable scatter. Using Kendall’s τ rank correlation test on the eight galaxies with measured $\text{HeI } 6678/\text{H}\alpha$, there is only a 5% chance that T_{eff} and $\text{HeI } 6678/\text{H}\alpha$ are uncorrelated.

2.4.4 Testing the Mid-Infrared Fine Structure Line Ratios

In the mid-infrared, ratios of the fine structure lines $[\text{NeIII}] 15.6 \mu\text{m}$, $[\text{NeII}] 12.8 \mu\text{m}$, $[\text{ArIII}] 8.99 \mu\text{m}$, $[\text{ArII}] 6.99 \mu\text{m}$, $[\text{SIV}] 10.5 \mu\text{m}$, and $[\text{SIII}] 18.7 \mu\text{m}$ have been used to test for the presence of hot stars in starbursts. From space, *ISO* measured these lines at low spatial resolution ($14''$ by $27''$ aperture for $[\text{NeIII}]/[\text{NeII}]$) (Thornley et al., 2000; Förster Schreiber et al., 2001; Kunze et al., 1996). Ground-based observations (Roche et al., 1991; Achtermann & Lacy, 1995) provide higher spatial resolution, but only the $[\text{SIV}]$, $[\text{ArIII}]$, and $[\text{NeII}]$ transitions can be observed through

Table 2.6. Testing optical T_{eff} diagnostics.

Galaxy	HeI 1.7 μm /Br10	HeI 2.06 μm /Br γ	[NeIII]/[NeII]	HeI 6678/H α	HeI 4471/H β
NGC 3628	...	< 0.11 (1)	...	not det	not det
M82 nucleus	< 0.16 (2)	...	0.16 ± 0.04 (2)	0.35	not det
NGC 6946	...	0.13 ± 0.06 (1)	0.10 (3)	not det	not det
NGC 972	0.15 (3)	0.4	not det
NGC 660	...	0.16 ± 0.02 (1)	...	0.5	not det
NGC 4102	0.143 ± 0.04	0.08 ± 0.08	...	0.51	not det
NGC 6240	...	0.20 ± 0.03 (1)	< 0.39 (3)	not obs	not obs
NGC 3690	0.3 to 0.7 ^a (3)	0.28	not det
NGC 278	0.68 (3)	not det	not det
NGC 3504	0.23 ± 0.06	0.36	not det
NGC 4214	0.31 ± 0.03	0.83	0.36
NGC 3077	0.46 ± 0.084	0.58	0.3

a: Two pointings. References: (1) Engelbracht (1997); (2) Förster Schreiber et al. (2001); (3) Thornley et al. (2000). All HeI 6678/H α and HeI 4471/H β flux ratios are from Ho et al. (1997), dereddened by us, given as fractions of the saturated values (0.014 and 0.05, respectively). Uncited near-infrared line ratios: this paper. “Not obs” means galaxy was not observed by Ho et al. (1997). “Not det” means galaxy was observed, but line was not detected. The HeI 2.06 μm /Br γ ratio is only listed if ≤ 0.2 , and therefore useful.

the atmosphere. As a result, ground-based studies must use heteronuclear line ratios, which are less ideal than homonuclear ratios available from space because they are much more sensitive to elemental abundances and dust depletion.

Table 2.7. Comparison of Mid-IR and Near-IR T_{eff} diagnostics.

Object	HeI 1.7 μm /Br10	HeI 2.06 μm /Br γ	ISO Mid-IR	Ground Mid-IR
M82-nucleus	< 0.13 (1)	0.48 ± 0.07 (1)	...	[ArIII]/[NeII] = 0.054 ± 0.02 (2a) [SIV]/[NeII] = 0.014 ± 0.007 (2a)
M82-E1	[ArIII]/[NeII] = 0.06 ± 0.01 (2) [SIV]/[NeII] = 0.026 ± 0.008 (2)
M82-W1/B2	0.22 ± 0.06 (1)	0.52 ± 0.02 (1)	...	[ArIII]/[NeII] = 0.039 ± 0.008 (2) [SIV]/[NeII] = 0.015 ± 0.005 (2)
M82-W2/B1	0.22 ± 0.05 (1)	0.55 ± 0.02 (1)	...	[ArIII]/[NeII] = 0.07 ± 0.01 (2) [SIV]/[NeII] = 0.013 ± 0.004 (2)
M82-SWS $14'' \times 20''$	0.2 ± 0.09 (1a)	0.51 ± 0.03 (1a)	[NeIII]/[NeII] = 0.16 ± 0.04 (1) [ArIII]/[ArII] = 0.26 ± 0.08 (1) [SIV]/[SIII] = 0.11 ± 0.04 (1)	[ArIII]/[NeII] = 0.025 ± 0.004 (2b) [SIV]/[NeII] = 0.007 ± 0.0015 (2b)
NGC 253	< 0.15 (3)	0.36 ± 0.05 (4)	[NeIII]/[NeII] = 0.06 (5)	[ArIII]/[NeII] < 0.3 (6) [SIV]/[NeII] < 0.3 (6)
NGC 4102	0.14 ± 0.04	0.08 ± 0.08	...	[ArIII]/[NeII] < 0.5 (6) [SIV]/[NeII] < 0.2 (6)
NGC 6946	...	0.13 ± 0.06 (4)	[NeIII]/[NeII] = 0.10 (5)	...
NGC 6240	...	$< 0.20 \pm 0.03$ (4)	[NeIII]/[NeII] < 0.39 (5)	...
He 2-010	0.273 ± 0.015	0.53 ± 0.03 (11,8)	...	[SIV]/[NeII] = 0.03 ± 0.02 (12) [ArIII]/[NeII] = 0.08 ± 0.03 (12)
II Zw40	0.43 ± 0.05 (7)	0.31 ± 0.02 (7)	[NeIII]/[NeII] = 12.0 (5)	[SIV]/[NeII] > 7 (6) [ArIII]/[NeII] > 3 (6)

In table 2.7, we collect measurements of the mid-infrared line ratios and HeI $1.7 \mu\text{m}/\text{Br}10$ in starburst galaxies, including five regions within M82. M82 provides a testing ground for the accuracy of the mid-infrared line ratios as T_{eff} diagnostics; *ISO* measured homonuclear line ratios in the center (Förster Schreiber et al., 2001), and this region has been mapped at $1''$ resolution in [NeII], [ArIII], and [SIV] (Achtermann & Lacy, 1995), identifying the nucleus and three infrared-bright regions nearby (all regions defined in the footnotes to table 2.7.)

Based on the heteronuclear mid-infrared line ratios and HeI $1.7 \mu\text{m}/\text{Br}10$, we find that region W2 and the nucleus of M82 both require $M_{up} < 65 M_{\odot}$, region E1 requires $M_{up} < 60 M_{\odot}$, and region W1 requires $M_{up} < 50 M_{\odot}$. The heteronuclear and homonuclear mid-infrared line ratios and HeI $1.7 \mu\text{m}/\text{Br}10$ within the SWS/*ISO* aperture require $M_{up} < 50 M_{\odot}$. Models with $M_{up} = 100, 75, 70$, or $65 M_{\odot}$ do not produce the observed ratios in any of these regions. Thus, we find that the heteronuclear line ratios give consistent ages and upper mass cutoffs for individual regions near the center of M82, in agreement with HeI $1.7 \mu\text{m}/\text{Br}10$, and when averaged over the SWS/*ISO* aperture, give answers consistent with the homonuclear line ratios.

We further test the mid-infrared line ratios using the five other solar-metallicity galaxies listed in table 2.7. For NGC 4102 and NGC 6240, the constraints are poor, and the line ratios can be fit by $M_{up} = 40$ to $100 M_{\odot}$. In NGC 6946, HeI $2.06 \mu\text{m}/\text{Br}\gamma$ and [NeIII]/[NeII] disagree unless $M_{up} < 65 M_{\odot}$, but as we cautioned in § 2.4.2, HeI $2.06 \mu\text{m}$ is not a reliable diagnostic. For NGC 253, HeI $1.7 \mu\text{m}/\text{Br}10$ and the neon ratio cannot be simultaneously matched by the $M_{up} = 100 M_{\odot}$ model, but models with $M_{up} \leq 75 M_{\odot}$ can fit the ratios. For He 2–10, the line ratios require $M_{up} < 65 M_{\odot}$, mostly because of low observed [ArIII]/[NeII].

Our conclusion is that in individual regions and entire starbursts, the different

Table 2.7—Continued

Object	HeI 1.7 μm /Br10	HeI 2.06 μm /Br γ	ISO Mid-IR	Ground Mid-IR
NGC 5253	0.19 ± 0.03 (8)	0.48 ± 0.01 (9)	[NeIII]/[NeII]= 3.5 (5)	[SIV]/[NeII]= 4 (10) [ArIII]/[NeII]= 0.7 (10)

Note. — References: (1) Förster Schreiber et al. (2001); (2) Achtermann & Lacy (1995); (3) Engelbracht et al. (1998); (4) Engelbracht (1997); (5) Thornley et al. (2000); (6) estimated from the spectra of Roche et al. (1991); (7) Vanzi et al. (1996); (8) Vanzi & Rieke (1997); (9) Lumsden et al. (1994); (10) Crowther et al. (1999); (11) (Doyon et al., 1992); (12) Beck et al. (1997); uncited values are from this paper. Positions in M82 are as follows: nucleus is defined at $9^{\text{h}}51^{\text{m}}43.6^{\text{s}}$, $69^{\circ}55'00''$ (1950) by (1) and (2); E1 is defined by (2) as the [NeII] knot at $9^{\text{h}}51^{\text{m}}44^{\text{s}}$, $69^{\circ}55'02''$ (1950); W1 is defined by (2) as the [NeII] knot at $9^{\text{h}}51^{\text{m}}42.5^{\text{s}}$, $+69^{\circ}54'59''$ (1950), which corresponds to the Br γ knot named B2 by (1); W2 is the [NeII] knot found at $9^{\text{h}}51^{\text{m}}41.5^{\text{s}}$, $69^{\circ}54'57''$ (1950), which corresponds to the Br γ knot named B1 by (1); and SWS is the $14'' \times 20''$ aperture of SWS/ISO, centered on $9^{\text{h}}51^{\text{m}}42.2^{\text{s}}$, $69^{\circ}55'00.7''$. Values labelled (1a) are the average over the $16'' \times 10''$ 3D field of (1), which is similar in coverage to the SWS field. Values labeled (2a) are estimated from figure 7 of (2). Values labelled (2b) are the average of knots W1 and W2 in (2), which provides similar coverage to the SWS field.

heteronuclear and homonuclear mid-infrared line ratios and HeI 1.7 μm /Br10 give consistent answers as to age and M_{up} . This agreement supports use of the mid-infrared line ratios as diagnostics of the ionizing radiation field. The mid-infrared lines have large equivalent widths and a range of excitation energies, making them potentially powerful diagnostics.

2.5 Diagnosing Ionizing Conditions in Starbursts

2.5.1 Mid-Infrared Line Ratio Dependencies

The mid-infrared line ratios depend on several physical parameters: metallicity, ionization parameter, morphology, and the strength and shape of the ionizing continuum. To be confident in applying these ratios, we need to disentangle these various effects. We consider each parameter in turn.

Metallicity. As metallicity decreases, the relative high-excitation line emission increases, because lower-metallicity stars have harder spectra and because lower-metallicity nebulae cool less efficiently. Another effect is that Wolf-Rayet stars require larger progenitor masses with decreasing metallicity. These effects can be seen by comparing the low-metallicity models (figure 2.4) with the solar-metallicity models (figure 2.3). Using Starburst99 and Cloudy, we find that $Z = 0.2$ times solar models have initial mid-infrared line ratios that are ~ 3 times greater than solar-metallicity models; these line ratios fall more slowly with time than in solar-metallicity models.

While metallicity affects the mid-infrared line ratios, metallicity can be measured and corrected for. Within galaxy samples that have similar measured metallicity, uncertainties in the metallicity should affect the mid-infrared line ratios by factors that are much smaller than the orders-of-magnitude changes in line ratio values expected due to T_{eff} (as discussed in § 2.3.2).

Ionization parameter and morphology. The ionization parameter, as the ratio of the spectral intensity to the gas density, combines two of the fundamental parameters that determine the degree of ionization in a nebula. In a Galactic HII region, the ionization parameter changes rapidly with radius because of the $1/R^2$ falloff and absorption of UV photons by the nebula (which also alters the spectral shape.) Morphology then determines which parts of the nebula influence others. A starburst galaxy, however, is much messier than an assembly of pseudo-spherical HII regions: the ISM is generally fragmented, and gas parcels are ionized by many stars. For example, in M82, it appears that the interstellar medium is highly fractionated (e.g., Seaquist, Frayer, & Bell 1998) and that the whole ~ 450 pc nuclear starburst and individual ~ 20 pc star-forming clusters can be described by a single ionization parameter (Thornley et al. (2000), citing the dissertation of N. Förster Schreiber.) Thus, it seems more appropriate to model a starburst as though the gas and stars are thoroughly mixed (by employing a mean UV spectrum and mean ionization parameter), rather than as a collection of spherical clouds, each with a single ionization source. This “mixed gas and stars” model is achieved in practice by assuming plane-parallel geometry and a composite ionizing spectrum.

Ionization parameters (U) have been estimated in several nearby starburst galaxies by measuring the number of Lyman continuum photons and the size of the starburst region. Thornley et al. (2000) summarize measurements in NGC 253, NGC 3256, and M82, which are all consistent with $\log U = -2.3$. Measurements have also been obtained for Arp 299 (Alonso-Herrero et al., 2000); NGC 1614 (Alonso-Herrero et al., 2001); NGC 1808 (Krabbe et al., 1994); IC 342 (Bosker et al., 1997); NGC 6946 (Engelbracht et al., 1996); and NGC 3049 (Engelbracht et al., 1996). In addition, Ho et al. (1990) measure the Lyman continuum flux in fourteen

nearby galaxies. Six of these galaxies have multiple measurements of $\log U$, which gives some estimate of the (often considerable) uncertainty.

In figure 2.10 we plot the ionization parameters derived from these studies. It should be noted that each of these U values is actually a *lower limit*, since we use the maximum radius of the starburst region to compute the ionization parameter. When the gas density was not measured, we assume $n_e = 300 \text{ cm}^{-3}$; the true ionization parameter scales as $IP = IP_{300} - \log(n_e/300 \text{ cm}^{-3})$. Figure 2.10 shows that the ionization parameter used in our simulations, $\log U \leq -2.3$, is a reasonable average value given the measurements available for nearby starbursts.

How sensitive are the mid-infrared line ratios to the ionization parameter? Reducing U in our models by a factor of 10 lowers the [Ne III] $15.6 \mu\text{m}$ / [Ne II] $12.8 \mu\text{m}$ line ratio by a factor of ~ 7 . Therefore, if the ionization parameters of starburst galaxies vary by a factor of ~ 10 or more, this parameter could account for considerable spread in observed mid-infrared line ratios. However, there is no tendency for galaxies with small [Ne III]/[Ne II] to have low ionization parameters in figure 2.10, indicating that U is not the dominant parameter determining this flux ratio. Comparing with the restricted range of U observed in starbursts, we conclude from the modeling in § 2.3.2 that T_{eff} dominates variations in this line ratio in such regions.

Starburst ISM morphologies are far too complex to reproduce in simulations; fortunately, parameterization of a starburst by a single, global ionization parameter and a mean ionizing spectrum is physically motivated, agrees with observations, and simplifies the problem sufficiently to allow modeling.

Another test of the diagnostic usefulness of the mid-infrared line ratios is provided by studies of Galactic H II regions. Martín-Hernández et al. (2002b) found that, in compact H II regions, the line ratios [Ne III] $15.6 \mu\text{m}$ / [Ne II] $12.8 \mu\text{m}$,

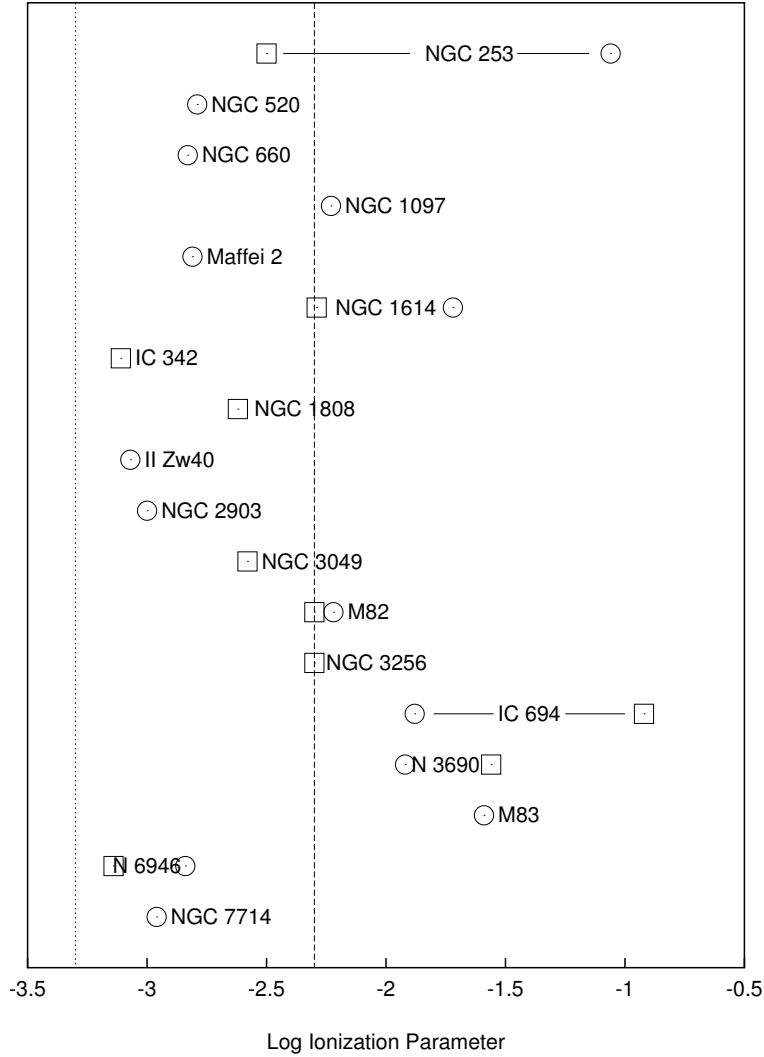


Figure 2.10 Ionization parameters for local starburst galaxies, found using Lyman continuum fluxes and starburst radii from the literature (see § 2.5.1 for references.) Data from Ho et al. (1990) are plotted as circles; other data are plotted as squares. The vertical dashed line shows $\log U = -2.3$, the value we have adopted as typical for starbursts. The vertical dotted line is the value that would depress $[\text{Ne III}]/[\text{Ne II}]$ by a factor of seven relative to our models, which is what is required to make the observed line ratios consistent with a $M_{\text{up}} = 100 M_{\odot}$ Salpeter IMF.

[ArIII] 8.99 μm / [ArII] 6.99 μm , and [SIV] 10.5 μm / [SIII] 18.7 μm correlate very well with each other, suggesting their reliability. Morisset (2003) has also demonstrated the use of these lines to estimate T_{eff} and U in Galactic HII regions, though as demonstrated by Morisset et al. (2003), outside constraints on ionization parameter and metallicity are usually necessary.

2.5.2 The Spectrum of the Ionizing Radiation

We now focus on using the fine structure line ratios to estimate the spectrum of the ionizing radiation in starbursts. As figure 2.3 illustrates, once an instantaneous burst is older than 6 Myr, [NeIII]/[NeII], [SIV]/[SIII], and [SIV]/[NeII] are so low (< 0.001) that the higher-ionization line should not be detected. [ArIII]/[ArII] and [ArIII]/[NeII] fall off more slowly, but still require a dynamic range exceeding 100 to detect both lines in each ratio. Such very low line ratios are not seen in Thornley et al. (2000), which with 27 [NeIII] 15.6 μm /[NeII] 12.8 μm measurements is the largest sample to date of mid-infrared fine structure lines in starburst galaxies. The lowest ratio detected by Thornley et al. (2000) is 0.05, and 5 galaxies have upper limits. The simplest explanation of this behavior is that massive stars continue to form at low rates after the peak of a starburst.

In the Thornley et al. (2000) sample, all but 3 galaxies have [NeIII]<[NeII]. The three outliers, with neon ratios from 1 to 12, are all low-mass, low-metallicity galaxies (NGC 55, NGC 5253, and II Zw 40). We will consider the higher-metallicity galaxies now, in the context of the solar-metallicity models, and defer discussion of the low-mass, low-metallicity galaxies to § 2.5.3.

In figure 2.3, as M_{up} decreases, the line ratios decrease during the main sequence phase (because the ionizing spectrum softens), and the gap widens between the two phases of high line ratios (because fewer stars become Wolf-Rayets.) We now consider these models in light of the measured neon ratios of Thornley

et al. (2000); the models and measurements are plotted in figure 2.11.

In the $M_{up} = 100 M_{\odot}$ model, for 46% of the first 5 Myr, the predicted $[\text{Ne III}]/[\text{Ne II}]$ exceeds the highest line ratio measured by Thornley et al. (2000) for a high-mass, \sim solar-metallicity galaxy; thus, this model poorly fits the data. A much better fit is the $Z = Z_{\odot}$, $M_{up} = 40 M_{\odot}$ model. For only 6% of the first 5 Myr does this model predict $[\text{Ne III}]/[\text{Ne II}] > 1$; for 65% of that time, it predicts neon line ratios within the range of the Thornley detections. The $M_{up} = 40 M_{\odot}$ model fits markedly better than the $M_{up} = 50$ and $30 M_{\odot}$ models. Because one-quarter of the Thornley data-points are upper limits (excluding the three low-mass, low-metallicity galaxies), the $M_{up} = 40$ model is a better fit to the Thornley data than the above percentages indicate.

One draws the same conclusion from continuous star formation models, as shown in figure 2.12. Such models with $M_{up} = 100$ and $75 M_{\odot}$ predict a constant neon ratio above 1, while the neon ratio for the $M_{up} = 30 M_{\odot}$ model falls below the Thornley range. The $M_{up} = 40$ and $50 M_{\odot}$ models predict neon line ratios within the Thornley range; the $M_{up} = 40$ model comes closer to the median.

These results are consistent with those of § 2.4.4, which found that the heteronuclear and homonuclear mid-infrared line ratios within four regions of M82 required $M_{up} < 50$ to $M_{up} < 65 M_{\odot}$ (depending on the region), that He 2–10 required $M_{up} < 65 M_{\odot}$, and that NGC 253 required $M_{up} < 100 M_{\odot}$. Thus, $[\text{Ne III}]/[\text{Ne II}]$ in the high-mass, solar-metallicity Thornley et al. (2000) galaxies, and a concordance of line ratios in M82 and He 2–10, are all significantly lower than the predictions of a Salpeter IMF extending to $100 M_{\odot}$. An IMF that is deficient in massive ($\gtrsim 40 M_{\odot}$) stars could produce the observed line ratios.

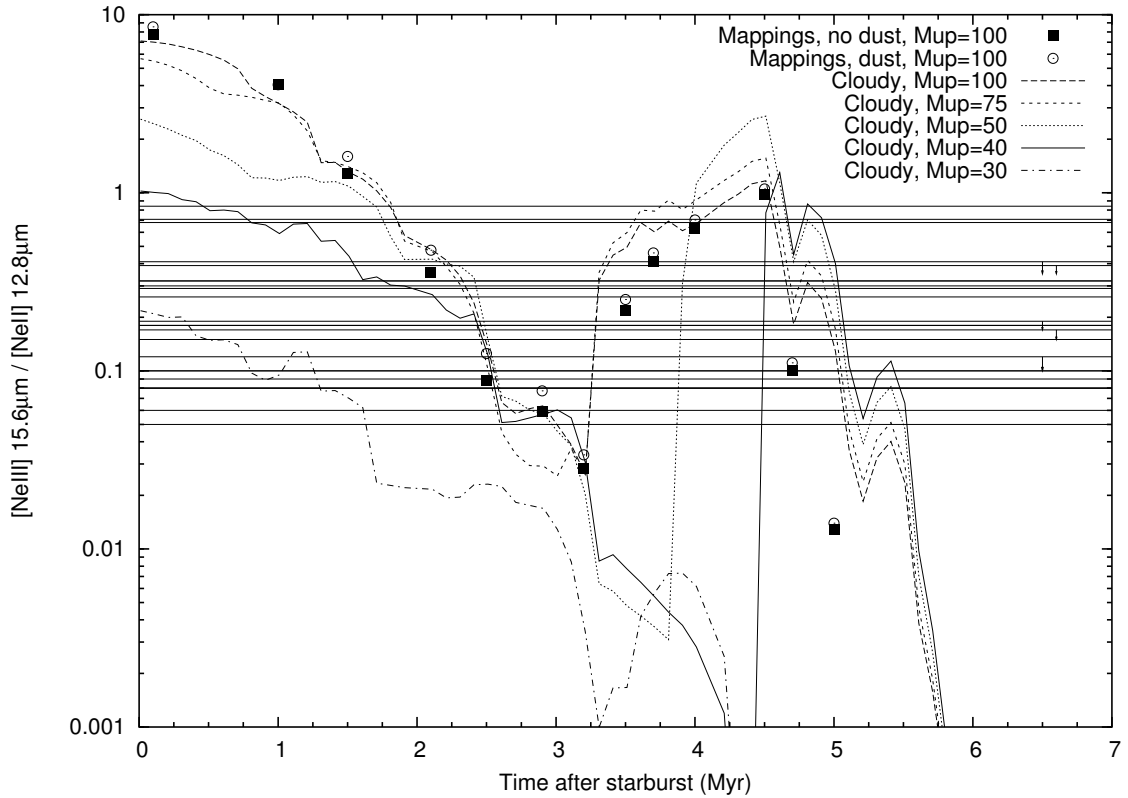


Figure 2.11 Burst models of $[\text{NeIII}]/[\text{NeII}]$ for solar metallicity, and observed values. The curves are Cloudy models with varying M_{up} ; squares show Starburst99/Mappings $M_{\text{up}} = 100 M_{\odot}$ models without dust; circles show dusty Starburst99/Mappings models with $M_{\text{up}} = 100 M_{\odot}$. The $M_{\text{up}} = 100 M_{\odot}$ Cloudy and Mappings models use the same ionizing spectra, but different photoionization codes and treatment of the mid-infrared lines; the two photoionization codes are in generally good agreement. Overplotted are the observed $[\text{NeIII}]/[\text{NeII}]$ ratios of Thornley et al. (2000). The neon line ratios of the three low-metallicity galaxies II Zw 40, NGC 5253, and NGC 55 are not plotted; they should be considered in light of the low-metallicity models of figure 2.4, and are overplotted there.

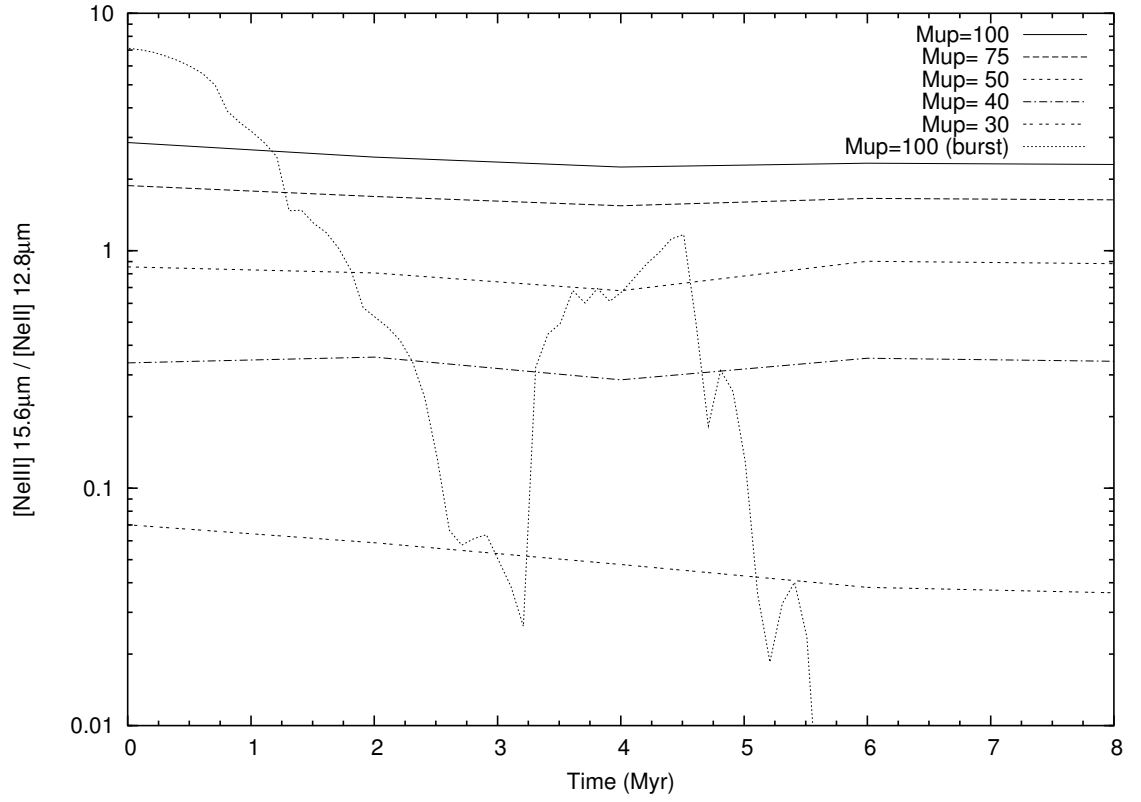


Figure 2.12 Continuous star-formation models of $[\text{Ne III}]/[\text{Ne II}]$ for solar metallicity. Five different M_{up} values are plotted. For reference, we overplot (finely dotted line) the solar-metallicity, $M_{up} = 100 M_{\odot}$, instantaneous burst model from figure 2.3.

2.5.3 Ionizing Conditions in Low Metallicity Starbursts

We now discuss mid-infrared line ratios in low metallicity starbursts. Lowering the metallicity from solar elevates the mid-infrared line ratios, and fills in the valley between the MS and WR phases. HeI 1.7 μm /Br10 is completely saturated until the WR stars die, by contrast to its double-peaked behavior for solar metallicity. Overplotted in figure 2.4 are the line ratios for II Zw 40, NGC 5253, and NGC 55, in order of decreasing [NeIII]/[NeII] ratio from Thornley et al. (2000). All three of these galaxies have low metallicity: II Zw 40 has measured [O/H] = 0.20 ± 0.01 (Diaz et al., 1990) and [O/H] = 0.19 ± 0.04 (Garnett, 1989), [S/H] = 0.12 ± 0.03 (Garnett, 1989), and [Ne/H] = 0.3 (Martín-Hernández et al., 2002a), all linear and relative to solar abundance. NGC 5253 has measurements of [O/H] = 0.28 (Storchi-Bergmann, Kinney, & Challis 1995) and [Ne/H] = 0.58 (Martín-Hernández et al., 2002a). NGC 55 has measured [O/H] = 0.25 to 0.37 (Webster & Smith, 1983).

We consider the line ratios of these galaxies in light of the low-metallicity models. For NGC 55, the only mid-infrared line ratio available in the literature is [NeIII]/[NeII]; the observed value can easily be produced by any M_{up} from 30 to 100 M_{\odot} . For II Zw 40, the observed [NeIII]/[NeII] = 12 cannot be achieved by Starburst99/Cloudy models with solar metallicity. With the low metallicity models, we find that the observed [NeIII]/[NeII], [SIV]/[NeII], and [ArIII]/[NeII] line ratios cannot be produced at any age unless M_{up} is greater than 40 M_{\odot} . The HeI 1.7 μm /Br10 ratio agrees that the ionizing field is rather hard, but is insensitive to M_{up} . For NGC 5253, unless the burst is < 0.5 Myr old, the measured [SIV]/[NeII] requires $M_{up} > 40 M_{\odot}$. This constraint is strengthened if we consider the [NeIII]/[NeII], [ArIII]/[NeII], and HeI 1.7 μm /Br10 ratios, which all predict ages within 3 to 5 Myr, for a broad range of M_{up} (40 to 100.) The HeI 1.7 μm /Br10

constraint is particularly insensitive to M_{up} . If one assumes this age range, the $[\text{SIV}]/[\text{NeII}]$ ratio requires $M_{up} > 60 M_{\odot}$.

Thus, while high-mass, solar-metallicity starburst galaxies are seen to have lower $[\text{NeIII}]/[\text{NeII}]$ ratios than a Salpeter IMF with $M_{up} = 100 M_{\odot}$ predicts, the low-metallicity galaxies II Zw 40 and NGC 5253 have the high neon ratios expected if they contain very massive stars.

2.5.4 Caveats and Assumptions

How robust is the conclusion that the nebular line ratios indicate that most high-mass, solar-metallicity starbursts have soft ionizing continua? First, we have assumed that the Thornley galaxies are generally of solar metallicity. If they were more metal-poor, this would raise the predicted line ratio curves, and thus increase the discrepancy between the predicted and observed ratios. The opposite effect (weakening our constraint) occurs if the Thornley galaxies have super-solar metallicity. Thornley et al. (2000) use the strong-line method to derive metallicities of $1.9 \pm 1 Z_{\odot}$ for 13 of their galaxies (excluding NGC 5253 and II Zw 40.) This result is consistent with the metallicities from optical line ratios, but we prefer the Thornley mid-infrared estimate because it should be reddening-independent. Starburst99 is not optimized for such metallicities, but we use twice-solar models nonetheless to crudely estimate whether super-solar metallicities could void our result. For $M_{up} = 100, 75, \text{ and } 60 M_{\odot}$, doubling the metallicity from solar lowers the $[\text{NeIII}]/[\text{NeII}]$ line ratios and increases the duration of the WR phase by ~ 0.5 Myr, which brings the models closer to agreement with observations, but deepens the trough between the main sequence and WR phases to $100\times$ below the lowest Thornley detection. These models predict neon line ratios within the observed Thornley range for $\sim 40\%$ of the first 6 Myr—little better than the solar-metallicity $M_{up} = 100$ model. To summarize, while uncertainties remain be-

cause metal-rich stellar evolution is not well understood, current models indicate that the low line ratios observed in starburst galaxies are unlikely to be explained away by metallicity effects.

Another way to negate the conclusion would be for the high-mass, solar-metallicity starburst galaxies to have much lower ionization parameters than we assumed. For the observed neon line ratios to arise in starbursts with $M_{up} = 100 M_{\odot}$, the starbursts must have U about 10 times weaker than our assumed $\log U_{max} = -2.3$. None of the 18 galaxies in figure 2.10 has a measured ionization parameter this low.

In fact, because in our models the ionization parameter starts at $\log U = -2.3$ and falls with the ionizing flux, the ionization parameter in our models is already fairly low. (For example, 5 Myr after a solar-metallicity, $M_{up} = 100 M_{\odot}$ burst, the ionization parameter has fallen to $\log U = -3.15$.) Thus, our ionization parameter assumptions are conservative in that they tend to predict low line ratios for a given M_{up} ; as a result, when comparing to observed line ratios, the models will be slightly biased toward finding high M_{up} . Thus, the choice of ionization parameter is not the reason we find generally low M_{up} in starburst galaxies; the models are actually biased against finding this result.

For simplicity, we have modelled star formation as an instantaneous burst. Starburst galaxies are of course more complicated. An instantaneous burst is the *most conservative* assumption of star formation history for the purpose of constraining M_{up} . As illustrated in figure 2.12, extended star formation or a series of bursts would elevate predicted line ratios above the instantaneous-burst case for most of the burst duration. As such, extended star formation would increase the discrepancy between the low ratios observed in starbursts and the high ratios predicted by high- M_{up} models.

Dust grains harden the ultraviolet ionizing continuum, as pointed out by Aannestad (1989). Thus, if dust competes for the ionizing photons, this elevates the line ratios, and our conclusions are strengthened. Figure 2.11 shows this effect in Starburst99/Mappings models with and without dust. These models were created using the Starburst99/Mappings III web interface, beta test version 3q (Kewley et al., 2003). That figure also shows that the two different photoionization codes Mappings and Cloudy, given the same input spectra and nebular conditions, predict very similar neon line ratios. This helps address the concern that our results depend on the reliability of photoionization codes and their input atomic constants.

The other major assumptions in our work are the choice of stellar evolution tracks and hot stellar spectra. Had we used the (hard-spectrum) CoStar models, they would have increased the predicted line ratios and made the Thornley et al. (2000) galaxies seem even more deficient in high-mass stars. Thus, our use of the softer Pauldrach et al. (2001) atlas is conservative in terms of existing hot star models. However, our conclusions could be invalidated if real stars have much softer ionizing continua than Pauldrach et al. (2001).

We note that NGC 3077, 4214, and 4861 now have well-measured, saturated HeI $1.7\ \mu\text{m}$ /Br 10, but no published mid-infrared spectra. Mid-infrared spectra of these galaxies should further test the trends in nebular line behavior discussed in this paper (all of these galaxies would appear to fall into the low-mass, low-metallicity category).

2.5.5 UV and Nebular Diagnostics in Conflict?

The very massive stellar populations of a number of starburst galaxies have been constrained by ultraviolet spectroscopy. In cases where the burst age is more than ~ 5 Myr, the UV spectra cannot test for stars above $40\ M_{\odot}$ because the most mas-

sive stars have already exploded as supernovae or evolved off the main sequence (e.g., González Delgado et al. (1999)). A small number of starbursts have strong P Cygni profiles indicative of a very young burst and the presence of very massive stars. Thus, there appears to be a tendency for ultraviolet spectra of stellar populations to indicate larger M_{up} than do the nebular lines (although the galaxy samples observed in the UV and mid-infrared hardly overlap). We now consider the cases of He 2–10 and NGC 3049; the UV spectra of both these starburst galaxies show P Cygni profiles, and nebular spectra are available (mid-infrared for the former galaxy, and optical for the latter.)

He 2–10 is an extremely rare case of a starburst which has available ultraviolet spectra of adequate quality to search for P Cygni line profiles as well as high-quality mid-infrared line measurements. Although He 2–10 is of low mass and metallicity globally, the abundances in its nuclear HII regions are approximately solar (Kobulnicky, Kennicutt, & Pizagno 1999). Best fits to the UV spectrum require $M_{up} \geq 60 M_{\odot}$ (Chandar et al., 2003). From our modelling of the mid-infrared line ratios, we find $M_{up} < 65 M_{\odot}$. Thus, these observations permit a discrepancy between the diagnostics, but do not require one.

For NGC 3049, mid-infrared spectra are not available, but optical and UV spectra are. This galaxy is of solar (or slightly higher) metallicity in the starburst regions (Guseva, Izotov, & Thuan 2000) although it is of low mass and luminosity, and hence probably of low global metallicity. González Delgado et al. (2002) find that the P Cygni line profiles of C IV and Si IV in NGC 3049 require $M_{up} \geq 60 M_{\odot}$, and rule out ages younger than 2.5 Myr and older than 4 Myr. Further, they find that the UV diagnostics disagree with optical nebular lines as to whether massive stars are present; they fit the optical nebular lines by a $M_{up} = 40 M_{\odot}$, $t = 2.5$ Myr model—parameters which would not create the observed P Cygni

profiles in the UV. Given these results, the authors question whether nebular line ratios can reliably indicate the presence of massive stars.

We therefore re-examine the nebular line results for NGC 3049. In modelling these lines, González Delgado et al. (2002) used an older version of Starburst99 that employed pure helium WR models (Schmutz, Leitherer, & Gruenewald 1992) and Kurucz O star atmospheres prepared by Lejeune, Cuisinier, & Buser (1997). An update of Starburst99 incorporating new stellar models (Pauldrach et al. (2001) and Hillier & Miller (1998), as packaged by Smith et al. (2002)) became available after submission of their paper. The authors note that these new stellar models would soften the ionizing spectrum and reduce the discrepancy with the UV results, but they did not make a detailed reconciliation.

Using our models, which make use of these new stellar atmospheres, we re-examine the nebular lines of NGC 3049. In González Delgado et al. (2002), $\log U$ is fixed with time, and varies with radius ($\log U = -2.58$ at $R_{max} = 100$ pc) in a spherical model. This results in a generally stronger U than in our models, in which U falls with time. To compare with the results of González Delgado et al. (2002), we ran new models with $\log U$ fixed at -2.3 . This value for $\log U$ is within the measurement uncertainties of n_H and $Q(H)$ of the value used by González Delgado et al. (2002). This choice of slightly higher ionization parameter biases our test toward low values of M_{up} (and agreement with the results of González Delgado et al. (2002)).

We consider the age range $3 \leq t \leq 4$ Myr, as required by the UV lines (González Delgado et al., 2002). Over this time period, He I 5876/H β can be fit by $40 < M_{up} \leq 100 M_{\odot}$, and [O III] 5007/H β by $40 \leq M_{up} \leq 100 M_{\odot}$. [N II] 6584/H β only requires $M_{up} < 75$, [S II] 6716/H β and [O II] 3727/H β can be fit by any M_{up} from 30 to 100, and [S II] 6731/H β and [O I] 6300/H β cannot be fit by any model.

Thus, even using a high U model, we do not find that low M_{up} is required. The updated stellar models remove the inconsistency between the UV and nebular lines noted by González Delgado et al. (2002) in NGC 3049.

2.6 Discussion

We have used a number of tests to show that the nebular line ratio $[\text{Ne III}] 15.6 \mu\text{m}/[\text{Ne II}] 12.8 \mu\text{m}$ is a robust measure of the hot stellar population in starbursts. The line ratio is virtually unaffected by extinction, and as a homonuclear ratio involving a rare gas it is not subject to abundance variation or depletion onto dust. Where it can be compared to other reliable T_{eff} indicators, the agreement is good. Since the mid-infrared neon lines vary over several orders of magnitude during a few million years of starburst evolution, measurements of moderate precision can give good T_{eff} constraints.

The neon ratio indicates low T_{eff} in all members of a reasonably large sample of massive, high-metallicity starburst galaxies (Thornley et al., 2000). We have shown that plausible modifications to the interpretive models (adding dust, lowering the metallicity, changing the ionization parameter) leave the basic constraint of low T_{eff} unchanged or strengthened.

The conclusion from $[\text{Ne III}] 15.6 \mu\text{m}/[\text{Ne II}] 12.8 \mu\text{m}$ contrasts with the evidence for massive, hot stars from P Cygni line profiles in the ultraviolet spectra of two galaxies, He 2–10 and NGC 3049. In the first case, we find that the infrared nebular lines are consistent with the hot stellar spectrum indicated in the UV. In the second case, no mid-infrared spectrum exists, and the optical spectrum of González Delgado et al. (2002) does not conflict with the UV result. Thus, there is no overt conflict between the P Cygni lines in UV starburst spectra and the limits on T_{eff} set by nebular lines. However, to account for the observed low-excitation

nebular spectra of starbursts, galaxies like NGC 3049 must represent a very rare stage in starburst evolution. Can the UV wind observations, infrared nebular line results, and starburst models be reconciled, given this new constraint?

Our calculations of the emission-line properties of starbursts are based on traditional synthesis modelling, as introduced by Rieke et al. (1980). Such modelling makes the assumption that newly-formed stars appear on the main sequence according to an assumed formation rate with masses given by an initial mass function. It has recently become popular to assume a Salpeter IMF, although Rieke et al. (1993) derived a very similar IMF *ab initio* to fit the starburst properties of M82. (Both of these IMFs differ significantly from estimates of the local IMF, in that both have a substantially larger portion of massive stars).

Assuming a Salpeter IMF extending to $100 M_{\odot}$, we have shown that these models predict an early phase in starburst evolution, of duration 3 to 4 million years, when hot, massive stars should produce high-excitation emission lines. “Starbursts” are identified as—such up to ages of 15 to 20 Myr; thus, about 20% of active starbursts should be in the early < 4 Myr phase. However, the data of Thornley et al. (2000) show no starbursts in massive, high-metallicity galaxies with the line ratios predicted for this early phase. One explanation for this discrepancy would be that the Salpeter IMF substantially overestimates the numbers of very massive stars. We have shown that the mid-infrared line ratios can be explained if the IMF cuts off at 40 to $50 M_{\odot}$. Parameterizing the IMF by a cutoff is an oversimplification; a substantial steepening of the IMF slope is probably a more appropriate description. One advantage of such an IMF is that it suppresses the production of oxygen, which can otherwise reach very high abundances in starbursts (Rieke et al., 1993).

However, in addition to the indications from UV spectra that stars more mas-

sive than $40 M_{\odot}$ can form in substantial numbers in starbursts, the Arches Cluster near the center of the Milky Way has a large population of $\sim 100 M_{\odot}$ stars (Figer et al., 2002). (The mid-infrared line ratios in the Arches (Giveon et al., 2002) are consistent with a burst of age 2–3 or 6 Myr in our models, assuming twice-solar metallicity.) None of these observations can confirm the standard assumption of a Salpeter IMF extending to $100 M_{\odot}$, and the possibility of rolloff in the IMF toward very high masses needs to be considered in detail. However, the Arches and the UV starburst results suggest it is unlikely that the lack of high-excitation emission lines can be explained entirely in terms of a substantial steepening in the IMF above $40 - 50 M_{\odot}$.

We have therefore searched for other causes for this behavior. We believe an explanation can be found in an incorrect assumption in the standard synthesis models: that the full luminous output of newly-formed stars escapes into surrounding diffuse gas. This assumption justifies modelling starbursts as traditional low-density HII regions. Instead, we suggest that the majority of massive stars in starbursts spend a substantial part of their main sequence lifetimes embedded within dense, highly-extincted regions—similar to the ultracompact HII regions of the Milky Way—and are thus invisible to optical, near-infrared, and mid-infrared nebular line studies.

In the solar neighborhood, it appears that about 15% of the main sequence life of a massive star is spent within an ultracompact HII region (Kurtz, Churchwell, & Wood 1994). Hanson, Luhman, & Rieke (1996) have detected in the near-infrared about half of a sample of radio-selected ultracompact HII regions. They conclude that the detected regions typically are obscured by $A_V = 30 - 50$. Since the undetected regions in their sample should be even more heavily obscured, we take a typical case to be $A_V \sim 50$. Thus, these objects would not contribute to

the optical or near-infrared emission-line spectra of the Milky Way. The heavy extinction would even diminish the fluxes of the mid-infrared fine structure lines such as [NeII] 12.8 μm and [NeIII] 15.6 μm by a magnitude or more. More importantly, the densities in many ultracompact HII regions exceed the critical densities for these lines (e.g., $2 \times 10^5 \text{ cm}^{-3}$ for [NeIII] 15.6 μm). Thus, even in the solar neighborhood, the accuracy of traditional synthesis models would be improved by assuming that massive stars contribute their bolometric luminosity to the region for their entire main sequence lifetimes, but influence the usual T_{eff} indicators in emission line spectra for only 85% of their lives.

The correction suggested above would be small for synthesis modelling of the solar neighborhood. However, if the ultracompact HII region lifetimes were significantly greater, a substantial deviation from traditional synthesis models would be expected. For nuclear starbursts in massive galaxies, the external pressure is large, due to both the high density and high temperature of the interstellar medium. As a result, the ultracompact HII regions of starbursts should be small and their expansion retarded compared with Galactic ones (De Pree, Rodríguez, & Goss 1995; Garcíá-Segura & Franco 1996). The gravitational field of the central star(s) should also play an important role, slowing the expansion further (Keto, 2002). Thus, it is likely that the massive stars in nuclear starbursts spend a substantial fraction of their lifetimes embedded in high-extinction regions. It is even plausible that this phase is only terminated when these stars begin to lose mass in strong winds—the evolutionary phase seen in UV spectra of starbursts. This possibility is suggested by the failure, to date, to detect any nuclear starburst that appears younger than about 3 million years, based on either nebular line ratios or UV spectroscopy.

Another indication supporting the UCHII hypothesis is that starburst models

under-predict the observed bolometric luminosities of starbursts. Further evidence is that radio recombination lines and free-free continua in starbursts indicate substantially more extinction than indicated by the Brackett lines. For example, Engelbracht et al. (1998) deduced $A_V \sim 50$ to the ionized gas in NGC 253 and suggested that much of this gas lies in very compact HII regions.

In addition, Beck, Turner, & Kovo (2000) found a substantial population of sources in young starburst galaxies whose spectra *rise* from $\lambda = 6$ cm to $\lambda = 2$ cm, indicating self-absorbed (optically thick to electron scattering) emission. Parsec-scale estimated sizes and large ionizing fluxes (estimated at roughly 10^3 to 10^4 OB stars) suggest that these sources are highly obscured young superstar clusters—similar to ultracompact HII regions, but containing many more stars. Ironically, these results apply to low-metallicity, low-luminosity galaxies similar to those that emit high-excitation nebular lines. The other galaxies known to have non-AGN rising spectrum sources are NGC 5253 (Turner, Ho, & Beck 1998) and He 2–10 (Kobulnicky & Johnson 1999; Vacca, Johnson, & Conti 2002). Massive spiral starburst galaxies do not show this self-absorbed emission, though it is plausible that such sources exist but are hidden by non-thermal emission from supernovae.

There are a number of consequences for starburst modelling. Because the duration of the obscured phase may depend on the mass of the central star, it may be difficult to deduce an accurate IMF in starbursts using nebular diagnostics. The derivation of the IMF from fitting UV spectra would also be suspect, since there could be a mass/age dependence on the stars contributing to these spectra rather than their providing a snapshot of the integrated hot stellar population. In addition, by suppressing the signatures of the youngest stars, the UCHII stage will tend to make the duration of starbursts appear artificially short.

2.7 Conclusion

We have obtained $1.7\ \mu\text{m}$ and $2.1\ \mu\text{m}$ spectra for six nearby circumnuclear starburst galaxies to measure the HeI $1.7\ \mu\text{m}/\text{Br}10$ and HeI $2.06\ \mu\text{m}/\text{Br}\gamma$ line ratios. Simple recombination physics and independence from nebular conditions and extinction make HeI $1.7\ \mu\text{m}/\text{Br}10$ an accurate diagnostic of the hardness of the ionizing continuum (" T_{eff} "). The lines are too weak to be used in distant galaxies, but in nearby galaxies can test more detectable but potentially problematic diagnostics.

We present models for the behavior of the T_{eff} diagnostics discussed in this paper. SEDs were generated by the spectral synthesis code Starburst99, which uses the most current O star and Wolf–Rayet model spectra (Pauldrach et al., 2001; Hillier & Miller, 1998). Although T_{eff} remains a useful shorthand term, accurate models of the ionizing continuum must consider the entire population of hot main sequence and Wolf–Rayet stars. Wolf–Rayet stars maintain high line ratio values after the O stars have left the main sequence. Our updated models may aid interpretation of IRS spectra from SIRTf.

We then test whether the observed line ratios are consistent with these new models. By comparison with HeI $1.7\ \mu\text{m}/\text{Br}10$, we confirm that HeI $2.06\ \mu\text{m}/\text{Br}\gamma$ is a problem–ridden diagnostic, as predicted (Shields, 1993). HeI $2.06\ \mu\text{m}/\text{Br}\gamma$ also fails to correlate with the mid–infrared diagnostic $[\text{NeIII}]/[\text{NeII}]$. However, we point out that a low HeI $2.06\ \mu\text{m}/\text{Br}\gamma$ ratio may indicate a soft UV continuum. NGC 4102, in which HeI $1.7\ \mu\text{m}/\text{Br}10$ and HeI $2.06\ \mu\text{m}/\text{Br}\gamma$ are both low, is an example.

We test $[\text{OIII}]\ 5007\ \text{\AA}/\text{H}\beta$ as a T_{eff} diagnostic in starburst galaxies. In comparison to HeI $6678/\text{H}\alpha$, $[\text{NeIII}]/[\text{NeII}]$, and HeI $1.7\ \mu\text{m}/\text{Br}10$, we find that $[\text{OIII}]/\text{H}\beta$ is systematically elevated. While aperture mismatch may contribute

to the poor correlation with $[\text{NeIII}]/[\text{NeII}]$, the other two diagnostics were observed with apertures comparable to that for $[\text{OIII}]/\text{H}\beta$. We suggest that shock-excitation of $[\text{OIII}]$ by supernovae is the likely cause of very high $[\text{OIII}]/\text{H}\beta$, and that this effect plus differing sensitivities to extinction may explain the considerable scatter and lack of correlation with the other T_{eff} diagnostics.

We attempt to test optical He and H recombination line ratios. Sample sizes in the literature are too small to compare $\text{HeI } 6678/\text{H}\alpha$ or $\text{HeI } 4471/\text{H}\beta$ to each other or to $[\text{NeIII}]/[\text{NeII}]$, $\text{HeI } 1.7 \mu\text{m}/\text{Br}10$, or $\text{HeI } 2.06 \mu\text{m}/\text{Br}\gamma$. Instead, we estimate T_{eff} in galaxies by the latter three diagnostics, and test for a correlation with $\text{HeI } 6678/\text{H}\alpha$. We find a correlation at 2σ significance. We re-evaluate the optical nebular lines of NGC 3049, and find them consistent with the age and IMF inferred from the UV spectrum; this removes the discrepancy between the UV and nebular diagnostics noted previously using less sophisticated stellar atmospheres.

We show that the mid-infrared lines and $\text{HeI } 1.7 \mu\text{m}/\text{Br}10$ give consistent answers for well-studied starbursts, lending credibility to the mid-infrared lines' use as diagnostics of starburst ionizing fields. We also demonstrate theoretically that the behavior of these lines in starbursts should be dominated by T_{eff} for galaxies with similar metallicity.

Having found the mid-infrared line ratios to be credible T_{eff} diagnostics, we use them to address the conditions in starbursts. Thornley et al. (2000) found low values of the $[\text{NeIII}] 15.6 \mu\text{m} / [\text{NeII}] 12.8 \mu\text{m}$ ratio in their sample of 27 starburst galaxies. In the context of our models, this result would suggest that high-mass, solar-metallicity starbursts form fewer $M \gtrsim 40 M_{\odot}$ stars than a Salpeter IMF. Adding dust, lowering the metallicity, choosing a different stellar atlas, or choosing a more extended star formation history would strengthen this conclu-

sion.

However, another more likely possibility can account for this result. The relatively high density and temperature of the interstellar medium in nuclear starbursts should increase the duration of the ultracompact HII region phase. As a result, most of the very massive stars may spend virtually their entire main sequence lifetimes embedded within dense, highly extincted regions, and thus will be nearly undetectable to conventional optical or near-to-mid-infrared spectroscopy. This situation will make it difficult to determine the high-mass IMF in starbursts.

In contrast to the high-mass, solar-metallicity starbursts, in the low-mass, low-metallicity galaxies II Zw 40 and NGC 5253, high neon line ratios seem to require stars more massive than $\sim 40\text{--}60 M_{\odot}$. This contrast can be understood if these galaxies form stars in regions where the interstellar medium is less effective at confining ultracompact HII regions, or if the lifetimes of these regions are reduced at low metallicity.

CHAPTER 3

THE 24 μm PROPERTIES OF X-RAY SELECTED AGN

We examine the 24 μm to X-ray color of 157 X-ray–selected AGN as a function of X-ray obscuration and optical classification in the Chandra Deep Field South. The sample consists of the Chandra hard–band detections with 2–8 keV flux $> 10^{-15} \text{ erg s}^{-1} \text{ cm}^{-2}$. A deep 24 μm mosaic obtained with *Spitzer* provides mid–infrared fluxes for the sample. Since obscured AGN locally have higher 24 μm /2–8 keV ratios than unobscured AGN, and since X-ray background models predict a large population of obscured AGN, we expect to find many X-ray–hard, IR–bright AGN. Instead, we find that the 24 μm to X-ray flux ratio does not depend on X-ray hardness in the full sample, nor does it differ between narrow–line and broad–line AGN. We identify 5 nearly Compton–thick AGN, and find they have similar 24 μm to X-ray flux ratios compared to the full sample. We consider AGN in the narrow redshift spikes at $z \sim 0.7$; for these AGN, there is some evidence that the flux ratio increases with X-ray hardness. The redshift slice also shows an odd trend, which is also prominent in the full sample: a group of X-ray–hard AGN with very low 24 μm to X-ray flux ratios.

3.1 Introduction

The hard spectrum of the X-ray background, which peaks at 30–40 keV, implies the existence of a large population of obscured active galactic nuclei (AGN) (Madau et al., 1994; Comastri et al., 1995; Gilli et al., 2001). Finding and understanding these obscured AGN is crucial to understanding the accretion history of the universe. These AGN are predicted to be particularly bright in the mid–infrared, as soft X-ray and ultraviolet emission is absorbed by the intervening material and

re-emitted by dust. With *ISO*, Fadda et al. (2002) reported elevated mid-infrared emission from obscured AGN, and Franceschini et al. (2002) found the majority of *ISO*-detected AGN to be obscured.

Spitzer can test these ideas about the obscuration of AGN and the interplay of the infrared and X-ray backgrounds. In this letter, by studying the Chandra Deep Field South (CDFS), we present a first look at the *Spitzer* mid-infrared properties of AGN.

3.2 The Data and Catalogs

We present deep new observations of the CDFS at $24\ \mu\text{m}$ obtained with the Multi-band Imaging Photometer for *Spitzer* (MIPS) (Rieke et al., 2004). These data were obtained with guaranteed time under program 81; the relevant AORs are 8950528, 8951296, 8954112, 8957696, 8958208, 8958464, 8958976, 8959488, 8960000, 8960512, 8961024, and 8961536. Slow scan-map mode was used, achieving an average integration of 1380 s. The data were reduced using the DAT package of the MIPS instrument team (Gordon et al., 2005). The resulting mosaic completely overlaps the $\sim 17'$ by $17'$ Chandra field. The 80% completeness limit, determined by adding artificial sources, is 0.083 mJy (Papovich et al., 2004). This flux limit is comparable to the 5σ noise, which, scaling from Dole et al. (2004), is 0.086 mJy at the CDFS exposure depth (accounting for detector and confusion noise (Dole et al., 2004).) Thus, the full mosaic is one of the deepest, widest-field $24\ \mu\text{m}$ maps yet obtained.

Sources were extracted from the $24\ \mu\text{m}$ mosaic as described by Papovich et al. (2004). In the $270\ \text{arcmin}^2$ region having X-ray exposure times exceeding 0.5 megaseconds, we detect 1147 $24\ \mu\text{m}$ sources brighter than the 80% completeness limit. In the $200\ \text{arcmin}^2$ region having $> 0.75\ \text{Ms}$ X-ray coverage, we detect 878 such

24 μm sources. (The X-ray depth of coverage varies across the field because the 11 observations comprising the full Chandra exposure have different roll angles.)

Two papers currently in preparation will publish 24 μm fluxes for ~ 90 X-ray sources in CDFS (Rigby et al., 2005, 2006); most of these sources are within the main sample of this letter.

The Chandra 1 megasecond CDFS is one of the deepest X-ray observations to date. Two reductions and source catalogs exist in the literature. The first is by the CDFS team, who find 304 sources detected jointly by SExtractor and wavdetect (Giacconi et al. 2002, hereafter G02). The second is by the CDF-N team, using the same processing and source extraction methods for CDF-S as they used for CDF-N (Alexander et al. 2003, hereafter A03). Their source catalog has 326 sources. A03 compare these two catalogs, finding 293 sources in common. Because the *Spitzer* cosmological surveys will also target the CDF North, in this paper we use the A03 catalog, to facilitate future comparisons between the North and South fields.

The astrometry of the CDFS Chandra catalogs is excellent. A03 registered their astrometry to the frame of the R-band ESO Imaging Survey (Arnouts et al., 2002); the median separation between X-ray and R-band positions is $0.37''$ (A03). Using the same R-band catalog,¹ we registered our 24 μm mosaic to their astrometric frame by adding a $0.52''$ global shift.

The other catalog used in this paper is that of Szokoly et al. 2004 (hereafter S04), who present secure spectroscopic redshifts for 137 X-ray-selected sources in the CDFS. They classify their sources in two ways: based on optical spectra, and based on X-ray luminosity and hardness.

¹From CDS, at <http://vizier.u-strasbg.fr>

3.3 Sample Selection

We select hard band (2–8 keV) detections in the CDFS from the catalog of A03; there are 198. Selecting hard band detections (rather than soft or any-band detections) reduces contamination from non-active galaxies. To further maximize the AGN fraction, we require the hard-band flux to exceed $10^{-15} \text{ erg s}^{-1} \text{ cm}^{-2}$, which reduces the sample to 157 sources. This is our main sample. None of these sources is classified by S04 as a star or a non-active galaxy. Almost all of these sources are likely to be AGN (see Figure 2 of Barger et al. (2003)); 65 have been identified as AGN by their X-ray hardness and luminosity (which requires a known redshift), and 39 have been identified as AGN by optical spectroscopy.

Because the soft band of Chandra (0.5–2 keV) is more sensitive than the hard band, sources in our main sample generally have a well-measured soft-band flux or a well-constrained limit.

For the main sample, we seek redshifts as available from S04. S04 targeted optical counterparts to X-ray sources from the G02 catalog (and thus associate redshifts with G02 X-ray sources), whereas we use the A03 X-ray catalog. As a result, it is necessary to associate the A03 and S04 catalogs, which we do by matching sources whose coordinates are separated by less than $2''$. Such a large separation is necessary to match sources at large off-axis angles, where Chandra centroiding is difficult. Since the only spectra in the S04 catalog are counterparts to X-ray sources, the source density is small ($\sim 0.5 \text{ arcmin}^{-2}$), so the probability of false matches with the A03 X-ray catalog is small. In the main sample, 65 AGN have secure redshifts and optical classifications.

For each X-ray source in our main sample, we search for a $24 \mu\text{m}$ counterpart from our catalog. To claim detection, we require the fractional flux uncertainty to be $< 50\%$ and the coordinates (X-ray and $24 \mu\text{m}$) to be offset by $< 1.2''$. (This small

separation is sufficient to match sources over most of the field, and is necessary to prevent false matches, since the $24\ \mu\text{m}$ source density is high.) No X-ray source has multiple $24\ \mu\text{m}$ sources within the permitted offset. Given the $24\ \mu\text{m}$ source density reported above, for the main sample of 157 X-ray sources, by chance we expect ~ 1 false $24\ \mu\text{m}$ counterpart using the P-statistic (see e.g. Lilly et al. (1999)). The result of the counterpart search is that 98 of the 157 sources in the main sample have $24\ \mu\text{m}$ counterparts. For sources not detected at $24\ \mu\text{m}$, we take the flux upper limit to be the 80% completeness limit (0.083 mJy).

Figure 3.1 displays the section of the $24\ \mu\text{m}$ mosaic that overlaps the Chandra field, with the main sample X-ray positions overlaid.

3.4 Comparing X-ray and $24\ \mu\text{m}$ colors

AGN are traditionally classified by optical spectroscopy. However, for distant sources, nuclear emission can be overwhelmed by stellar emission, especially for low-luminosity AGN (Moran et al., 2002). Obscuration or lack of the narrow lines may also play a role (Maiolino et al., 2003). Consequently, 43% of X-ray selected AGN in the CDFS are not classified as active by optical spectroscopy (S04). Because of this, many authors have argued that X-rays are a better way to *select* AGN than optical spectroscopic surveys.

Further, X-rays may be a more effective way to *classify* AGN (Hasinger et al., 2001). AGN with harder X-ray spectra are generally measured to have thicker columns of absorbing gas than do X-ray-soft AGN. Similarly, in unification models, optical Type 2 AGN are drawn from the same population of objects as Type 1 AGN, but they are viewed through thicker columns of obscuring gas and dust. Thus, X-ray hardness can estimate the obscuration of AGN when optical spectroscopy cannot.

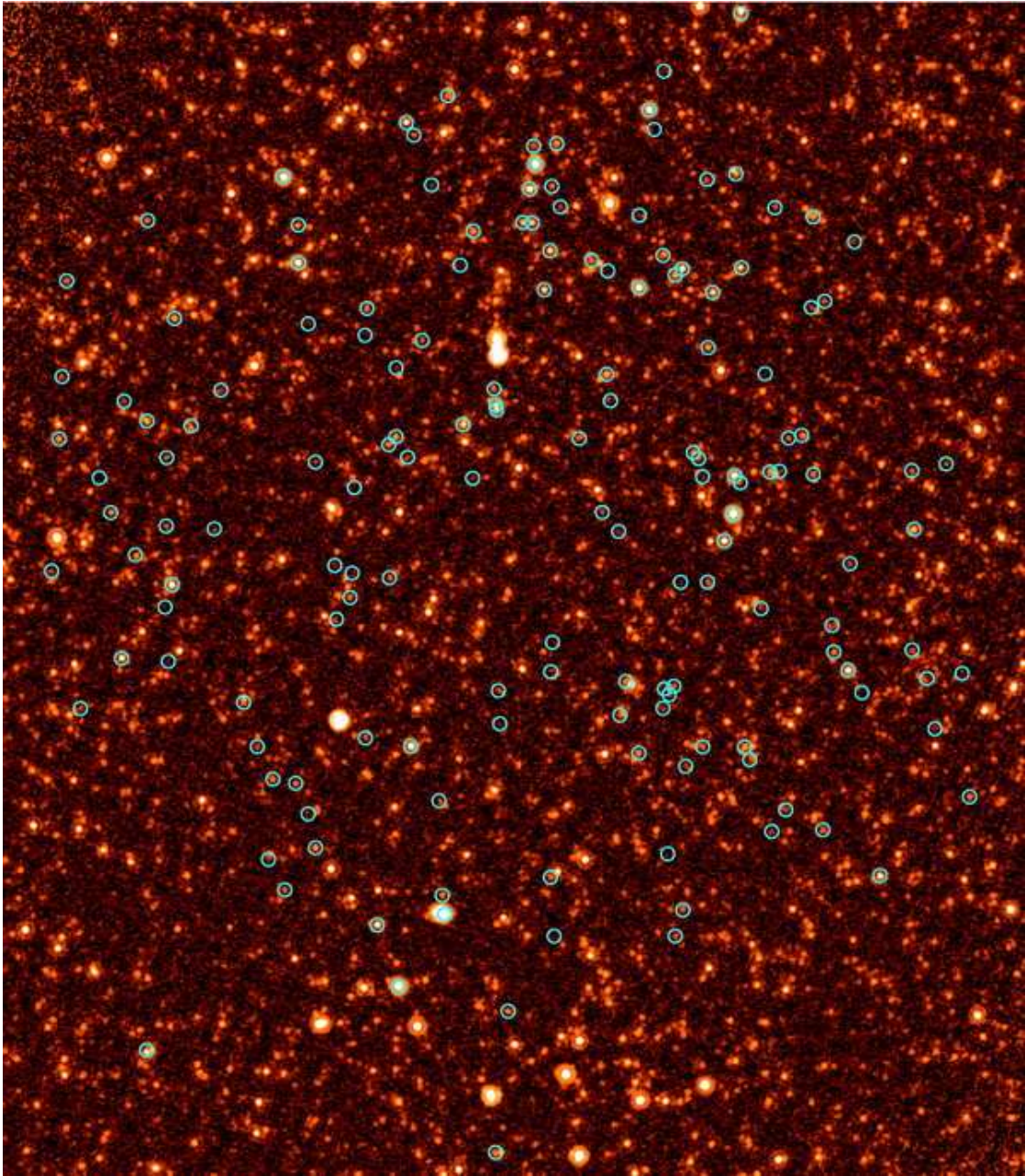


Figure 3.1 Image of CDF-S at $24\ \mu\text{m}$. Overplotted are the X-ray positions of the main sample. The circles are large ($R=8''$) for presentation purposes. The scale is $20.3'$ by $23.3'$; North is up and East is left. The resolution of this image has been reduced; the full-resolution image can be obtained from Rigby et al. (2004) in the electronic edition of the *Astrophysical Journal*.

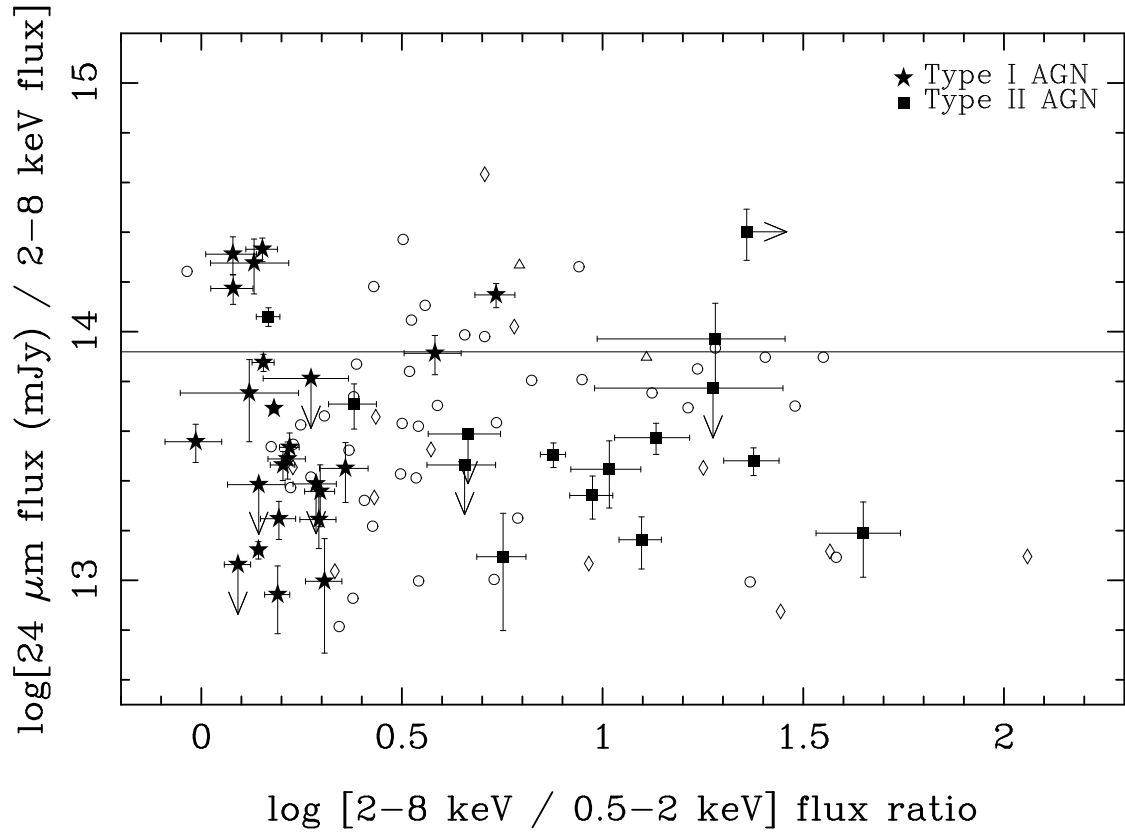


Figure 3.2 Symbol types indicate classification from optical spectroscopy: broad-line AGN and QSOs (*star symbols*) as well as AGN with high-excitation narrow lines (*filled squares*). These are the classical Type 1 and Type 2 categories, respectively. Also plotted are sources whose optical spectra show low-excitation emission lines (*diamonds*) or absorption lines (*triangles*), as well as sources lacking optical classification (*circles*). To improve plot clarity, for the last three categories, sources with non-detections in $24 \mu\text{m}$ or soft X-ray are omitted, and errorbars are omitted. Optical spectroscopy and classification are from S04.

Figure 3.2 compares optical and X-ray classification of the CDFS AGN. The x-axis is an indicator of spectral hardness: we define the ratio of the hard to soft X-ray fluxes as $H/S = \log[\text{flux}(2-8 \text{ keV})/\text{flux}(0.5-2 \text{ keV})]$. Sources with broad emission lines (optically-selected Type 1 Seyferts and QSOs) cluster toward the X-ray-soft side of the figure. These objects are well-separated in X-ray hardness from the sources with optical high-excitation narrow emission lines (optically-selected Type 2 AGN), which span a range of higher X-ray hardness. This clear separation validates the use of the hard/soft X-ray flux ratio H/S as a tool to classify AGN, as also found by Mainieri et al. (2002). Indeed, S04 also used X-ray hardness to classify these CDFS AGN, using the same Chandra data and very similar energy bands to this work, but a counts ratio rather than a flux ratio; their division between Type 1 and Type 2 AGN lies at $H/S \approx 0.6$ in our Figure 3.2, and agrees well with the boundary between optically classified Type 1 and 2 AGN.

In Figure 3.3, we now examine how X-ray hardness affects the behavior of the $24 \mu\text{m}$ to X-ray flux ratio, defined as $24/X = \log[(24\mu\text{m flux density, mJy})/(2-8 \text{ keV flux, erg s}^{-1} \text{ cm}^{-2})]$. There is a factor of 100 spread in both the H/S and $24/X$ flux ratios. The spread in H/S reflects the range of X-ray hardness found in AGN. The reasons for the spread in the $24/X$ flux ratio we discuss below.

The horizontal line in Figures 3.2 and 3.3 is the $24/X$ color of a source with hard X-ray flux at the sample cutoff, and $24 \mu\text{m}$ flux at the 80% completeness limit. Since the sample is X-ray selected, we are reasonably complete to colors above the line, while we may be missing sources with colors below the line (because the $24 \mu\text{m}$ flux may fall below the detection limit.)

Figures 3.2 and 3.3 show that overall, the $24 \mu\text{m}/2-8 \text{ keV}$ flux ratio does **not** depend on the hardness of the AGN. There is no global trend of the $24/X$ flux ratio with H/S . Nor does the $24/X$ ratio differ significantly between the X-ray-

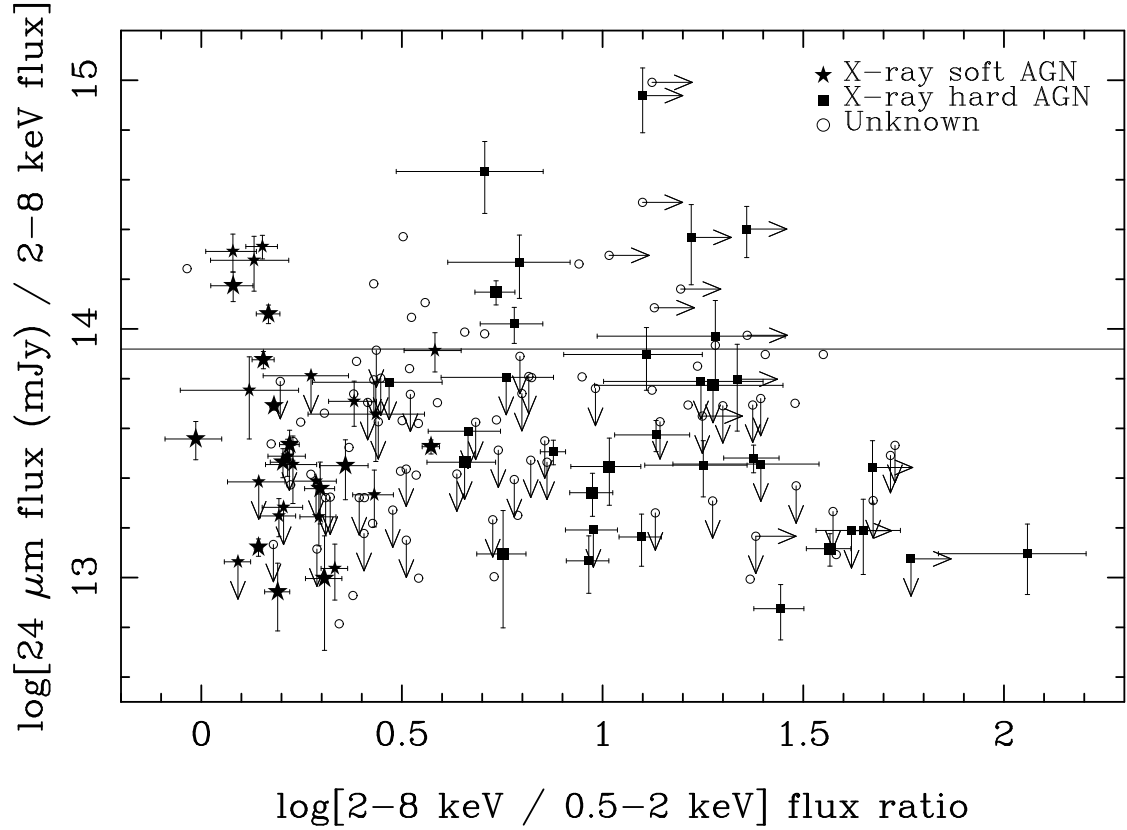


Figure 3.3 All sources in the main sample are plotted, and symbol types indicate X-ray classification from S04: X-ray-classified soft AGN (*star symbols*); X-ray-classified hard AGN (*solid squares*); and unclassified sources (*circles*). Sources lacking measured redshifts are “unclassified”, since a redshift is necessary to measure the X-ray luminosity, which S04 required along with X-ray hardness to classify sources. For clarity, errorbars are not plotted for the unclassified sources. Larger symbols indicate QSO luminosities.

classified hard and soft AGN in Figure 3.3, nor between the optically-classified Type 1 and Type 2 AGN in Figure 3.2.

Fadda et al. (2002) found that 5–10 keV XMM sources were twice as likely to have 15 μm counterparts compared with 0.5–2 keV sources; however, this result was based on just 28 IR-detected hard X-ray sources. The authors used the IR/X-ray spectral slope to classify sources as Type 1 or Type 2 AGN or dominated by star formation, and then applied these classifications to estimate the AGN contribution to the IR background. (They did find some X-ray-soft AGN with high IR/X ratios, which they attributed to host galaxy contamination.) As discussed above, our full sample (Figure 3.3) contradicts the Fadda et al. (2002) result that the mid-IR flux of AGN is a strong function of hardness.

3.5 Discussion

To understand the behavior of the 24/X flux ratio, in Figure 3.4 we present the flux ratios predicted by local AGN templates with a range of obscuration (Silva et al., 2004). These templates were obtained by interpolating nuclear infrared photometric data of a sample of 33 Seyferts. Each infrared SED was normalized to the absorption-corrected hard X-ray luminosity, and then averaged within bins of absorbing N_H . Using these empirical templates, Silva et al. (2004) derived the contribution of AGN to the mid-IR background and successfully matched the observed fraction.

In Figure 3.4, at $z = 0$ as the obscuring column increases, the predicted 24/X ratio increases (since the 24 μm flux rises due to reprocessing and the 2–8 keV flux falls dramatically due to absorption.) This effect grows weaker with increasing redshift because of K-corrections: as the 2–8 keV band samples progressively higher rest-frame energies, the band is less absorbed for a given column. Gen-

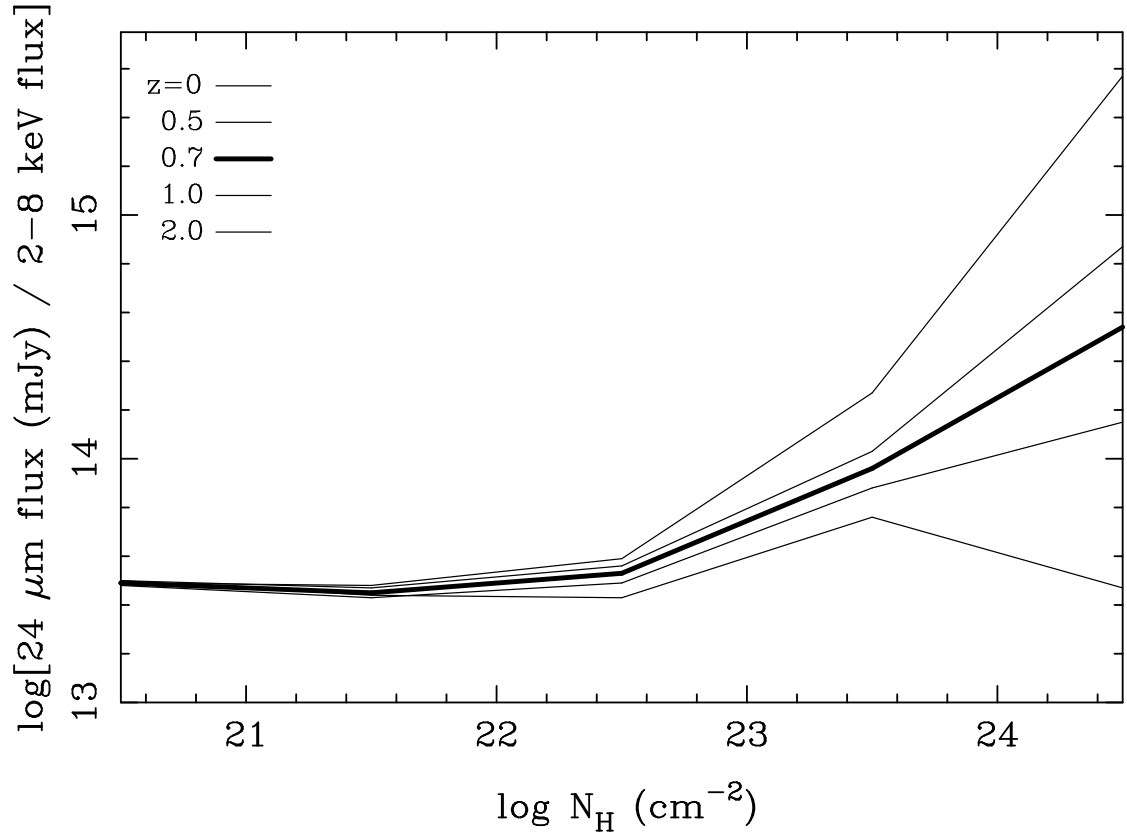


Figure 3.4 Behavior of $24 \mu\text{m}/2\text{-}8 \text{ keV}$ flux ratio with increasing obscuration. From top to bottom, lines show line ratios for local templates (Silva et al., 2004) redshifted to $z = 0, 0.5, 0.7$ (*dark line*), 1.0 , and 2.0 . Intrinsic differences in the template SEDs create a $24/X$ scatter of about ± 0.5 dex around the mean values plotted.

erally in the deep X-ray surveys, Type 1 AGN have $\log N_H \lesssim 22 \text{ cm}^{-2}$, whereas Type 2 have $22 \lesssim \log N_H \lesssim 24 \text{ cm}^{-2}$ (Gilli, 2004).

A basic conclusion from Figure 3.4 is that local AGN with $\log N(H) \lesssim 23.2 \text{ cm}^{-2}$ cannot produce $24/X > 14$ for $0 < z < 2$. When X-ray-soft AGN are observed to have such high 24/X ratios (as seen for a minority of sources in Figure 3.3), this suggests that the 24 μm flux is dominated by star formation in the host galaxy, not by accretion. (Some of the harder sources with high 24/X may also be star-formation dominated.) Using this rule of thumb, we see that star formation does not dominate most of the sources in Figure 3.3; their 24/X ratios are consistent with AGN power. (See also Alonso-Herrero et al. (2004).)

To disentangle the effects of redshift and compare the distant AGN to local templates, in Figure 3.5 we plot all hard-band detected AGN in the redshift range $0.65 < z < 0.75$. This range encompasses the prominent $z = 0.674$ and $z = 0.734$ redshift spikes (S04), which allows us to restrict the redshift range (and thus the spread in K-correction) while maximizing the sample size.

We first examine the X-ray-soft AGN in Figure 3.5. Their 24/X ratios agree well with the local templates, which predict $24/X \approx 13.5$ for AGN with $\log N_H < 22.5 \text{ cm}^{-2}$ at this redshift. The spread in template SEDs predicts a scatter in the flux ratio of about ± 0.5 in log units, which is consistent with the data.

We now examine the 24/X ratio for the hard ($H/S \gtrsim 0.6$) AGN. We propose two possible interpretations of the trends in Figure 3.5:

- There is no trend of 24/X with X-ray hardness in Figure 3.5. The distribution simply reflects the scatter seen in Figure 3.3.
- The 24/X ratio does indeed increase with hardness in this subsample, as expected from reprocessing: $H/S \sim 0.8$ AGN have higher 24/X than $H/S < 0.5$ AGN. However, there are several strange exceptions: AGN with very

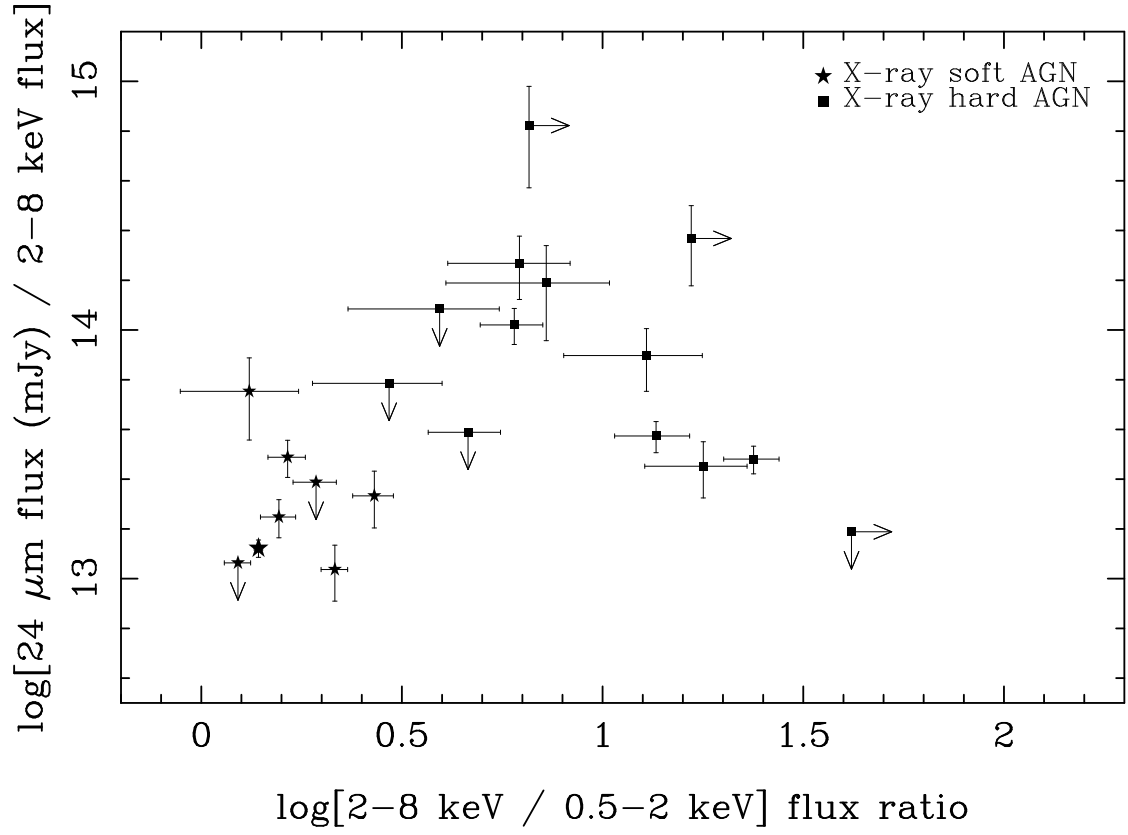


Figure 3.5 IR/X color for the $0.65 < z < 0.75$ AGN of the CFDS. All AGN with spectroscopic redshifts in this range have been plotted; no X-ray flux cut has been imposed. Symbols and classification as in figure 3.3.

hard X-ray flux ratios and very low 24/X.

This population of X-ray-hard AGN with low 24/X is also seen in the full redshift sample (Figure 3.3), where there are ~ 15 such sources. Their 24/X ratios are 0.5–1 dex lower than predicted by the templates. These sources are surprising within the unification paradigm: the hardness ratios indicate large column density, which unification scenarios associate with a dusty molecular torus; this column should absorb the X-ray radiation, thus increasing the 24/X ratio relative to lower-column AGN. Additionally, dust in the torus should absorb a large fraction of the UV continuum and re-emit that energy in the mid-infrared, further increasing 24/X. In the X-ray-hard 24 μm -faint sources in question, this expectation is not observed. Thus, these sources merit further investigation; there may be a real difference between these AGN and local AGN (for example in their dust properties or absorbing geometries.) Though the average 24/X value for the X-ray-hard AGN may be higher than it appears in Figure 3.3 due to selection effects, the sources with low 24/X still beg explanation.

While the H/S X-ray flux ratio is a useful diagnostic, the more fundamental parameter is the amount of obscuring column. For the very hard ($H/S > 1$) AGN with known redshifts, we examine the X-ray spectral information derived by Gilli (2004). Ten of the 16 spectra are fit by $\log N_H \approx 23 \text{ cm}^{-2}$, while only 5 fits require $23.7 < \log N_H < 24 \text{ cm}^{-2}$. Those five nearly Compton-thick AGN have 24/X values spanning 13.2 to 14.4, which is the same range populated by the other AGN (soft and hard).

Could we have missed the majority of the highly obscured, high 24/X AGN? Since Compton-thick AGN should be fainter at 2–8 keV than less obscured AGN, it is quite possible that the most obscured AGN are the faintest in our survey. The faint (hard flux $\lesssim 3 \times 10^{-15} \text{ erg s}^{-1} \text{ cm}^{-2}$) AGN are less likely to have known

spectroscopic redshifts and reliable X-ray spectral fits. Since they are faint in the hard band and undetected in the soft, they have lower limits on H/S that permit but do not require extreme hardness. Several such objects have high 24/X. Thus, these AGN are good candidates for being highly obscured. If they are, they would populate the high H/S, high 24/X region of Figure 3.3 where obscured AGN are expected, but not seen.

3.6 Conclusions

We present the first look at the 24 μm to X-ray colors of X-ray-selected AGN. The expectation that harder AGN should be relatively brighter at 24 μm is not confirmed. Rather, there is large scatter and no trend in 24/X color with X-ray hardness in our sample of 157 AGN (with dynamic range of 100 in both flux ratios). In addition, the 24/X colors of optically-identified Type 1 and 2 AGN are indistinguishable.

In a narrow redshift slice (picked to minimize differential K-corrections), we see hints that 24/X may increase with X-ray hardness (though this effect is not seen in the full sample). However, in both the restricted-redshift and full samples, we identify AGN with unusual colors: very hard X-ray flux ratios and surprisingly low 24/X ratios. These AGN merit further investigation.

X-ray spectral fits to 16 of the X-ray-hard AGN find column densities of $10^{23-24} \text{ cm}^{-2}$, most toward the lower end of this range. Thus, only a handful are nearly Compton-thick ($N_H \approx 10^{24} \text{ cm}^{-2}$). Even these sources do not distinguish themselves in 24/X color from the lower-column AGN.

Thus, while this initial survey has not yet confirmed expectations for a population of X-ray-obscured, infrared-bright AGN, we have raised new questions: What explains the factor of ~ 100 range in 24 μm to 2–8 keV flux ratio? Why do

many of the hardest AGN have very low $24/X$ ratios compared with local templates? And if hard X-ray selection and $24\ \mu\text{m}$ follow-up finds few Compton-thick AGN, what is a better way to search? Future surveys and follow-up observations are clearly needed to address these questions.

CHAPTER 4

THE NATURE OF LUMINOUS X-RAY SOURCES WITH MID-INFRARED COUNTERPARTS

4.1 Explanatory Note

This chapter originally appeared as a paper by A. Alonso-Herrero, P. G. Pérez-González, J. Rigby et al. (2004). With the permission of my thesis advisor, I include it in my thesis due to my substantial contributions as a co-author, including:

- reducing the Chandra observations of the Extended Groth Strip, including solar flare removal, flux calibration, source detection, photometry, and merging of the photometry across four energy bands;
- conducting the collaboration with M. Page that provided the XMM data;
- band-merging the XMM and 24 μm source lists in the Lockman Hole, as well as the Chandra and 24 μm catalogs in the Extended Groth Strip; and
- developing new diagnostic X-ray hardness flux ratios.

4.2 Introduction

The very rapid evolution of quasars from $z \sim 2$ to the present (Boyle et al. 1987) raises the question of whether any properties of these sources other than space density have changed over this interval. One way to probe changes in the AGN population is to compare spectral energy distributions (SEDs) over a broad frequency range as a function of redshift. The SED of an active galaxy reflects the presence of the underlying AGN, plus the luminosity of the host galaxy stellar

population, the reddening of the AGN, and the role of star formation, all in different frequency regimes. SED determination in large samples of high- z AGN using imaging detectors is therefore an efficient way to survey for evolutionary trends in quasars and AGN, and in their host galaxies.

A number of trends might be expected. Will we be able to confirm predictions that the relative number of obscured AGN was higher at large lookback times than now, to fit models of the X-ray background (e.g., Gilli, Risaliti, & Salvati 1999)? AGN activity may be triggered by gas inflow caused by galaxy interactions. Interactions also trigger starbursts — will we find that an elevated rate of star formation in the host galaxy is a typical characteristic of distant AGN? Will younger AGN host galaxies have more material in their ISM than current-epoch ones, causing greater extinction of their nuclei?

To probe such questions, we have used IRAC (Fazio et al. 2004), MIPS (Rieke et al. 2004), and ancillary data to assemble SEDs for AGN in the Lockman Hole (LH) and Extended Groth Strip (EGS). We have made use of deep X-ray images to locate the AGN. For this initial survey, we wanted an unambiguous detection of an infrared (IR) excess to make SED classification robust. We have included objects detected at $24\,\mu\text{m}$, although we briefly discuss galaxies not detected at $24\,\mu\text{m}$. We compare the results with SEDs of a sample of nearby ($z < 0.12$) hard X-ray selected AGN that are bright in the mid-IR, and hence nominally similar to the sources identified in the deep *Spitzer*/X-ray fields. This comparison allows us to make tentative identifications of trends in the AGN/host galaxy behavior from the typical redshift of the AGN in the survey fields ($z \sim 0.2$ to 1.6) to the present.

4.3 Spitzer Observations

We have obtained 24 μm MIPS observations of two fields in the LH: primary field (area of $5' \times 5'$) at RA = $10^{\text{h}} 52^{\text{m}}$ and Dec = $57^\circ 25'$ (J2000), and parallel field (area of $7' \times 6'$) at RA = $10^{\text{h}} 52^{\text{m}}$ and Dec = $57^\circ 37'$. We also obtained MIPS observations of the EGS overlapping with the *Chandra* observation ($\simeq 180 \text{ arcmin}^2$, see next section) at RA = $14^{\text{h}} 17^{\text{m}}$ and Dec = $52^\circ 28'$. Gordon et al. (2004), Egami et al. (2004), Papovich et al. (2004), and Le Floch et al. (2004) describe the data reduction and photometry in detail. The astrometric uncertainties of *Spitzer* observations are $< 1''$. The 80% completeness limits at 24 μm are: 0.17 mJy and 0.1 mJy for the LH primary and parallel fields, and 0.11 mJy for the EGS (Papovich et al. 2004).

The LH primary field and the EGS were observed by IRAC at 3.6, 4.5, 5.8, and 8 μm . The data reduction is discussed in Huang et al. (2004) for the LH and Barmby et al. (2004, in preparation) for the EGS. Counterparts of all MIPS and X-ray sources were nearly pointlike, and the photometry used circular apertures and the standard point-source calibration (see Huang et al. 2004).

4.4 X-ray Observations

The *XMM* images of the LH were formed from seven datasets taken in 2000 and 2001 to a total integration time of 150 ks. The data cover entirely both the primary and parallel 24 μm MIPS fields. We produced images in the energy bands 0.2 – 0.5 keV, 0.5 – 2 keV, 2 – 5 keV, and 5 – 10 keV, and searched for sources simultaneously in an iterative process to optimize the background model and thereby the sensitivity. In the LH we have detected 35 *XMM* sources with X-ray fluxes down to $f_{0.2-10\text{keV}} \simeq 10^{-15} \text{ erg cm}^{-2} \text{ s}^{-1}$. The astrometric uncertainties are better than $1''$ for bright sources, and less than $3''$ for the faintest sources.

For the EGS, three *Chandra* ACIS datasets were taken from the CXC archive

with an exposure time of 131 ks. We searched for sources separately in four bands ($0.5 - 8$ keV, $0.5 - 2$ keV, $2 - 8$ keV, and $4 - 8$ keV) using WAVDETECT. In the overlapping area between the *Chandra* and MIPS fields we have detected 77 sources in the full band with fluxes down to $f_{0.5-8\text{keV}} \simeq 10^{-15} \text{ erg cm}^{-2} \text{ s}^{-1}$. Of these, 40 are detected in the $2 - 8$ keV band. Astrometric uncertainties are $1 - 2''$, where the high value is for sources at large off-axis angles.

4.5 Cross-correlation of X-ray and $24 \mu\text{m}$ sources

Taking into account the astrometric uncertainties we used radii of $2.2''$ and $3''$ for matching $24 \mu\text{m}$ sources to *Chandra* and XMM sources, respectively. Within the LH approximately 57% of the XMM sources are detected at $24 \mu\text{m}$. 75% of LH X-ray sources with $f_{5-10\text{keV}} > 10^{-15} \text{ erg cm}^{-2} \text{ s}^{-1}$ have $24 \mu\text{m}$ counterparts. In the EGS approximately 50% of *Chandra* sources have a $24 \mu\text{m}$ counterpart, and this fraction is $\simeq 60\%$ for sources detected in the hard ($2 - 8$ keV) band. Taking into account the surface density of $24 \mu\text{m}$ sources (80% completeness limit), the probability of a chance match with an X-ray source is $2 - 3\%$ for both the LH and EGS.

4.6 Activity classification

Hard X-ray to mid-IR flux ratios are known to be different for AGN dominated galaxies and starbursts in the Local Universe, and can be used to assess if the AGN emission is dominant in the mid-IR. Fig. 1 shows the $24 \mu\text{m}$ fluxes vs. $2 - 10$ keV X-ray fluxes for our sample. As a comparison we plot the extrapolation to fainter fluxes of the region occupied by hard X-ray selected AGN from Piccinotti et al. (1982) with detected mid-IR emission and $z < 0.12$. This sample should be nominally similar to the sources studied here. The effect of increasing redshift

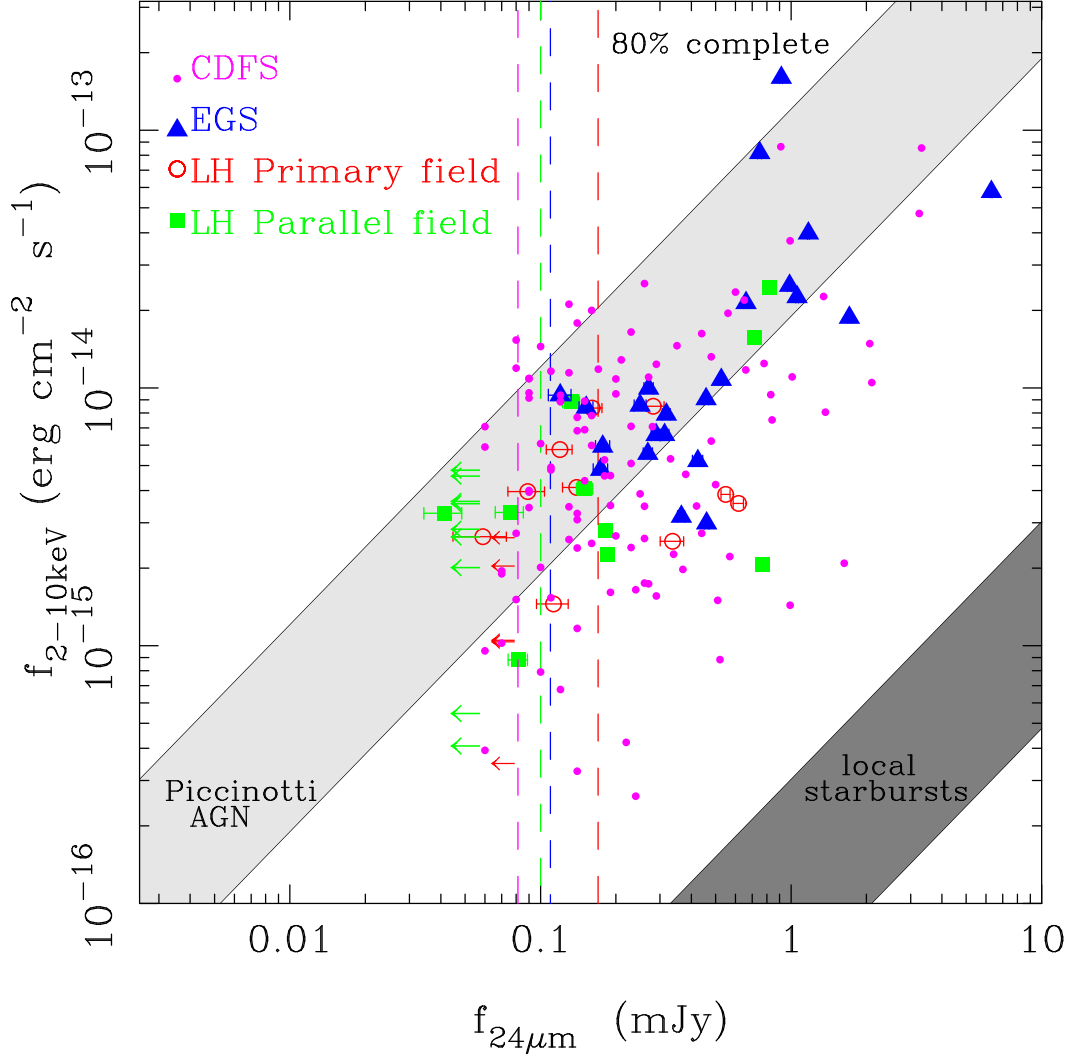


Figure 4.1 $24\mu\text{m}$ fluxes vs. $2 - 10\text{ keV}$ X-ray fluxes: XMM sources (squares and open circles) in the LH and Chandra sources in the EGS (filled triangles). The Chandra $2 - 8\text{ keV}$ fluxes have been converted to $2 - 10\text{ keV}$ assuming a power law with photon index $\Gamma = 1.4$. Also shown are X-ray/ $24\mu\text{m}$ sources in the CDF-S (dots, Rigby et al. 2004). The $24\mu\text{m}$ non-detections of LH X-ray sources are shown as upper limits at a 5σ confusion limit. The dashed lines are the 80% completeness limits for the different fields (color coded as the symbols for the different fields). The lightly shaded area is the extrapolation of the median hard X-ray to mid-IR ratios ($\pm 1\sigma$) of local ($z < 0.12$) hard X-ray selected AGN (Piccinotti et al. 1982) with mid-IR emission. The dark shaded area is the extrapolation of local starburst galaxies from Ranalli, Comastri, & Setti (2003).

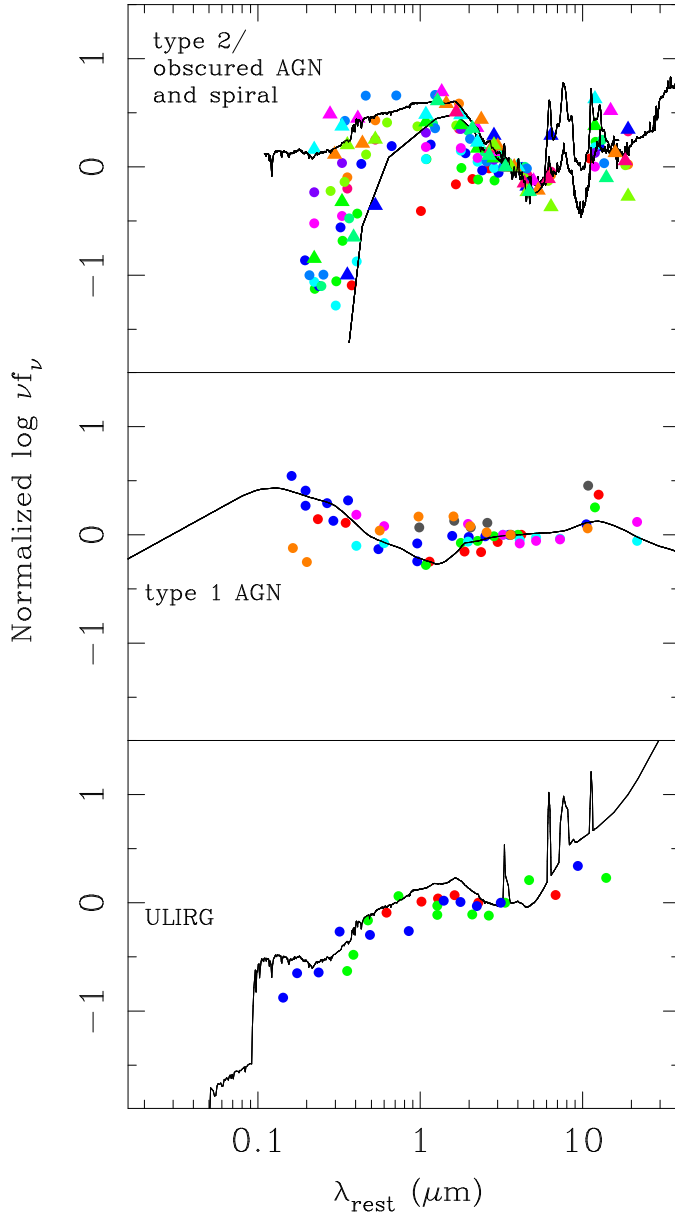


Figure 4.2 SED (normalized at $\lambda_{\text{rest}} \simeq 3.5 \mu\text{m}$) types for EGS X-ray/ $24 \mu\text{m}$ sources (filled circles or triangles of different colors, for clarity; Table 1) with photometric redshifts estimated by us or redshifts from the literature. The ULIRGs SED class is shown with the Mkn 273 template from Devriendt et al. (1999); the type 1 AGN SED class is shown with the median QSO of Elvis et al. (1994). Obscured AGN/type 2 AGN/spiral SED galaxies are intermediate between the Circinus template (lower one) and the M82-like template (upper one) of Le Floc'h et al. (2004).

on the observed ratio of hard X-ray to mid-IR fluxes is small for AGN with low X-ray column densities, but it will make this ratio increase for Compton thick AGN at higher z (Alexander et al. 2001). For starbursts at $z < 1$, Alexander et al. (2001) predict just a slight decrease of the ratio of hard X-ray to mid-IR emission for increasing z . The majority of sources in this study appear to derive their X-ray emission from powerful AGN because they lie in the region of Fig. 1 populated by local hard X-ray-selected AGN extrapolated to fainter fluxes (Fadda et al. 2002; Franceschini et al. 2001; Alexander et al. 2001), and because for our sample the z -dependent effects (see next section) in this figure are small.

Also shown in Fig. 1 are sources in the Chandra Deep Field South (CDF-S) from Rigby et al. (2004). The greater sensitivity of the CDF-S X-ray data (compared with the EGS and LH) results in detection of relatively weaker X-ray sources that either have a greater portion of their luminosity generated from star formation, or are obscured in the X-rays (compare to figure 1 in Alexander et al. 2002). Indeed, spectroscopic observations of faint sources detected in the deepest X-ray surveys to date indicate that these are starbursts and low-redshift normal galaxies (Barger et al. 2003).

All X-ray sources in the LH not detected at $24\mu\text{m}$ appear to be consistent with being type 1 AGN or S0/elliptical galaxies (see next section). Alexander et al. (2002) found that most X-ray emitting galaxies in the HDF-N with no mid-IR emission are classified spectroscopically as S0/elliptical galaxies; that is, they showed no emission-line evidence for activity.

X-ray hardness ratios can be used to distinguish between low-obscuration (soft) and high-obscuration (hard) AGN (e.g., Hasinger et al. 2001; Mainieri et al. 2002; Szokoly et al. 2004). This X-ray classification agrees with the spectroscopic classification of type 1 (broad lines) and type 2 (narrow lines) AGN, respectively.

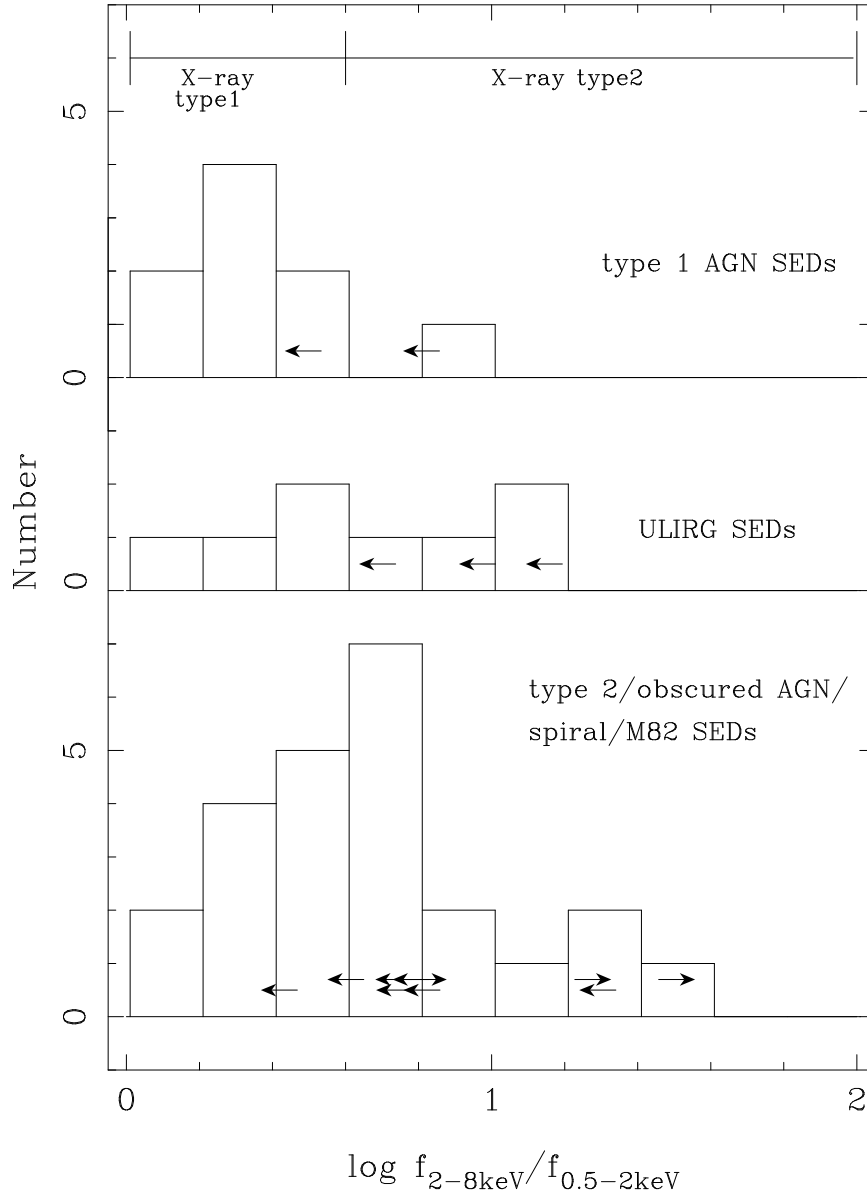


Figure 4.3 Hard to soft flux ratio distributions for the SED types (Fig. 2) of bright X-ray/ $24\,\mu\text{m}$ sources in the LH and EGS. The approximate division between type 1 and type 2 AGN is also shown (Rigby et al. 2004 based on Szokoly et al. 2004). The arrows inside the histogram bins indicate sources with upper or lower limits to the hard to soft flux ratios.

Based on their hard to soft flux ratios, there are approximately equal numbers of type 1 and type 2 AGN among the hard X-ray selected sources in the LH and EGS with and without mid-IR emission. This finding is in contrast with the local sample of hard X-ray selected AGN of Piccinotti et al. (1982) where most of the sources are classified as type 1 AGN (70 – 80% for AGN at $z < 0.12$).

4.7 Spectral Energy Distributions

We have collected optical and near-IR data for all the X-ray/ $24\mu\text{m}$ sources in the EGS and LH (Cristóbal-Hornillos et al. 2003; Wilson 2003). The observations have been band merged with the *Spitzer* data as described by Le Floc'h et al. (2004). We used spectroscopic and photometric redshifts for 5 X-ray sources in the LH (Lehmann et al. 2001; Mainieri et al. 2002) and 9 sources in the EGS (from the Deep Extragalactic Evolutionary Probe and Miyaji et al. 2004). For the remaining sources, we estimated photometric redshifts where possible from the stellar spectral peak at $\lambda_{\text{rest}} = 1.6\mu\text{m}$ (see Le Floc'h et al. 2004).

We then classified the X-ray/ $24\mu\text{m}$ sources according to the shape of their SEDs. Sources that are relatively flat in νf_ν from the optical through the mid-IR, resembling the median QSO SED of Elvis et al. (1994), are termed type 1 AGN (Fig. 2). Sources that are relatively flat in νf_ν at the IRAC and MIPS wavelengths, but whose spectra drop toward the blue are consistent with being obscured AGN. Although the redshifts cannot be estimated well for these two types of objects, the SEDs are distinctive and the classification unambiguous. Galaxies with decreasing νf_ν in the range $\lambda_{\text{obs}} = 3.6 - 8\mu\text{m}$ and a significant stellar contribution in the optical and near-IR resemble type 2 AGN or spiral/starburst galaxies, and their SEDs appear intermediate between that of Circinus and that of M82 (Fig. 2). The majority of these sources have spectroscopic/photometric redshifts in the range

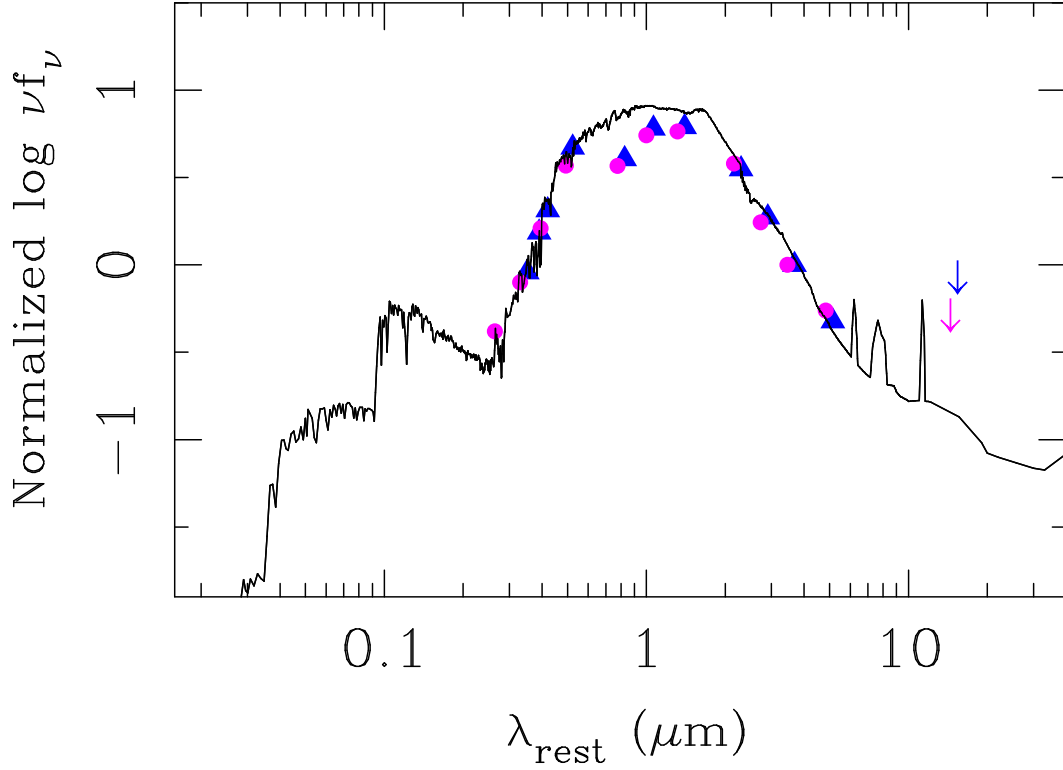


Figure 4.4 SEDs (normalized as in Fig. 2) of two LH sources — XMMJ105154.3+572753.2 (circles) and XMMJ105203.8+572339.3 (triangles) — not detected at $24\mu\text{m}$. Their SEDs are shown with an S0/Sa galaxy template from Devriendt et al. (1999).

$z = 0.2 - 1.6$. A few galaxies have increasing νf_ν for $\lambda_{\text{obs}} \geq 3.6\mu\text{m}$, and look similar to local ULIRGs (Fig. 2). Table 1 lists the X-ray properties and SED types for those EGS sources with well determined SEDs (Fig. 2).

For the 45 X-ray/ $24\mu\text{m}$ sources in our sample with SED type, we find that 10 can be classified as pure type 1 AGN SED, 27 as obscured AGN, type 2 AGN, or spiral/M82-like SED, and 8 as ULIRG-like SED. In the absence of quality X-ray data, the optical-to-mid-IR SED does not unambiguously identify AGN activity. This will complicate efforts to identify complete samples of AGN via optical and *Spitzer* photometry.

Fig. 3 shows the hard to soft X-ray flux ratio distributions for the three dif-

ferent types of SEDs. All galaxies with type 1 AGN-like SEDs show a range of hard to soft flux ratios consistent with those of spectroscopically classified type 1 AGN (that is, broad-line AGN). Galaxies with obscured AGN, type 2 AGN, and spiral/M82-like SEDs include a fraction of sources that would be classified as type 1 AGN based on their X-ray properties. ULIRG-SED objects appear to have a tendency toward softer X-ray flux ratios characteristic of type 1 AGN.

More than half of the bright X-ray/ $24\,\mu\text{m}$ sources in our sample have SEDs dominated by stellar emission or show a significant level of obscuration. This is consistent with the finding that 40 – 60% of the Chandra selected galaxies have optical spectra with no signs of nuclear AGN activity (e.g., Barger et al. 2001; Hornschemeier et al. 2001). Many of these galaxies have colors of old stellar populations (Barger et al. 2003). It is possible that their AGN emission lines are overwhelmed by stellar light (see Moran, Filippenko, & Chornock 2002). Others appear highly absorbed in X-rays (Barger et al. 2001, see also Fig. 3); if a similar level of absorption applies to their emission lines, these lines will be undetectable. In agreement with the finding that spectroscopic type 1 (broad lines) AGN behavior is relatively rare (e.g., Hornschemeier et al. 2001), the fraction of type 1 AGN SED dominated X-ray sources in our sample is small.

About one-third of the sources with emission in hard X-rays are not detected at $24\,\mu\text{m}$. Fig. 4 shows two such X-ray sources in the LH whose SEDs are consistent with being S0 or elliptical galaxies, with no evidence for the presence of hot dust. Based on findings by Alexander et al. (2002) for the HDF-N, a significant fraction of X-ray sources detected by IRAC but not by MIPS at $24\,\mu\text{m}$ are likely to have SEDs like elliptical and S0 galaxies.

To put these trends on a more quantitative basis, we have used local hard-X-ray selected AGN from Piccinotti et al. (1982) and Kuraszkiewicz et al. (2003) to

construct a comparison sample consisting of all galaxies with $z \leq 0.12$ and a mid-IR $25\ \mu\text{m}$ flux density $> 100\ \text{mJy}$. In this local sample, 19 of 32 galaxies, more than half the sample, would be classified by us as type 1 AGN based on their SEDs. From the hard X-ray/ $24\ \mu\text{m}$ detections in the EGS and LH, we classify 7 of 29 as having SEDs resembling those of type 1 AGN. Since only 2/3 of sources with hard X-ray emission were detected at $24\ \mu\text{m}$, some caution is needed in interpreting this result. However, since a significant fraction of the X-ray sources without $24\ \mu\text{m}$ detections are likely to have S0/elliptical type SEDs, it is possible that there is a trend away from pure type 1 AGN behavior with increasing redshift. This possibility will be probed by further *Spitzer* observations of deep X-ray fields that are currently under analysis.

Table 4.1. Positions, fluxes, and SEDs types for X-ray–selected AGN.

RA	DEC	d	$f(0.5-8\text{keV})$	err	d	$f(0.5-2\text{keV})$	err	d	$f(2-8\text{keV})$	err	SED
214.18961	52.48514	1	0.24E-13	0.2E-14	1	0.42E-14	0.5E-15	0	0.23E-13	–	ULIRG
214.33336	52.41668	1	0.57E-14	0.1E-14	1	0.71E-15	0.2E-15	1	0.47E-14	0.1E-14	ULIRG
214.48695	52.52348	1	0.80E-14	0.1E-14	1	0.13E-14	0.3E-15	1	0.52E-14	0.1E-14	ULIRG
214.35562	52.59547	1	0.53E-14	0.1E-14	1	0.10E-14	0.3E-15	0	0.77E-14	–	t1 AGN
214.22297	52.35219	1	0.19E-13	0.3E-14	0	0.56E-14	–	0	0.225E-13	–	t1 AGN

Note. — [Abridged. The complete table is published in the electronic edition of the *Astrophysical Journal*.]
NOTES — In this table we list those EGS galaxies with well determined SED types and with an estimate of the redshift, that is, galaxies plotted in Fig. 2. Column (1): Chandra RA (J2000). Column (2): Chandra DEC (J2000). Column (3): detection in the full (0.5 – 8keV) band (1=detection, 0= 3σ upper limit). Column (4): flux in the full (0.5 – 8keV) band in $\text{erg cm}^{-2} \text{s}^{-1}$. Column (5): error of flux in the full (0.5 – 8keV) band in $\text{erg cm}^{-2} \text{s}^{-1}$. Column (6): detection in the soft (0.5 – 2keV) band (1=detection, 0= 3σ upper limit). Column (7): flux in the soft (0.5 – 2keV) band in $\text{erg cm}^{-2} \text{s}^{-1}$. Column (8): error of flux in the soft (0.5 – 2keV) band in $\text{erg cm}^{-2} \text{s}^{-1}$. Column (9): detection in the hard (2 – 8keV) band (1=detection, 0= 3σ upper limit). Column (10): flux in the hard (2 – 8keV) band in $\text{erg cm}^{-2} \text{s}^{-1}$. Column (11): error of flux in the hard (2 – 8keV) band in $\text{erg cm}^{-2} \text{s}^{-1}$. Column (12): SED type (see Fig. 2, and text). “obsc AGN” = Obscured AGN; “sp” = spiral.

CHAPTER 5

WHY OPTICALLY-FAINT AGN ARE OPTICALLY-FAINT: THE *Spitzer*
PERSPECTIVE

Optically-faint X-ray sources (those with $f_X/f_R > 10$) constitute about 20% of X-ray sources in deep surveys, and are potentially highly obscured and/or at high redshift. Their faint optical fluxes are generally beyond the reach of spectroscopy. For a sample of 20 optically-faint sources in CDFS, we compile 0.4–24 μm photometry, relying heavily on *Spitzer*. We estimate photometric redshifts for 17 of these 20 sources. We find that these AGN are optically-faint both because they lie at significantly higher redshifts (median $z \sim 1.6$) than most X-ray-selected AGN, and because their spectra are much redder than standard AGN. They have 2–8 keV X-ray luminosities in the Seyfert range, unlike the QSO-luminosities of optically-faint AGN found in shallow, wide-field surveys. Their contribution to the X-ray Seyfert luminosity function is comparable to that of $z > 1$ optically-bright AGN.

5.1 Introduction

Deep X-ray surveys have resolved the X-ray background into discrete sources, verifying that it is the combined output of obscured and unobscured active galactic nuclei (AGN) (e.g., Moretti et al. 2003). The challenge now is to establish the redshift, luminosity, and column density distributions of these AGN, and the properties of their host galaxies, to understand AGN evolution and accretion history. About 35% of the X-ray detections in 1 Ms observations are beyond the reach of spectroscopy. They are expected to be more heavily obscured and/or at higher redshift than the brighter population. A subset of these X-ray sources are

much dimmer in the optical, relative to their X-ray fluxes, than ordinary AGN, and have thus been termed the “optically-faint AGN.” They are interesting in two ways.

First, they are likely to be highly obscured: they lack the bright blue continua so prominent in unobscured AGN, and their X-ray photon indices indicate more obscuration than in Type 1 AGN. Obscured AGN are expected to dominate the faint number counts and the power in the background above a few keV.

Second, these optically-faint AGN may lie at high redshift. Pre-*Chandra* X-ray background models predicted an AGN redshift distribution that peaked at $z = 1.3\text{--}1.5$ (Gilli et al., 1999, 2001). By contrast, the redshift distribution of *Chandra*-selected AGN with spectroscopic follow-up is much lower, peaking near $z \sim 0.7$ (Gilli, 2004). Models using a post-*Chandra* luminosity function (LF) can accommodate a lower-redshift distribution (Ueda et al., 2003), but an alternative possibility is that the distribution does peak at higher redshift, but significant numbers of high-redshift AGN have been systematically excluded from the spectroscopic surveys.

The general properties of optically-faint AGN and similar objects have been studied by Alexander et al. (2001), Yan et al. (2003), and Koekemoer et al. (2004), but without redshift estimation. Zheng et al. (2004) used optical and near-infrared photometry to obtain photometric redshifts for 99% of the X-ray-selected AGN in the CDFS, including most of the optically-faint objects. However, such redshifts are extremely difficult to obtain for optically-faint sources, and of unproven reliability. We combine optical, near-infrared, and most importantly, mid-infrared (from *Spitzer*) photometry to obtain independent redshifts. *Spitzer* is ideally suited to find redshifts for these sources: the IRAC bands (at 3.6, 4.5, 5.8, and 8.0 μm) are well-placed to sample the stellar emission of even very high redshift galaxies.

Additionally, the rest-frame near infrared (which *Spitzer* probes for $z \geq 1$) typically offers the highest contrast to detect the normal stellar population against the AGN light. Thus, the IRAC bands have the best chance of revealing stellar features that can yield redshift determinations.

5.2 The X-ray-to-Optical Flux Ratio and Sample Selection

The optical R-band to hard X-ray (usually 2–10 keV or 2–8 keV) flux ratio, (f_X/f_R), can be used to classify the emission mechanisms of X-ray sources (e.g. Maccacaro et al. 1988; Comastri et al. 2002; Barger et al. 2003). A value < 0.01 indicates the X-ray emission is powered by star formation, while $0.1 < f_X/f_R < 10$ indicates that the X-rays arise in an AGN. Optically-faint X-ray sources are defined to have $f_X/f_R > 10$, making them poor emitters at optical wavelengths given their X-ray fluxes. The f_X/f_R ratio is defined in the observed frame, and as such is subject to K-corrections.

In this paper, we use the f_X/f_R ratio to select optically-faint AGN. The region sampled is the overlap between the Chandra Deep Field South 1 Ms Chandra observation (Giacconi et al., 2002; Alexander et al., 2003) and the GOODS ACS optical mosaic (Giavalisco et al., 2004). We start by choosing objects from the Giacconi et al. (2002) X-ray catalog that have 2–10 keV band detections and $f_X/f_R > 10$. When Giacconi et al. (2002) list multiple R-band candidate counterparts for an X-ray source, we require they all be optically-faint. If no R-band counterpart is detected, we require a flux upper limit stringent enough to insure $f_X/f_R > 10$. These criteria select 48 sources.

We then switch to the Alexander et al. (2003) CDFS X-ray catalog, since it has smaller R-to-X-ray positional offsets than does Giacconi et al. (2002) catalog (see the appendix of Alexander et al. 2003.) We do this by cross-correlating

the two X-ray catalogs, requiring hard-band detection in both catalogs within $1.6''$. This drops 9 sources from the sample: 3 of the sources have no counterpart in the Alexander et al. (2003) catalog, even out to $5''$; and 6 are 2–8 keV non-detections (but are detected in another band) in the Alexander et al. (2003) catalog, and thus are dropped from our sample. The 9 dropped sources are fainter than the optically-faint sample, with 2–8 keV fluxes $\lesssim 10^{-15} \text{ erg s}^{-1} \text{ cm}^{-2}$, as compared to the median 2–8 keV flux for the 39 optically-faint sources of $3.6 \times 10^{-15} \text{ erg s}^{-1} \text{ cm}^{-2}$.

All but 6 of the 39 optically-faint sources have 2–8 keV and 0.5–2 keV fluxes that agree within 20% between both X-ray catalogs.¹ Sources are identified by ID numbers from Alexander et al. (2003) (abbreviated AID).

To obtain a sample with high-quality SEDs, we then a) choose those sources that lie within the GOODS ACS field, which reduces the sample to 25; and b) require each source to have at least two photometric detections at wavelengths below $1 \mu\text{m}$, which further reduces the sample to 20 AGN. We term the resulting sample of 20 AGN the “complete-SED sample (CSS)”.

There are two potential sources of biases to this sample. First, it may be somewhat brighter than the remaining optically-faint AGN, due to the requirement for multiple-band optical detections. Second, requiring $\lambda < 1 \mu\text{m}$ detections might possibly bias the CSS toward low redshifts compared to the full sample of optically-faint AGN; we explore this possibility in § 5.5, by examining the redshifts of sources that would be excluded by the $\lambda < 1 \mu\text{m}$ detection requirement.

¹The rest have fluxes in agreement within a factor of two.

5.3 *Spitzer* Observations, Photometry, and SEDs

With *Spitzer* (Werner et al., 2004), we obtained IRAC (Fazio et al., 2004) measurements of the CDFS with 500 s of integration. The images were reduced by the *Spitzer* Science Center using the standard pipeline. We also obtained MIPS (Rieke et al., 2004) 24 μm scan map images with a total integration time of ~ 1200 s per position, nominally composed of 120 individual sightings per source. These data were reduced using the instrument team data analysis tool (Gordon et al., 2005), creating the image presented by Rigby et al. (2004).

We created a database to combine the MIPS and IRAC images with the following optical and near-infrared imagery: the ACS/HST *bviz* images from GOODS (Giavalisco et al., 2004); *RIz* frames from the Las Campanas Infrared Survey (Marzke et al., 1999); and the *BVRI* images released by the ESO Imaging Survey (Arnouts et al., 2002); the *JK* images from GOODS (Giavalisco et al., 2004); and the *JK* images from the EIS Deep Infrared Survey². We also added the *Chandra* images from the website³ of the HDF-N team (Alexander et al., 2003).

For each source, any object detected in the K band within 2'' of the X-ray position was selected for photometry in all available bands. The source selections were reviewed visually, and when necessary, were modified so that the same source was photometered in each band. The result is closely-sampled, deep photometry from 0.4 to 8 μm , with additional coverage at 24 μm .

We now discuss the few sources that have multiple K-band components within 2'', where extra care was needed to obtain accurate photometry:

AID 100: There are four K-band sources (or components) within 3'' of the X-ray position, with offsets of 0.1, 1.3, 2.9, and 2.9''. These same components are

²http://www.eso.org/science/eis/surveys/strategy_EIS-deep_infrared_deep.html

³<http://www.astro.psu.edu/users/niel/hdf/hdf-chandra.html>

also present in the ACS z-band image. We quote photometry for the closest (0.1'' offset) source.

AID 218: The K-band counterpart is clearly the source located only 0.3'' from the X-ray coordinates. However, a second source (located 2.1'' from the X-ray source, and 1.5'' from the K-band counterpart) contaminates the measured IRAC fluxes in channels 2–4. Therefore, we plot these fluxes as upper limits in figure 5.2.

AID 241: There are two K-band components, one located 0.4'' away, and a fainter source 1.6'' from the X-ray position. We photometer the closer source.

AID 245: There are two K-band components, located 0.4'' and 1.9'' from the X-ray position. The measured IRAC fluxes are contaminated by contribution from the farther component.

AID 281: There is a K and ACS source 0.3'' from the X-ray coordinates; it appears to be extended (or double) out to 0.7'' from the X-ray source. We photometer only the closer component of the extended source.

5.4 Properties of the Complete SED sample

5.4.1 Spectral Properties

Figure 5.1 shows the distribution of X-ray photon index Γ (defined as $f_\nu \propto \nu^{1-\Gamma}$) for the CSS. Unobscured AGN generally have $\Gamma \approx 2$ (and are thus flat in νf_ν), whereas obscured AGN generally have $\Gamma \lesssim 1$ (and thus νf_ν rises with increasing frequency). The optically-faint Γ distribution appears to be intermediate in obscuration, with a significant number of obscured AGN.

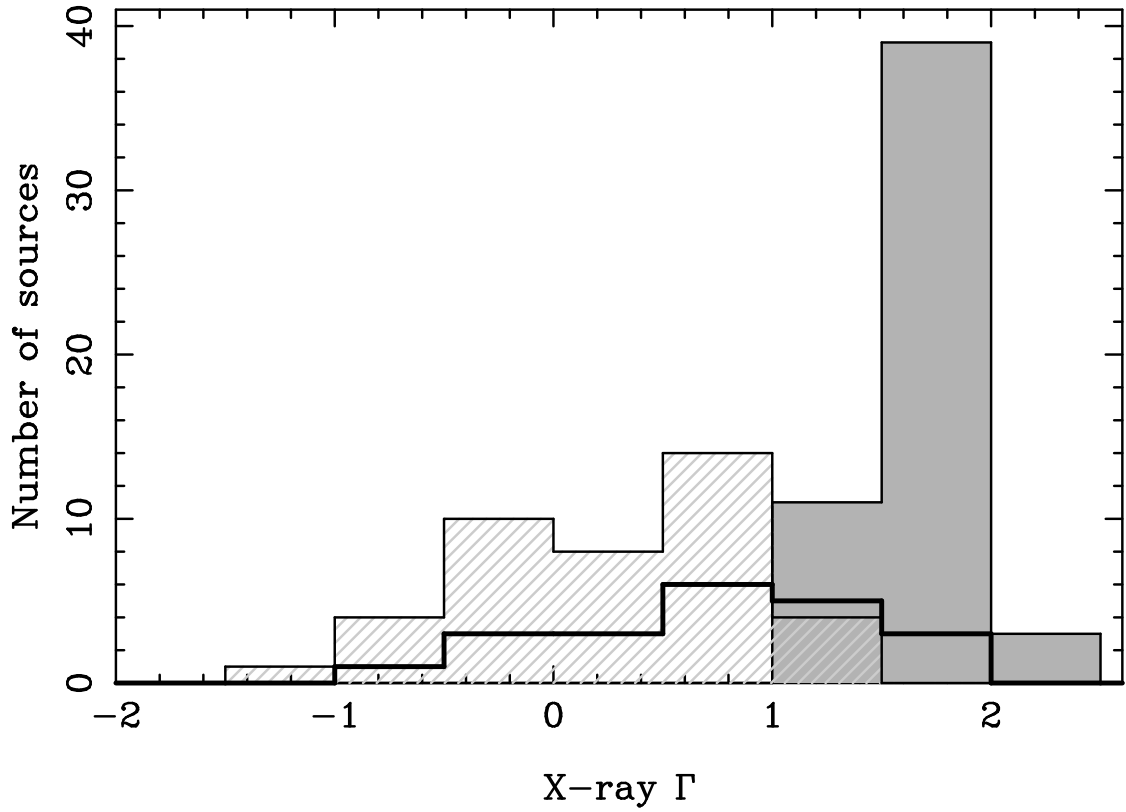


Figure 5.1 Distribution of X-ray photon index Γ (defined as $f_\nu \propto \nu^{1-\Gamma}$). Plotted are the optically-faint CSS AGN (*thick line*); X-ray-selected Type 1 AGN (*shaded region*); and X-ray-selected Type 2 AGN (*cross-hatched region*). Classifications are from Szokoly et al. (2004). Photon index values are from Alexander et al. (2003); we omit sources where Γ is undetermined or is uncertain by more than ± 0.5 .

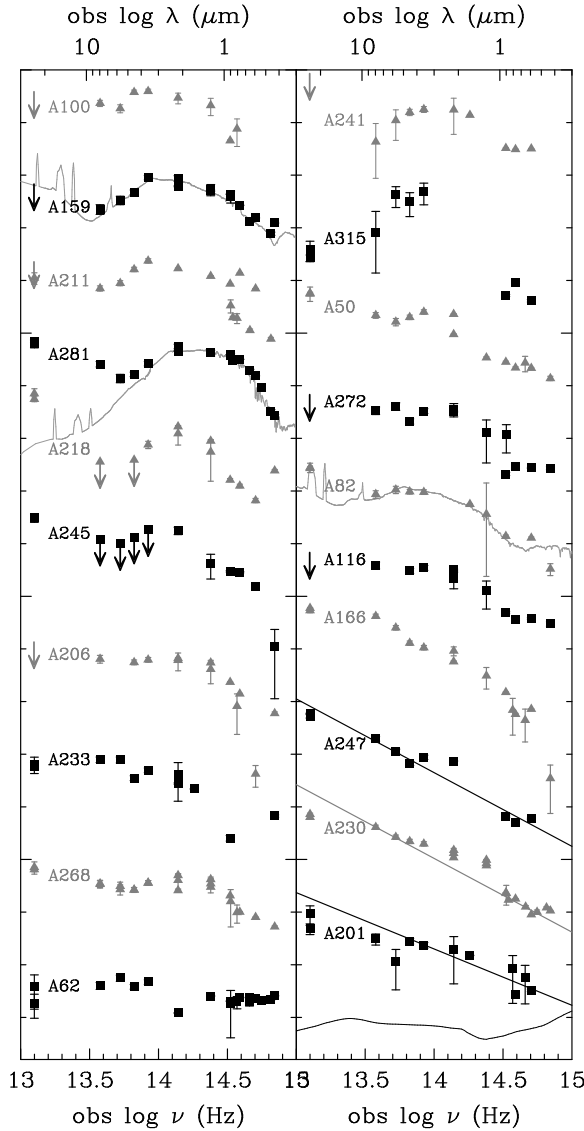


Figure 5.2 The sample of complete SEDs. Sources with strong stellar features are plotted first, progressing to weaker stellar features and finally to sources with power-law SEDs. Wavelengths and frequencies are as observed. For illustration, we overplot three templates from Devriendt et al. (1999): M82 with an additional $E(B-V)=0.2$ of reddening (plotted with source AID 159); early-type galaxy Virgo 1003 (plotted with AID 281); and rapidly star-forming galaxy IRAS 05189-2524 from Devriendt et al. (1999) (plotted with AID 82). We also plot the median Type 1 QSO spectrum of Elvis et al. (1994) (bottom right) in order to illustrate how much redder are the optically-faint AGN.

Table 5.1. Multi-band Photometry and Redshifts for Optically-Faint AGN.

AID/XID	optical	Ks	3.6 μm	4.5 μm	5.7 μm	8.0 μm	24 μm	α	Lit. redshift	Our redshift
50/227	R= 0.24 ± 0.08	4.7 ± 2	12 ± 1	12 ± 1	12.4 ± 2	23.0 ± 3	180 ± 55	-2.3	$2.18 (1.78\text{-}2.54)^1$	2.8–3.5
62/64	R= 0.76 ± 0.07	1.39 ± 0.03	8.9 ± 0.9	9 ± 1	17 ± 2	17 ± 2.4	49 ± 30	-0.88	1.27 ± 0.2^2	...
82/58	z= 0.26 ± 0.01	...	7.2 ± 0.7	9 ± 1	1.3 ± 2	15 ± 2	141 ± 28	-2.0	$0.92 (0.58\text{-}1.22)^1$	1.8–3.8
100/82	i= 0.65 ± 0.3	6.7 ± 3	15 ± 1.4	18 ± 1.7	11 ± 2	20 ± 3.0	< 98		$1.89 (1.69\text{-}2.05)^1$	1.1–1.8
116/205	i= 0.15 ± 0.01	3.1 ± 0.6	6.6 ± 0.7	7.3 ± 0.8	...	16 ± 2	< 86	-2.3	$1.56 (1.31\text{-}2.3)^1$	1.3–1.5
159/48	R= 0.46 ± 0.03	8.5 ± 1.5	17 ± 2	11.6 ± 1	10.1 ± 2	9.6 ± 2	< 86		$1.26 (1.03\text{-}1.49)^1$	0.7–1.1
166/45	R= 0.11 ± 0.07	6.0 ± 1.4	14 ± 1	21.8 ± 2	53.9 ± 5	125 ± 12	480 ± 45	-2.6	$2.29 (2.14\text{-}2.60)^3$	1.0–2.5
201/515	R= 0.13 ± 0.09	1.4 ± 1.1	2.8 ± 0.4	4.2 ± 0.5	2.2 ± 1.5	8.2 ± 2	75 ± 30	-2.1	$2.19 (2.15\text{-}2.45)^1$	1.3–4.8
206/265	i= 0.29 ± 0.01	3.6 ± 0.2	5.9 ± 0.6	6.7 ± 0.7	...	14 ± 2	< 86		$1.16 (1.02\text{-}1.32)^1$	1.0–1.4
211/35	R= 0.39 ± 0.02	19 ± 0.4	44 ± 4	39 ± 4	27 ± 3	30 ± 3	140 ± 35		1.14 ± 0.14^2	0.9–1.4
218/148	i= 0.064 ± 0.005	2.1 ± 0.3	1.8 ± 0.3	< 1.2	...	< 1.9	112 ± 27		$1.74 (1.50\text{-}2.02)^1$...
230/31	R= 0.55 ± 0.03	18.8 ± 3	47 ± 4	$66. \pm 6$	100 ± 9	217 ± 20	1008 ± 62		$1.603^4; 1.1 \pm 0.1^2$	1.5–2.0
233/79	z= 0.097 ± 0.01	3.1 ± 0.6	7.4 ± 0.7	6.7 ± 0.7	19 ± 2	26 ± 3	65 ± 22	-1.8	$1.91 (1.77\text{-}1.97)^1$	1.0–2.5
241/201	i= 0.098 ± 0.007	1.6 ± 1	2.7 ± 0.3	3.0 ± 0.4	2.6 ± 1.5	1.4 ± 1.4	< 86	-0.90	$0.679^4; 0.14, 1.0^2$	1.5–2.2
245/27	i= 0.47 ± 0.02	8.0 ± 1.3	< 14	< 12.6	< 12	< 20	155 ± 28	-2.0	3.064^4	1.0–1.4

Table 5.1—Continued

AID/XID	optical	Ks	3.6 μm	4.5 μm	5.7 μm	8.0 μm	24 μm	α	Lit. redshift	Our redshift
247/25	i= 0.21 ± 0.01	8.4 ± 0.1	16.5 ± 2	16 ± 1.5	34 ± 4	82 ± 8	660 ± 50	-2.4	2.26 (1.89-2.58) ¹	1.7–4.7
268/147	i= 0.41 ± 0.01	4.4 ± 1	6.8 ± 0.7	6.3 ± 0.7	8.1 ± 2	15 ± 2	90 ± 23	-2.0	0.99 (0.79-1.21) ¹	0.8–1.1
272/146	i= 0.12 ± 0.01	3.9 ± 0.2	6.2 ± 0.6	5.0 ± 0.6	12 ± 2	14 ± 2	< 86	-2.5	2.67 (2.47-2.85) ¹	2.4–3.4
281/159	R= 1.7 ± 0.08	14.6 ± 1.5	12 ± 1	9.9 ± 1	11 ± 2	27 ± 3	200 ± 36		3.30 (3.04-3.62) ¹	0.2–0.6
315/506	i= 1.0 ± 0.1	...	260 ± 115	210 ± 100	360 ± 150	100 ± 100	140 ± 60	-2.9	3.69 (3.12-4.19) ¹	...

Note. — Column 1: AID/XID are the source identification numbers in the Alexander et al. (2003) and Giacomoni et al. (2002) catalogs, respectively. Column 2 is optical flux density: we quote R-band when available, then i, then z. Columns 2–8: optical, Ks, IRAC, and MIPS flux densities are all listed in μJy . Column 9: the 0.4–8 μm spectral index α is defined in the text. Column 10: “Lit. Redshift” is the source redshift found in the literature. Column 11: “Our Redshift” is the redshift found using our techniques, as described in the text. REFERENCES— [1] Photometric redshift using BPZ and HyperZ, from Zheng et al. (2004); [2] Photometric redshift from Combo-17 (Wolf et al., 2004); [3] Redshift from single-line spectrum (Szokoly et al., 2004) and HyperZ, from Zheng et al. (2004); [4] Spectroscopic redshift from Szokoly et al. (2004).

Table 5.2. X-ray Photometry for the Optically-Faint AGN Sample.

AID/XID	offset	0.5–2 keV flux	2–8 keV flux	X-ray Γ
50/227	0.4	1.2 ± 0.4	36.2 ± 5.2	$-0.43^{+0.31}_{-0.32}$
62/64	0.2	21.7 ± 1.2	55.2 ± 4.7	1.36 ± 0.09
82/58	0.2	7.1 ± 0.7	19.6 ± 3.1	$1.30^{+0.18}_{-0.16}$
100/82	0.4	2.4 ± 0.4	15.1 ± 2.8	$0.71^{+0.24}_{-0.22}$
116/205	0.3	1.5 ± 0.5	14.4 ± 4.1	$0.41^{+0.41}_{-0.37}$
159/48	0.9	9.1 ± 0.9	48.6 ± 5.4	0.83 ± 0.13
166/45	0.4	10.9 ± 0.9	49.4 ± 4.9	$0.94^{+0.12}_{-0.11}$
201/515	0.3	0.9 ± 0.3	15.1 ± 3.0	$0.02^{+0.33}_{-0.31}$
206/265	0.5	2.2 ± 0.5	40.8 ± 5.8	-0.08 ± 0.25
211/35	0.9	40.8 ± 6.4	142.0 ± 35	$1.13^{+0.28}_{-0.24}$
218/148	0.5	3.9 ± 0.5	28.5 ± 3.8	$0.61^{+0.18}_{-0.17}$
230/31	0.3	59.7 ± 1.9	87.8 ± 5.2	1.75 ± 0.06
233/79	0.2	8.8 ± 0.9	15.5 ± 2.8	$1.62^{+0.19}_{-0.18}$
241/201	0.3	4.6 ± 0.6	21.4 ± 3.4	$0.93^{+0.19}_{-0.18}$
245/27	0.3	7.5 ± 0.7	70.6 ± 5.6	0.42 ± 0.11
247/25	1.0	5.4 ± 0.7	93.4 ± 7.9	-0.02 ± 0.14
268/147	0.1	1.9 ± 0.4	72.6 ± 7.0	-0.61 ± 0.22
272/146	1.1	4.6 ± 0.6	25.5 ± 4.0	$0.81^{+0.19}_{-0.18}$
281/159	0.7	24.0 ± 1.3	75.3 ± 5.7	1.21 ± 0.08

Table 5.2—Continued

AID/XID	offset	0.5–2 keV flux	2–8 keV flux	X-ray Γ
315/506	0.7	6.9 ± 0.9	9.3 ± 3.7	$1.81^{+0.45}_{-0.33}$

Note. — Column 1: AID/XID are the source identification numbers in the Alexander et al. (2003) and Giacconi et al. (2002) catalogs, respectively. Column 2: “Offset” is the offset (in ") between the Alexander et al. (2003) and Giacconi et al. (2002) X-ray coordinates. Column 3–4: X-ray fluxes are quoted from Alexander et al. (2003), and have units of 10^{-16} erg s $^{-1}$ cm $^{-2}$. Column 5: The X-ray photon index Γ is defined in the text.

The 0.4–24 μ m spectral energy distributions of the CSS are plotted in figure 5.2. Optical through 24 μ m photometry is reported in table 5.1; X-ray photometry is reported in table 5.2. All but 3–4 of the SEDs show strong stellar features—either breaks or the characteristic broad stellar hump peaking near 1.6 μ m rest-frame. The remaining sources show a red, power-law continuum, with a spectral break between 8 and 24 μ m.

5.4.2 Redshift Techniques and Previously–Estimated Redshifts

There are three published spectroscopic redshifts for CSS sources, measured by Szokoly et al. (2004) and listed in our table 5.1. Of these, AID 230 and 245 have redshifts of $z = 1.603$ and $z = 3.064$, respectively. Also, for AID 241 there is a published redshift of $z = 0.679$ for an optical counterpart 1.6" from the Alexander et al. (2003) position (which is source number 201b in Szokoly et al. 2004). However, we feel that this is not the most likely counterpart to the X-ray source,

since there is a closer, fainter source: Szokoly source 201a, located just 0.6 " from the Alexander et al. (2003) position. This closer source lacks a spectroscopic redshift.

Since only a few spectroscopic redshifts are available for the sample, one must turn to photometric techniques. Two groups, Zheng et al. (2004) and COMBO-17 (Wolf et al., 2004), have estimated photometric redshifts for some of the CSS sources. The former group used 10 photometric bands from 0.3 to 2.1 μm ; the latter group used 17 passbands from 0.35 to 0.93 μm . The redshift estimates from these two groups, as applicable to the CSS, are compiled in table 5.1.

Adding IRAC fluxes to photometric redshift methods should dramatically improve the results, since IRAC samples the peak and red side of the stellar emission out to high redshift. Several groups are currently searching for the best way to do exactly that—the question is not trivial, partly because of the lack of good templates over this wide redshift range. One solution, adopted by Pérez-González et al. (2005), is to use empirical templates compiled from sources in deep fields that have spectroscopic redshifts in order to fit photometric redshifts to other faint sources. Their photo-z technique is described in detail in the appendix to that paper.

Unfortunately, for galaxies that host AGN, template-fitting of any sort (whether the high-resolution templates of standard photo-z techniques, or the low-resolution templates used by (Pérez-González et al., 2005)) can be difficult and potentially unreliable. First of all, each source has a differing contribution of host galaxy and AGN light. Secondly, some of the high-redshift, red AGN have SED shapes that are quite different from the templates, which are based on lower-redshift, bluer samples.

Clearly, caution is warranted when resorting to photometric redshifts, since

the techniques are unproven when applied to sources as extreme as the optically-faint AGN. Different techniques of redshift determination should be tested against each other for consistency, and the widest possible range of templates should be used.

5.4.3 New Photometric Redshift Estimations

To estimate redshifts from our 0.4–8 μm data, we adopt a different, more conservative approach than simply adopting the results of a best-template fitting program. Our goal is not to find the best or most likely redshift, but rather to constrain the redshift range of each source with high confidence.

In our technique, we manually compared the photometry of each source to a range of SED templates from Devriendt et al. (1999), namely the early-type galaxy Virgo 1003, spiral galaxies including Virgo 1987, the starburst galaxy M82, and the ultraluminous infrared galaxy IRAS 05189-2524. We chose these templates to sample a wide range of star formation rate.

In a few cases, we needed to add extra reddening (a few tenths of a magnitude in $E(B-V)$) to the Devriendt et al. (1999) templates to match the optical fluxes, since these sources are much redder than the Devriendt et al. (1999) galaxies. (For example, see AID 281 in figure 5.2). We also add varying amounts of dust to make sure our redshift results are not highly dependent on the chosen extinction.⁴

For each source, we compare these templates to the photometry, and find the redshift range for which *any* template provides a good match to the photometry. For example, a source might be fit by the M82 template at $1 < z < 1.3$, as well as by the M82 template with added extinction at $0.8 < z < 1.1$. In this case, we would quote the range $0.8 < z < 1.3$.

⁴We do not bother to add this absorbed UV and optical energy back to the templates as re-emitted infrared light, since it would only contaminate the longest, non-stellar wavelengths which are not important in stellar feature fitting.

Our resulting redshift ranges are tabulated in table 5.1.

Our redshift ranges agree reasonably well with the other techniques. In 10 out of 13 cases, our redshifts agree with those of Zheng et al. (2004). Zheng et al. (2004) estimates redshifts for two power-law objects for which we cannot quote a redshift, and we quote redshifts for four sources that lack redshifts in Zheng et al. (2004).

COMBO-17 lists three redshifts for CSS sources; we can estimate redshifts for two, and agree in one case. Three CSS sources have spectroscopic redshifts; our photo-zs agree in two cases (AID 166 and 230), and strongly disagree in one case (AID 245, with $z_{spec} = 3.064$, for which we securely find $z=1.1-1.4$).

Thus, 12 CSS sources (57%) have redshifts confirmed by two different techniques (COMBO-17 and our method, or Zheng et al. (2004) and our method). Also, five additional CSS sources have single-source redshift estimates at high confidence (four from our technique, and one from Szokoly et al. (2004).) Thus, 17/20 CSS sources (85%) have useful redshift information.

We can also test the agreement between our redshift estimates and those found using the empirical template technique of Pérez-González et al. (2005). For 11 of the 17 sources with useful redshift information, the Pérez-González et al. (2005) photo-z falls within the quoted redshift range. This is fairly good agreement, considering that the empirical template technique has not been optimized to deal with AGN SEDs.

One notable problem with the photometric redshifts is the case of AID 245. It's spectroscopic redshift of $z=3.065$ (Szokoly et al., 2004), based on two narrow emission lines, appears to be solid. However, we have estimated its redshift as 1.0–1.3. The photometry is well-measured, so why is the photometric method in such disagreement with the spectroscopic redshift?

We inferred a redshift of $z \sim 1$ for AID 245 based on the apparent stellar hump from $\lambda_{obs} = 1.6\text{--}6\ \mu\text{m}$, with peak at $\sim 3\ \mu\text{m}$. Such a spectral shape is not consistent with any stellar template at $z \sim 3$ (which should peak in emission at $\lambda_{obs} \sim 6.5\ \mu\text{m}$). Clearly, the problem is not with the template-fitting, but with the photometry.

Close examination of the images indicates that the IRAC photometry of AID 245 is contaminated by a neighboring source. Thus, the photometry is probably a composite of two sources, which together simulate a stellar hump at $z \sim 1$. This could explain why the hump appears narrower (and rises more quickly from J to K-band) than stellar templates.

Thus, it appears that the redshift discrepancy for AID 245 results from a perverse case of source blending, in that the composite SED looks stellar (but at a fictitious redshift) rather than obviously composite. In section § 5.3, we looked for evidence of other blending problems, and found that cases like AID 245 are rare in the CSS sample.

5.4.4 The Redshift Distribution of the Optically-Faint CSS AGN

We now consider the redshifts of the 17/20 CSS sources with useful redshift information. When a spectroscopic redshift has been published, we use it; otherwise, we use the redshift ranges found using our technique in §5.4.3.

Almost all (14/17) of the CSS AGN lie at $z > 1$, and at least 25% lie at $z > 2$. By contrast, of the 99 reliable⁵ spectroscopic redshifts available for X-ray-selected AGN in CDFS (Szokoly et al., 2004), only 42% lie at $z > 1$; only 17% lie at $z > 2$. Thus, the optically-faint X-ray sources lie at higher redshift than other X-ray-selected AGN, although their redshifts are typical of the optical QSO population.

Since the redshift distribution of optically-bright AGN in CDFS is strongly

⁵“Reliable” in this context means a quality flag $Q \geq 2$.

influenced by large-scale structure (two redshift spikes at $z = 0.674$ and 0.734), we now compare with several other fields. Gilli (2004) has compiled the redshift distribution of X-ray-selected sources with $f_{2-10\text{keV}} > 5 \times 10^{-15} \text{ erg s}^{-1} \text{ cm}^{-2}$ in CDFS, CDFN, Lockman Hole, Lynx field, and SSA13. After excluding large scale structures from CDFN and CDFS, 49% of the sources lie at $z > 1$, and 14% lie at $z > 2$. This distribution, too, lacks high-redshift objects compared with our results for the optically-faint AGN.

5.4.5 The Luminosity Function of Optically-Faint AGN

We now compute the rest-frame 2–8 keV luminosity function of optically-faint AGN. We use the standard V_{max} method (Schmidt, 1968; Huchra & Sargent, 1973), and do not correct for incompleteness.⁶ We assume $\Omega_m = 0.27$, $\Omega_\Lambda = 0.73$, $H_o = 72$. Because the X-ray sensitivity varies strongly over the field, we calculate V_{max} for each source by summing the volume contribution from each *Chandra* pixel in the GOODS ACS field. The 5σ limiting flux in each pixel was calculated by the method of Muno et al. (2003), using the CDFS exposure map (Alexander et al., 2003) and an analytic approximation of the *Chandra* point spread function⁷.

Figure 5.3 plots the resulting LF, based on the redshift constraints given in table 5.1 (using the spectroscopic redshift if available, and otherwise our redshift range found in §5.4.3.) Within the GOODS ACS field, there are 27 optically-faint sources with high-confidence hard-band detections (detected by both Alexander et al. 2003 and Giacconi et al. 2002); of these, we found redshift information for 17. Therefore, we have multiplied the optically-faint AGN LF found for the 17 sources by 27/17 (which assumes the redshift distributions are similar.)

For comparison, we plot the spectroscopically-determined rest-frame 2–8 keV

⁶since we do not know the intrinsic V/V_{max} distribution.

⁷<http://cxc.harvard.edu/chandra-users/0195.html>

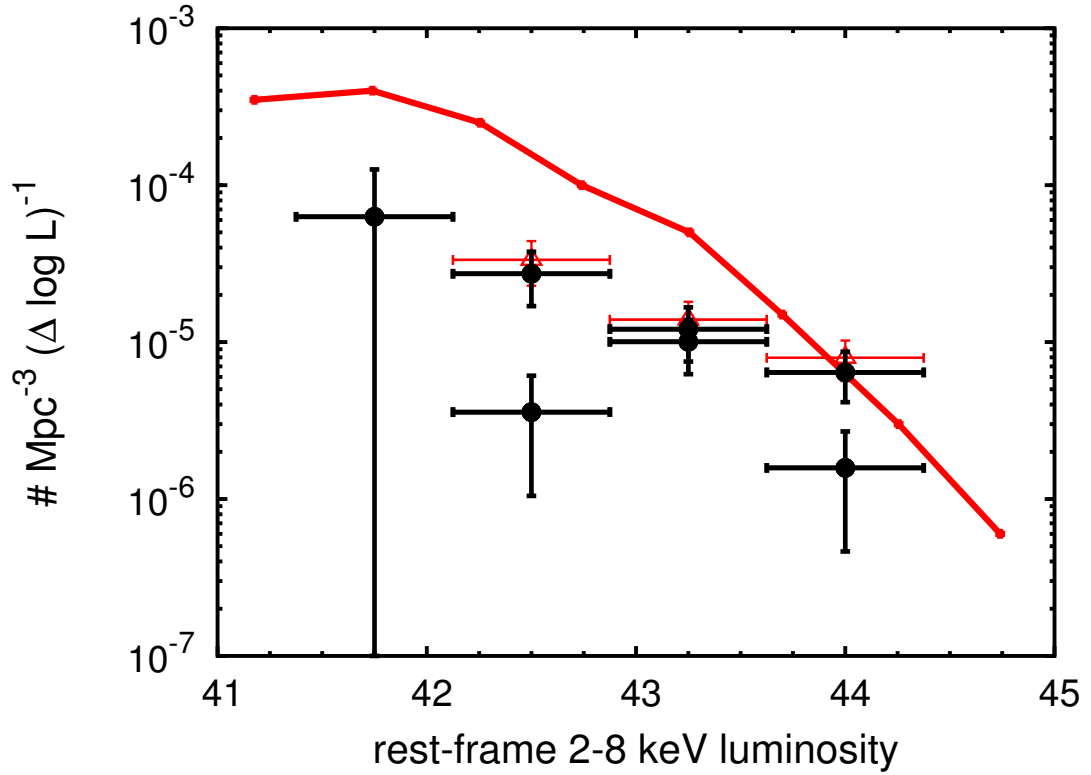


Figure 5.3 The rest-frame 2–8 keV AGN luminosity function. Filled circles show the optically-faint AGN LF, computed using the 17 CSS AGN with constrained redshifts. We compute this LF twice, once using the lowest permitted redshift for each source, and again using the highest redshift. The LF has been corrected for known AGN lacking redshifts (see § 5.4.5); we do not otherwise correct for incompleteness. For comparison, we plot the $0.1 < z < 1$ LF (*red solid line*) for AGN with spectroscopic redshifts (Steffen et al., 2003). We also compute the LF for those $1 < z < 4$ AGN in the GOODS field with Szokoly et al. (2004) redshifts (*red triangles*). All luminosities are in erg s^{-1} .

LF for X-ray–selected AGN from $0.1 < z < 1.0$ (Steffen et al., 2003). Two general conclusions are apparent. First, the optically–faint AGN are not terribly luminous—most have $\log L_x \sim 42.5\text{--}44 \text{ erg s}^{-1}$. Thus, we sample lower luminosities than the optically–faint QSOs discovered in shallow, wide-field surveys, (Fiore et al., 2003; Mignoli et al., 2004; Brusa et al., 2005) as expected given the survey sensitivities. Second, the number density of the optically–faint AGN in CDFS is comparable to that of $1 < z < 4$ AGN that have been identified by optical spectroscopy. Therefore, optically–faint AGN boost the high–redshift tail of the X-ray–selected AGN redshift distribution, but only by a factor of ~ 2 .

Thus, we find that the optically–faint sources have moderate redshifts ($1 < z < 3$) and Seyfert luminosities ($\log L_{2\text{--}8\text{keV}} < 44 \text{ erg s}^{-1}$), rather than higher redshifts and QSO luminosities. As such, they are not expected to contribute strongly to the X-ray background, as compared to $z < 1$ Seyferts and $z > 2$ QSOs (see for example figures 16 and 17 of Ueda et al. (2003)). Several techniques are presently being tested to identify additional high–obscuration AGN (for example, see Alonso-Hererro et al. (2006) and Donley et al. (2005). When results from such studies are available, it will be valuable to determine the overlap between selection methods, calculate the discovered sources’ contribution to the X-ray background (as well as the contribution from the optically–faint AGN), and re-evaluate what fraction of the obscured AGN have been identified.

5.5 Other Optically–Faint Sources

Some sources, especially at high redshift, may be too faint to be identified by our f_X/f_R flux criterion. Further, absorption from the Lyman α forest will suppress the R-band flux for $z \gtrsim 4$.

Therefore, we examine the most extreme optically faint cases: X-ray detec-

tions that are undetected even in extremely deep $z' > 28$ imaging with HST. Koekemoer et al. (2004) have identified seven such sources in the CDFS/GOODS field, and suggested they may lie at $z > 6$ or be very dusty. To test the nature of these AGN, we have combined the *Spitzer* bands with the GOODS photometry (Koekemoer et al. (2004)). We find several source categories: 1.) Source K4 is an X-ray detection, but an otherwise blank field—lacking an optical, near-infrared, or *Spitzer* counterpart; 2.) Sources K1 and K6 have power-law SEDs; and 3.) Sources K2, K3, and K7 have stellar-featured SEDs, with nominal photometric redshifts of $z \sim 3$, $z \sim 2$, and $2 < z < 6$ respectively. Source K5 is intermediate between these last two categories.

A number of optically-faint sources outside the CSS have steep power-law SEDs: AID 4, 42, 45, 64, 79, 92, and 283. They may be related to the optically-faint, power-law members of the flat spectrum 1 Jy (at 5 GHz) sample (Stickel et al. (1996)). The faint 1 Jy power-law sources have spectral indices $\alpha \geq -2.5$ (with α defined as $f_\nu \propto \nu^\alpha$). The spectral indices of our objects are listed in table 5.1; they are generally in agreement with the limit derived by Stickel et al. (1996) for the radio sample. The steep power law sources comprise only about 2% of the flat spectrum 1 Jy sample; their incidence in the CDFS appears to be as high or higher.

5.6 Conclusions

We report reliable (e.g. confirmed by independent methods) photometric redshifts for a representative sample of optically-faint X-ray sources in the CDFS. We find that they have higher redshifts ($z > 1$) than most X-ray-selected AGN, but only $\sim 30\%$ lie at $z > 2$. Thus, they populate the redshifts where optical QSOs are most numerous. Their 0.4–24 μm SEDs are intrinsically redder than typical

AGN, and notably lack bright blue continua. Their X-ray spectra indicate significant absorption. Their X-ray luminosities are modest ($\log L_x \sim 42.5\text{--}44 \text{ erg s}^{-1}$), and they boost the high-redshift tail of the X-ray-selected AGN distribution by a factor of 2.

CHAPTER 6

WHY X-RAY-SELECTED AGN APPEAR OPTICALLY DULL

We investigate why half of X-ray-selected active galactic nuclei (AGN) in deep surveys lack signs of accretion in their optical spectra. The majority of these “optically-dull” AGN are no more than ~ 6 times fainter than their host galaxies in rest-frame R-band; as such, AGN lines are unlikely to be overwhelmed by stellar continuum in at least half the sample. We find that optically-dull AGN have the mid-infrared emission and L_x/L_{IR} ratios characteristic of local Seyferts, suggesting that the cause of optical dullness is not missing UV-optical continua. We compare the morphologies of 22 optically-dull and 9 optically-active AGN at $0.5 < z < 0.8$, and find that optically-dull AGN show a wide range of axis ratio, but optically-active AGN have only very round axis ratios. We conclude that hard X-rays select AGN in host galaxies with a wide range of inclination angle, but only those AGN in the most face-on or spheroidal host galaxies show optical emission lines. Thus, extranuclear dust in the host galaxy plays an important role in hiding the emission lines of optically-dull AGN.

6.1 Introduction

Deep X-ray surveys have found large numbers of active galactic nuclei (AGN) at $z \sim 1$, as predicted by models of the X-ray background (e.g. Setti & Woltjer 1989; Comastri et al. 1995). Most of these AGN have hard X-ray flux ratios that indicate obscured accretion, which is consistent with the hardness of the X-ray background. In the local universe, AGN that are similarly X-ray obscured have optical high-excitation emission lines that classify them as Seyfert 2 galaxies. Surprisingly, in deep surveys, 40–60% of X-ray-selected AGN show **no evidence** of

nuclear accretion in optical spectra (see discussion and references in Moran et al. 2002.) Such sources are variously termed “optically–dull”, “optically–normal”, or “X-ray–Bright Optically–Normal (XBONG)”. By this, one means that these galaxies *lack evidence for accretion activity* in optical spectroscopy. They are therefore quite unlike a “normal” AGN, i.e. a QSO or Seyfert galaxy.¹

Thus, what is so interesting about these AGN is precisely that they are “dull”: How can nuclei produce high X-ray luminosities (most have $41 < \log L_x < 44 \text{ erg s}^{-1}$ in rest-frame 2–8 keV) that clearly require power from nuclear accretion, yet not show optical evidence of accretion? The puzzle deepens when we consider that optically–dull AGN are rare in the local universe. As we discuss in §6.5.1, at most 10–20% of local hard X-ray–selected AGN are optically dull. Has the AGN population evolved?

In this paper, we test three explanations for optical dullness: a) these AGN have weak ionizing continua, which do not excite the narrow line regions (e.g. Barger et al. 2001b.) b) these are faint AGN in bright galaxies that overwhelm the AGN lines; c) the host galaxies of these AGN have obscured their AGN lines. Explanations b) and c) are effects seen in low–redshift samples, as we summarize in § 6.2. Explanation a) would require the AGN population to evolve strongly, from optical–dullness at $z \sim 1$ to optical activity at $z \sim 0$. Before appealing to AGN evolution, we should consider whether explanations b) and c), which are motivated by the behavior of local Seyferts, can fully explain optical dullness.

¹Terminology for deep X-ray sources can be confusing. “Optically dull” or “optically normal” AGN are X-ray–selected AGN that lack AGN emission lines, but otherwise have typical host galaxies. They are an entirely different population than the optically–bright X-ray–faint sources in deep surveys (in which the X-rays come from X-ray binaries, not AGN) which are sometimes called “normal galaxies.”

6.2 Insight from low-redshift Seyfert samples

Samples of nearby Seyferts suggest two likely causes for optical dullness in AGN. The first possible explanation is that optically-dull AGN have been observed in ways that dilute or hide their optical activity. This explanation was advanced by Moran et al. (2002), who observed 18 local Seyfert 2s with large apertures (to simulate observations at high redshift), and demonstrated that in 11 cases, the nuclear activity was drowned out by stellar light. (Nine of those sources showed early-type spectra, and two showed starburst spectra). This “dilution” hypothesis predicts that optically-dull AGN should inhabit high-luminosity host galaxies, which generate enough continuum to drown out the AGN lines.

Another possible explanation is that the narrow-line regions of optically-dull AGN have been obscured by their host galaxies. This hypothesis is motivated by selection effects observed in local Seyfert samples. Keel (1980) first demonstrated a deficiency of nearby Seyfert 1s in edge-on host galaxies. McLeod & Rieke (1995) later showed that much larger samples of nearby optically-selected Seyfert 1 and 2 AGN are biased against having inclined spiral hosts. They found samples of soft X-ray-selected QSOs to be similarly biased. By contrast, they found that nearby samples of Seyferts selected by hard X-rays or $12\ \mu\text{m}$ emission showed relatively flat distributions of axis ratio from 0.2 to 1, which is the expectation for randomly-oriented disk galaxies. Based on the known spatial scales of narrow-line regions, and on the differing biases of soft and hard-X-ray selected samples, they concluded that many Seyfert galaxies have several magnitudes of A_V at scale-heights of $\geq 100\ \text{pc}$ —which puts the extinction outside the classical nuclear “torus”. They proposed that molecular rings of star-forming disturbed gas could account for the obscuring column. (Alonso-Herrero et al. 2003 also invoked $A_V \lesssim 5$ of galactic extinction outside the torus, to explain the nuclear

SEDs of optically-classified Seyfert 1.8 and 1.9 AGN.) Thus, the circumnuclear region is not the only absorbing column that matters to a nearby AGN; gas in the host galaxy matters too. This low redshift work suggests that at $z \sim 1$, where Chandra observes rest-frame hard X-rays, the deep surveys should select AGN independent of inclination. Inclined disk galaxies within these surveys should have preferentially weak broad- and narrow-lines. The relatively large fraction of optically-dull AGN at high redshift then arises from the comparatively low ratio of signal to noise in spectra of those faint objects, combined with the poor physical resolution to isolate their nuclei. Are these trends observed?

6.3 Sample selection and data

To investigate optically-dull behavior, we need a uniform sample of such AGN at $z \sim 1$. We start with the Szokoly et al. (2004) catalog of X-ray-selected AGN with spectroscopic redshifts, all in the Chandra Deep Field South (CDFS). These AGN were originally selected from the Chandra 1 Ms observations (Giacconi et al., 2002; Alexander et al., 2003), and were followed up with optical spectroscopy (Szokoly et al., 2004) obtained with the FORS1/FORS2 at the VLT ($R = 5.5 \text{ \AA pix}^{-1}$). In this paper we use both the Szokoly et al. (2004) catalog and electronic versions of their published spectra, available online².

From the spectroscopic catalog, we select AGN with X-ray luminosities that indicate AGN activity (which corresponds to Szokoly X-ray classifications of AGN-1, AGN-2, QSO-1, or QSO-2). We then select the subset of those sources that have non-active optical spectral classifications: either “LEX” (sources with low-excitation narrow emission lines, as expected from star formation) or “ABS” (sources with stellar absorption-line spectra). These criteria select 45 sources, all of which

²<http://www.mpe.mpg.de/CDFS/data/>

have a spectroscopic redshift; 34 of these redshifts are listed as “reliable” (flag $Q=3$). Nine of the 45 sources have “ABS” spectra, and the rest have “LEX” spectra. Table 6.3 lists source positions, redshifts, optical spectral classifications, and X-ray classifications, all from Szokoly et al. (2004). We use source identification numbers from Alexander et al. (2003), abbreviated “AID”.

Table 6.1. Optically–Dull AGN

AID	SID	A-RA	A-DEC	S-RA	S-DEC	off	2-8 keV flux	log f(H)/f(S)	f_{ν} 24 μ m	L_x	corr L_x	est N(H)	X class	Opt	Q	z	SED
12	121	52.96316	−27.84766	52.96316	−27.84766	0.0	1.4(±0.4) E-15	0.47 ^{+0.13} _{−0.19}	< 96	1.8E42	2.6E42	1.9E22	AGN-2	LEX	3	0.674	O
16	76	52.96875	−27.83819	52.96870	−27.83822	0.2	8.6(±0.7) E-15	0.73 ^{+0.05} _{−0.05}	87 ± 30	9.3E43	3.9E44	3.2E23	QSO-2	LEX	1	2.394	F
28	73	52.99208	−27.80944	52.99175	−27.80963	1.3	4.8(±0.5) E-15	0.43 ^{+0.05} _{−0.05}	82 ± 9	7.9E42	1.1E43	2.0E22	AGN-1	LEX	3	0.734	O
44	66	53.01520	−27.76769	53.01529	−27.76772	0.3	1.7(±0.1) E-14	1.44 ^{+0.06} _{−0.07}	126 ± 30	7.5E42	2.2E43	1.1E23	AGN-2	LEX	3	0.574	O
48	267	53.02037	−27.69100	53.02029	−27.69100	0.3	5.7(±1) E-15	> 1.38	91 ± 10	3.8E42	1.3E43	> 1.4E23	AGN-2	LEX	1	0.720	F
60	155	53.03295	−27.71091	53.03325	−27.71094	0.9	1.2(±0.4) E-15	0.71 ^{+0.15} _{−0.22}	520 ± 20	8.3E41	1.4E42	3.3E22	AGN-2	LEX	3	0.545	R
65	538	53.03541	−27.78016	53.03562	−27.78011	0.7	1.1(±0.3) E-15	> 1.10	990 ± 80	2.1E41	3.4E41	> 4.6E22	AGN-2	LEX	3	0.310	O
80	535	53.04758	−27.78050	53.04758	−27.78055	0.2	1.3(±0.3) E-15	0.76 ^{+0.12} _{−0.16}	< 80	9.8E41	1.7E42	3.7E22	AGN-2	LEX	3	0.575	O
83	534	53.05062	−27.75825	53.05087	−27.75838	0.9	< 4.8 E-16	< 0.87	< 80	< 6.9E41	< 9.3E41	< 6.2E22	AGN-2	LEX	3	0.676	O
84	149	53.05104	−27.77247	53.05125	−27.77272	1.1	1.3(±0.3) E-15	0.94 ^{+0.14} _{−0.20}	239 ± 40	2.5E42	7.3E42	1.2E23	AGN-2	LEX	1	1.033	Y
87	156	53.05504	−27.92469	53.05512	−27.92463	0.3	7.0(±0.9) E-15	> 1.77	116 ± 10	5.6E42	5.5E43	> 4.2E23	AGN-2	ABS	3	1.185	I
90	600	53.05762	−27.75711	53.05783	−27.75736	1.1	8.1(±3) E-16	> 1.21	< 80	1.6E42	8.4E42	> 2.7E23	AGN-2	LEX	3	1.327	I
91	266	53.05779	−27.71338	53.05775	−27.71361	0.8	1.2(±0.4) E-15	> 1.22	289 ± 40	9.9E41	3.0E42	> 1.2E23	AGN-2	LEX	3	0.735	Y
126	50	53.07912	−27.79872	53.07916	−27.79872	0.1	2.3(±0.4) E-15	0.86 ^{+0.09} _{−0.11}	< 80	2.2E42	4.4E42	5.4E22	AGN-2	ABS	1	0.670	F
129	525	53.08254	−27.68975	53.08250	−27.68966	0.3	< 9.4 E-16	< 0.62	3018 ± 90	< 1.1E41	< 1.4E41	< 1.6E22	AGN-2	LEX	3	0.229	O
131	253	53.08362	−27.74638	53.08366	−27.74644	0.2	4.2(±0.5) E-15	1.55 ^{+0.12} _{−0.16}	333 ± 30	1.3E42	3.6E42	1.2E23	AGN-2	LEX	1	0.481	F?
134	151	53.08529	−27.79233	53.08533	−27.79230	0.2	7.6(±0.7) E-15	2.06 ^{+0.15} _{−0.22}	65 ± 20	2.2E42	1.1E43	2.2E23	AGN-2	LEX	3	0.604	O
139	602	53.09141	−27.78219	53.09158	−27.78216	0.5	3.3(±1) E-16	> 0.82	222 ± 70	4.7E41	6.3E41	> 5.0E22	AGN-2	ABS	3	0.668	O
146	188	53.09400	−27.83050	53.09400	−27.83050	0.0	6.3(±2) E-16	0.86 ^{+0.16} _{−0.25}	69 ± 10	7.0E41	1.5E42	6.4E22	AGN-2	LEX	3	0.734	F
155	49	53.10095	−27.69066	53.10104	−27.69069	0.3	3.1(±0.4) E-15	0.23 ^{+0.06} _{−0.07}	68 ± 9	2.9E42	3.4E42	5.8E21	AGN-1	LEX	3	0.534	O
157	598	53.10283	−27.90325	53.10283	−27.90322	0.1	< 5.5 E-16	...	< 80	< 6.4E41	< 8.5E41	...	AGN-2	ABS	3	0.617	I
161	47	53.10416	−27.68383	53.10404	−27.68377	0.5	5.5(±0.8) E-15	1.25 ^{+0.11} _{−0.15}	155 ± 10	4.2E42	1.3E43	1.3E23	AGN-2	LEX	3	0.733	Y
162	260	53.10466	−27.84538	53.10462	−27.84536	0.2	1.3(±0.3) E-15	1.24 ^{+0.16} _{−0.24}	30 ± 10	1.8E42	7.7E42	1.9E23	AGN-2	LEX	3	1.043	F
164	150	53.10487	−27.91377	53.10483	−27.91391	0.5	3.9(±0.6) E-15	> 1.67	108 ± 30	3.3E42	2.5E43	> 3.4E23	AGN-2	ABS	3	1.090	O
166	45	53.10700	−27.71827	53.10700	−27.71825	0.1	4.9(±0.5) E-15	0.66 ^{+0.05} _{−0.06}	480 ± 50	5.7E43	2.0E44	2.4E23	QSO-2	LEX	1	2.291	R
171	519	53.10770	−27.91875	53.10779	−27.91844	1.1	< 7.8 E-16	< 0.64	63 ± 10	< 2.1E42	< 4.3E42	< 5.8E22	AGN-2	LEX	3	1.034	F
176	43	53.11150	−27.69600	53.11150	−27.69600	0.0	3.7(±0.5) E-15	0.78 ^{+0.07} _{−0.08}	385 ± 40	4.4E42	8.7E42	5.4E22	AGN-2	LEX	3	0.734	I
196	516	53.13058	−27.79027	53.13083	−27.79019	0.9	< 3.7 E-16	< 0.71	116 ± 8	< 5.1E41	< 6.8E41	< 3.9E22	AGN-1	LEX	3	0.665	F
212	512	53.14329	−27.73061	53.14312	−27.73063	0.5	6.8(±2) E-16	0.59 ^{+0.15} _{−0.23}	< 80	7.9E41	1.3E42	2.8E22	AGN-2	LEX	3	0.668	O
216	171	53.14629	−27.73627	53.14662	−27.73655	1.5	< 4.3 E-16	< 0.54	202 ± 40	< 1.0E42	< 1.4E42	< 3.3E22	AGN-2	LEX	1	0.839	F
220	190	53.14933	−27.68333	53.14941	−27.68322	0.5	5.4(±0.8) E-15	> 1.62	< 80	3.0E42	1.3E43	> 1.9E23	AGN-2	LEX	3	0.735	O

We also list, in table 6.3, several derived quantities for each source: 1) rest-frame 2–8 keV luminosity (using the photon index inferred from the observed 0.5–2 keV / 2–8 keV flux ratio, and normalizing by the observed 2–8 keV flux); 2) the absorption-corrected rest-frame 2–8 keV X-ray luminosity, which we find by extrapolating the observed 2–8 keV flux assuming an intrinsic photon index $\Gamma = 2$, where $f_\nu \propto \nu^{1-\Gamma}$; and 3) the estimated column density N_H , which would make an intrinsic $\Gamma = 2$ power-law spectrum at the source’s redshift show the observed 0.5–2 keV / 2–8 keV flux ratio. When the source was not detected in the hard (2–8 keV) band, we quote upper limits on N_H , L_x , and absorption-corrected L_x . When the source was not detected in the soft (0.5–2 keV) band, we quote an upper limit on N_H . The median N_H errorbars, from the uncertainty in the X-ray flux ratio, are -29% and $+39\%$.

From the same catalog, we also create a comparison sample of “optically-active AGN”: X-ray-selected AGN that have either broad emission lines (“BLAGN”) or high-excitation narrow emission lines (“HEX”) according to Szokoly et al. (2004). Observed and derived quantities are listed in table 6.3.

Table 6.1—Continued

AID	SID	A-RA	A-DEC	S-RA	S-DEC	off	2-8 keV flux	$\log f(\text{H})/\dot{f}(\text{S})$	f_{ν} , 24 μm	L_x	corr L_x	est N(H)	X class	Opt	Q	z	SED
221	100	53.14991	-27.81397	53.14991	-27.81400	0.1	3.1(± 1.3) E-16	0.17 $^{+0.16}_{-0.27}$	43 \pm 9	2.6E42	3.1E42	9.9E21	AGN-1	LEX	1	1.309	F
227	33	53.15295	-27.73508	53.15329	-27.73533	1.4	8.6(± 0.6) E-15	0.33 $^{+0.03}_{-0.03}$	94 \pm 20	1.2E43	1.6E43	1.1E22	AGN-1	LEX	3	0.665	I
247	25	53.17016	-27.92961	53.17020	-27.92972	0.4	9.3(± 0.8) E-15	1.24 $^{+0.06}_{-0.07}$	661 \pm 50	5.6E42	1.5E43	9.5E22	AGN-2	ABS	0.5	0.625	R
259	132	53.18358	-27.91502	53.18337	-27.91502	0.7	8.4(± 3) E-16	0.55 $^{+0.15}_{-0.24}$	< 80	1.9E42	3.4E42	3.5E22	AGN-2	LEX	1	0.908	F?
264	85	53.18587	-27.80991	53.18583	-27.80997	0.2	1.3(± 0.3) E-15	0.45 $^{+0.09}_{-0.11}$	< 80	2.9E43	7.1E43	1.5E23	QSO-1	LEX	1	2.593	F
269	170	53.19329	-27.90383	53.19337	-27.90388	0.3	1.4(± 0.4) E-15	0.79 $^{+0.13}_{-0.18}$	218 \pm 30	1.3E42	2.6E42	4.7E22	AGN-2	ABS	3	0.664	O
271	252	53.19575	-27.72950	53.19595	-27.72966	0.9	2.9(± 0.5) E-15	1.39 $^{+0.15}_{-0.22}$	< 80	3.8E42	2.2E43	2.9E23	AGN-2	LEX	3	1.178	Y
274	18	53.19941	-27.70911	53.19958	-27.70911	0.5	3.0(± 0.1) E-14	0.57 $^{+0.02}_{-0.02}$	1114 \pm 10	7.7E43	1.4E44	4.5E22	QSO-1	LEX	3	0.979	F?
276	184	53.20075	-27.88236	53.20075	-27.88244	0.3	2.0(± 0.4) E-15	1.11 $^{+0.14}_{-0.21}$	156 \pm 30	1.5E42	3.7E42	8.6E22	AGN-2	ABS	3	0.667	O
285	242	53.21595	-27.70802	53.21600	-27.70822	0.7	< 1.5 E-15	< 0.62	437 \pm 30	< 5.3E42	< 8.1E42	< 5.5E22	AGN-1	LEX	3	1.027	Y
298	110	53.24429	-27.77569	53.24420	-27.77555	0.6	< 8.3 E-16	< 0.43	< 80	< 9.4E41	< 1.3E42	< 1.5E22	AGN-1	LEX	3	0.622	F
303	12	53.24858	-27.84172	53.24870	-27.84177	0.5	4.3(± 0.5) E-15	0.21 $^{+0.05}_{-0.05}$	< 80	7.4E41	7.9E41	3.0E21	AGN-1	ABS	3	0.251	O
304	10	53.24904	-27.77394	53.24904	-27.77400	0.2	9.2(± 0.7) E-15	0.97 $^{+0.05}_{-0.06}$	108 \pm 30	3.3E42	5.8E42	4.4E22	AGN-2	LEX	3	0.424	O
324	176	53.28829	-27.74688	53.28854	-27.74722	1.4	2.7(± 0.8) E-15	0.44 $^{+0.12}_{-0.17}$	125 \pm 30	5.2E42	7.7E42	2.1E22	AGN-1	LEX	3	0.786	Y

Columns: (1) X-ray source identification from Alexander et al. (2003). (2) Source ID from Szokoly et al. (2004), which is identical to the Giacconi et al. (2002) XID. (3)–(4) RA and DEC (J2000) of the X-ray source, from Alexander et al. (2003) (5)–(6) RA and DEC (J2000) of the optical counterpart, from Szokoly et al. (2004). (7) Offset between X-ray and optical coordinates, in arcseconds. (8)–2-8 keV X-ray flux in $\text{erg s}^{-1} \text{cm}^{-2}$, from Alexander et al. (2003). (9) \log of the 2-8 keV / 0.5–2 keV flux ratio. (10) observed MIPS f_{ν} (24 μm) in μJy . (11) rest-frame 2-8 keV X-ray luminosity, using the photon index inferred from the 2-8 keV / 0.5–2 keV flux ratio, and the 2-8 keV flux for normalization. (12) absorption-corrected rest-frame 2-8 keV X-ray luminosity, extrapolated from the observed 2-8 keV flux, assuming an intrinsic photon index $\Gamma = 2$ and concordance cosmology ($\Omega_m = 0.27$, $\Omega_{\Lambda} = 0.73$, $h = 0.72$). (13) Estimated column density: the column density which would produce the observed 2-8 keV / 0.5–2 keV flux ratio, given an intrinsic $\Gamma = 2$ power-law spectrum. (14)–(17) X-ray source classification, optical source classification, redshift quality flag, and redshift, all from Szokoly et al. (2004). (18) SED classification, this paper: O=old stellar population; Y=young stellar population; I=intermediate stellar population; F=flat in νf_{ν} ; R=rising in νf_{ν} .

Table 6.2. Optically-Active AGN

AID	SID	A-RA	A-DEC	S-RA	S-DEC	off	2-8 keV flux	log f(H)/f(S)	f_{ν} 24 μ m	L_x	corr L_x	est N(H)	X class	Opt	Q	z
5	238	52.94991	-27.84597	52.94987	-27.84597	0.1	3.4(\pm 0.5)E-15	0.14 $^{+0.07}_{-0.08}$	< 80	1.8E43	2.1E43	6.5E21	AGN-1	BLAGN	3	1.065
14	112 _a	52.96658	-27.89075	52.96641	-27.89094	0.9	<1.3E-15	< 0.67	340 \pm 10	< 2.3E43	< 9.9E43	< 3.8E23	QSO-2	HEX	3	2.940
18	230	52.97312	-27.81197	52.97312	-27.81197	0.0	<8.0E-16	< 0.33	< 80	< 1.6E43	< 2.9E43	< 6.4E22	AGN-1	BLAGN	3	2.185
22	75	52.98079	-27.91325	52.98075	-27.91344	0.7	1.7(\pm 0.2)E-14	1.13 $^{+0.08}_{-0.10}$	73 \pm 13	1.5E43	4.2E43	1.1E23	AGN-2	HEX	3	0.737
34	71	53.00158	-27.72211	53.00145	-27.72211	0.4	7.0(\pm 0.6)E-15	0.29 $^{+0.04}_{-0.05}$	100 \pm 10	2.9E43	3.9E43	1.6E22	AGN-1	BLAGN	3	1.037
39	68	53.00662	-27.72419	53.00658	-27.72416	0.2	5.6(\pm 0.5)E-15	0.31 $^{+0.04}_{-0.05}$	< 80	1.9E44	3.4E44	8.8E22	QSO-1	BLAGN	3	2.726
41	67	53.01025	-27.76675	53.01029	-27.76677	0.2	8.6(\pm 0.6)E-15	0.30 $^{+0.04}_{-0.04}$	200 \pm 50	9.5E43	1.4E44	3.0E22	QSO-1	BLAGN	3	1.616
43	117	53.01262	-27.74738	53.01270	-27.74727	0.5	9.0(\pm 3)E-16	0.12 $^{+0.12}_{-0.16}$	< 80	3.9E43	4.9E43	2.1E22	QSO-1	HEX	3	2.573
63	89	53.03433	-27.69822	53.03450	-27.69822	0.5	<8.1E-16	< 0.23	< 80	< 2.6E43	< 4.0E43	< 4.5E22	AGN-1	BLAGN	3	2.47
66	63	53.03608	-27.79288	53.03616	-27.79288	0.3	6.8(\pm 0.1)E-14	0.18 $^{+0.01}_{-0.01}$	3300 \pm 100	6.8E43	7.6E43	4.3E21	QSO-1	BLAGN	3	0.543
68	62	53.03937	-27.80188	53.03941	-27.80188	0.1	6.0(\pm 0.5)E-15	0.73 $^{+0.05}_{-0.05}$	840 \pm 60	8.2E43	3.9E44	4.1E23	QSO-2	BLAGN	3	2.810
76	60	53.04545	-27.73752	53.04550	-27.73755	0.2	9.8(\pm 0.6)E-15	0.20 $^{+0.03}_{-0.03}$	290 \pm 30	1.2E44	1.6E44	1.8E22	QSO-1	BLAGN	3	1.615
86	57	53.05395	-27.87686	53.05400	-27.87691	0.2	4.7(\pm 0.5)E-15	0.75 $^{+0.06}_{-0.07}$	49 \pm 9	5.4E43	2.5E44	3.8E23	QSO-2	HEX	3	2.562
88	56 _a	53.05516	-27.71136	53.05516	-27.71141	0.2	1.9(\pm 0.1)E-14	0.88 $^{+0.03}_{-0.03}$	700 \pm 20	1.4E43	2.8E43	5.3E22	AGN-2	HEX	3	0.605
94	55	53.05837	-27.85022	53.05841	-27.85025	0.2	9.1(\pm 0.7)E-15	1.10 $^{+0.05}_{-0.06}$	140 \pm 90	2.7E41	3.4E41	3.0E22	AGN-2	HEX	3	0.122
96	531	53.06012	-27.85305	53.06016	-27.85302	0.2	1.2(\pm 0.3)E-15	1.28 $^{+0.17}_{-0.29}$	100 \pm 10	2.6E42	1.9E43	3.8E23	AGN-2	HEX	3	1.544
98	54	53.06070	-27.90600	53.06087	-27.90575	1.0	2.9(\pm 0.4)E-15	0.66 $^{+0.08}_{-0.09}$	< 80	4.0E43	1.5E44	2.9E23	QSO-2	HEX	3	2.561
103	53	53.06245	-27.85755	53.06245	-27.85755	0.0	3.4(\pm 0.4)E-15	0.29 $^{+0.05}_{-0.06}$	75 \pm 25	5.2E42	6.5E42	1.0E22	AGN-1	BLAGN	3	0.675
109	206	53.06754	-27.65844	53.06750	-27.65850	0.2	1.8(\pm 0.1)E-14	0.15 $^{+0.03}_{-0.03}$	1350 \pm 75	1.5E44	1.9E44	8.9E21	QSO-1	BLAGN	3	1.324
117	52	53.07141	-27.71758	53.07145	-27.71761	0.2	6.4(\pm 0.5)E-15	0.15 $^{+0.04}_{-0.04}$	1370 \pm 90	7.3E42	8.1E42	3.2E21	AGN-1	BLAGN	3	0.569
122	87	53.07600	-27.87819	53.07604	-27.87816	0.2	6.3(\pm 2)E-16	0.24 $^{+0.13}_{-0.19}$	< 80	2.6E43	4.2E43	6.4E22	AGN-1	BLAGN	3	2.801
123	153	53.07641	-27.84866	53.07645	-27.84869	0.2	7.4(\pm 0.7)E-15	1.65 $^{+0.09}_{-0.12}$	130 \pm 14	8.9E42	1.1E44	5.9E23	AGN-2	HEX	3	1.536
163	46	53.10487	-27.70522	53.10483	-27.70525	0.2	3.3(\pm 0.4)E-15	0.08 $^{+0.05}_{-0.06}$	500 \pm 40	5.2E43	5.7E43	5.9E21	QSO-1	BLAGN	3	1.617
177	42 _a	53.11250	-27.68475	53.11250	-27.68475	0.0	6.9(\pm 0.2)E-14	0.14 $^{+0.01}_{-0.01}$	910 \pm 70	1.4E44	1.6E44	4.3E21	QSO-1	BLAGN	3	0.734
179	41	53.11504	-27.69583	53.11508	-27.69583	0.1	1.2(\pm 0.1)E-14	1.38 $^{+0.06}_{-0.07}$	390 \pm 10	6.9E42	2.2E43	1.2E23	AGN-2	HEX	3	0.668
188	202	53.12441	-27.85163	53.12441	-27.85161	0.1	3.2(\pm 0.4)E-15	1.02 $^{+0.08}_{-0.10}$	86 \pm 11	3.2E43	4.1E44	1.0E24	QSO-2	HEX	3	3.700
191	39	53.12491	-27.75827	53.12525	-27.75852	1.4	1.3(\pm 0.1)E-14	0.22 $^{+0.02}_{-0.03}$	440 \pm 60	8.3E43	1.0E44	1.3E22	QSO-1	BLAGN	3	1.218
193	78	53.12525	-27.75652	53.12525	-27.75655	0.1	2.2(\pm 0.3)E-15	0.08 $^{+0.06}_{-0.07}$	120 \pm 10	9.4E42	1.0E43	2.6E21	AGN-1	BLAGN	3	0.960
195	38	53.12591	-27.75125	53.12625	-27.75150	1.4	7.2(\pm 0.5)E-15	0.09 $^{+0.03}_{-0.03}$	175 \pm 30	1.6E43	1.7E43	2.5E21	AGN-1	BLAGN	3	0.738
197	563	53.13112	-27.77305	53.13141	-27.77350	1.9	<3.3E-16	< 0.71	370 \pm 110	< 6.1E42	< 1.2E43	< 2.5E23	AGN-1	HEX	3	2.223
214	34 _a	53.14558	-27.91972	53.14566	-27.91977	0.3	3.6(\pm 0.4)E-15	0.38 $^{+0.06}_{-0.06}$	230 \pm 10	8.4E42	1.2E43	1.9E22	AGN-1	HEX	3	0.839

Having selected a sample, we assembled a multiwavelength photometric database. Using *Spitzer* (Werner et al., 2004), we obtained IRAC (Fazio et al., 2004) images of the CDFS with 500 s of integration. The images were reduced by the *Spitzer* Science Center using the standard pipeline. We also obtained MIPS (Rieke et al., 2004) 24 μm scan map images with a total integration time of ~ 1400 s per position, nominally composed of 120 individual sightings per source. These data were reduced using the instrument team data analysis tool (Gordon et al., 2005), creating the image presented by Rigby et al. (2004).

We add the following optical and near-infrared imagery: ACS/HST *bviz* images from GOODS (Giavalisco et al., 2004); *Riz* frames from the Las Campanas Infrared Survey (Marzke et al., 1999); *BVRI* images released by the ESO Imaging Survey (Arnouts et al., 2002); *JK* images from GOODS (Giavalisco et al., 2004); and *JK* images from the EIS Deep Infrared Survey³.

Unlike optically-faint AGN (Rigby et al., 2005), optically-dull AGN have relatively bright, unambiguous optical and near-infrared counterparts. Therefore, creating SEDs is straightforward. The result is closely-sampled, deep photometry from 0.4 to 8 μm , with additional coverage at 24 μm . We classify the 0.4–8 μm SEDs into 5 categories, based on the Devriendt et al. (1999) templates: old stellar population; young stellar population; intermediate-age stellar population; flat in νf_ν ; or rising in νf_ν with increasing wavelength. We deliberately ignore 24 μm flux density when classifying, as it can be elevated by star formation or accretion. Table 6.3 lists the SED classifications.

Using these data, we now examine the three most likely explanations for optical dullness: a) weak ionizing continua; b) dilution by the host galaxy continuum; and c) obscuration.

³http://www.eso.org/science/eis/surveys/strategy.EIS-deep_infrared_deep.html

Table 6.2—Continued

AID	SID	A-RA	A-DEC	S-RA	S-DEC	off	2-8 keV flux	$\log f(\text{H})/f(\text{S})$	f_{ν} 24 μm	L_x	corr L_x	est N(H)	X class	Opt	Q	z
219	901	53.14883	−27.82111	53.14883	−27.82111	0.0	7.0(±2)E-16	$1.11^{+0.34}_{-0.19}$	610 ± 10	3.8E42	3.8E43	8.3E23	AGN-1	HEX	3	2.578
229	32	53.15600	−27.66680	53.15612	−27.66675	0.5	2.4(±0.8)E-15	$0.12^{+0.17}_{-0.12}$	140 ± 30	4.2E42	4.5E42	3.1E21	AGN-1	BLAGN	3	0.664
230	31	53.15737	−27.87011	53.15741	−27.87011	0.1	8.9(±0.5)E-15	$0.17^{+0.03}_{-0.03}$	1150 ± 60	1.1E44	1.5E44	1.4E22	QSO-1	HEX	3	1.603
234	30 _a	53.15875	−27.66261	53.15887	−27.66250	0.6	1.6(±0.2)E-14	$-0.01^{+0.06}_{-0.08}$	560 ± 50	5.3E43	5.1E43	5.8E22	QSO-1	BLAGN	3	0.837
241	201 _b	53.16275	−27.74419	53.16225	−27.74427	1.6	2.1(±0.3)E-15	$0.66^{+0.10}_{-0.08}$	< 80	2.4E42	4.2E42	3.8E22	AGN-2	HEX	3	0.679
242	28	53.16283	−27.76713	53.16287	−27.76722	0.3	3.1(±0.4)E-15	$0.58^{+0.08}_{-0.07}$	250 ± 30	1.2E43	2.5E43	5.8E22	AGN-1	BLAGN	3	1.216
245	27	53.16533	−27.81408	53.16529	−27.81402	0.2	7.1(±0.6)E-15	$0.97^{+0.05}_{-0.06}$	150 ± 30	6.4E43	5.8E44	7.6E23	QSO-2	HEX	3	3.064
251	24	53.17445	−27.86736	53.17441	−27.86738	0.2	3.8(±0.5)E-15	$0.36^{+0.06}_{-0.06}$	110 ± 30	2.0E44	4.6E44	1.8E23	QSO-1	BLAGN	3	3.610
254	91	53.17850	−27.78400	53.17850	−27.78405	0.2	1.6(±0.3)E-15	$0.41^{+0.09}_{-0.08}$	< 80	5.8E43	1.5E44	1.9E23	QSO-1	BLAGN	1	3.193
261	21	53.18458	−27.88086	53.18466	−27.88091	0.3	6.8(±2)E-16	$0.10^{+0.18}_{-0.12}$	560 ± 100	6.1E43	7.6E43	3.3E22	QSO-1	BLAGN	3	3.471
275	19	53.19945	−27.69663	53.19966	−27.69666	0.7	1.3(±0.1)E-14	$0.19^{+0.04}_{-0.05}$	230 ± 35	2.7E43	3.1E43	6.2E21	AGN-1	BLAGN	3	0.733
278	268 _a	53.20512	−27.68050	53.20500	−27.68072	0.9	8.3(±2)E-15	> 1.36	2360 ± 600	1.2E43	7.1E43	> 2.7E23	AGN-2	HEX	3	1.222
286	15	53.22029	−27.85547	53.22033	−27.85555	0.3	5.4(±0.8)E-15	$0.27^{+0.05}_{-0.04}$	140 ± 50	3.3E43	4.6E43	1.9E22	AGN-1	BLAGN	1	1.227
290	101 _a	53.23116	−27.79763	53.23125	−27.79775	0.5	1.3(±0.3)E-15	$0.27^{+0.09}_{-0.12}$	80 ± 20	1.5E43	2.2E43	2.7E22	AGN-1	BLAGN	3	1.625
301	13	53.24595	−27.72766	53.24620	−27.72763	0.8	8.7(±0.8)E-15	$0.22^{+0.05}_{-0.04}$	270 ± 40	1.7E43	2.0E43	7.2E21	AGN-1	BLAGN	3	0.733
305	11	53.24929	−27.79669	53.24929	−27.79672	0.1	1.1(±0.6)E-14	$0.19^{+0.03}_{-0.03}$	100 ± 30	4.3E44	6.2E44	4.0E22	QSO-1	BLAGN	3	2.579
311	77	53.25641	−27.76175	53.25641	−27.76183	0.3	1.8(±0.4)E-15	$0.13^{+0.11}_{-0.09}$	380 ± 20	2.6E42	2.8E42	3.0E21	AGN-1	BLAGN	3	0.622
316	4 _a	53.26500	−27.75513	53.26512	−27.75525	0.6	6.4(±0.6)E-15	$0.29^{+0.05}_{-0.04}$	< 80	4.1E43	5.8E43	2.0E22	AGN-1	BLAGN	1	1.260

Columns are as in table 6.3.

We adopt an $\Omega_m = 0.26$, $\Omega_\Lambda = 0.74$, $h_o = 0.72$ cosmology throughout. When we take luminosities and absolute magnitudes from the literature, we convert them to this cosmology.

6.4 Do optically–dull AGN have weak ionizing continua?

One of the proposed causes for optical dullness is intrinsically weak ionizing continua, such that the narrow line regions are not excited. We perform two tests of this hypothesis.

6.4.1 Do the low-obscuration AGN have big blue bumps?

First, do low–X-ray obscuration AGN show the “big blue bumps” (Filippenko, 1988) attributed to normal, UV–bright accretion disks? Such low–X-ray obscuration AGN are likely to have low–extinction lines of sight to the nucleus, and thus are likely to show bright blue continua if they have accretion disks. However, differential extinction along the different lines of sight to the optical and X-ray components could result in a lack of big blue bumps. How many of the X-ray–soft (and therefore presumably low obscuration) AGN in the sample have indications of “big blue bumps”? Of the 10 AGN with lowest estimated column densities ($N_H < 3 \times 10^{22} \text{ cm}^{-2}$), only 2 have flat νf_ν SEDs; the rest have stellar SEDs that fall quickly in the blue.⁴ So among these presumably low-obscuration AGN, big blue bumps appear to be rare. This is consistent with dust extinguishing the blue continuum, or with an intrinsically weak blue continuum, although it is more difficult to explain under the dilution hypothesis.

There are indeed 14 sources with flat or probably flat SEDs—if these are not the lowest–column sources, what are they? Of the 14, 7 have low–reliability spectral quality flags (Szokoly et al., 2004); emission lines may well show up in better–

⁴Nine of the ten sources have reliable redshifts according to Szokoly et al. (2004).

quality spectra, and thus these sources may not be true “optically–dull AGN”.

Thus, blue non–stellar SEDs are not common in the optically–dull sample, consistent with their having weak UV continua but also with their having UV of normal strength but obscured along our sightline. We need another test to distinguish these possibilities.

6.4.2 Do the SEDs of optically–dull AGN show AGN-like mid-IR emission?

If the UV continua of the optically–dull objects really are weak, then the mid-IR emission should be abnormally weak for AGN. Local Seyferts characteristically have bright mid-IR emission (c.f. Spinoglio & Malkan 1989, Rush et al. 1993, Spinoglio et al. 1995, Maiolino et al. 1995) that is attributed to heating of dust by UV energy from the central engine. Assuming similarity in other regards, AGN with weak UV should also have weak IR. However, since dust heated by star formation also emits in the mid-infrared, we must choose our tests and samples carefully.

To first order, most of the rest-frame optical/near-IR SEDs in the sample are stellar. We select two subsamples that are unlikely to be dominated in the mid-infrared by emission from star-formation. As subsample A, we select the 9 optically–dull AGN whose optical spectra are dominated by absorption lines. Of these, seven have old stellar SEDs.⁵ This subsample should be the least contaminated by star formation. We create subsample B by selecting optically–dull AGN whose SEDs (in observed $0.4 < \lambda < 8 \mu\text{m}$) are dominated by old stars, but whose spectra show low-excitation emission lines that indicate some HII regions are present. Eight optically–dull sources match these criteria.

In figures 6.1, 6.2, and 6.3 we plot the SEDs of the optically–dull AGN. Com-

⁵The other two, AID 126 and 247, have power-law SEDs, but both have low-quality spectra (Szokoly et al. (2004) flags of 1.0 and 0.5, respectively), and thus may not have been classified as ABS given better spectra.

pared to an Sa galaxy template (Devriendt et al., 1999), 5 of 7 subsample A (ABS) sources show elevated $24\ \mu\text{m}$ emission, as do 6 of 8 subsample B sources. Thus, this test supports the presence of significant UV luminosity. However, this simple test is not definitive because the templates do not reflect the observed range of SEDs observed with *Spitzer*. Additionally, the SED test is not clear-cut for the subsample B sources, which by definition contain some low-level star formation that could elevate the $24\ \mu\text{m}$ flux density.

6.4.3 Do optically-dull AGN have stellar or AGN-like $\text{H}\beta/24\ \mu\text{m}$ ratios?

Since Balmer emission and mid-infrared flux density are both strongly influenced by the star formation rate, we can use the observed $\text{H}\beta$ emission-line flux to predict the observed $24\ \mu\text{m}$ flux density predicted by star formation, and test whether the optically-dull AGN violate this expectation (by having $24\ \mu\text{m}$ excess.)

We obtain optical emission line fluxes using the VLT spectra of Szokoly et al. (2004) discussed in § 6.3. For the two subsamples, the VLT spectra cover $[\text{O II } \lambda 3727]$, and generally cover all of the Balmer series except $\text{H}\alpha$. In subsample A, no source shows Balmer emission; 4/7 show Balmer absorption, and 3/7 show non-existent or very weak Balmer lines. Only 1 of 8 subsample B sources show $\text{H}\beta$ emission; the rest have non-detected Balmer lines.

We fit continua at the Balmer lines and sum line fluxes. When Balmer lines are not detected or appear in absorption, we take a conservative upper limit on emission flux as $f(\text{H}\beta) = 3 \times 10^{-16} \text{erg s}^{-1}$ (which is the five σ limiting $\text{H}\beta$ emission flux of the spectrum with lowest signal-to-noise ratio). We deredden the Balmer fluxes by a standard extinction value⁶ of $E(\text{B-V}) = 0.435$.

⁶This corresponds to $A_{\text{H}\alpha} = 1.1$ and $A_{\text{H}\beta} = 1.57$. It is the extinction value applied by Roussel et al. (2001), and is the average extinction observed by Kennicutt (1998a).

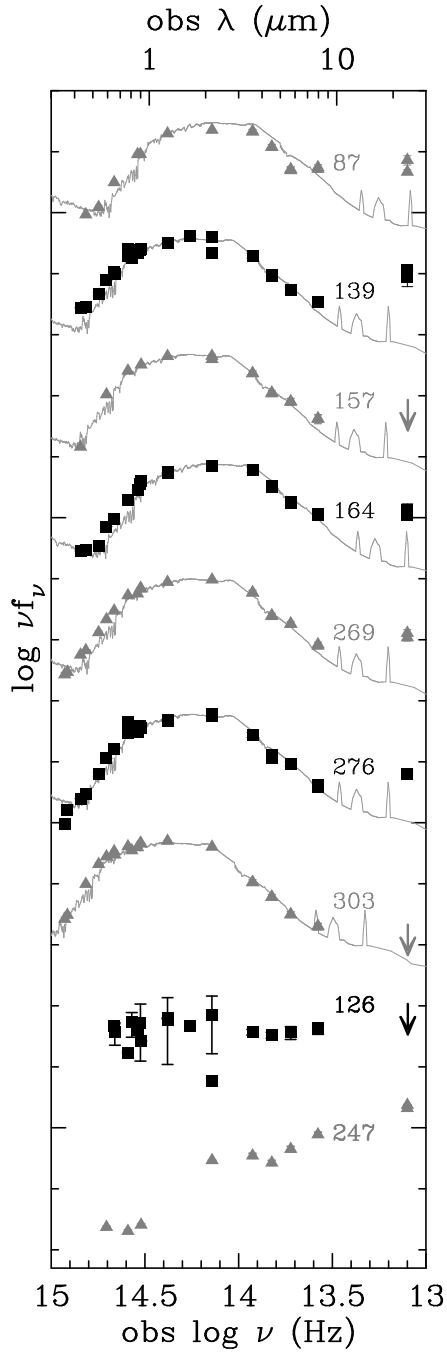


Figure 6.1 Spectral energy distributions of subsample A (optically-dull AGN with absorption-line (ABS) spectral classifications.) Wavelengths are as observed. For comparison, we plot templates of the SA galaxy VCC 1003 in the Virgo cluster (Devriendt et al., 1999).

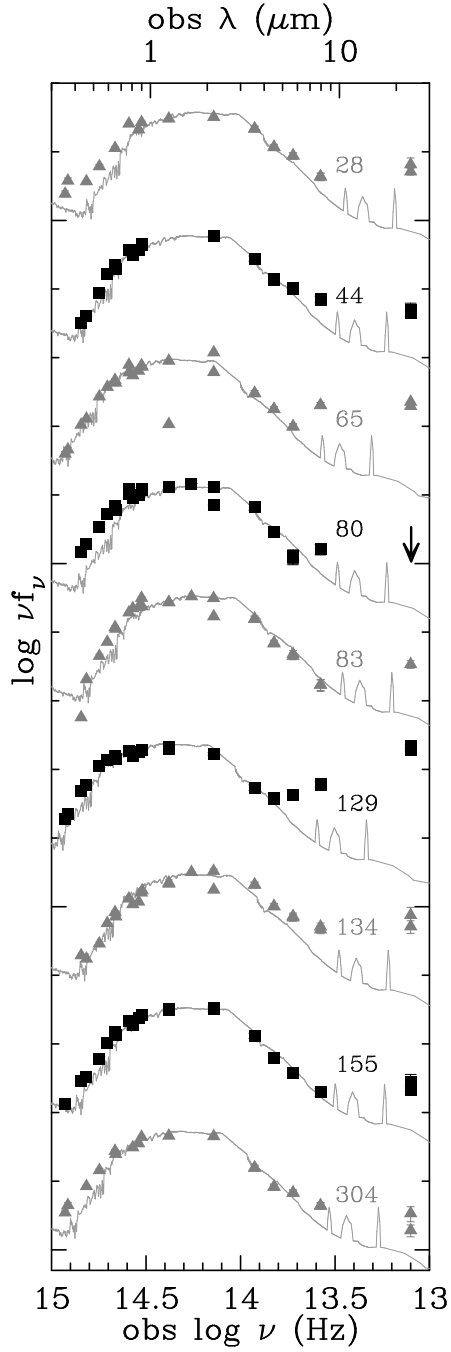


Figure 6.2 SEDs of subsample B. Wavelengths are as observed. For comparison, we plot the SA galaxy VCC 1003 in the Virgo cluster (Devriendt et al., 1999).

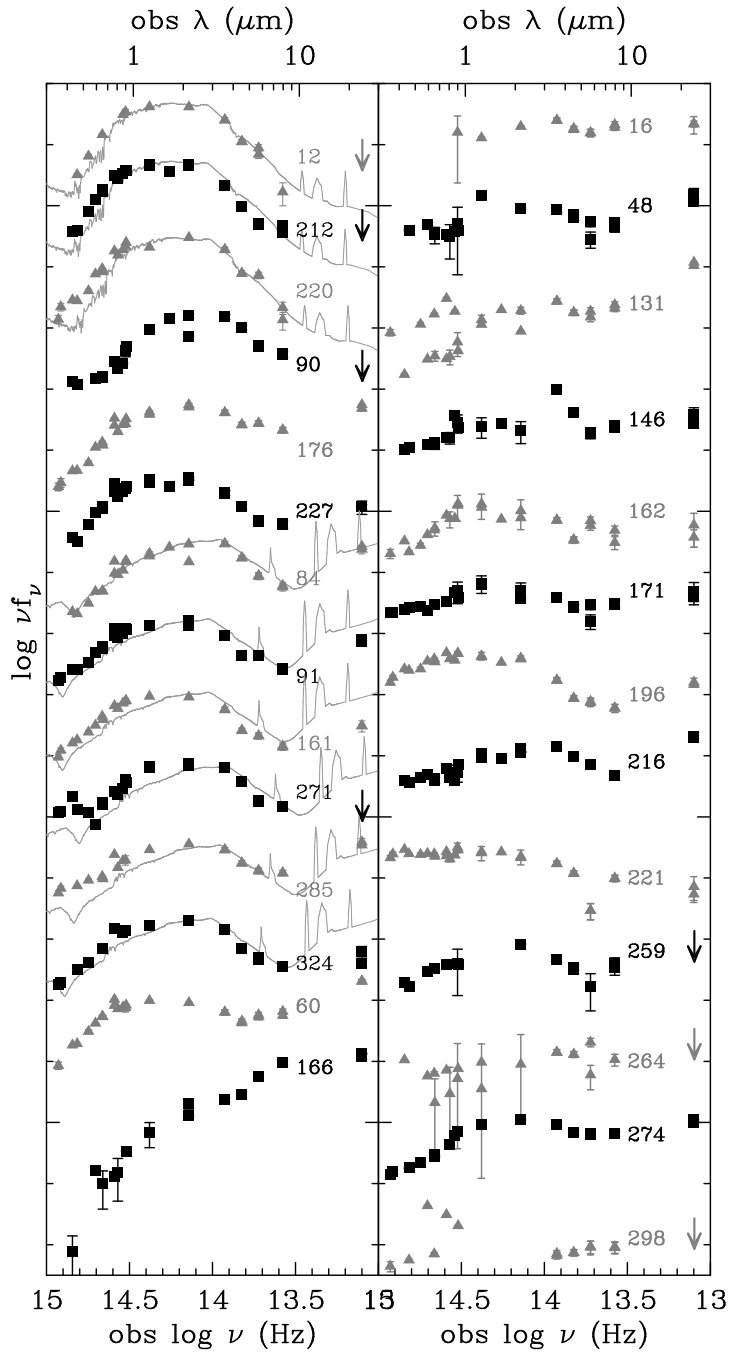


Figure 6.3 SEDs of the remaining optically-dull AGN. Wavelengths are as observed. Left panel, top to bottom: 3 old stellar pop SEDs; 3 intermediate SEDs; 6 young stellar pop SEDs; and 2 non-stellar rising-spectrum SEDs. Right panel: the non-stellar flat SEDs. For comparison, we plot the SA galaxy VCC 1003 with the old-type SEDs, and M82 with the young-type SEDs (Devriendt et al., 1999).

In figure 6.4 we plot the observed $f_\nu(24 \mu\text{m})/f(H\beta)$ ratios for subsamples A and B (lower panel), as well as for several comparison samples (upper panel). The first comparison sample is a sample of star-forming galaxies at $z \sim 0.7$, generated by cross-correlating the $H\beta$ catalog of Lilly et al. (2003) with a $24 \mu\text{m}$ catalog obtained from our GTO *Spitzer* images of the Extended Groth Strip. The second is a sample of low-redshift PG quasars, with $24\mu\text{m}$ flux densities taken from the MIPS GTO AGN survey (D. Hines, private communication) and $H\beta$ fluxes from Marziani et al. (2003); these quasars are unlike our sample in that they are generally unobscured AGN. The third sample consists of radio galaxies and quasars from Shi et al. (2005); the radio galaxies are more like our optically-dull sample in that their nuclei are obscured.

We also plot the Chary & Elbaz (2001) star-forming galaxy models with bolometric luminosities from $10^9 L_\odot$ to $10^{12} L_\odot$ along with the K-correction paths of two median PG quasar SEDs, the Elvis, Risaliti, & Zamorani (2002) template and the normalized (at $\lambda_{rest} = 25 \mu\text{m}$), de-redshifted median photometry of the Haas et al. (2003) sample.

We predict how K-corrections should affect the observed $f_\nu(24 \mu\text{m})/f(H\beta)$ ratio, as follows. We redshift each Chary & Elbaz (2001) model to find the observed $24 \mu\text{m}$ flux density normalized to the rest-frame $15 \mu\text{m}$ flux density; this is a K-correction and thus depends on redshift and SED shape. We normalize to $15 \mu\text{m}$ in order to take advantage of the empirical relation between $15 \mu\text{m}$ and Balmer emission measured by Roussel et al. (2001), which, combining equations from Roussel et al. (2001) and Kennicutt (1998a), we can write as follows:

$$\left(\frac{f_\nu(15 \mu\text{m})^{rest}}{f(H\beta)^{rest}} \right) = \left(\frac{14 \times 10^{26}}{\Delta\nu_{ISO}} \right) \frac{mJy}{erg s^{-1} cm^{-2}} \quad (6.1)$$

where $\Delta\nu_{ISO} = 6.75 \times 10^{12} \text{ Hz}$.

We can now combine this $15 \mu\text{m}$ –Balmer relation with the K-correction to cal-

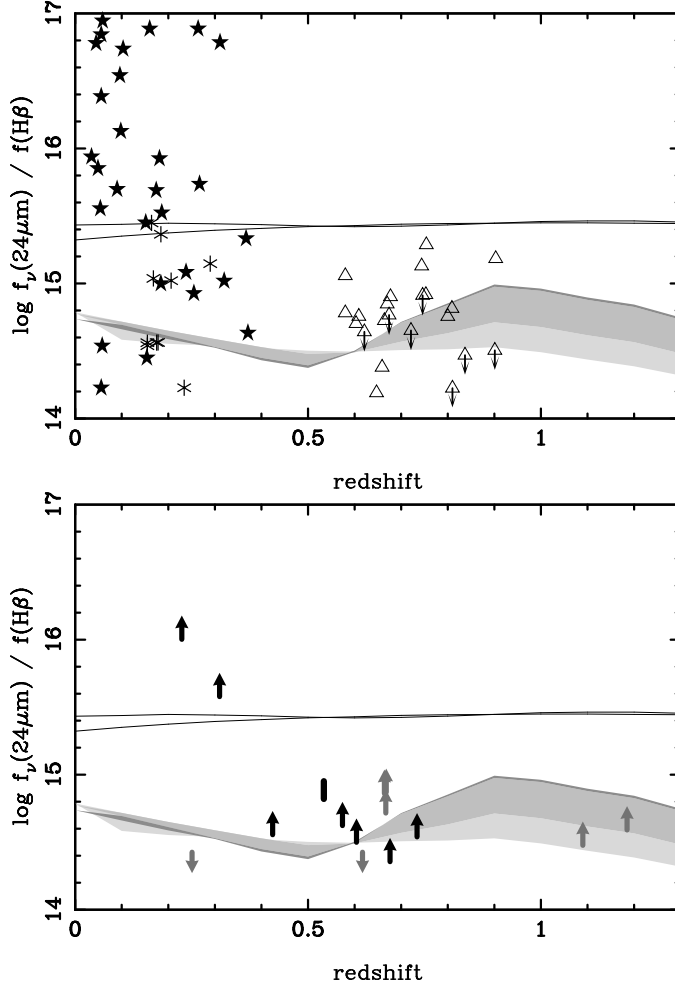


Figure 6.4 The observed $f_\nu(24\mu\text{m})/f(H\beta)$ ratio. The upper panel shows the comparison samples: PG quasars (*asterisks*, $24\mu\text{m}$ data from D. Hines, private communication, $H\beta$ from the literature); radio quasars and FRII radio galaxies (*filled stars*, $24\mu\text{m}$ data from Shi et al. 2005, $H\beta$ from the literature); star-forming galaxies from the Extended Groth Strip (*triangles*, unpublished $24\mu\text{m}$ data, $H\beta$ from Lilly et al. 2003); and star-forming galaxy models with $\log L_{\text{bol}} = 9-10 L_\odot$ (*darkest shaded region*); $\log L_{\text{bol}} = 10-11 L_\odot$ (*lighter shaded region*); and $\log L_{\text{bol}} = 11-12 L_\odot$ models (*lightest shaded region*), all from Chary & Elbaz (2001). Solid lines show the expected K-corrections for median PG QSOs, from Elvis, Risaliti, & Zamorani (2002) and Haas et al. (2003), with arbitrary normalization. The bottom panel shows the optically-dull AGN from subsample A (*grey arrows*) and subsample B (*black arrows and bar*). The units of the y-axis are $\text{mJy}/(\text{erg s}^{-1} \text{cm}^{-2})$.

culate how the observed $f_\nu(24 \mu\text{m})/f(H\beta)$ ratio changes as the source is moved to higher redshift.

$$\left(\frac{f_\nu(24 \mu\text{m})^{obs}}{f(H\beta)^{obs}} \right) = \left(\frac{f_\nu(15 \mu\text{m})^{rest}}{f(H\beta)^{rest}} \right) \left(\frac{f_\nu(24 \mu\text{m})^{obs}}{f_\nu(15 \mu\text{m})^{rest}} \right) \quad (6.2)$$

In figure 6.4 we plot this result, the expected $f_\nu(24 \mu\text{m})/f(H\beta)$ ratios for Chary & Elbaz (2001) models.

There are several points to take from figure 6.4.

First, the galaxies from Lilly et al. (2003) are in the general range of the predictions of the Chary & Elbaz (2001) models. This suggests that the empirical relation between $H\beta$ and mid-infrared flux density in star-forming galaxies at $z \sim 0$ (Roussel et al., 2001) holds reasonably well out to $z \sim 1$.

Second, at least two optically-dull AGN have $f_\nu(24 \mu\text{m})/f(H\beta)$ ratios that are too high to be consistent with star formation. These are the highest of the upward-pointing arrows, i.e., those with $\log f_\nu(24 \mu\text{m})/f(H\beta) > 15.4 \text{ mJy} / (\text{erg s}^{-1} \text{ cm}^{-2})$. *Thus, we see strong mid-infrared evidence of accretion in a few optically-dull AGN from the $24 \mu\text{m}/H\beta$ test.*

Third, the $f_\nu(24 \mu\text{m})/f(H\beta)$ ratio *is not* a useful diagnostic of AGN versus star formation activity for most of these sources. The problem is, the range of ratios seen for $0.5 < z < 1$ star-forming galaxies overlaps with the range seen in PG quasars and radio galaxies. Therefore, the ratio for the optically-dull galaxies are consistent with AGN-powered IR excesses, but the majority of sources have ratios that could also arise from star formation.

6.4.4 Do optically-dull AGN have AGN-like mid-IR to X-ray luminosities?

The previous two subsections have shown that some optically-dull AGN appear to have AGN-powered excess $24 \mu\text{m}$ emission. The rest are consistent with this possibility, but differential extinction and inadequate comparison templates

make arguments based on optical SEDs or $H\beta$ line strength inconclusive for many of these galaxies. Therefore, we now compare the mid-infrared and X-ray luminosities of the optically-dull AGN, since both should be robust to large amounts of obscuration.

In figure 6.5 we plot the ratio of the absorption-corrected rest-frame 2–10 keV luminosity to the rest-frame 6 μm luminosity, as a function of estimated column density. We calculate rest-frame $\nu L_\nu(6 \mu\text{m})$ by extrapolating from the observed 24 μm flux density, assuming $f_\nu \propto \nu^{-1}$ ⁷. Figure 6.5 should be compared with figure 7 of Lutz et al. (2004), which is the corresponding plot for ~ 40 nearby active galaxies with *ISO* spectra.

The first insight to gain from figure 6.5 is that the $z \sim 0.7$ AGN behave much like the low-redshift AGN of Lutz et al. (2004). The range of L_x/L_{IR} is similar (apart from a few outliers at low L_x/L_{IR}). Lutz et al. (2004) showed that the luminosity ratio does not depend on column density for local AGN; this finding constrains unification geometry, since many unification models predict a dependence on N_H . The CDFS sample shows that L_x/L_{IR} of AGN does not depend on column density at $z \sim 0.7$, either, a result first indicated by Rigby et al. 2004 from flux ratios, and also demonstrated by figure 9 of Alonso-Hererro et al. (2006).)

The second insight is that the optically-dull and optically-active AGN in the CDFS do not have significantly different L_x/L_{IR} ratios. Specifically, figure 6.5 does *not* show that optically-dull AGN have abnormally low mid-infrared luminosities given their X-ray luminosities. This result, along with those of the previous two section, argues strongly that *optically-dull AGN have Seyfert-like mid-infrared emission*.

The third insight is that the sources with young and old stellar SEDs do not

⁷Very similar luminosities are obtained if we instead calculate 6 μm luminosity by interpolating between the observed 24 μm and 8 μm flux densities.

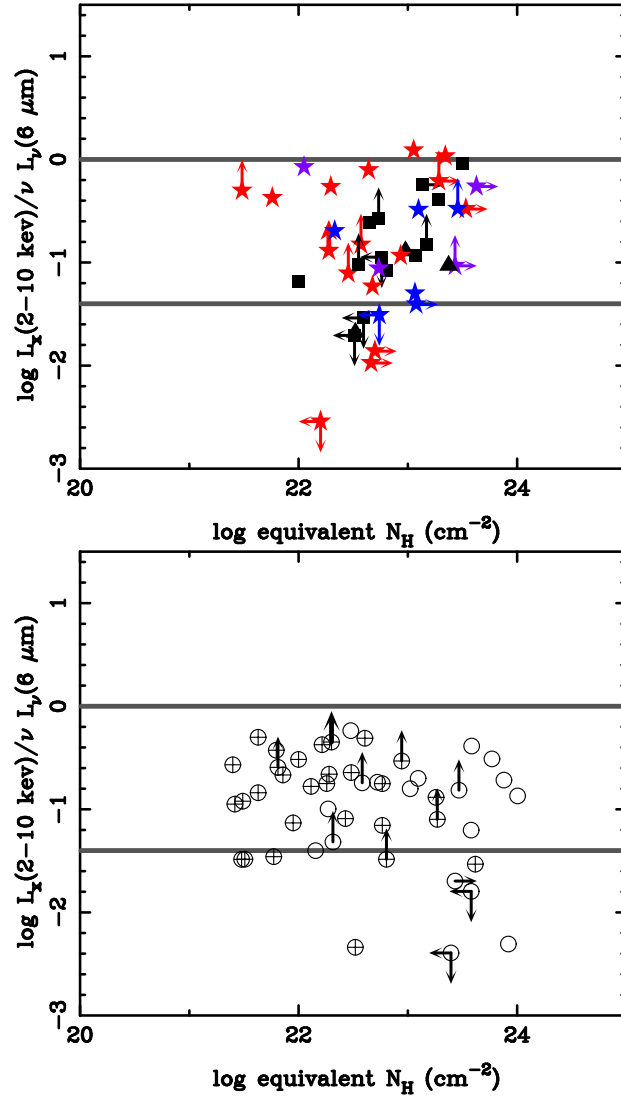


Figure 6.5 Ratio of 6 μm and X-ray luminosity versus inferred column density. Optically-dull AGN are plotted in the upper panel, with symbols coded by SED type: old stellar pop(*red stars*); intermediate (*purple stars*); young stellar pop(*blue stars*); flat in νf_ν (*black squares*); rising in νf_ν with increasing wavelength (*black triangles*). Optically-active AGN, both BLAGN (*crossed circles*) and narrow-line AGN (*open circles*) are plotted in the lower panel. Horizontal lines mark the approximate luminosity ratio range observed in the low-redshift sample of Lutz et al. (2004) (see their figure 7.) Star-forming galaxies without AGN would have y-axis values in the range of -1.3 to -2.7, using data from Zezas et al. (2001) for three galaxies and the 6 μm -to-FIR relation of Elbaz et al. (2002).

have significantly different L_x/L_{IR} . This tentatively suggests that the scatter in L_x/L_{IR} for AGN is not primarily caused by emission from star formation. It is unknown what causes the considerable scatter in L_x/L_{IR} ; both quantities should be reasonably robust to extinction and other line-of-sight effects. The observed scatter is larger than that expected from photometric uncertainties alone (the median fractional error in L_x/L_{IR} is 25%.)

Last, we note that the CDFS AGN include a handful with lower L_x/L_{IR} than seen by Lutz et al. (2004).

Thus, we conclude that the optically-dull AGN have X-ray and mid-IR luminosities within the normal ranges seen for local Seyferts. The SED and $24\ \mu\text{m}/\text{H}\beta$ tests are consistent with the behavior seen in the L_x/L_{IR} test, and in some cases independently corroborate it. We conclude that *optically-dull AGN have the normal mid-IR emission expected for Seyfert galaxies*. This argues that optically-dull AGN have normal AGN blue and UV continua, to produce a normal AGN mid-IR luminosity. Thus, the lack of big blue bumps in the X-ray-soft AGN is probably not caused by intrinsically weak optical and UV continua.

6.5 How important is dilution to optical dullness?

We now estimate quantitatively the importance of “dilution” (bright galaxy continua overwhelming lines from faint AGN) in causing optical dullness. Dilution has been argued to be important in local samples of weak-line AGN, and so we first examine how similar these local AGN are to the $z \sim 1$ optically-dull AGN. Next, we examine the optical-to-X-ray flux and luminosity ratios, to estimate the importance of dilution in our $z \sim 1$ sample.

6.5.1 Are optically–dull AGN at $z \sim 1$ like weak-line AGN at $z \sim 0$?

Several studies have searched for local examples of optically–dull AGN, since such sources are amenable to detailed follow-up. These searches generally obtain optical spectroscopy for sources in wide-area hard-band X-ray surveys, and identify the handful that lack optical emission lines. Several examples:

1. The 2–10 keV–selected HEAO-1 sample (Piccinotti et al., 1982) contains 39 sources that are not galaxy clusters; 30 of these have emission–line signatures of AGN, 7 were not identified with known sources, and only 1 corresponds to an optically non-active (i.e., an optically–dull) galaxy.
2. Follow-up spectroscopy of 5–10 keV Hellas Beppo-SAX sources found optical counterparts for 61/74 sources; 6 are apparently AGN without optical AGN signatures (La Franca et al., 2002) and have emission-line $\text{EW}(\text{H}\beta) \sim 1\text{--}5 \text{ \AA}$.
3. The ASCA 2–10 keV Medium Sensitivity Survey identified 28 sources at $z < 0.2$ (Akiyama et al., 2003). All are broad-line, narrow-line, or BL Lac AGN, but five have weak emission lines ($\text{H}\beta$ and $[\text{O III}]$ equivalent widths below 10 \AA), and consequently might look optically–dull at higher redshift.
4. Watanabe et al. (2002) followed up the hardest 2% of the ASCA detections, and found three ($z \sim 0.05$) sources with $N_H \sim 10^{23} \text{ cm}^{-2}$ and abnormally low–luminosity Seyfert/LINER emission lines. At redshifts typical of the deep surveys, these 3 sources should look like optically–dull AGN.
5. Using a different search method, Hornschemeier et al. (2005) correlated Chandra images with spectroscopy from the Sloan Digital Sky Survey. They found no X-ray sources that lacked optical signs of nuclear accretion. How-

ever, 4 of their 19 AGN would not be identified as AGN through optical spectroscopy if their redshifts exceeded ~ 0.5 .

Although it is not always clear for these studies whether additional members of the sample would appear optically–dull at high redshift, they agree that locally, optically–dull AGN are not common in samples selected on the basis of X-ray emission.

In figure 6.6 we plot the column densities and redshifts of these local AGN⁸. For comparison, we also plot inferred column densities for the CDFS optically–dull AGN (see §6.3). Figure 6.6 clearly demonstrates that many low–redshift AGN with weak emission lines have very low ($< 10^{22} \text{ cm}^{-2}$) column densities, much lower than the CDFS AGN. Since they are so much less obscured, they are not true analogues to the sources in the deep fields, and so the importance of dilution to local weak–line AGN should not argue for the importance of the effect in very different AGN at $z \sim 1$.

Thus, dilution may be important for the low–column, local AGN with weak lines; but the much higher column densities of the CDFS AGN argue, at the very least, that these populations are not similar. This opens the possibility that extinction or other effects may be more important for the distant AGN than for local weak–line AGN.

6.5.2 X-ray to optical flux and luminosity ratios

To further understand the importance of dilution to distant optically–dull AGN, in figure 6.7 we plot the observed R-band and 2–8 keV fluxes of the CDFS sample. This figure should be compared to figure 3 of Comastri et al. (2002). Comastri et al. (2002) looked at ten $z \sim 0.2$ optically–dull AGN from HELLAS2XMM

⁸Hornschemeier et al. (2005) and Piccinotti et al. (1982) do not list flux ratios, so we cannot infer a column density.

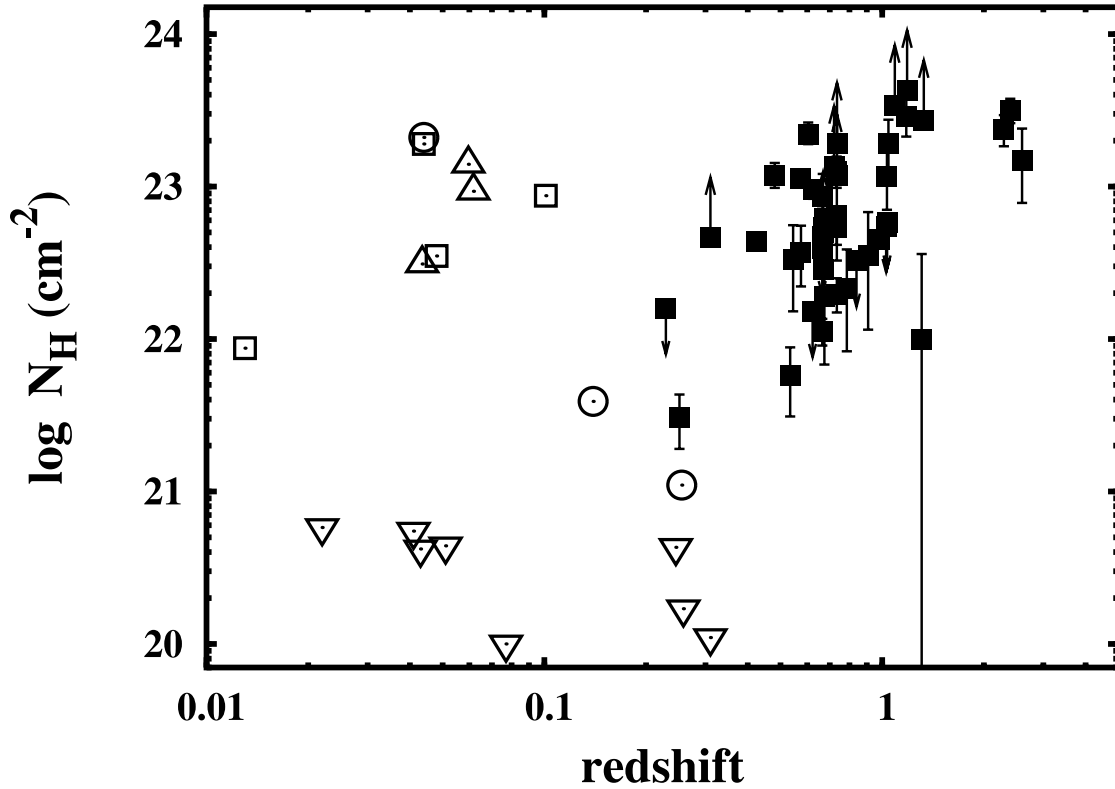


Figure 6.6 Column densities of optically-dull AGN. The low-redshift samples are: XMM serendipitous sources from (Severgnini et al., 2003) (*open circles*); hard ASCA sources from Watanabe et al. (2002) (*up-pointing triangles*); hard ASCA sources from Akiyama et al. (2003) with emission line equivalent widths $< 10 \text{ \AA}$ (*down-pointing triangles*); and 5–10 keV BeppoSAX sources without AGN emission lines (La Franca et al., 2002) (*open squares*), where we have used the (1.3–4.5 keV)/(4.5–10 keV) count ratios derived from Fiore et al. (2001) to estimate the column density. The higher redshift sources are our CDFS sample (*filled squares*), with N_H values inferred from the flux ratio of the observed 2–8 keV and 0.5–2 keV bands (fluxes from Alexander et al. 2003).

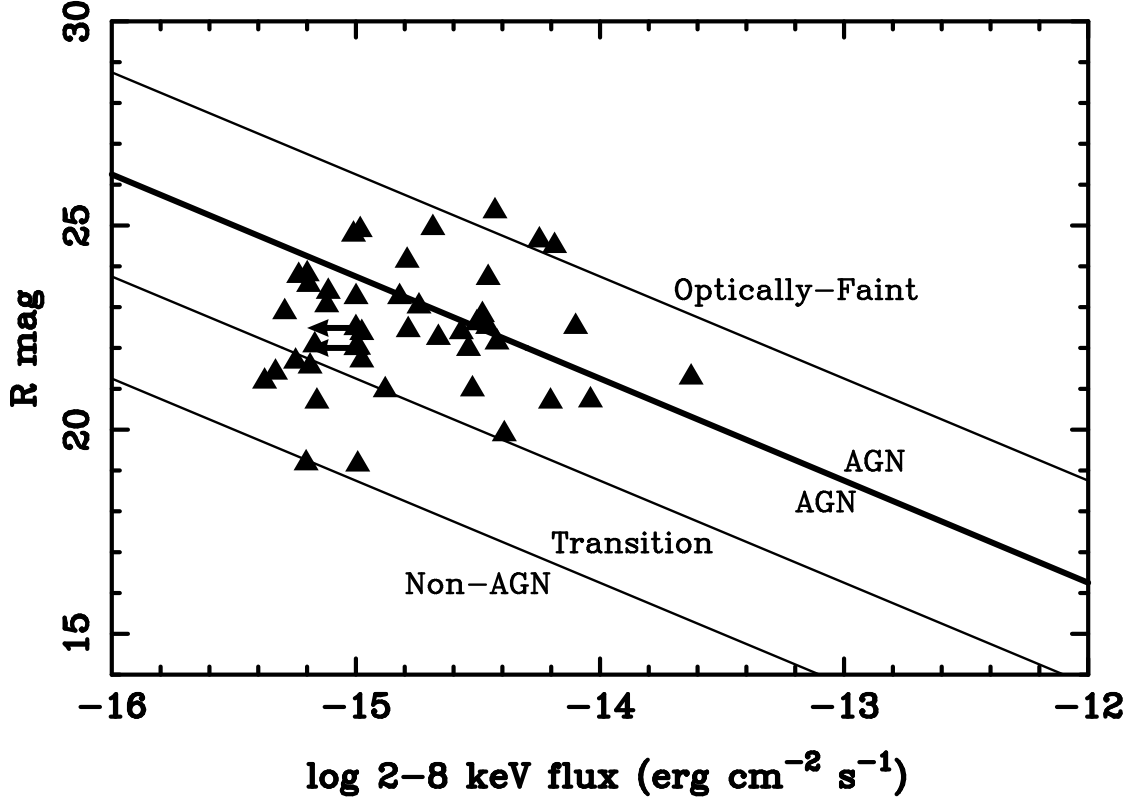


Figure 6.7 Observed R-band magnitude and X-ray flux for the optically-dull AGN. Data are from Giacconi et al. (2002). Lines mark flux ratios of $F_x/F_R = 0.1, 1$, and 10 , following figure 3 of Comastri et al. (2002).

and Chandra (Barger et al., 2001b), and found that most have high f_r/f_x ratios—which suggests that they have very luminous host galaxies (which makes spectral dilution likely.) In contrast, our figure 6.7 demonstrates that this effect is *not* common for the 45 CDFS optically-dull AGN: all but a handful have optical/X-ray flux ratios that are typical of AGN. Thus, this plot does not support the dilution hypothesis for optically-dull AGN in the CDFS.

However, figure 6.7 is not an ideal diagnostic tool, since it uses observed fluxes and thus does not K-correct. Accordingly, in figure 6.8 we plot the rest-frame absolute R magnitudes and rest-frame absorption-corrected 2–8 keV luminosities of the optically-dull sample. (We also plot the local-universe weak-line

AGN from figure 6.6, and the optically-active AGN in the CDFS.) In each panel of figure 6.8, the thick diagonal line shows the M_R/L_x ratio of the composite radio-quiet QSO SED from Elvis, Risaliti, & Zamorani (2002). The thin diagonal lines mark flux ratios 10 and 100 times brighter in the optical than the QSO M_R/L_x ratio. Panel b of figure 6.8 shows the M_R/L_x ratios of the optically-active AGN; 96% of those sources lie above the $10\times$ Elvis line; as such, their AGN should contribute at least 10% of their optical luminosities, and in many cases should dominate. Comparison with panel c then shows that 67% of the optically-dull sources have M_R/L_x ratios above the $10\times$ Elvis line. A more restrictive cut would be the $6.3\times$ Elvis line: 94% of the optically-active sources fall above it; and 56% optically-dull sources do.

Thus, we conclude, based on figures 6.7 and 6.8, that the R-band to X-ray luminosity ratios *suggest that less than half* of the optically-dull AGN are dull because a bright galaxy drowns out the AGN optical flux. However such dilution is likely at work in the optically-dull AGN whose total (AGN+host) optical luminosities are $\gtrsim 6$ times brighter than the X-rays the AGN should be; this effect may be important for local weak-line AGN. Thus, we conclude that dilution is only a plausible explanation for half or less of the CDFS optically-dull AGN. We need a cause for optical-dullness in the remaining half.

6.6 Can Host Galaxy Obscuration Cause Optical-Dullness in AGN?

Having shown that spectral dilution cannot account for the optical dullness of half the sample, and that the ionizing continua are unlikely to be missing given the normal mid-IR luminosities, we now examine the role that host galaxy obscuration may play in causing optical dullness. To do this, we examine the axis ratios of the optically-dull and optically-active AGN in the CDFS. Most (80%)

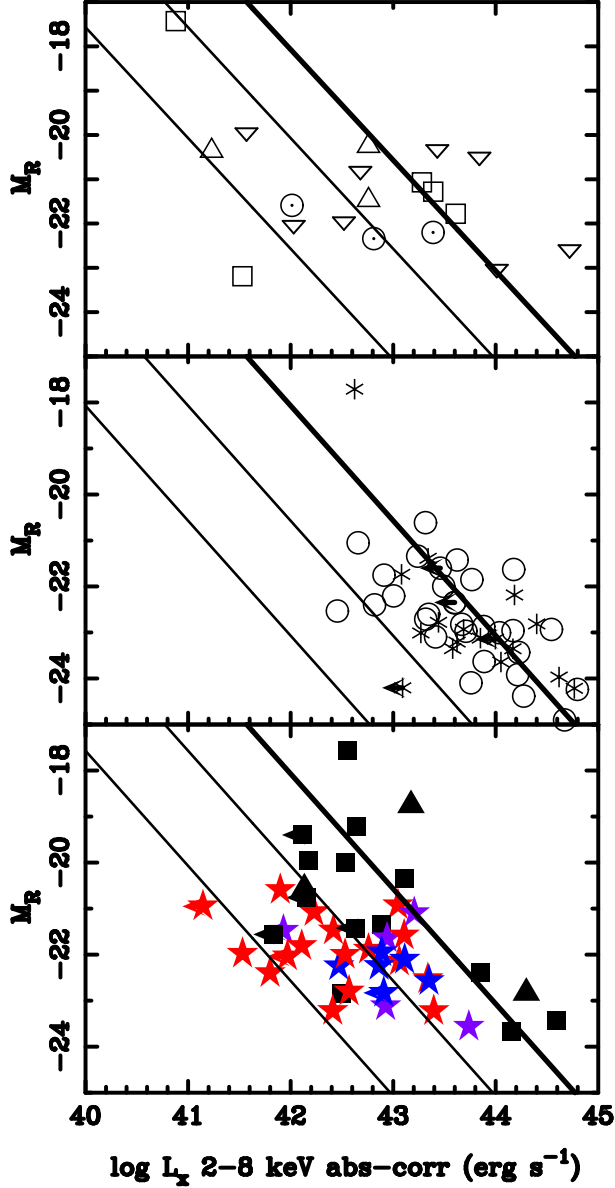


Figure 6.8 Absolute magnitude M_R versus absorption-corrected rest-frame 2–8 keV L_x . *Top panel*: Low-redshift weak-line AGN samples, with symbols as in fig 6.6. *Middle panel*: Optically-active AGN from the CDFS, both broad-line (*asterisks*) and narrow-line (*circles*). *Bottom panel*: Optically-dull AGN from the CDFS, symbols as in figure 6.5. The plotted X-ray luminosity is absorption-corrected, in the rest-frame 2–8 keV band, and is calculated from the observed 2–8 keV flux (Alexander et al., 2003) by assuming the intrinsic spectrum is a $\Gamma = 2$ power-law. M_R is calculated by linearly interpolating between bands that bracket the rest-frame R-band. The thick diagonal line shows the luminosity ratio of the composite Elvis, Risaliti, & Zamorani (2002) QSO SED. The thin diagonal lines mark ratios with 10 and 100 times higher optical luminosity.

of the optically–dull AGN lie within the ACS GOODS survey described by Giavalisco et al. (2004). These deep, high–resolution images provide morphology information even on distant sources. In the following analysis, we use the i-band images from the v1.0 public release of the GOODS ACS images. Measured axis ratios of most sources vary by only a few percent among the v, i, and z-band catalogs; therefore, we are free to choose the i-band, to optimize depth and spatial resolution (sampling rest-frame optical light at $z \sim 0.7$).

6.6.1 Measuring Axis Ratios

For each AGN, we measure the axis ratio, b/a , using two methods.

First, we simply take the b/a values from the GOODS v1.0 public release i-band Source Extractor catalogs. While Source Extractor (Bertin & Arnouts, 1996) is not optimized for morphological parameter fitting, it is a widely-available tool that can quickly estimate axis ratios for thousands of galaxies, and thus is of potential interest for large surveys.

Second, we iteratively fit multi-component Galfit models (Peng et al. 2002, Galfit v2.0.3b) to each source. This method is more time-consuming, but potentially more robust in its measurement of b/a than Source Extractor. We fit the following four Galfit models to each source:

- a point source, i.e. the HST PSF (which we created from stars in the GOODS i-band images).
- a single Sersic component.
- a point source plus a Sersic component.
- a deVaucouleurs component plus an exponential disk component.

We adopted the b/a ratio of the best-fitting model, as follows:

- If the PSF provided the best fit, we considered the source to be unresolved, and so we have no knowledge of the true b/a ratio.
- If the Sersic or PSF+Sersic models fit best, we adopted the Sersic component's b/a .
- If the bulge+disk model fit best, and both components had effective radii greater than the PSF FWHM, then we adopted as b/a the weighted mean of the two component b/a values, weighted by the fluxes of the model components. If only one component had $R_e > \text{FWHM}$, then we used the b/a value of that component. (Since any $R_e < \text{FWHM}$ component is essentially unresolved, the b/a value galfit assigns it is not meaningful.) (This weighting may over-estimate b/a in very inclined galaxies, since the bulge will generally be rounder than the disk.)

When sources were fit well by more than one Galfit model, the axis ratios of the models agreed well. Also, the b/a values measured by Source Extractor and Galfit are quite similar for each source, though Galfit tends toward smaller b/a ratios since it can fit multiple components. We quote axis ratios from Galfit unless otherwise indicated.

6.6.2 Axis Ratios of the $0.5 < z < 0.8$ Subsample

We can now compare the axis ratios of the optically-dull and optically-active AGN. We must take care because the luminosity and redshift distributions of the two samples differ. Specifically, the optically-active AGN tend to be more luminous and lie at higher redshift, and thus the HST images provide lower physical resolution; this means that the optically-active sources are more likely to be unresolved or have limited morphology information. To minimize this bias, we consider the subsample of optically-dull and optically-active AGN with GOODS

coverage that have redshifts between 0.5 and 0.8⁹. Because this includes the “redshift spike” in the CDFS, the subsample contains more sources than one would expect in an average field: there are 22 optically-dull AGN, and 9 optically-active AGN¹⁰. The absorption-corrected X-ray luminosity distributions of these two samples are comparable.

Tables 6.3 and 6.4 list the measured axis ratios for the optically-dull and active samples. Figure 6.9 shows cutouts of the GOODS i-band images for the $0.5 < z < 0.8$ AGN. Figure 6.10 plots the axis ratio distributions. Clearly, the b/a distributions of the two samples are very different: the optically-active galaxies are round, and the optically-dull galaxies have a range of b/a .

⁹All of the optically-active sources in this redshift range have reliable redshifts, and all but 3/22 of the optically-dull sources do.

¹⁰Three are narrow-line AGN (88, 179, and 241), and the rest are broad-line AGN.

Table 6.3. Axis Ratios for the Optically-Dull Sample.

AID	Best Model	galfit b/a	sextr b/a	morphology notes
AGN with redshifts $z < 0.5$ or $z > 0.8$				
65	34	0.24	0.34	dusty edge-on galaxy
84	-	int	0.60	small antennae
90	4	irr	—	irregular
131	1	pt	0.95	pt source
139	4	0.68	0.65	face-on spiral w bright bulge?
162	4	0.87	0.77	compact
164	2	0.74	0.76	face-on disk +br bulge
166	1	pt	0.35	faint pt. src
171	2	irr	0.51	irr with central bulge
216	34	0.63	0.49	compact w fuzz
221	4	0.68	0.77	compact w fuzz
259	-	irr	0.80	irregular
264	1	pt	0.86	compact w fuzz
271	4	0.62	0.59	bulge + fuzz
303	3	0.33	0.37	edge-on spiral
AGN with redshifts $0.5 < z < 0.8$				

Table 6.3—Continued

AID	Best Model	galfit b/a	sextr b/a	morphology notes
44	4	0.43	0.69	edge-on bulge+disk galaxy
48	-	irr	0.64	clumpy, v. faint
60	-	irr	0.38	compact src + fuzz
80	4	0.84	0.88	pt + fuzz
83	24	0.87	0.86	compact but extended
91	2	0.34	0.43	large clumpy spiral
126	13	pt	0.86	compact w some faint emiss
129	4	< 0.61	0.94	edge-on Sp w bright bulge
134	2	0.32	0.47	edge-on sp w bright bulge
146	2	0.26	0.41	edge-on sp w bright bulge
155	2	0.73	0.75	irr w bright bulge
157	4	0.50	0.57	somewhat inclined disk
161	4	0.85	0.90	compact
176	4	0.68	0.66	face-on Sp w central bulge
196	-	int	0.72	merger/interaction
212	24	0.89	0.84	compact
220	23	0.63	0.68	compact w fuzz
227	4	0.61	...	compact w fuzz
247	24	0.74	0.89	compact w faint fuzz

Table 6.3—Continued

AID	Best Model	galfit b/a	sextr b/a	morphology notes
269	24	0.60	0.60	bright bulge +disk
276	23	0.78	0.75	compact+fuzz

Columns: (1) X-ray source identification from Alexander et al. (2003). (2) Best-fitting Galfit model (1=PSF, 2=Sersic, 3=PSF+Sersic, 4=bulge+disk). (3) Axis ratio from best-fitting Galfit model. (4) Axis ratio from best-fitting Source Extractor model. (5) Notes on galaxy morphology.

Table 6.4. Axis Ratios for the Optically-Active Sample.

AID	Best Model	galfit b/a	sextr b/a	morphology notes
AGN with $z < 0.5$ or $z > 0.8$				
34	1	pt	0.99	slightly resolved
39	1	pt	0.93	point source
41	1	pt	0.98	point source + faint compact fuzz
43	1	pt	0.96	point source
68	1	pt	0.98	point source
76	1	pt	0.94	point source + faint compact fuzz
86	-	-	0.56	small interm spiral or irr
94	4	0.97	0.82	irr. intereaction?
96	4	irr	0.74	irregular
122	1	pt	0.91	point source
123	4	0.94	0.85	compact src + fuzz
163	1	pt	0.87	compact src
188	1	pt	0.83	point source
191	4	0.54	0.50	compact src + round fuzz
193	-	int	0.97	2 bright peaks + fuzz, merger?
197	-	irr	...	irr : bright core + offset fluff

Table 6.4—Continued

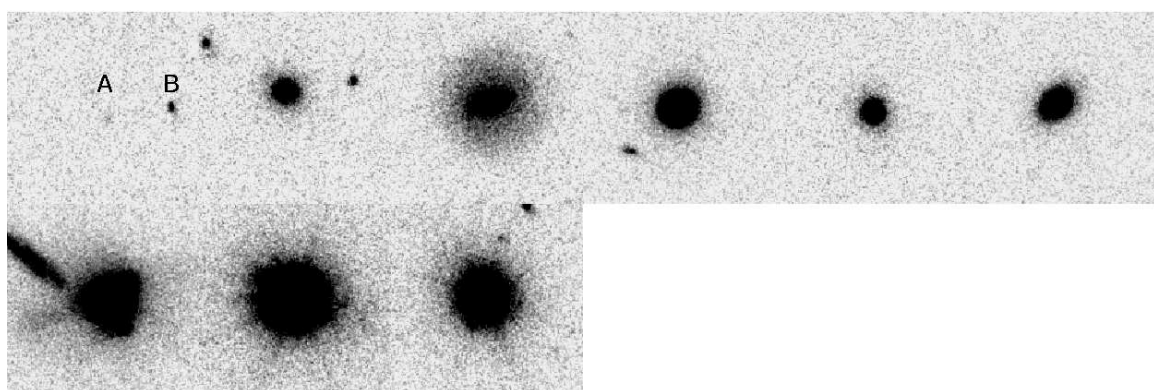
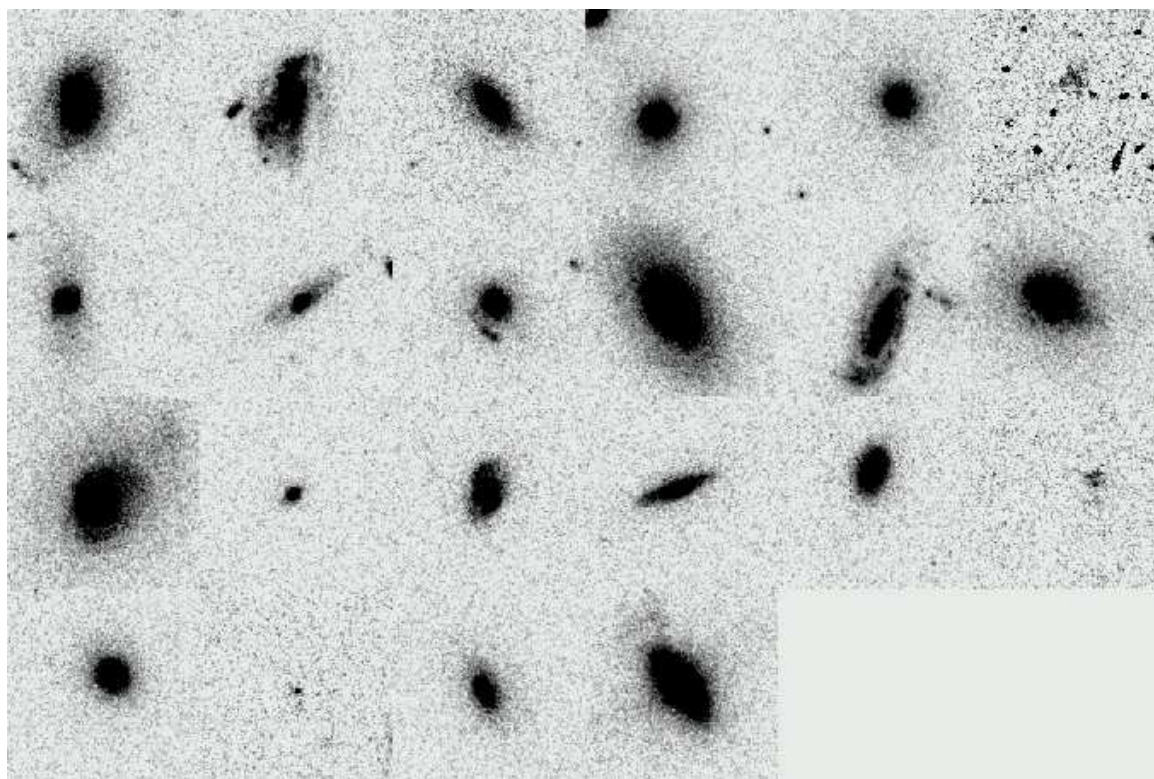
AID	Best Model	galfit b/a	sextr b/a	morphology notes
214	-	**	0.69	face-on sp or interaction?
219	1	pt	0.49	faint point source + fuzz
230	1	pt	0.92	point source + faint compact fuzz
234	14	pt	0.89	point source + faint fuzz
242	1	pt	0.87	point source + fuzz
251	1	pt	0.99	point source
254	1	pt	0.91	point source
261	1	pt	0.96	point source
286	14	0.59 ^a	0.70	psf + outer ring
AGN with $0.5 < z < 0.8$				
66	3	0.86	0.92	point source + face-on disk
88	-	—	0.62	interacting face-on spiral?
103	4	0.86	0.93	round halo + possible inclined disk
117	-	0.88 ^a	0.79	compact, round
177	3	0.90	0.93	psf + face-on disk
179	3	0.79	0.81	compact
195	-	0.85 ^a	...	compact, round

Table 6.4—Continued

AID	Best Model	galfit b/a	sextr b/a	morphology notes
229	4	0.88	0.90	bright center + fuzz
241	1	–	0.73	very faint fuzz

Columns: (1) X-ray source identification from Alexander et al. (2003). (2) Best-fitting Galfit model (1=PSF, 2=Sersic, 3=PSF+Sersic, 4=bulge+disk). (3) Axis ratio from best-fitting Galfit model. (4) Axis ratio from best-fitting Source Extractor model. (5) Notes on galaxy morphology.

a: Galfit crashed, so the axis ratio was fit using IRAF's task **ellipse**.



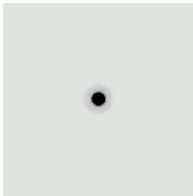


Figure 6.9 Postage stamps of the optically–dull AGN (top panel) and optically–active AGN (middle panel) at $0.5 < z < 0.8$. Data are ACS/HST i-band images from GOODS (Giavalisco et al., 2004); each postage stamp is $4.8''$ on a side. Sources are plotted top to bottom, left to right in order of increasing absorption–corrected X-ray luminosity, as follows: Optically–dull AID: 139, 196, 157, 83, 212, 298, 60, 146, 80, 269, 91, 155, 276, 126, 176, 134, 22, 48, 161, 247, 227, 44. Optically–active AID: 241, 229, 103, 117, 195, 179, 88, 66, 177. Also shown for comparison is the ACS/HST PSF in i-band, at the same pixel scale as the images (bottom panel). For clarity, we label the two possible counterparts of X-ray source AID 241 as “A” and “B”, following (Szokoly et al., 2004) who identified the two potential optical counterparts, and obtained a spectrum of B and found high–excitation emission lines, and thus is presumed to be the X-ray counterpart.

Let us explore the differences between these distributions in more detail. *All the $0.5 < z < 0.8$ optically–active sources are less concentrated than the PSF* (using concentration parameter $C = 5 \log r_{80}/r_{20}$ from Kent 1985), and half are much less concentrated. Of the optically–active AGN, all but one have $b/a > 0.79$ ¹¹. Only two sources, AID 88 and 94, show complicated (and perhaps disturbed) morphologies. Only one source (AID 103) shows any evidence for a possible inclined disk.

The optically–dull AGN are also all resolved. By contrast with the optically–active AGN, the optically–dull AGN show a range of axis ratio: $0.26 < b/a < 0.89$. One source is possibly interacting (AID 196), and there are two irregulars (48 and 60). Of the spirals, 3 are highly inclined (AID 44, 134, 146); 2 are close to face-on (AID 139, 176) and 2 have intermediate inclinations (AID 91, 157, 269). The two–sided Kolmogorov–Smirnov test disproves, at 99.7% confidence, the null

¹¹The one exception is AID 88, whose complicated morphology may indicate an interaction.

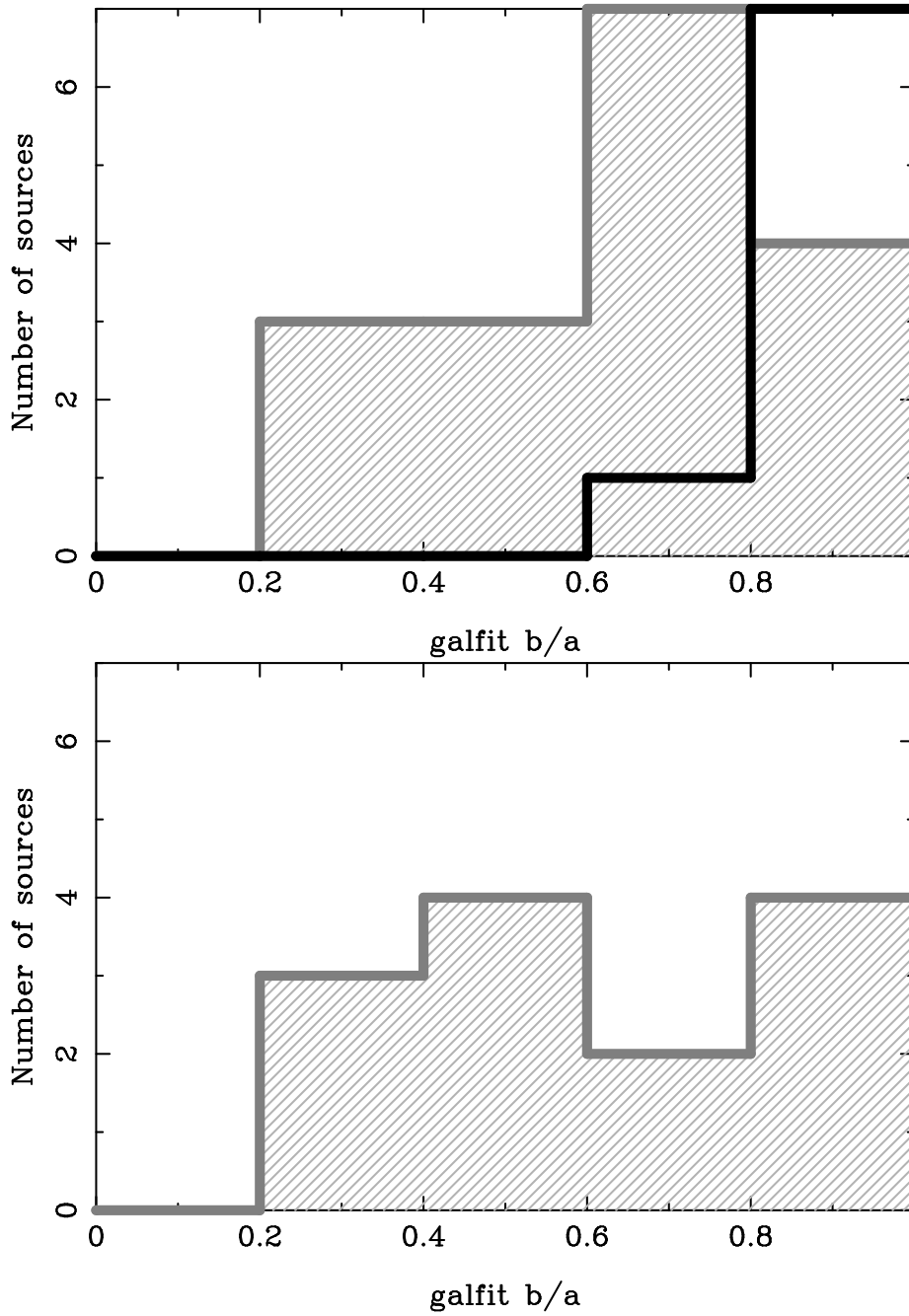


Figure 6.10 Axis ratio distributions of the optically-dull and optically-active AGN with redshifts $0.5 < z < 0.8$. Axis ratios are from Galfit models. Upper panel: The black histogram shows the distribution of the optically-active AGN; the hatched histogram shows the distribution of the optically-dull AGN. Lower panel: Axis ratios for the optically-dull AGN, if a nuclear point source is added to each.

hypothesis that the optically-dull and optically-active $0.5 < z < 0.8$ AGN are drawn from the same parent distribution.

We separate out the optically-dull $0.5 < z < 0.8$ AGN that have low rest-frame optical-to-X-ray luminosity ratios (no more than $\times 6.3$ the Elvis ratio in figure 6.8c); they, too, have an axis ratio distribution that differs, at 99.8% confidence, from that of the optically-active AGN. These are sources whose L_R/L_x ratios are not high enough for spectral dilution to be an important cause of optical dullness, and so it is important to note that their axis ratios are significantly different from that of the optically-active AGN. (The optically-dull AGN with high and low L_R/L_x do not have significantly different axis ratio distributions, but the size of each sample is small.)

Is the optically-active sample biased by nuclear point sources toward high axis ratios? This question arises since 6/9 have broad emission lines, and four of these galaxies are centrally concentrated, though not as much as a PSF. Therefore, for each optically-active AGN in our $0.5 < z < 0.8$ sample, we measure the *maximum* flux that could come from a central point source, assuming no galaxy emission. The maximal PSF flux is, in the median, 25% of the total source flux, and corresponds to $i_{AB} = 22.36$. We then add a PSF of this median brightness, with Poisson noise, to the centroid of each optically-dull source, and repeat the galfit axis ratio measurements. Figure 6.10 shows the result: adding artificial point sources to the optically-dull AGN means that some sources are no longer fit well by any model; but most sources are still fit acceptably, and the resulting b/a distribution does *not* resemble the optically-active distribution. Galfit is able to fit the artificial point source and still correctly measure the axis ratio of the galaxy.

Thus, we conclude that the host galaxies of optically-dull AGN more fully

sample the expected range of random inclination angles than do optically-active AGN.

6.6.3 Additional Axis Ratios from $z < 0.5$ and $z > 0.8$ AGN

Though the $0.5 < z < 0.8$ redshift sample should be the most robust against morphological bias, we do have morphological information on the rest of the sample, and we now briefly examine it. Since this sample may be biased, it should not be used to argue that the optically-dull AGN have a more diverse distribution of axis ratio than the optically-active AGN. But if the trends from the previous section are not present in the full redshift range, that would weaken the evidence that the trends are real.

Twenty-five optically-active AGN in the CDFS have GOODS ACS imaging and $z < 0.5$ or $z > 0.8$. Most (17) of these are well-fit by a point source (of which 8 show some faint extended emission after PSF subtraction.) Thus, only eight sources have morphology information: one PSF + ring galaxy (with $b/a = 0.6$); two compact but resolved galaxies; two sources that appear to be undergoing interactions (AID 193 and 214); and three irregular galaxies. Their b/a ratios are listed in table 6.4.

There are 15 optically-dull AGN with GOODS imaging and $z < 0.5$ or $z > 0.8$. Of these, only 3 are point sources, 4 are irregular or interacting galaxies, and the remaining 8 sources have b/a ratios from 0.2 to 0.9. The K-S test finds that the any-redshift optically-dull and any-redshift optically-active samples are drawn from different populations, at 99.5% significance. Thus, the higher and lower redshift sources do not contradict the results of the $0.5 < z < 0.8$ sample.

6.6.4 Column density evidence for extra obscuration

If host galaxy obscuration is a cause of optical dullness, then we might expect higher X-ray column densities for the optically-dull AGN than the optically-active. In figure 6.11 we plot the column density distributions for the optically-dull and optically active sources with absorption-corrected L_x below 10^{44} erg s $^{-1}$. The optically-dull sources appear to have higher column densities, as expected if the host galaxy contributes extra extinction. This result is marginally significant: the two-sided Kolmogorov-Smirnov test estimates a 95% probability that the two distributions are drawn from different parents. Adding back in the high-luminosity sources would increase the significance. Any such offset is not expected to be large, given the ROSAT extinction relation $A_V = N_H / (1.8 \times 10^{21})$ mag cm $^{-2}$ (Cox, 2000).

6.7 Discussion

We showed in §6.4 that optically-dull AGN do not have unusually weak ionizing continua; we instead found that optically-dull AGN have normal Seyfert (UV-powered) mid-infrared emission (and thus the optical may be the only wavelength range where these AGN appear odd). Further, in §6.5 we demonstrated (by comparing the rest-frame hard X-ray and optical luminosities) that dilution by stellar continuum is unlikely to explain the optical dullness of at least half our sample. We thus needed a primary cause for optical dullness in the majority of the sample.

In §6.6 we show that obscuration by host galaxies is a likely cause of optical dullness for these AGN, which can explain the missing emission lines and big blue bumps, and the normal Seyfert-like X-ray and mid-IR emission. We did this by showing that the host galaxies of X-ray-selected AGN have a range of axis

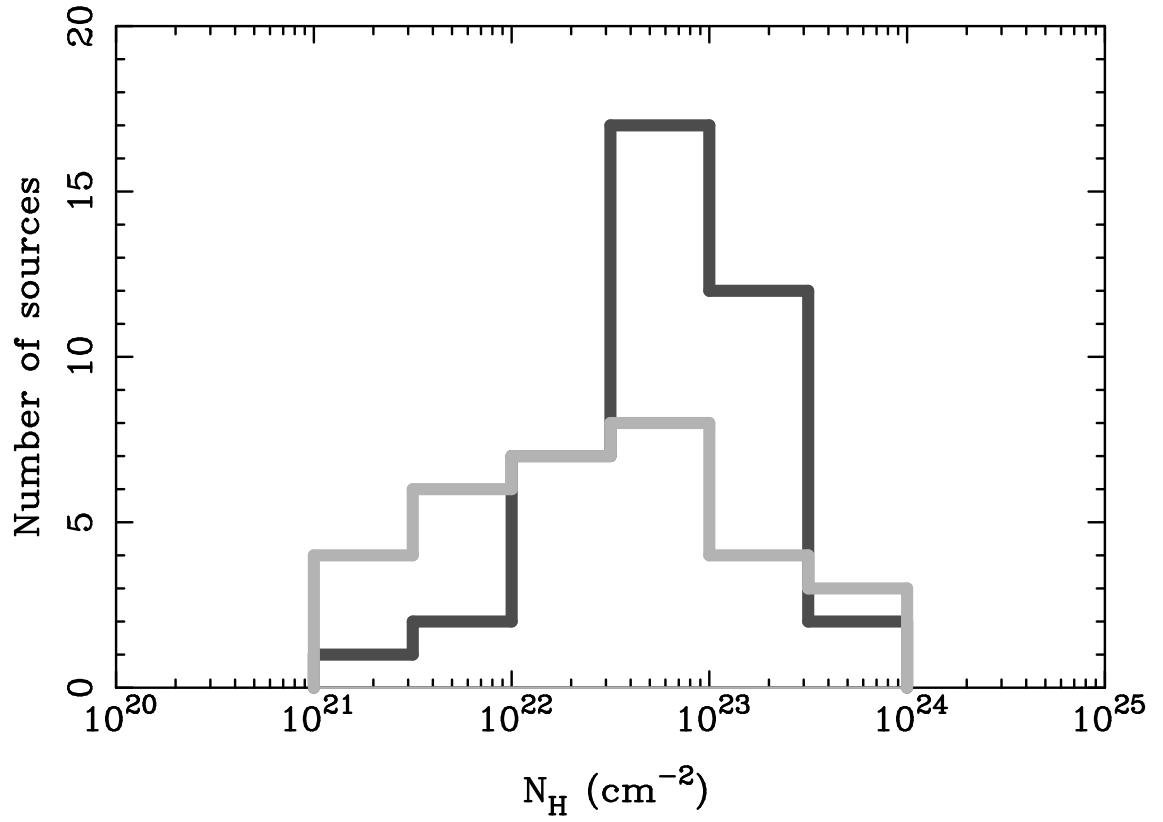


Figure 6.11 X-ray Column density distributions for the optically-dull (*dark histogram*) and optically-active (*light histogram*) AGN with absorption-corrected X-ray luminosities below 10^{44} erg s^{-1} . A K-S test shows the two distributions are different at the 95% confidence level; adding back in the QSOs increases the significance.

ratio consistent with a wide range of inclination angle, but that the subset with optical emission lines have a much narrower range of b/a , which is consistent with occurring either in nearly face-on galaxies, or in spheroid-dominated galaxies. Since at $z = 1$, the observed 2–8 keV band samples rest-frame 4–16 keV energies, the Chandra-selected AGN in the deep fields are selected by fairly hard X-rays, and thus it is not surprising that they, like local hard X-ray-selected samples, show a large range of axis ratio. Redshift will also act to increase the net obscuration in the observed optical wavelengths of these sources, which should increase the disparity between optically-selected and hard X-ray-selected samples. In addition, bright diagnostic lines like $H\alpha$ are redshifted out of the optical bands, further increasing the disparity. Therefore, we propose that the selection effects demonstrated in McLeod & Rieke (1995) for local AGN explain many of the “optically-dull” AGN: they are missing narrow emission lines due to absorption by extranuclear dust in their host galaxies.

This behavior has been modeled by Maiolino & Rieke (1995) (see their figure 3). They show that the expected distribution for an unbiased sample of b/a ratios for randomly oriented disk galaxies is very similar to the distribution of b/a ratios we measure in figure 6.10 using Galfit. They also demonstrate that, when observations are deep enough to provide a virtually complete sample independent of orientation, then the distribution of b/a for local Seyfert galaxies follows this distribution. The local Type 1 galaxies all have b/a near 1, while the galaxies with significantly smaller b/a are observed to be preferentially types 1.8, 1.9, and 2, thus directly demonstrating the influence of obscuration in the galaxy disk.

To be precise, the obscuration hypothesis predicts that b/a should be biased against face-on galaxies. Such a bias is not seen in figure 6.10, although the sam-

ple size is too small to test the detailed shape of the distribution. The handful of high b/a sources in the $0.5 < z < 0.8$ optically-dull sample are consistent with having spectral dilution explain their optical dullness; they are centrally concentrated, and have higher-than-average M_R/L_x (at low significance given the small sample size).

Maiolino & Rieke (1995) also demonstrated that the proportion of missing AGN—or optically dull X-ray sources—depends critically on the quality of the spectra used for classification. For the nearby Seyferts in the Revised Shapley Ames catalog, the bias is almost absent, while there is a strong bias in the more distant CfA sample. The small proportion of optically dull X-ray galaxies in recent studies, as described in §6.5.1, is probably a result of the high quality spectra that can be obtained on relatively nearby galaxies.

For standard dust-to-gas ratios, this picture suggests that a considerable fraction of the column that obscures the soft X-rays may come from outside the obscuring torus. This complicates attempts to interpret X-ray column as a proxy for accretion disk inclination, as well as attempts to use obscured-to-unobscured AGN ratios to estimate torus geometries. In this picture, X-ray column is not solely a description of the nuclear obscuration, but of the galactic obscuration as well. This complex extinction geometry should be included in studies relating high-redshift AGN to the X-ray background, for example.

Also, this picture may partially explain the lack of dependence of the hard X-ray to $24\ \mu\text{m}$ flux ratio on the X-ray hardness ratio (a proxy for column density). If many X-ray sources are partially obscured by gas and dust far away from the AGN, then the dust will not be heated sufficiently to emit in the mid-infrared. Thus, having the obscuration take place in the host galaxy as well as the torus will dilute the signatures of torus obscuration that were searched for, but not

seen, in Rigby et al. (2004) and Lutz et al. (2004).

6.8 Conclusions

We have investigated the column densities, X-ray and IR luminosities, and morphologies of 45 X-ray–selected AGN in the CDFS that lack optical AGN emission lines (and are thus termed “optically–dull AGN”).

We test whether these sources are low–luminosity AGN in very luminous galaxies; this would support the hypothesis that the AGN emission lines are drowned out by bright galactic continua (“dilution”). Fifty-six percent of our sample have rest frame R-band luminosities no more than ~ 6 times larger than that expected for the AGN (scaling from the X-ray luminosity), and thus *we conclude that dilution is not the primary cause of optical dullness* for at least half the sample. This should be contrasted with the bright $z \sim 0.2$ optically–dull AGN of Comastri et al. (2002), which have high optical–to–X-ray flux ratios that make dilution likely.

About half of the local weak–line AGN have column densities much lower than those of the CDFS sample ($\log N_H < 22 \text{ cm}^{-2}$). In addition, it has been shown that dilution can account for the optical dullness of many of these low–redshift galaxies. Thus, they are not true analogues to the $z \sim 1$ population.

Optically–dull AGN have the normal mid–infrared emission we expect from Seyfert galaxies; in short, they look like AGN at $24 \mu\text{m}$. Since AGN IR emission is powered by UV continua, it is likely that they have normal amounts of UV emission.

We test whether the morphologies of optically–dull AGN are atypical. The optically–dull AGN have host galaxies with a large range of inclination angle, whereas the optically–active AGN hosts are nearly–face-on spirals or spheroids

(and thus should have less dust extinction). From this, we conclude that X-ray-selected AGN in deep fields are selected fairly independently of their inclination angle, but that only the most face-on or spherical show optical emission lines. In the rest, extranuclear dust in the host galaxy may obscure the narrow-line regions. This scenario is consistent with samples of Seyferts in the local universe, where hard X-ray and mid-IR-selected samples have unbiased b/a distributions, but optically-selected samples of Seyfert 1 and 2 AGN are systematically biased against inclined disk galaxies.

Thus, part of the column density that obscures the soft X-rays may come from the host galaxy, outside the obscuring torus. This complicates using the X-ray column to infer torus properties. It may also partially explain why the mid-infrared to X-ray luminosity ratio does not depend on column density in AGN.

Thus, we conclude that host galaxy obscuration is the primary cause of optical dullness, with spectral dilution a likely contributor for sources with high optical to absorption-corrected X-ray luminosity ratios.

CHAPTER 7

CONCLUSIONS, CONTEXTUALIZATION, AND FUTURE DIRECTIONS

We now summarize the key results of the previous chapters, their relationship to other work, and outline some directions for future progress.

7.1 Starburst Effective Temperature and the Starburst Initial Mass Function

The main results of chapter 2 were: a) the validation of mid-IR forbidden line ratios as diagnostics of the hardness of the ionizing radiation field; and b) that ISO [NeIII] 15.6 μm /[NeII] 12.8 μm line ratios in 27 nearby starburst galaxies indicate softer ionizing fields than would be produced by young starbursts containing very massive stars. This new interpretation of the ISO spectra was enabled by the availability of new UV massive star templates (Pauldrach et al., 2001; Hillier & Miller, 1998), which I folded into the photoionization code Cloudy (Ferland, 1997). The low [NeIII]/[NeII] line ratio values led us to conclude either that solar-metallicity starburst galaxies are deficient in high-mass ($\gtrsim 40$) M_{\odot} stars, or that such stars exist, but are heavily embedded such that the mid-infrared lines do not escape or are never created. This idea is based on the observation that in our Galaxy, massive stars spend $\sim 15\%$ of their lifetimes heavily embedded (Kurtz, Churchwell, & Wood 1994), and that the confinement times should be longer in the higher pressures of a starbursting galaxy.

This picture, in which the most massive stars in starbursts are heavily embedded for much of their lifetimes, is consistent with several other lines of evidence from recent work. Valdés et al. (2005) report a deficit of recombination lines in LIRG and ULIRGs compared to IR luminosities; in other words, the star formation rates derived from Paschen α or Brackett γ are considerably less than the

rates derived from the $8\text{ }\mu\text{m}$ – $1000\text{ }\mu\text{m}$ IR luminosity. Those authors searched for and did not find evidence that AGN make up the difference, and consequently suggested that the recombination lines are subject to heavy extinction ($A_V \sim 20$). Consistent results were reported by Goldader et al. (1997), in that ULIRGs had weaker $\text{Br}\gamma$ lines, relative to L_{IR} , than did lower-luminosity galaxies; this indicates a non-linear relationship between $L(\text{Bracket } \gamma)$ and L_{IR} , that could well be due to heavy obscuration.

This work can be extended using the Infrared Spectrograph (IRS) onboard Spitzer. IRS has been used in the SINGS Legacy program to spectrally map the nuclei and extended regions of 75 nearby galaxies. Resulting forbidden mid-IR line ratio maps for these galaxies should test how strongly the result we report in chapter 2 was affected by averaging line ratios over the large ($14''$ by $27''$) slit of SWS/ISO. In addition, for low-metallicity galaxies, where high ISO line ratios indicated that large numbers of massive stars indeed contribute to the ionizing field, Spitzer should enable spatial mapping of ionizing fields, so that we may understand where massive stars reside in the context of an extended, spatially resolved starburst galaxy. As an example case, Devost et al. (2004) clearly detect radial gradients of the ionizing radiation, as measured by NeIII/NeII in NGC 253, which they attribute to a metallicity gradient.

The photoionization models we developed in chapter 2 can also be used for an additional purpose—to search for AGN—by identifying the ranges of line ratios that can only be produced by the very hard ionizing radiation of an AGN, and not by those of massive stars. This follows the success of previous AGN/starburst line diagnostic diagrams, e.g. Genzel et al. (1995). Such diagrams should aid analysis of nuclear spectroscopy of active galaxies with IRS/Spitzer, for example Seyfert nuclei with very high $[\text{NeIII}]/[\text{NeII}]$ line ratios (V. Gorjian private com-

munication.)

7.2 Infrared SEDs of X-ray–Selected AGN, and Nuclear Geometry

Chapters 3 and 6 showed that highly X-ray–obscured AGN are no more luminous in the mid-infrared (given their absorption–corrected X-ray luminosity) than low–obscuration AGN. This result has several ramifications. First of all, this suggests that highly X-ray–obscured AGN will not be particularly easy to find in deep surveys by their mid–IR fluxes alone. Multiple bands will be needed, so that sources can be selected by their spectral shapes. In shallow surveys the task may be easier (Barmby et al., 2006; Stern et al., 2005), since the brightest $24\ \mu\text{m}$ sources are often AGN.

Why is it that, over a wide range of redshift and luminosity, AGN show a consistent range of $L_x/L_{6\ \mu\text{m}}$ values, and that these values do not correlate with X-ray column density? Lutz et al. (2004) reported this behavior in $z \sim 0$ AGN; we report this behavior in chapters 3 and 6 for $z \gtrsim 1$ X-ray–selected AGN; and the same trends can be seen in the table of data from Sturm et al. (2006). Since L_x is absorption–corrected, it should not depend on N_H . Therefore, the lack of correlation means that the mid–infrared luminosity does not depend strongly on N_H . There is evidence that $24\ \mu\text{m}$ emission from AGN is optically thick (Shi et al., 2005); given that, the lack of correlation of L_{IR} with N_H means that the surface area of the IR-emitting region is rather constant with orientation angle—in other words, the IR-emitting region should look fairly isotropic. How can this be accomplished?

Models of the gas and dust distribution around supermassive black holes are constrained by timing arguments (e.g. Rieke & Lebofsky 1979) as well as dynamical arguments (e.g. large volumes of gas and dust at large radii would

be more massive than the black hole). Within these constraints, solutions to the lack of L_{IR} – N_H correlation would be for the infrared to be emitted from a quasi-spherical cloud or flared disk, outside the dust sublimation radius. Flared disk and torus models are currently in fashion (Fritz et al., 2006; van Bemmell & Dullemond, 2003; Manske et al., 1998; Efstathiou & Rowan-Robinson, 1995), and were invoked by Shi et al. (2006) to explain the observed correlation between the strength of the $10\ \mu\text{m}$ silicate feature and X-ray column density. Very flared disks can produce quasi-isotropic IR emission, and thus can explain the observed lack of correlation.

7.3 Redshift Distribution of X-ray–Selected AGN

Chapter 5 addressed the question of why 20% of X-ray–selected AGN in deep surveys have X-ray–to–optical flux ratios much higher than observed in local AGN. This question is important because the redshift distribution of X-ray–selected AGN is known through optical spectroscopy, which cannot generally be obtained for optically–faint AGN at $z \sim 1$. Optically–faint AGN had been proposed to lie at very high ($z \sim 5$) redshift (Koekemoer et al., 2004), which would alter the redshift distribution of AGN, and thus change one of the basic inputs to models of the X-ray background, as well as to our understanding of when most black holes were accreting.

In chapter 5, we used $0.4 < \lambda < 8\ \mu\text{m}$ SEDs of optically–faint AGN to constrain their redshifts, and found that optically–faint AGN lie at systematically higher redshifts (median $z = 1.6$) than most X-ray–selected AGN (median $z = 1$.) While these new redshifts double the number density of known $z > 1$ X-ray–selected AGN, they do not seriously alter the redshift distribution. Mainieri et al. (2005) estimated similar ranges of photometric redshifts, using optical and near-IR pho-

tometry. Thus, the *rest-frame* optical-to-near-IR SEDs of optically-faint AGN reveal them to have moderate redshifts. Though Chandra and XMM are sensitive to AGN at very high ($z > 3$) redshifts, such AGN do not appear to be common.

The scientific problem attacked in chapter 5 required only crude photometric redshift estimates. There is much effort in the community at present to develop precise, accurate photometric redshift algorithms based on Spitzer + near-IR + optical SEDs ($0.4 < \lambda < 8 \mu\text{m}$), as this is an obviously important problem (Caputi et al., 2006; Pérez-González et al., 2005). One complication is IR-luminous galaxies at moderate to high redshifts show a wide diversity of SEDs; thus, algorithms that rely on local templates can be led astray. This is another motivation to better catalog the observed SEDs of star-forming galaxies and AGN, as in chapter 4.

One eventual outcome of chapter 5 and related work is to fold back into models of the X-ray background this better understanding of the true redshift distribution of X-ray-selected AGN. We will discuss this in more detail below.

7.4 Nuclear and Host Galaxy Obscuration of AGN

Chapter 6 examined why X-ray and optical selection of AGN return very different samples—specifically, why half of X-ray-selected AGN in deep surveys lack evidence for non-star-forming nuclear activity in their optical spectra. We found that such AGN have normal mid-IR luminosities for active galaxies, and thus show indirect evidence of having typical UV and optical AGN continua; this argues against the hypothesis that optically-dull AGN lack narrow lines because they have weak ionizing continua that cannot excite narrow line regions. Also, we found that less than half the galaxies in our sample have rest-frame R-band stellar continua bright enough that the AGN lines are likely to have been washed out. We also found that the host galaxies of optically-dull AGN have axis ratios

consistent with random inclinations, whereas the host galaxies of optically-active AGN are very round, consistent with face-on or spheroidal galaxies. Thus, extinction from host galaxies is likely to cause much of the observed phenomenon of “optical-dullness”.

The hypothesis that host galaxy extinction is important can be tested by obtaining near-IR spectra of optically-dull AGN. If host galaxy obscuration extinguishes the blue AGN lines available to optical spectroscopy at moderate redshift, then the redder lines should be more robust to extinction, and thus near-IR spectra should reveal AGN-like values of classic line ratio diagnostics such as $H\alpha$ to $[N\ II]\ 6583\ \text{\AA}$ or $[S\ II]\ 6717,6731\ \text{\AA}$. If host galaxy extinction is indeed important, then X-ray and infrared background models need to start incorporating it.

Since optical dullness can be explained by observational effects and host galaxy extinction, there’s no need for the optical/UV continua of AGN to have evolved from $z \sim 0$ to $z \sim 1$. However, evolution of other AGN properties has been reported: Barger et al. (2005) find that the obscured/unobscured AGN ratio does evolve with redshift. Ballantyne et al. (2006) have argued that the evolution of the obscured fraction is driven by star formation: in the past, the higher merger and star formation rates meant that more galaxies had disturbed extra-planar gas and dust that could absorb light from the central source. In this picture, the disturbed gas is responsible for obscuring the central source, and a central obscuring geometry (e.g. a Unification-style torus) is not required or at least is less important. A similar picture has been proposed by Hopkins et al. (2006). In both of these pictures, the Unification paradigm, which explains much behavior of local AGN, becomes much less important at $z \sim 1$, and the role of AGN-obscurer is instead played by merger-disrupted gas and dust. It’s important to this discussion that we find host galaxies play a significant role in obscuring the central

black holes in $z \sim 1$ galaxies, as they do at $z \sim 0$. More detailed morphological studies (including, if possible, adaptive optics imaging of nuclei) are needed to determine whether the obscuring column is circumnuclear or extra-nuclear. In addition, several groups are already testing whether star-formation and black hole accretion are indeed as temporally correlated as these theoretical models predict (Kauffmann et al., 2003; Ho, 2005; Kim et al., 2006). Thus, these investigations will test the relevance of AGN Unification in the distant universe, and test how tight is the phenomenological linkage between black hole accretion and star formation.

7.5 Missing and Highly Obscured AGN

This thesis concentrated on AGN that were selected by hard X-rays. But especially from an infrared perspective, it's important to find the most obscured AGN, which should be largely missing from current Chandra and XMM surveys.

It is likely that such “missing” AGN are very common in the universe. Locally, 40% of AGN are so obscured by such thick columns ($N_H > 10^{24} \text{ cm}^{-2}$) that very few $\gtrsim 8 \text{ keV}$ photons escape (Risaliti et al., 1999; Maiolino & Rieke, 1995; Comastri, 2004), as demonstrated in figure 7.1. If these “Compton-thick” AGN were moved to $z \sim 1$, Chandra would miss almost all of them. Such AGN are indeed thought to be roughly as common at $z = 1$ as at $z = 0$ (Comastri et al., 2001; Gilli et al., 2001; Ueda et al., 2003), in order for X-ray background models to properly fit the shape of the XRB's $E \sim 30 \text{ keV}$ peak. They're also predicted by unification. If such buried AGN exist in the distant universe, they likely make an important contribution to the cosmic IR background, and are missing from current samples of X-ray or optically-selected AGN. Thus, an important extension of this thesis is to develop AGN selection techniques that are not based on X-rays

and are able to select highly-obscured AGN.

X-ray selection works because the coronae of AGN emit copious X-rays, whereas the relics of star formation (supernovae and X-ray binaries) are not bright and numerous enough to produce X-ray luminosities above a few 10^{40} erg s⁻¹ (Hornschemeier et al., 2003). This results in very clean samples, e.g. only a few bright sources will not be AGN. However, the method is not complete, because large obscuring columns ($N_H \gtrsim 10^{24}$ cm⁻²) will, through a combination of photoelectric absorption and Compton scattering, absorb almost all $E < 8$ keV photons, and thus render such sources undetectable to Chandra or XMM.

Several new methods have recently been developed to select AGN, in order to test the reliability of X-ray selection and find very obscured AGN. Some of these new methods focus on the mid-infrared spectral shapes of AGN (Stern et al., 2005; Alonso-Hererro et al., 2006). The principle at work is that the SEDs of star-forming galaxies have two humps, one stellar (peaking at $1.6 \mu\text{m}$), and one from thermal dust emission (peaking in the mid to far IR). Between these two peaks is a nadir at $5 \mu\text{m}$. By contrast, AGN have hot dust that emits at a wide range of temperatures, which acts to simulate a power-law shape and fill in the $5 \mu\text{m}$ nadir. Thus, AGN can be selected by their power-law mid-IR colors. Of the AGN selected in this way, 47% lack X-ray detections in 1 Ms exposures (Alonso-Hererro et al. 2006, J. Donley private communication.)

Another new way to select AGN is by the ratio of their radio to mid-infrared fluxes. The principle at work is that star-forming galaxies and radio-quiet AGN follow the radio-IR correlation. By contrast, some AGN have “radio excesses” due to jets, and thus have radio/IR fluxes that exceed the radio-IR correlation. Donley et al. (2005) selected AGN on this principle, finding 27 AGN candidates in HDF-N. Of these, 60% lacked X-ray detections in the 2 Ms Chandra catalog,

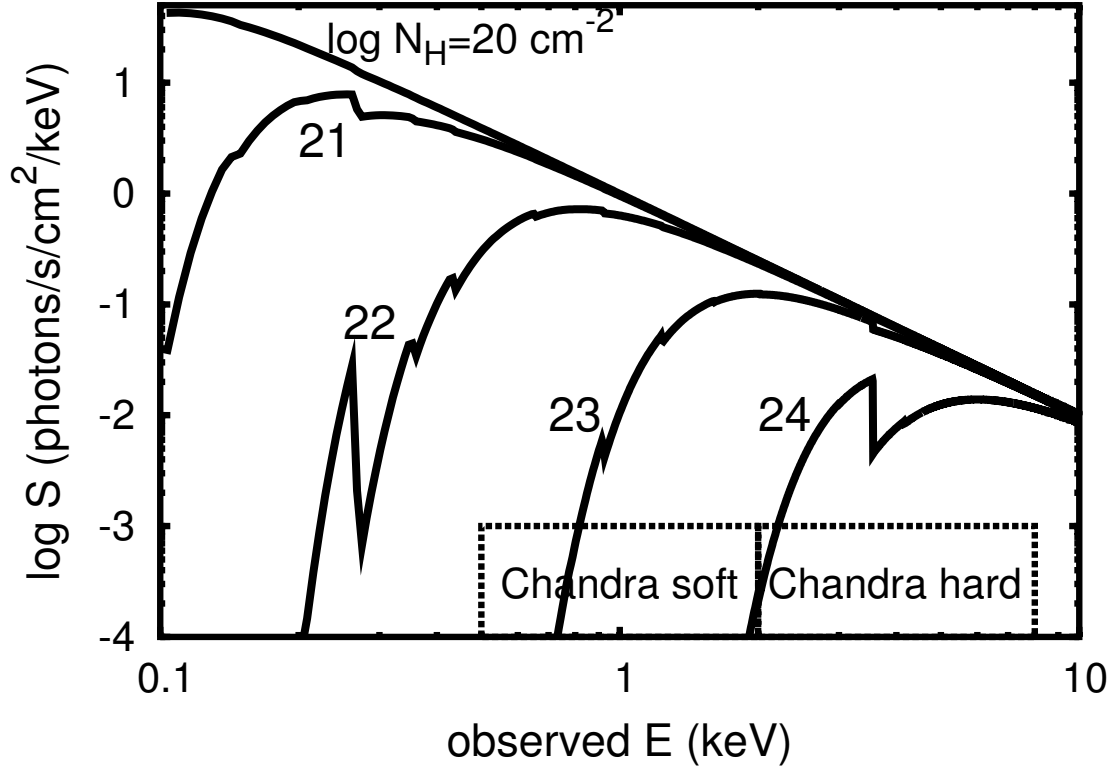


Figure 7.1 Effect of photoelectric absorption and Compton scattering by intervening gas on a typical AGN spectrum ($f_\nu \propto \nu^{-1}$). Source and gas are at $z = 1$; boxes mark the observed *Chandra* 0.5–2 and 2–8 keV bands, which for a source redshift of $z = 1$ correspond to rest-frame energies of 1–4 and 4–16 keV. The emergent spectrum is shown for five values of column density, from $N_H = 10^{20} \text{ cm}^{-2}$ to $N_H = 10^{24} \text{ cm}^{-2}$. Note that a Compton-thick column ($N_H = 10^{24} \text{ cm}^{-2}$) completely suppresses the soft band, and significantly suppresses the hard band. As a result, *Chandra* can detect very few distant, Compton-thick AGN. The absorption is even stronger for lower- z sources, since lower rest energies are probed.

and are therefore interesting as potentially highly-obscured AGN.

Once these new AGN-selection methods have been further developed, the next step will be to synthesize the results of different selection methods, understand the overlap, and develop the most complete AGN sample possible. We can then better understand the frequency of buried AGN among IR-luminous star-forming galaxies, and better measure the total bolometric output of AGN and their contribution to the IR background. New models of both the IR and X-ray backgrounds could then be developed that use several new ingredients: the most complete AGN sample possible (using multiple selection techniques); new measurements of the AGN redshift distribution (e.g. chapt. 5); the true range of observed AGN SEDs (e.g. chapters 4, 5, and 6); and a better understanding of the relative contribution to the SED from reprocessed light from AGN versus star-formation; and how that contribution depends on IR luminosity. We will then have a much firmer understanding of the sources that create the infrared and X-ray backgrounds, in terms of star formation and black hole accretion histories, and the inter-relatedness of the two processes.

REFERENCES

- Aannestad, P. A. 1989, *ApJ*, 338, 162
- Achtermann, J. M., & Lacy, J. H. 1995, *ApJ*, 439, 163
- Akiyama, M., Ueda, Y., Ohta, K., Takahashi, T., & Yamada, T. 2003, *ApJS*, 148, 275
- Alexander, D. M. et al. 2001, *ApJ*, 554, 18
- Alexander, D. M., Aussel, H., Bauer, F. E., Brandt, W. N., Hornschemeier, A. E., Vignali, C., Garmire, G. P., & Schneider, D. P. 2002, *ApJL*, 568, L85
- Alexander, D. M., Brandt, W. N., Hornschemeier, A. E., Garmire, G. P., Schneider, D. P., Bauer, F. E., & Griffiths, R. E. 2001, *AJ*, 122, 2156
- Alexander, D. M., et al. 2003, *AJ*, 126, 539
- Alonso-Herrero, A., Rieke, G. H., Rieke, M. J., & Scoville, N. Z. 2000, *ApJ*, 532, 845
- Alonso-Herrero, A., Engelbracht, C. W., Rieke, M. J., Rieke, G. H., & Quillen, A. C. 2001, *ApJ*, 546, 952
- Alonso-Herrero, A., Quillen, A. C., Rieke, G. H., Ivanov, V. D., & Efstathiou, A. 2003, *AJ*, 126, 81
- Alonso-Herrero et al. 2004, *ApJS*, 154, 155
- Alonso-Herrero, A. et al. 2006, *ApJ*, in press
- Andersen, J. 1991, *A&A Rev.*, 3, 91
- Armus, L., Heckman, T. M., & Miley, G. K. 1989, *ApJ*, 347, 727

- Arnouts, S., Vandame, B., Benoist, C., Groenewegen, M. A., da Costa, L., Schirmer, M., Mignani, R. P., & Slijkhuis, R. 2002, *VizieR Online Data Catalog*, 337, 90740
- Ballantyne, D. R., Everett, J. E., & Murray, N. 2006, *ApJ* in press
- Barmby, P., et al. 2006, *ApJ* in press
- Barger, A. J., Cowie, L. L., Bautz, W., Brandt, W. N., Garmire, G. P., Hornschemeier, A. E., Ivison, R. J., & Owen, F. N. 2001, *AJ*, 122, 2177
- Barger, A. J., Cowie, L. L., Mushotzky, R. R., & Richards, E. A. 2001, *AJ*, 121, 662
- Barger, A. J., et al. 2003, *AJ*, 126, 632
- Barger, A. J., Cowie, L. L., Mushotzky, R. F., Yang, Y., Wang, W.-H., Steffen, A. T., & Capak, P. 2005, *AJ*, 129, 578
- Bashkin, S., & Stoner, J. O. 1975, *Atomic Energy Levels and Grotrian Diagrams*, Vol. 1 (Amsterdam: North-Holland Pub.)
- Beck, S. C., Kelly, D. M., & Lacy, J. H. 1997, *AJ*, 114, 585
- Beck, S. C., Turner, J. L., & Kovo, O. 2000, *AJ*, 120, 244
- Bertin, E. & Arnouts, S. 1996, *A&AS*, 117, 393
- Bono, G., Balbi, A., Cassisi, S., Vittorio, N., & Buonanno, R. 2002, *ApJ*, 568, 463
- Boker, T., Forster-Schreiber, Natascha M., Genzel, R. 1997, *AJ*, 114, 1883
- Boyle, B. J., Fong, R., Shanks, T., & Peterson, B. A. 1987, *MNRAS*, 227, 717
- Bregman, J. N., Glassgold, A. E., Huggins, P. J., & Kinney, A. L. 1985, *ApJ*, 291, 505

- Brusa, M., et al. 2005, *A&A*, 432, 69
- Caputi, K. I., et al. 2006, *ApJ*, in press (astro-ph/0510070)
- Cardelli, J. A., Clayton, G. C., & Mathis, J. S. 1989, *ApJ*, 345, 245
- Chandar, R., Leitherer, C., Tremonti, C., Calzetti, D. 2003, *ApJ*, 586, 939
- Chary, R. & Elbaz, D. 2001, *ApJ*, 556, 562
- Chernoff, D. A. & Weinberg, M. W. 1990, *ApJ*, 351, 121
- Comastri, A. 2004, astro-ph/0403693
- Comastri, A., Setti, G., Zamorani, G., Hasinger, G. 1995, *A&A*, 296, 1
- Comastri, A., Fiore, F., Vignali, C., Matt, G., Perola, G., La Franca, F. 2001, *MNRAS*, 327, 781
- Comastri, A. et al. 2002, astro-ph/0203019
- Comastri, A., et al. 2002, astro-ph/0211306
- Cowie, L. L., Barger, A. J., Brandt, W. N., & Garmire, G. P. 2003, *ApJL*, 584, L57
- Cox, A. N. 2000, *Allen's Astrophysical Quantities*, 4th ed. Publisher: New York: AIP Press; Springer, 2000
- Cristóbal-Hornillos, D., Balcells, M., Prieto, M., Guzmán, R., Gallego, J., Cardiel, N., Serrano, Á., & Pelló, R. 2003, *ApJ*, 595, 71
- Crowther, P. A., Beck, S. C., Willis, A. J., Conti, P. S., Morris, . W., & Sutherland, R. S. 1999, *MNRAS*, 304, 654

- De Pree, C. G., Rodríguez, L. F., & Goss, W. M. 1995, *Rev. Mexicana Ast. y Ast.*, 31, 39.
- Devost, D., et al. 2004, *ApJS*, 154, 242
- Devriendt, J., Guiderdoni B. & Sadat, R. 1999, *A&A*, 350, 381
- Diaz, A. I., Terlevich, E., Pagel, B. E., Vilchez, J. M., & Edmunds, B. E. 1990, *RMxAA*, 21, 223
- Doherty, R. M., Puxley, P. J., Lumsden, S. L., & Doyon, R. 1995, *MNRAS*, 277, 577
- Doyon, R., Puxley, P. J., & Joseph, R. D. 1992, *ApJ*, 397, 117
- Dole, H., et al. 2004, *ApJS*, 154, 93
- Donley, J. L., Rieke, G. H., Rigby, J. R., & Pérez-González, P. G. 2005, *ApJ*, 634, 169
- Egami, E. et al. 2004, *ApJS*, 154, 130
- Elbaz, D., Cesarsky, C. J., Chanial, P., Aussel, H., Franceschini, A., Fadda, D., & Chary, R. R. 2002, *A&A*, 384, 848
- Elvis, M. et al. 1994, *ApJS*, 95, 1
- Elvis, M., Risaliti, G., & Zamorani, G. 2002, *ApJL*, 565, L75
- Engelbracht, C. W. 1996, Supplement to Data Reduction for FSpec, Univ. Arizona Internal Report
- Engelbracht, C. W., Rieke, M. J., Rieke, G. H., & Latter, W. B. 1996, *ApJ*, 467, 227
- Engelbracht, C. W. 1997, Ph.D. Dissertation, Univ. Arizona
- Engelbracht, C. W., Rieke, M. J., & Rieke, G. H. 1998, *ApJ*, 505, 639

- Efstathiou, A., & Rowan-Robinson, M. 1995, MNRAS, 273, 649
- Fadda, D., Flores, H., Hasinger, G., Franceschini, A., Altieri, B., Cesarsky, C. J., Elbaz, D., & Ferrando, P. 2002, A&A, 383, 838
- Fazio, G. G., et al. 2004, ApJS, 154, 10
- Ferland, G. J. 1997, Hazy, Univ. Kentucky Internal Report
- Feuchtgruber, H. et al. 1997, ApJ, 487, 962
- Feuchtgruber, H., Lutz, D., Beintema, D. 2001, ApJS, 136, 221
- Figer, D. F., et al. 2002, ApJ, 581, 258
- Filippenko, A. V. 1988, Advances in Space Research, 8, 5
- Fiore, F., et al. 2001, MNRAS, 327, 771
- Fiore, F., et al. 2003, A&A, 409, 79
- Förster Schreiber, N. M., Genzel, R., Lutz, D., Kunze, D., & Sternberg, A. 2001, ApJ, 552, 544
- Franceschini, A., Fadda, D., Cesarsky, C. J., Elbaz, D., Flores, H., Granato, G. L. 2002, ApJ, 568, 470
- Fritz, J., Franceschini, A., & Hatziminaoglou, E. 2006, MNRAS, 366, 767
- Galavis, M. E., Mendoza, C., & Zeippen, C. J. 1997, A&A Supplement, 123, 159
- García-Segura, G., & Franco, J. 1996, ApJ, 469, 171.
- Garnett, D. R. 1989, ApJ, 345, 282
- Genzel, R., & Cesarsky, C. J. 2000, ARA&A, 38, 761

- Genzel, R., Weitzel, L., Tacconi-Garman, L. E., Bleitz, M., Cameron, M., Krabbe, A., Lutz, D., & Sternberg, A. 1995, *ApJ*, 444, 129
- Genzel, R., et al. 1998, *ApJ*, 498, 579
- Giacconi, R., et al. 2002, *ApJS*, 139, 369
- Giavalisco, M., et al. 2004, *ApJ*, 600, L93
- Gies, D. R., Penny, L. R., Mayer, P., Drechsel, H., & Lorenz, R. 2002, *ApJ*, 574, 957
- Gilli, R. 2004, *Adv Space Res.*, in press (astro-ph/0303115)
- Gilli, R., Risaliti, G., & Salvati, M. 1999, *A&A*, 347, 424
- Gilli, R., Salvati, M., & Hasinger, G. 2001, *A&A*, 366, 407
- Giveon, U., Sternberg, A., Lutz, D., Feuchtgruber, H., & Pauldrach, A. W. 2002, *ApJ*, 566, 880
- Goldader, J. D., Joseph, R. D., Doyon, R., & Sanders, D. B. 1997, *ApJ*, 474, 104
- González Delgado, R., García-Vargas, M. L., Goldader, J., Leitherer, C., & Pasquali, A. 1999, *ApJ*, 513, 707
- González Delgado, R., Leitherer, C. L., Stasińska, G., & Heckman, T. M. 2002, *ApJ*, 580, 824
- Gordon, K. D. et al. 2005, *PASP*, 117, 503
- Guseva, N. G., Izotov, Y. I., & Thuan, T. X. 2000, *ApJ*, 531, 776
- Haas, M. et al. 2003, *A&A*, 402, 87
- Hameed, S. & Devereus, N. 1999, *AJ*, 118, 730

- Hammer, F., et al. 1997, *ApJ*, 481, 49
- Hanson, M. M., Luhman, K., L., & Rieke, G. H. 2002, *ApJS*, 138, 35
- Hasinger, G., et al. 2001, *A&A*, 365, L45
- Hauser, M. G., & Dwek, E. 2001, *ARA&A*, 39, 249
- Heckman, T. M. 1997, in *Star Formation Near and Far*, ed. S. S. Holt & L. G. Mundy (Wodbury, NY: AIP Press), 271
- Hillier, D. J., & Miller, D. L., 1999, *ApJ*, 496, 407
- Ho, L. C. 2005, *ApJ*, 629, 680
- Ho, P. T., Beck, S. C., & Turner, J. L. 1990, *ApJ*, 349, 57
- Ho, L. C., Filippenko, A. V., & Sargent, W. L. W. 1997, *ApJS*, 112, 315
- Hopkins, P. F., Hernquist, L., Cox, T. J., Di Matteo, T., Robertson, B., & Springel, V. 2006, *ApJS*, in press
- Hornschemeier, A. E. et al. 2001, *ApJ*, 554, 742
- Hornschemeier, A. E., et al. 2003, *AJ*, 126, 575
- Hornschemeier, A. E., Heckman, T. M., Ptak, A. F., Tremonti, C. A., & Colbert, E. J. M. 2005, *AJ*, 129, 86
- Huang, J.-S. et al. 2004, *ApJS*, 154, 44
- Huchra, J., & Sargent, W. L. 1973, *ApJ*, 186, 433
- Hummer, D. G., & Storey, P. J. 1987, *MNRAS*, 224, 801
- Izotov, Y. I., & Thuan, T. X. 1998, *ApJ*, 500, 188

- Kauffmann, G., et al. 2003, MNRAS, 346, 1055
- Keel, W. C. 1980, AJ, 85, 198
- Kennicutt, R. C., 1998, ARA&A, 36, 189
- Kennicutt, R. C., 1998, in ASP Conf. Ser. 142, The Stellar Initial Mass Function, ed. G. Gilmore & D. Howell (San Francisco: ASP), 61
- Kennicutt, R. C., Bresolin, F., French, H., & Martin, P. 2000, ApJ, 537, 589
- Kent, S. M. 1985, ApJS, 59, 115
- Keto, E. 2002, ApJ, 580, 980.
- Kewley, L., Dopita, M., Evans, I., Groves, B., Sutherland, R., Binette, L., Allen, M., & Leitherer, C. 2006, in preparation
- Kim, M., Ho, L. C., & Im, M. 2006, ApJ, in press (astro-ph/0601316)
- Kobulnicky, H. A., & Johnson, K. E. 1999, ApJ, 527, 154
- Kobulnicky, H. A., Kennicutt, R. C., Jr., & Pizagno, J. L. 1999, ApJ, 514, 544
- Koekemoer, A. M., et al. 2004, ApJ, 600, L123
- Krabbe, A., Sternberg, A., & Genzel, R. 1994, ApJ, 425, 72
- Kunze, D. et al. 1996, A&A, 315, L101
- Kuraszkiewicz, J. K. et al. 2003, ApJ, 590, 128
- Kurtz, S., Churchwell, E., & Wood, D. O. S. 1994, ApJS, 91, 659.
- La Franca, F. et al. 2002, ApJ, 570, 100

- La Franca, F., et al. 2005, *ApJ*, 635, 864
- Le Floc'h, E. et al. 2004, *ApJS*, 154, 170
- Le Floc'h, E., et al. 2005, *ApJ*, 632, 169
- LeFevre et al. 2004, *A&A*, submitted
- Lehmann, I. et al. 2001, *A&A*, 371, 833
- Lehnert, M. D., & Heckman, T. M. 1996, *ApJ*, 472, 546
- Leitherer, C. 1998, in *ASP Conf. Ser. 142, The Stellar Initial Mass Function*, ed. G. Gilmore & D. Howell (San Francisco: ASP), 61
- Leitherer, C., Ferguson, H. C., Heckman, T. M., & Lowenthal, J. D. 1995, *ApJL*, 454, L19
- Leitherer, C. et al. 1999, *ApJS*, 123, 3
- Lejeune, T., Cuisinier, F., & Buser, R. 1997, *A&AS*, 125, 229
- Lester, D. F., Gaffney, N., Carr, J. S., & Joy, M. 1990, *ApJ*, 352, 544
- Lilly, S. J., et al. 1999, *ApJ*, 518, 641
- Lilly, S. J., Carollo, C. M., & Stockton, A. N. 2003, *ApJ*, 597, 730
- Livingston, W. & Wallace L. 1991, N.S.O. Technical Report #91-001
- Lumsden, S. L., Puxley, P. J., & Doherty, R. M. 1994, *MNRAS*, 268, 821
- Lumsden, S. L., Puxley, P. J., & Hoare, M. G. 2001a, *MNRAS*, 320, 83
- Lumsden, S. L., Puxley, P. J., & Hoare, M. G. 2001b, *MNRAS*, 328, 419

- Lutz, D., Maiolino, R., Spoon, H. W., & Moorwood, A. F. 2003, *A&A*, 418, 465
- Maccacaro, T., Gioia, I. M., Wolter, A., Zamorani, G., & Stocke, J. T. 1988, *ApJ*, 326, 680
- Madau, P., Ghisellini, G., & Fabian A.C. 1994, *MNRAS*, 267, L17
- Mainieri, V., Bergeron, J., Hasinger, G., Lehmann, I., Rosati, P., Schmidt, M., Szokoly, G., & Della Ceca, R. 2002, *A&A*, 393, 425
- Mainieri, V., et al. 2005, *A&A*, 437, 805
- Maiolino, R. & Rieke, G. 1995, *ApJ*, 454, 95
- Maiolino, R., Rieke, G. H., & Rieke, M. J. 1996, *AJ*, 111, 537
- Maiolino, R., Ruiz, M., Rieke, G. H., & Keller, L. D. 1995, *ApJ*, 446, 561
- Maiolino, R., et al. 2003, *MNRAS*, 344, L59
- Mal'Kov, Y. F. 1997, *Astronomy Reports*, 41, 760
- Manske, V., Henning, T., & Men'shchikov, A. B. 1998, *A&A*, 331, 52
- Martín-Hernández, N. L., Vermeij, R., van der Hulst, J. M., & Peeters, E. 2002, *A&A*, 389, 286
- Martín-Hernández, N. L., et al. 2002, *A&A*, 381, 606
- Marziani, P., Sulentic, J. W., Zamanov, R., Calvani, M., Dultzin-Hacyan, D., Bachev, R., & Zwitter, T. 2003, *ApJS*, 145, 199
- Marzke et al. 1999, in *PASP Conf. Ser. 191: Photometric Redshifts and Detection of High Redshift Galaxies*, 148

- McLeod, K. K. & Rieke, G. H. 1995, *ApJ*, 441, 96
- Mignoli, M., et al. 2004, *A&A*, 418, 827
- Mihalas, D. 1972, *Non-LTE Model Atmospheres for B and O Stars*, NCAR-TN/STR-76
- Miyaji, T., Sarajedini, V., Griffiths, R. E., Yamada, T., Schurch, M., Cristóbal-Hornillos, D., & Motohara, K. 2004, *AJ*, 127, 3180
- Montgomery, E. F., Connes, P., Connes, J., & Edmonds, F. N. 1969, *ApJS*, 167, 19
- Moran, E. C., Filippenko, A. V., & Chornock, R. 2002, *ApJ*, 579, 71
- Moretti, A., Campana, S., Lazzati, D., & Tagliaferri, G. 2003, *ApJ*, 588, 696
- Morisset, C., 2004, *ApJ*, 601, 858
- Morisset, C., Schaerer, D., Bouret, J.-C., & Martins, F. 2003, *A&A*, 415, 577
- Muno, M. P., et al. 2003, *ApJ*, 589, 225
- Mushotzky, R. F., Cowie, L. L., Barger, A. J., & Arnaud, K. A. 2000, *Nature*, 404, 459
- Nagamine, K. 2002, *ApJ*, 564, 73
- Neugebauer, G., et al. 1984, *Science*, 224, 14
- Niemela, V. S., & Bassino, L. P. 1994, *ApJ*, 437, 332
- Oey, M. S., Dopita, M. A., Shields, J. C., & Smith, R. C. 2000, *ApJS*, 128, 511
- Oke, J. B., Neugebauer, G., & Becklin, E. E. 1970, *ApJ*, 159, 341

- Osterbrock, D. E. 1989, *Astrophysics of Gaseous Nebulae and Active Galactic Nuclei* (Sausalito: University Science Books)
- Osterbrock, D. E., & Pogge, R. W. 1987, *ApJ*, 323, 108
- Ostrov, P. G., Lapasset, E., & Morrell, N. I. 2000, *A&A*, 356, 935
- Papovich, C., et al. 2004, *ApJS*, 154, 70
- Pauldrach, A. W. A., Hoffmann, T. L., & Lennon, M. 2001, *A&A*, 375, 161
- Pauldrach, A. W. A., Lennon, M., Hoffmann, T. L., Sellmaier, F., Kutritzki, R.-P., & Puls, J. 1998, in *ASP Conf. Ser. 131, Properties of Hot Luminous Stars*, ed. I. Howarth (San Francisco: ASP), 258
- Peng, C. Y., Ho, L. C., Impey, C. D., & Rix, H.-W. 2002, *AJ*, 124, 266
- Penzias, A. A., & Wilson, R. W. 1965, *ApJ*, 142, 419
- Pérez-González, P. G., et al. 2005, *ApJ*, 630, 82
- Piccinotti, G., Mushotzky, R. F., Boldt, E. A., Holt, S. S., Marshall, F. E., Serlemittos, P. J., & Shafer, R. A. 1982, *ApJ*, 253, 485
- Pogge, R. 1989, *ApJS*, 71, 433
- Pompilio, F., La Franca, F., & Matt, G. 2000, *A&A*, 353, 440
- Ranalli, P., Comastri, A., & Setti, G. 2003, *A&A*, 399, 39
- Raymond, J. C., Hester, J. J., Cox, D., Blair, W. P., Fesen, R. A., & Gull, T. R. 1988, *ApJ*, 324, 869
- Rieke, G. H. 1978, *ApJ*, 226, 550

- Rieke, G. H. 2000, in Springer Proc. in Physics 88, Starburst Galaxies: Near and Far, ed. L. Tacconi & D. Lutz (Berlin: Springer), 73
- Rieke, G. H., & Lebofsky, M. J. 1979, ARA&A, 17, 477
- Rieke, G. H., & Lebofsky, M. J. 1985, ApJ, 288, 618
- Rieke, G. H., Loken, K., Rieke, M. J., & Tamblyn, P. 1993, ApJ, 412, 99
- Rieke, G. H., Lebofsky, M. J., Thompson R. I., Low, F. J., & Tokunaga, A. T. 1980, ApJ, 238, 24
- Rieke, G. H., et al. 2004, ApJS, 154, 25
- Rigby, J. R., Rieke, G. H., Donley, J. L., Alonso-Herrero, A., & Pérez-González, P. G., 2006, ApJ, submitted
- Rigby, J. R., Rieke, G. H., Pérez-González, P. G., Donley, J. L., Alonso-Herrero, A., Huang, J.-S., Barmby, P., & Fazio, G. G. 2005, ApJ, 627, 134
- Rigby, J. R., et al. 2004, ApJS, 154, 160
- Risaliti, G., Maiolino, R., Salvati, M. 1999, ApJ, 522, 157
- Roche, P. F., Aitken, D. K., Smith, C. H., & Ward, J. M. 1991, MNRAS, 248, 606
- Rousell, H., Sauvage, M., Vigroux, L., & Bosma, A. 2001, A&A, 372, 427
- Rowan-Robinson, M., et al. 2004, MNRAS, 351, 1290
- Rush, B., Malkan, M. A., & Spinoglio, L. 1993, ApJS, 89, 1
- Salpeter, E. E. 1955, ApJ, 121, 161
- Schaerer, D., & de Koter, A. 1997, A&A, 322, 598

- Schaerer, D., de Koter, A., Schmutz, W., & Maeder, A. 1996a, *A&A*, 310, 837
- Schaerer, D., de Koter, A., Schmutz, W., & Maeder, A. 1996b, *A&A*, 312, 475
- Schmidt, M. 1968, *ApJ*, 151, 393
- Schmutz, W., Leitherer, C., & Gruenwald, R. 1992, *PASP*, 104, 1164
- Schinnerer, E., Eckart, A., Quirrenbach, A., Boker, T., Tacconi-Garman, L. E., Krabbe, A., & Sternbert, A. 1997, *ApJ*, 488, 174
- Schneider, D. P., et al. 2005, *AJ*, 130, 367
- Seaquist, E. R., Frayer, D. T., & Bell, M. B. 1998, *ApJ*, 507, 745
- Setti, G., & Woltjer, L. 1989, *A&A*, 224, L21
- Severgnini, P. et al. 2003, *A&A*, 406, 483
- Shi, Y. et al. 2005, *ApJ*, 629, 88
- Shi, Y. et al. 2006, in preparation
- Shields, J. C. 1993, *ApJ*, 419, 181
- Silva, L., Maiolino, R., Granato, G. L. 2004, *MNRAS*, 355, 973
- Smith, L. J., Norris, R. P. F., & Crowther, P. A. 2002, *MNRAS*, 337, 1309
- Soifer, B. T., et al. 1984, *ApJL*, 278, L71
- Spinoglio, L., & Malkan, M. A. 1989, *ApJ*, 342, 83
- Spinoglio, L., Malkan, M. A., Rush, B., Carrasco, L., & Recillas-Crus, E. 1995, *ApJ*, 453, 616

- Stasińska, G. & Leitherer, C. 1996, *ApJS*, 107, 661
- Steffen, A. T., Barger, A. J., Cowie, L. L., Mushotzky, R. F., & Yang, Y. 2003, *ApJL*, 596, L23
- Stern et al. 2005, *ApJ*, 631, 163
- Stickel, M., Rieke, G. H., Kühr, H., & Rieke, M. J. 1996, *ApJ*, 468, 556
- Storchi-Bergmann, T., Kinney, A. L., & Challis, P. 1995, *ApJS*, 98, 103
- Sturm, E., Hasinger, G., Lehmann, I., Mainieri, V., Genzel, R., Lehnert, M. D., & Lutz, D. 2006, *ApJ* in press
- Sugai, H., & Taniguchi, Y., 1992, *AJ*, 103, 1470
- Szokoly, G. P., et al. 2004, *ApJS*, 155, 271
- Thornley, M. D., Förster Schreiber, N. M., Lutz, D., Genzel, R., Spoon, H. W. W. & Kunze, D. 2000, *ApJ*, 539, 641
- Turner, J. L., Ho, P. T. P., & Beck, S. C. 1998, *AJ*, 116, 1212
- Ueda, Y., Akiyama, M., Ohta, K., & Miyaji, T. 2003, *ApJ*, 598, 886
- Vacca, W. D., & Conti, P. S. 1992, *ApJ*, 401, 543
- Vacca, W. D., Johnson, K. E., & Conti, P. S. 2002, *AJ*, 123, 772
- Vaceli, M. S., Viegas, S. M., Gruenwald, R., & de Souza, R. E. 1997, *AJ*, 114, 1345
- Valdés, J. R., Berta, S., Bressan, A., Franceschini, A., Rigopoulou, D., & Rodighiero, G. 2005, *A&A*, 434, 149
- van Bemmell, I. M., & Dullemond, C. P. 2003, *A&A*, 404, 1

- van Hoof, P. A., Beintema, D. A., Verner, D. A., Ferland, G. J. 2000, *A&A*, 354, 41
- Vanzi, L. & Rieke, G. H. 1997, *ApJ*, 479, 694
- Vanzi, L., Rieke, G. H., Martin, C. L., & Shields, J. C. 1996, *ApJ*, 466, 150
- Vílchez, J. M., & Pagel, B. E. J. 1988, *MNRAS*, 231, 257
- Watanabe, S., Akiyama, M., Ueda, Y., Ohta, K., Mushotzky, R., Takahashi, T., & Yamada, T. 2002, *PASJ*, 54, 683
- Webster, B. L., & Smith, M. G. 1983, *MNRAS*, 204, 743
- Werner, M. W., et al. 2004, *ApJS*, 154, 1
- Williams, D. M., Thompson, C. L., Rieke, G. H., & Montgomery, E. F. 1993, *Proc. SPIE*, 1946, 482
- Wilman, R. J., & Fabian, A. C. 1999, *MNRAS*, 309, 862
- Wilman, R. J., Fabian, A. C., & Nulsen, P. E. J. 2000, *MNRAS*, 319, 583
- Wolf, C., et al. 2004, *A&A*, 421, 913
- Worsley, M. A., et al. 2005, *MNRAS*, 357, 1281
- Wu, H., Zou, Z. L., Xia, X. Y., & Deng, Z. G. 1998, *A&A Supplement*, 127, 521
- Yan, H., Windhorst, R. A., Röttgering, H. J., Odewahn, S. C., Chapman, S. C., & Keel, W. C. 2003, *ApJ*, 585, 67
- Zezas, A., Alonso-Herrero, A., & Ward, M. J. 2001, *Ap&SS*, 276, 601
- Zheng, W. et al. 2004, *ApJS*, 155, 73